Geophysical Investigations to Image Crustal Features and Potential Mineralization in the Philippine Island Arc System

メル アンソニー アシス カスラ

出版情報：Kyushu University, 2022, 博士（工学）, 課程博士
バージョン：
権利関係：

Geophysical Investigations to Image Crustal Features and Potential Mineralization in the Philippine Island Arc System

by

Mel Anthony Asis Casulla

A Dissertation Submitted in Partial Fulfillment of
the Requirements for the Degree of

Doctor of Engineering
(Earth Resources Engineering)

Supervised by
Dr. Hideki MIZUNAGA

Exploration Geophysics Laboratory
Department of Earth Resources Engineering
Graduate School of Engineering
Kyushu University
Japan

January 2023

Abstract

The Philippine archipelago is a complex island arc system where many regions still lack geophysical studies. When using geophysical surveys to explore mineral deposits, it is important to conduct both wide-area explorations to narrow down the prospective areas and localized exploration to examine detailed information such as the size and depth of the deposit in the prospective areas. This dissertation describes a wide-area exploration using gravity prospecting for mineralization (e.g., regional geology, structures) in the Philippines and a detailed exploration in Eastern Labo, Bicol, which was chosen as one prospective area.

In the first half of this paper, this research presents the high-resolution isostatic anomaly and free-air anomaly digital grids from the World Gravity Map (WGM). It provides a general discussion of the Philippines' gravity signatures to contribute to an understanding of its regional geology and tectonics. The isostatic anomaly map was continued upward to investigate the high-density ophiolitic basement rocks and low-gravity sedimentary basins at depth. The first vertical derivative (1VD) filter was applied to the free-air anomaly grid map to locate regional structures represented by density contrast boundaries. The depths to the top of the Moho and basement rock over the Sulu Sea were computed using the two-dimensional (2-D) radially-averaged power spectrum analysis. Three-dimensional (3-D) gravity inversion was applied to some significant sedimentary basins in the Philippines to present 3-D subsurface density contrast models. The interpreted gravity maps highlighted prominent geologic features (e.g., trench manifestation, ophiolite distribution, basin thickness). The negative isostatic anomalies (< 0 mGal) represent the thick sedimentary basins, while the moderate signatures (0 to 80 mGal) correspond to the metamorphic belts. The distinct high gravity anomalies (> 80 mGal) typify the ophiolitic basement rocks. The gravity data's upward continuation revealed contrasting deep gravity signatures; the central Philippines with continental affinity (with 20 to 35 mGal) was distinguished from the regions with oceanic affinity (with 45 to 200 mGal). The 1VD map over the Sulu Sea showed anomalies associated with shallow features dominantly related to the Cagayan Ridge. The 2-D radially-averaged power spectrum analysis exposed gravity anomalies with tectonic significance (e.g., basement characterization, Moho depth estimation). The estimated Moho depth in the Sulu Sea is from 12 to 22 km, while the average basement depth is 5 to 11 km. Lastly, the 3-D subsurface density contrast models characterized the low-density zones representing the deep (>7 km) sedimentary basins in the northern Cagayan Valley and southern Central Luzon basins. Furthermore, thin (~ 3.5 km)

sedimentary formations are inferred for the low-density areas in the northern Agusan-Davao and eastern Cotabato basins.

The second half of this paper focuses on the electrical resistivity, and induced polarization (ER-IP) surveys carried out in Eastern Labo, Bicol, Philippines, to assess the potential Cu-Au mineralization overlain by thick pyroclastic deposits. An electrical resistivity tomography (ERT) method with a dipole-dipole array was used, and the L1 norm (robust) inversion approach was employed to generate the sixteen 2-D ER-IP models. The analysis of the resistivity and chargeability classified the underlying lithology into eight zones. Zones from C to F are the potential mineralized zones, while Zones A and B (Labo Volcanic Complex) and Zones G and H (Tumbaga Formation and Tamisan Diorite) are the non-mineralized zones. Zone C, represented by low chargeability (< 15 mV/V) and intermediate resistivity (15 to 100 ohm-m) values, is characterized by a high concentration of disseminated sulfide minerals (e.g., chalcopyrite). Zone D has a chargeability range comparable to Zone C but higher resistivity (> 100 ohm-m), which might be due to silicification. Zone E corresponds to the oxide zone with concentrated sulfide minerals along clayey, weathered, fractured areas; it has moderate to high chargeability (>15 mV/V) and low resistivity (< 15 ohm-m) signatures. Zone F has a similar resistivity range to Zone E but has lower chargeability (< 15 mV/V) values. The interpreted underlying lithological units were confirmed using borehole data. Because of the extensive occurrence of high chargeability zones with moderate resistivity anomalies, potentially mineralized areas for further investigation (e.g., drilling) were identified in the northwestern portion of the study area.

Acknowledgments

I would like to express my appreciation and gratitude to the Department of Environment and Natural Resources - Mines and Geosciences Bureau (DENR - MGB), Philippines, and Japan International Cooperation Agency (JICA) for supporting and financing this study. I also thank the Exploration Geophysics Laboratory members at the Kyushu University - Department of Earth Resource Engineering for their comments and suggestions that improved the scope of my research.

Thank you to my adviser, Dr. Hideki Mizunaga, for his encouragement and constructive criticism of my studies. He provided me with crucial guidance during my scholarship and associated research. I also want to express my gratitude to Dr. Yasuhiro Fujimitsu and Dr. Satoru Yamaguchi for their insightful comments and questions that helped improve my dissertation's quality. Aside from my adviser, I would like to thank Dr. Toshiaki Tanaka and Dr. Koji Hashimoto for their help during my stay in the Exploration Geophysics Laboratory.

Collaboration with researchers and scientists outside Kyushu University greatly increased this work's depth. Dr. Carla Dimalanta (University of the Philippines - Diliman), Mr. Aniano D. Torres (Mines and Geosciences Bureau - Central Office), Ms. Princess Danielle Matas (Mines and Geosciences Bureau - Region 12), Mr. Aeron Elvin Dela Cruz (Mines and Geosciences Bureau - Central Office), and Mr. Nelson Romero (Mines and Geosciences Bureau - Central Office) are greatly appreciated for their contributions to this study (e.g., logistical support for the fieldworks).

I also want to say thank you to my international friends (e.g., Friday Meeting) for the research-related brainstorming and thought-provoking discussions. A particular thanks to Kevin Gutierrez and Pagna Lim; I consider them my brothers here in Japan.

I also want to thank my Paj for her unfailing support from the beginning to the end of my studies. My brothers, Mel Xaviery, Mel Angelo, and Mel Francis, assisted and motivated me in pursuing my research and life goal. Finally, I want to thank my parents, Angelina and Melchor Casulla, for inspiring me to pursue a career in geology and geophysics and teaching me the core values of life. Most of all, I am eternally grateful to God for his unending kindness, mercy, and guidance in my existence on Earth.

Table of Contents

List of Figures

List of Tables

List of Abbreviation

1VD:	First Vertical Derivative
AD:	Agusan-Davao Basin
BGI:	Bureau Gravimetrique International
C:	Cotabato Trench
CP:	Central Philippines
CR:	Cagayan Ridge
CV:	Cagayan Valley Basin
DEM:	Digital Elevation Model
DENR:	Department of Environment and Natural Resources
ELT:	East Luzon Trough
EGM2008:	Earth Gravitational Model 2008
ER-IP:	Electrical Resistivity-Induced Polarization
FAA:	Free-air Gravity Anomaly
GEBCO:	General Bathymetric Chart of the Oceans
ICL:	Ilocos-Central Luzon Basin
JICA:	Japan International Cooperation Agency
KPG:	Cretaceous-Paleogene
LZN:	Luzon
MGB:	Mines and Geosciences Bureau
MDN:	Mindanao
NP:	Neogene Pluton
NS:	Negros and Sulu Trenches
NWB:	Northwest Basin
OUM:	Oligocene-Upper Miocene
PMB:	Philippine Mobile Belt
SEB:	Southeast Basin
SMB:	Sierra Madre Basin
SRTM:	Shuttle Radar Topographic Mission
UTM:	Universal Transverse Mercator
VLF-EM:	Very Low Frequency Electromagnetic
WGM:	World Gravity Map
WGS:	World Geodetic System
ZOE:	Zambales Ophiolite Complex Extension

For I know the plans I have for you," declares the LORD, "plans to prosper you and not to harm you, plans to give you hope and a future.

Jeremiah 29:11

CHAPTER 1
General Introduction

1.1 Background

Geophysical investigation entails methods that use remote measurements of physical properties to determine subsurface information; it involves measuring and interpreting specific physical properties (e.g., density, electrical resistivity) to detect or infer the presence and location of economically valuable geological deposits (e.g., ore minerals, groundwater reservoir). Geophysical methods solve a wide range of problems rapidly, allowing for the investigation of a large area in a reasonable amount of time (Telford et al., 1990; Lowrie, 2007; Milsom and Eriksen, 2011). Geophysical exploration generally employs simple and portable field instruments, making it cost-effective because only physical properties are measured (unlike consuming chemicals for geochemical investigations). Geophysical investigations can also be applied to collect subsurface data for interpreting geologic structures, assessing hydrocarbon potential, and locating pollution contamination at the local and regional scales (Parasnis, 1979; Reynolds, 1997; Hinze et al., 2013; Loke et al., 2013). Many geophysical methods have different applications, including gravity, magnetics, electrical resistivity, seismic, radiometric, and electromagnetics (Table 1-1). For this study, the gravity, electrical-resistivity-induced polarization (ER-IP), and very low frequency-electromagnetics (VLF-EM) were used to investigate subsurface features related to the geology, tectonics and mineralization potential in the Philippine island arc system.

The Department of Environment and Natural Resources (DENR) is the Philippines' primary government agency responsible for appropriately using, developing, managing, and conserving the country's environment and natural resources. It is mandated to ensure equitable sharing of the benefits of natural resources for the welfare of Filipinos' present and future generations. One of its primary objectives is to increase the productivity of natural resources to meet the demands for mineral resources of a growing Filipino population and enhance the contribution of natural resources for achieving national economic and social development (DENR, 2016). The Mines and Geosciences Bureau (MGB) is under the umbrella of the DENR. It is committed to promoting sustainable mineral resources development and contributing to national economic growth and countryside community development (MGB, 2022).

Table 1-1 *Common geophysical techniques with the related physical properties being utilized and their main applications (modified from Reynolds, 1997). Italicized texts are the geophysical methods used in this study.*

Geophysical Method	Physical Property	Primary Applications
Magnetic	Susceptibility	Hydrocarbon exploration, Regional geologic studies, Exploration of mineral deposits
Gravity	Density	Regional geologic studies, Hydrocarbon exploration
Seismic refraction	Density, Elastic moduli	Hydrocarbon exploration, Regional geologic studies, Engineering site investigations
Seismic reflection	Density, Elastic moduli	Hydrocarbon exploration, Regional geologic studies
Spontaneous potential	Potential differences	Exploration of mineral deposits, Hydrogeological investigations
DC resistivity	Resistivity	Exploration of mineral deposits, Engineering site investigations, Hydrogeological investigations, Detection of sub-surface cavities, Mapping of contaminant plumes, Archaeological geophysics
Induced polarization	Resistivity, Capacitance	Exploration of mineral deposits
Electromagnetic (EM)	Conductance, Inductance	Regional geologic studies, Exploration of mineral deposits, Engineering site investigations, Hydrogeological investigations, Detection of sub-surface cavities, Mapping of contaminant plumes, Location of buried metallic objects, Archaeological geophysics
Very Low Frequency (VLF)-EM	Conductance, Inductance	Exploration of mineral deposits
Ground Penetrating Radar (GPR)-EM	Permittivity, Conductivity	Engineering site investigations, Hydrogeological investigations, Detection of sub-surface cavities, Location of buried metallic objects, Archaeological geophysics, Forensic geophysics
Magnetotelluric	Resistivity	Regional geologic studies, Exploration of mineral deposits

The MGB, through the Lands Geological Survey Division (LGSD), manages the national geosciences programs on geoscientific land surveys (e.g., geological mapping, mineral exploration), establishes mineral reservations, and conducts research and development on geosciences. In recent years, the DENR-MGB has intensified its plan to identify more mineral

areas throughout the Philippines for a possible declaration of mineral reservations. The mineral reservation program of MGB focuses on identifying potential areas in the country to be declared as new mineral reservations. The proper scientific assessment of the expansion of the mineral reservations will optimize the nation's benefits in developing and utilizing mineral wealth. The MGB has identified several regions as potential candidates to be declared as new mineral reservation areas, including the extension of Zambales Chromite Mineral Reservation (ZCMR) (Fig. 1-1). Originally, the main goal of this study was to supplement and augment the scientific assessment to declare the extension of ZCMR in Luzon, Philippines, as a new mineral reservation. This research initially aims to generate new detailed geological and geophysical data, estimate the chromite deposits, and propose a subsurface model of the ZCMR extension. Geological and geophysical surveys (e.g., gravity, magnetic, and electrical resistivity) were planned to be carried out in the ZCMR extension to gather new field data that will help understand the mineral deposit on regional and local scales.

Unfortunately, this research was conducted during the novel coronavirus (COVID-19) pandemic outbreak. The planned field survey to gather detailed gravity data was canceled because of the extreme restrictions (e.g., countries closing their borders to prevent the spread of COVID-19) brought by the pandemic. When travel to the Philippines was not yet permitted, freely available gravity data were used to study the crustal features in the Philippine Island Arc System (Chapter 2). This gravity method-related research is in preparation for the detailed gravity survey for chromite deposit exploration in the extension of ZCMR, which was planned to be implemented during overseas research in the Philippines. However, since the schedule of the overseas field survey was delayed and the restrictions brought by the pandemic were still strict (e.g., considering the instrument's availability), the study area was changed from Zambales Province to Camarines Norte Province (Fig. 1-1). The type of deposit in Camarines Norte (i.e., porphyry-epithermal) differs from Zambales (podiform chromite). Thus, the geophysical properties of the target anomaly that defines the mineral deposit also change from density (chromite) to electrical resistivity and chargeability (porphyry epithermal). With this regard, the geophysical investigation technique was also changed from the gravity method to electrical resistivity-induced polarization (ER-IP) and very low frequency-electromagnetics (VLF-EM) methods (Chapter 3). Interpretation of regional gravity data (from Chapter 2), along with remote sensing analysis were performed to delineate the major structures in Camarines Norte Province and narrow the scope of the study area. These are the rationale behind using different geophysical methods in this research to investigate the geology, tectonics, and mineralization potential in the Philippine Island Arc System.

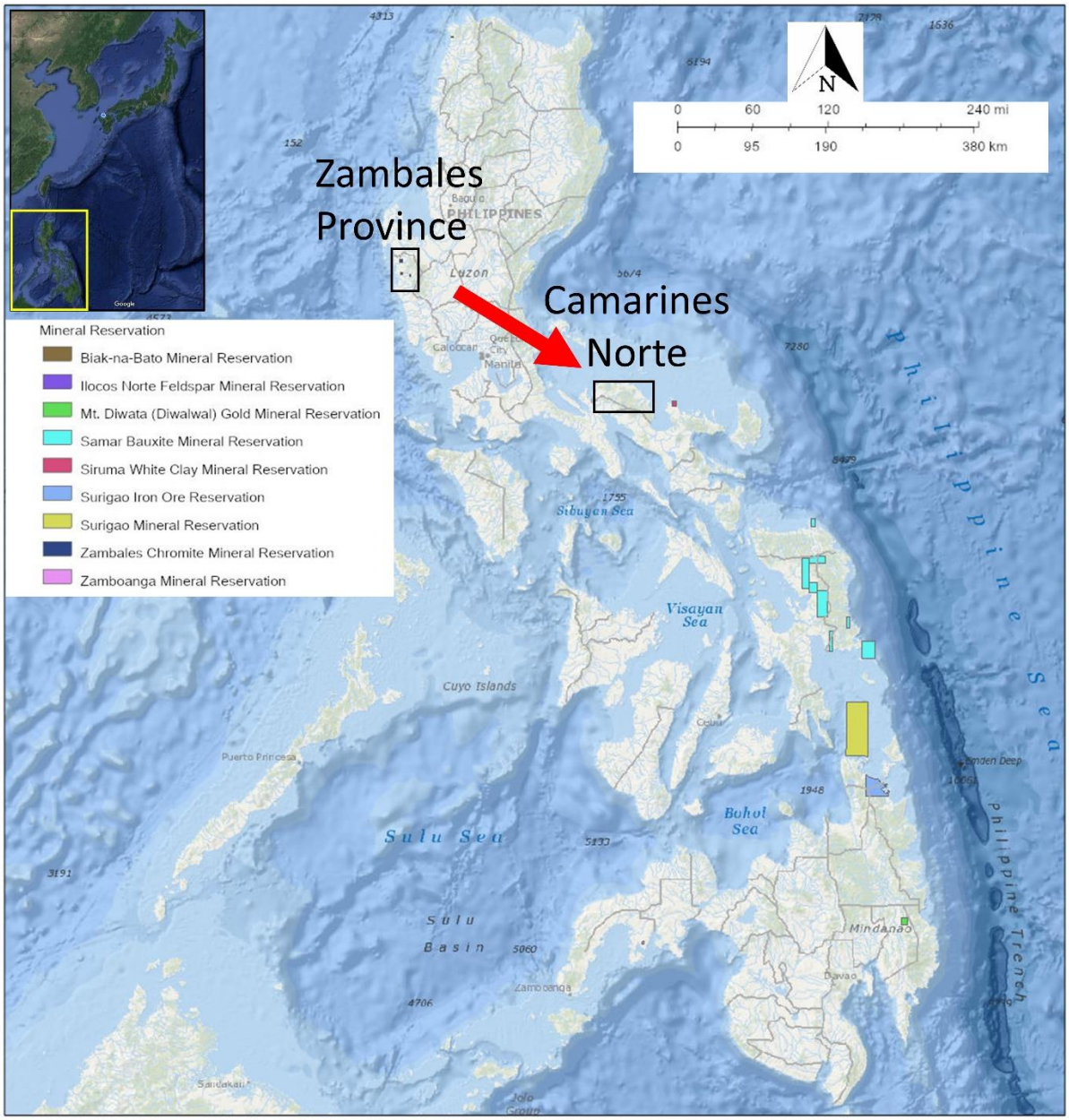

Figure 1-1. *Mineral reservation map of the Philippines modified from MGB (2010). The blue box marks the location of the initially planned study area, while the red box represents the specific study area of this research. The inset map shows the location of the Philippines relative to Japan.*

1.2 Gravity Studies in the Philippines

The oldest published paper about regional gravity exploration in the Philippines was documented in the twentieth century when Teodoro (1970) compiled Luzon Island gravity data. A comprehensive Bouguer anomaly map could not have been generated in those years due to the lack of detailed topographic maps (Teodoro, 1970). However, the earlier work (with about 200 data points) using inverted pendulums of Holweek-Lejay-type is considered the oldest

gravity survey in the Philippines (Lejay, 1938). The first use of the gravity method applied to a small study area was done by Yokoyama et al. (1975) by confirming the graben structure of Taal Volcano. The oldest regional gravity anomaly maps (i.e., free-air, Bouguer, isostatic) covering the whole Philippines were presented, and different gravity anomalies were discussed relative to various geologic factors by Sonido (1981). Gravity surveys have continuously developed over the past forty years and have been applied in different fields of research in the Philippines, including geothermal exploration, geological investigation, and tectonic studies. The gravity studies and their main applications in the Philippines are presented in chronological order in Table 1-2.

Table 1-2 *Gravity studies in the Philippines and their applications.*

Author	Application	Title
Lejay (1938)	General	The General Characters of the Gravity in the Philippines
Teodoro (1970)	General	General Characteristics of Gravity in the Island of Luzon, Philippines
Yokoyama et al. (1975)	Structural	Gravimetric Studies of Taal Volcano, Philippines
Sonido (1981)	Geological	The State of Gravity Works in the Philippines
San Andres and Pedersen (1993)	Geothermal	Monitoring the Bulalo Geothermal Reservoir, Philippines, using Precision Gravity Data
Los Banos et al. (1996)	Geothermal	Geophysical Model of Mt. Labo Geothermal Field, Southeastern Luzon, Philippines
Rigor et al. (1998)	Geothermal	Magnetotelluric and Gravity Measurements in the Northern Negros Geothermal Field, Central Philippines
Jentzsch et al. (2001)	Geothermal	Mayon Volcano, Philippines: Change of Monitoring Strategy after Microgravity and GPS Measurements from 1992 to 1996
Camacho et al. (2007)	Geothermal	Interpretation of 1992-1994 Gravity Changes around Mayon Volcano, Philippines, Using Point Sources
Tiampo et al. (2007)	Geothermal	Modeling of Stress Changes at Mayon Volcano, Philippines. Pure and Applied Geophysics
Komazawa et al. (2014)	Geothermal	Caldera Structure Inferred from Gravity Basement around Bulusan Volcano, Southern Luzon, Philippines
Vajda et al. (2012)	Geothermal	Inversion of Temporal Gravity Changes by the Method of Local Corrections: A case study from Mayon Volcano, Philippines

Monasterial (2015)	Geothermal	Microgravity Survey in 2009-2010 Around Bacman Geothermal Field, Philippines - Gravity Corrections and Interpretations
Hayes and Lewis (1984)	Tectonics/ Structural	A Geophysical Study of the Manila Trench, Luzon, Philippines. 1. Crustal Structure, Gravity, and Regional Tectonic Evolution.
Lewis and Hayes (1984)	Tectonics/ Structural	A Geophysical Study of the Manila Trench, Luzon, Philippines: 2. Fore Arc Basin Structural and Stratigraphic Evolution
Dimalanta (1993)	Geological	Geologic interpretation of Gravity Anomalies over the Baguio Mineral District
Rangin et al. (1996)	Tectonics/ Structural	Collision and Strike-slip Faulting in the Northern Molucca Sea (Philippines and Indonesia): Preliminary Results of a Morphotectonic Study
Yumul et al. (2000)	Tectonics/ Structural	Geology of the Southern Zambales Ophiolite Complex, Luzon, Philippines
Barretto et al. (2000)	Tectonics/ Geological	Gravity Variations along the Southeast Bohol ophiolite complex (SEBOC), Central Philippines: Implications on ophiolite emplacement
Dimalanta and Yumul (2004)	Tectonics/ Structural	Crustal Thickening in an Active Margin Setting (Philippines): The Whys and the Hows
Milsom et al. (2006)	Tectonics/ Structural	Peculiar Geometry of Northern Luzon, Philippines: Implications for Regional Tectonics of New Gravity and Paleomagnetic Data
Dimalanta et al. (2009)	Tectonics/ Structural	New features from the Romblon Island Group: Key to Understanding the Arc-continent Collision in Central Philippines
Armada et al. (2012)	Tectonics/ Structural	Possible Northward Extension of the Philippine Fault Zone offshore Luzon Island (Philippines)
Liu et al. (2012)	Tectonics/ Structural	Tectonics of the Philippines and Ambient Regions from Geophysical inversions
Manalo et al. (2015)	Tectonics/ Structural	Crustal Thickness Variation from a Continental to an Island Arc Terrane: Clues from the Gravity Signatures of the Central Philippines
Gabo et al. (2015)	Tectonics/ Structural	Terrane Boundary Geophysical Signatures in Northwest Panay, Philippines: Results from Gravity, Seismic Refraction and Electrical Resistivity Investigations
Salapare et al. (2015)	Tectonics/ Structural	Upper Crustal Structure Beneath the Zambales Ophiolite Complex, Luzon, Philippines Inferred from Integrated Gravity, Magnetic and Geological Data
Armada et al. (2020)	Tectonics/ Structural	Forearc Structures and Deformation along the Manila Trench

Yumul et al. (2020a)	Tectonics/ Structural	Mineralization Parameters and Exploration Targeting for Gold-Copper Deposits in the Baguio (Luzon) and Pacific Cordillera (Mindanao) Mineral Districts, Philippines: A Review
Yumul et al. (2020b)	Tectonics/ Structural	Adakitic Paracale Granodiorite in Southeastern Luzon, Philippines: A peek at a Proto-Philippine Sea Plate-related Magmatic Arc
Parcutela et al. (2022)	Tectonics/ Structural	Arc-crustal Compression and its Effects on the Underlying Mantle Geometry as Elucidated from the Potential Field Signatures of the Buckled Cretaceous Cebu Lithosphere, Philippines
Casulla et al. (2022)	Tectonics/ Structural	Imaging crustal Features and Moho Depths through Enhancements and Inversion of Gravity Data from the Philippine Island Arc System

In the 1980s, scientists in the field of geothermal research started to use the gravity method for monitoring geothermal reservoirs. San Andres and Pedersen (1993) reported a gravity decrease due to fluid withdrawals based on the precision gravity data collected from 1980 to 1991. The geophysical model of the Mt. Labo geothermal field was constrained with the help of gravity surveys; the results indicate that the delineated gravity high is associated with the intrusive cooling body of Mt. Labo (Los Banos et al., 1996). Rigor et al. (1998) presented the result of gravity measurements in the northern Negros geothermal field. They reported that the steep gravity gradient in the southern part of the geothermal fields bounds the hydrothermal system. The gravity method was also used for monitoring volcanic activities. The microgravity measurements around Mayon Volcano from 1992 to 1996 were studied by Jentzsch et al. (2001); they found that the gravity increase after the 1993 eruption was due to a mass redistribution process in the volcanic vent. Changes in gravity signatures were also interpreted by Camacho et al. (2007) to be related to an increase in mass and pressure changes within Mt. Mayon. The stress change was modeled at Mt. Mayon by Tiampo et al. (2007), who found that the stress change could be associated with modifying the water storage in the fractured rocks. Using gravity data, Mt. Bulusan was studied by Komazawa et al. (2014); their study delineated the caldera structure based on a semi-circular gravity feature with a steep gradient. In 2012, Vajda et al. (2012) inverted the potential field data of Mayon Volcano and inferred that the sources of the gravity signal indicate a process of magma injection into the shallow voids of the mountain. The recent result of the microgravity surveys in the Bacman geothermal field was presented by Monasterial (2015), which gave a better picture of the location and depth of the intrusive rock and other underlying lithologies.

Ground and marine gravity surveys were employed by several studies focusing on geologic and tectonic investigations. For example, Hayes and Lewis (1984, 1985) presented the crustal structure and tectonic evolution along Manila Trench, while Lewis and Hayes (1984) discussed the fore arc basin structural and stratigraphic evolution. Dimalanta (1993) made a geologic interpretation of the Baguio Mineral District from the gravity anomalies that correspond to the rocks and structures in the area. Gravity data and other geophysical data (e.g., seismic) were used to map the collision and faulted zone in the northern Molucca Sea (Rangin et al., 1996). In 2000, Yumul et al. (2000) conducted gravity surveys in conjunction with other geophysical and geochemical investigations in the southern Zambales Ophiolite Complex (ZOC) to help elucidate the processes that pave the way to the ZOC's current configuration. Gravity surveys were implemented in the central Philippines to better understand the emplacement of Bohol ophiolite (Barretto et al., 2000). Dimalanta and Yumul (2004) used available geochemical and geophysical data, including gravity data, to estimate the crustal thickness in the Philippines. The regional tectonics of northern Luzon (Milsom et al., 2006) and the arc-continent collision in the central Philippines (Dimalanta et al., 2009) were also studied by implementing gravity surveys. Armada et al. (2012) used gravity and seismic data to examine the northward marine extension of the Philippine Fault. Liu et al. (2012) used available regional gravity and magnetic data to study the tectonics of the Philippines and presented several results. These include the accurate description of the Manila Trench structure and the delineation of the boundaries of the Palawan-Mindoro microcontinent block (PMB), Philippine Mobile Belt (PMB), and Sulu Celebes Block (SCB) (Liu et al., 2012). By employing gravity surveys, the central Philippines' tectonics was reexamined by further constraining its crustal thickness (Manalo et al., 2015) and delineating a local terrane boundary in northwest Panay (Gabo et al., 2015). The upper crustal structure beneath the Zambales Ophiolite Complex was characterized by Salapare et al. (2015) with the help of gravity data. Armada et al. (2020a) analyzed the Bouguer Anomaly to image the subsurface extent of the basement units in central Cebu. Gravity data was also used to discuss the tectonics and mineralization parameters in Luzon and Mindanao, Philippines (Yumul et al., 2020b, a). The most recent gravity studies in the Philippines focus on characterizing the arc-crustal compression in Cebu (Parcutela et al., 2022) and regional understanding of crustal features in the Philippine island arc system (Casulla et al., 2022).

Table 1-2 summarizes the available published gravity studies in the Philippines. This historical overview of gravity studies shows different scales and applicability of gravity surveys. Earlier studies generated and presented gravity maps based on limited point data from

local to regional surveys (e.g., ground, marine). With the advent of satellite-derived gravity data and global gravity datasets, geological studies' scope is no longer limited to the previously available point data. Using the wide-ranging and complete gravity datasets from the World Gravity Map (WGM) 2012, this research contributes to gravity studies in the Philippines by investigating gravity anomalies in the Philippine island arc system and identifying regional geologic and tectonic features (e.g., structures, sedimentary basins, and basement rocks).

1.3 Electrical Resistivity and Induced Polarization Studies in the Philippines

This section presents a brief outline of published studies about applications of electrical resistivity (ER) and induced polarization (IP) methods in the Philippines. Only a few ER and IP surveys were conducted in the Philippines, highlighting their uses in geothermal, geologic, and hydrogeologic assessments. ER surveys are often implemented after reconnaissance (e.g., geologic, remote sensing) investigations have recognized the particular area of interest (Parasnis, 1979; Telford et al., 1990; Reynolds, 1997).

The oldest available published ER and IP research in the Philippines is the paper of Pelton and Smith (1976). Their research presented the use of the IP method to detect concealed disseminated sulfide deposits in different parts of the Philippines. It highlighted the importance of mapping the alteration zones using the IP method before delineating the possible location of the mineralization zones (Pelton and Smith, 1976). James and Fuchs (1990) conducted ER and IP surveys to delineate the northern extension of the concealed mineralized zone of the Exciban gold-copper-tellurium vein system in Camarines Norte. They interpreted that the strongest ER and IP anomalies are related to the faulted extension of the mineralization zone. Aside from their application to mineral exploration, ER and IP surveys can also be used in geothermal, hydrogeological, and geological studies. Table 1-3 summarizes ER and IP studies conducted in the Philippines.

Table 1-3 *Electrical resistivity and induced polarization studies in the Philippines and their applications.*

Author	Application	Title
Pelton and Smith (1976)	Mineral Exploration/ Geological	Mapping Porphyry Copper Deposits in the Philippines with IP
Smith (1978)	Geothermal	Report on Resistivity Survey (Dipole-Dipole) Mambucal, Negros Occidental
Bromley (1981)	Geothermal	Baslay-Dauin Resistivity Surveys-VES Interpretation

Bromley and Espanola (1982)	Geothermal	Resistivity Methods Applied To Geothermal Exploration in the Philippines
Delfin et al. (1984)	Geothermal	Mt. Apo Geothermal Project: First Stage Exploration
James and Fuchs (1990)	Mineral Exploration/ Geological	Exploration of the Exciban Gold-Copper-Tellurium Vein System, Camarines Norte, Philippines
Taniguchi et al. (2008)	Hydrogeological	Groundwater Discharge as an Important Land-Sea Pathway into Manila Bay, Philippines
Armada et al. (2009)	Hydrogeological	Georesistivity Signature of Crystalline Rocks in the Romblon Island Group, Philippines
Los Baños et al. (2010)	Geothermal	The Resistivity Model of the Mindanao Geothermal Project, South Central Mindanao, Philippines
Cardenas et al. (2010)	Hydrogeological	Linking Regional Sources and Pathways for Submarine Groundwater Discharge at a Reef by Electrical Resistivity Tomography, 222 Rn, and Salinity Measurements
Fikos et al. (2012)	Structural/ Geological	Electrical Resistivity Tomography Study of Taal Volcano Hydrothermal System, Philippines
Gabo et al. (2015)	Structural/ Geological	Terrane boundary geophysical signatures in Northwest Panay, Philippines: Results from Gravity, Seismic Refraction and Electrical Resistivity Investigations
Palattao et al. (2015)	Structural/ Geological	Implementation of the Borehole Disposal Project for Disused Sealed Radioactive Sources in the Philippines.
MGB (2014)	Hydrogeological	Groundwater Assessment of the Southwestern Portion of Bohol Island through Geo-resistivity Survey
MGB (2017)	Hydrogeological	Groundwater Resource Assessment of Bohol Province
Racasa et al. (2018)	Hydrogeological	Lacustrine Groundwater Discharge in Southern Laguna de Bay, Philippines
Casulla et al. (2020)	Hydrogeological	Subsurface Characterization using Geophysical and Hydrochemical Data: An Application to Groundwater Resources Management in Pampanga, Philippines

In geothermal research, the work of Bromley and Espanola (1982) is considered as the oldest available published paper that uses ER method. Their study reviews the strengths and weaknesses of the resistivity methods applied to geothermal explorations in the Philippines. Some older unpublished reports were also mentioned in their report, including the ER surveys using dipole-dipole array in Mambucal, Negros Occidental (Smith, 1978) and VES interpretation of ER data in Baslay-Dauin, Negros Oriental (Bromley, 1981). They concluded that the results from vertical electrical sounding (VES) and dipole-dipole techniques should be interpreted together to acquire the appropriate information about the subsurface (Bromley and

Espanola, 1982). Los Baños et al. (2010) also discussed the resistivity model of the Mindanao geothermal project and cited other unpublished reports of ER surveys for geothermal exploration in Mt. Apo, Philippines (e.g., Delfin et al., 1984).

ER surveys were also applied to assess and address hydrogeological issues in the Philippines. Taniguchi et al. (2008) studied the possible significance of groundwater seepage to nutrient inputs into Manila Bay using a multi-disciplinary approach. They employed the ER method, which provided a picture of the saline-freshwater interface that varies based on tidal timescale. The groundwater conditions within a collision zone and hardrock regions were investigated by Armada et al. (2009) using the ER method. The results presented relatively low resistivity values of the regolith compared with the fresh ultramafic and metamorphic rocks due to the higher groundwater content (Armada et al., 2009). The ER method was also applied to investigate submarine groundwater discharge (SGD) in Pangasinan. ER profiles from the work of Cardenas et al. (2010) illustrate the relatively resistive zones close to the seawater, which indicates the preferential pathways of the fresh groundwater discharge. The lacustrine groundwater discharge (LGD) in southern Laguna de Bay was also examined using the ER method; the anomalous narrow resistive zones were interpreted as the fault-controlled LGD (Racasa et al., 2018). A recent study by Casulla et al. (2020) presented the use of ER method along with hydrochemical data to characterize the groundwater in Pampanga. There are other unpublished reports limited to the application of ER method to groundwater exploration in the Philippines (e.g., MGB; 2014, 2017).

Some ER studies focus on characterizing subsurface geology and structures. The hydrothermal system of a volcano can also be understood using the ER method. Fikos et al. (2012) employed electrical resistivity tomography (ERT) surveys on two hydrothermal areas in the Taal Volcano area. Their study delineated two geothermal fields and presented water movement from the central crater lake to the surrounding rocks (Fikos et al., 2012). The ER method was also used to constrain the interpreted subsurface structure in Northwest Panay (Nabas Fault) by locating the zones with an abrupt decrease in resistivity (Gabo et al., 2015). An investigation of geologic structures to help locate the potential site for the borehole disposal of diffused sealed radioactive sources (BOSS) was also conducted in the Philippines using the ER method (Palattao et al., 2015).

Table 1-3 summarizes the few ER and IP studies published in the Philippines. Ducut et al. (2022) also mentioned that despite the numerous applications of the ER method, particularly the ERT, the Philippines (e.g., government, private sector) still lacks published studies. Research on ER and IP methods should be developed in the Philippines. This study promotes

the ER and IP studies in the Philippines by presenting the results of two-dimensional (2-D) and three-dimensional (3-D) inversions of apparent resistivity and chargeability field data to locate the promising mineralization zones in eastern Labo, Camarines Norte.

1.4 Dissertation Objectives

This research aims to contribute novel information to the geoscience, geophysics, and mining community by offering new data and interpretations of the geology, tectonics, and mineral potentials in the Philippine island arc system using gravity and electrical resistivity-induced polarization (ER-IP) methods.

Earlier gravity studies in the Philippines generated and presented gravity maps based on limited point data from local to regional surveys (e.g., ground, marine). Because of the availability of satellite-derived gravity data and global gravity databases, the scope of geological research is no longer confined to previously accessible point data. The first part of this study aims to investigate the gravity anomalies in the Philippine island arc system and to identify regional geologic and tectonic features (e.g., structures, sedimentary basins, and basement rocks) using the isostatic and free-air anomaly grids from World Gravity Map (WGM). These identified features may not have been previously delineated on gravity anomaly maps.

The second part of this research focuses on the ER-IP and VLF-EM surveys conducted to investigate the mineralization potential over a thick overburden in Eastern Labo, Camarines Norte, Philippines. Areas adjacent to Mt. Labo have poor bedrock exposure due to the thick pyroclastic deposit and lush vegetation. Thus, mineral exploration in areas with concealed mineralized zones receives lesser attention than in regions with exposed mineral deposits. The second part of this study specifically aims to generate detailed geophysical data (i.e., ER-IP, VLF-EM), identify the geophysical signatures of the potential mineralized regions, delineate the distribution of the potential Cu-Au mineralization, and propose a subsurface model characterizing the depth, thickness, and extent of the mineralized zones in the study area. This research yields new information about the local subsurface features that help locate promising targets for Cu-Au exploration in Eastern Labo, Camarines Norte, Philippines.

1.5 Dissertation Structure

This dissertation has four chapters and can be generally subdivided into two: the application of gravity techniques for imaging crustal features and Moho depths in the Philippine island arc system and the application of Electrical Resistivity-Induced Polarization

(ER-IP) and Very Low Frequency-Electromagnetics (VLF-EM) techniques for the characterization of potential Cu-Au mineralization in Eastern Labo, Camarines Norte, Philippines. The results of the two major sections were already published or under consideration in international peer-reviewed journals.

Chapter 1: This section presents the background and rationale of this research. This chapter also reviews the past published gravity and ER-IP studies in the Philippines and their applications. The objectives and structure of this dissertation are included in this section.

Chapter 2: This section focuses on the regional investigation of gravity signatures in the Philippine island arc system. The first part presents the theory of gravity method followed by the regional geologic and tectonic setting of the Philippines. The enhancement and inversion techniques used were discussed before presenting the results of the methodologies. The gravity signatures (e.g., basement rocks, basins) over the Philippine island arc system were initially presented to give a general overview of their corresponding regional geologic and tectonic features. The last part discusses the crustal features and Moho depths in the Sulu Sea and 3-D gravity inversion results in the representative sedimentary basins in the Philippines.

Chapter 3: This section emphasizes the characterization of potential mineralization in Eastern Labo, Camarines Norte, Philippines using ER-IP and VLF-EM methods. This chapter begins with the presentation of exploration history in Camarines Norte. Before presenting the results, a brief discussion about the ER-IP and VLF-EM theories was introduced. The theory section follows an overview of the geologic, tectonic, and metallogenic settings on regional and local scales. The presentations of the applied methodologies (e.g., Hjelt and Fraser derivatives, 2-D and 3-D ER-IP inversions) and the corresponding results and discussion are also included in this section. The last part offers a combined discussion of the ER-IP and VLF-EM results and exploration implications of this research.

Chapter 4: This section concludes this dissertation by summarizing the two main chapters and offering the possible future studies that can be initiated from this research.

CHAPTER 2

Imaging Crustal Features and Moho Depths in the Philippine Island Arc System using Gravity Data

2.1 Introduction

Gravity data is fundamental in understanding and modeling Earth's interior (e.g., subsurface, crust), especially in studying its relationship to geology and structures. With the advancement of technology, high-resolution satellite gravity data are being utilized for geologic exploration and tectonic studies. Satellite gravity data were processed and interpreted for bathymetry prediction (Majumdar and Bhattacharyya, 2005), lineament investigation (Braitenberg et al., 2011), crust-mantle boundary study (Steffen et al., 2011), sediment basin survey (Vaish and Pal, 2015), and geologic mapping (Pal et al., 2016). This area of research was made possible by acquiring a more precise Earth gravitational model. The Earth Gravitational Model 2008 (EGM2008) is a recent Earth's geopotential field model. This model integrates satellite gravimetry, satellite altimetry, and surface gravity measurements (Pavlis et al., 2008). Several studies have already assessed and validated the accuracy of EGM2008 (Arabelos and Tscherning, 2010; Pavlis et al., 2012). The gravity data from the high-resolution World Gravity Map 2012 (WGM2012) is derived from the EGM2008.

The Philippines' historical overview of gravity surveys presents a wide range of gravity survey scales and applicability (discussed in Chapter 1). Earlier studies generated and presented gravity maps based on limited local and regional data. This study used the isostatic and free-air anomaly grids from WGM to investigate the gravity anomalies in the Philippine island arc system and to identify regional geologic and tectonic features that may not have been previously delineated on gravity anomaly maps. Two-dimensional (2-D) radially-averaged power spectrum analysis was employed to calculate new depth estimates to the top of the Moho and basement rock over the Sulu Sea. Three-dimensional (3-D) gravity inversion was applied to characterize the density contrast of the subsurface geology of major sedimentary basins in the Philippines. This work offers an efficient and effective means of understanding the Philippines' regional geology and tectonics through gravity signatures.

2.2 Gravity Method Theory

The gravity method measures the changes in acceleration due to gravity. It detects changes in the Earth's gravitational field produced by variances in the density of subsurface features (e.g., rocks). Given the gravitational field of the Earth (m_1), a unit mass (m_2) above it experiences an attraction force ($\boldsymbol{F}$) (Fig. 2-1). The force on m_2 due to another mass m_1 at a distance r is defined by Newton's law of gravitation as

$$\boldsymbol{F} = G\frac{m_1 m_2}{r^2}. \qquad (2.1)$$

G is the gravitational constant defined as 6.6743×10^{-11}m^3 kg^{-1} s^{-2}.

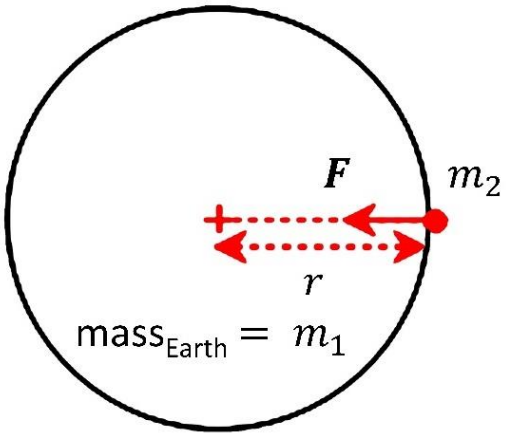

Figure 2-1. *Simple representation of gravitational attraction on a point mass (red dot) on Earth's surface (modified from Lowrie, 2007).*

Newton's second law describes the force on an object (free-falling mass) in the Earth's gravitational field experiencing acceleration as

$$\boldsymbol{F} = m\boldsymbol{a}. \qquad (2.2)$$

Combining Eq. 2.1 and Eq. 2.2, the acceleration can be generally represented as

$$\boldsymbol{a} = G\frac{m}{r^2}, \qquad (2.3)$$

where $\vec{a}$ is the gravitational acceleration (g) of approximately 9.8 m/s^2 on the surface of the Earth (at the equator). The variations in m or r are the sources of the local variations in *g*. The gravity method measures variations in the intensity of the planetary force field over time and space. Actual measurements are made indirectly by observing parameters such as time, displacement, spring tension, or an electrical component that can be related to the fundamental relationships to the value of planetary gravity or its spatial rate of change (Telford et al., 1990; Reynolds, 1997; Hinze et al., 2013).

For a simple spring example, according to Hooke's Law, the force ($\boldsymbol{F}$) required to extend or compress a spring by a given distance (dx) scales linearly with that distance:

$$\boldsymbol{F} = k(dx), \qquad (2.4)$$

where k is the elastic spring constant (e.g., stiffness property). A force applied to the mass attached to the spring will stretch the spring (Fig. 2-2).

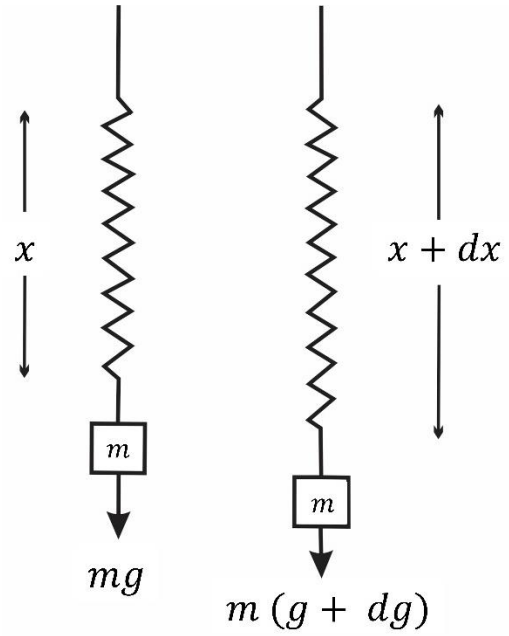

Figure 2-2. *A simple illustration of how a stable gravimeter works. The dx represents the spring's extension due to additional gravitational pull (dg) (modified from Reynolds, 1997; Kearey et al., 2002).*

The spring's extension is proportional to the force ($\boldsymbol{F} = m\boldsymbol{a}$). The combination of Eq. 2.2 and Eq. 2.4 arrives at the equation

$$m(dg) = k(dx). \qquad (2.5)$$

where dg is a slight change in gravitational acceleration and dx is a small change in spring length. With the known values of mass and the spring constant, gravitational acceleration can be acquired after measuring the change in spring length:

$$(dg) = \frac{k(dx)}{m}. \qquad (2.6)$$

The standard SI unit of measurement for gravitational acceleration is m/s^2, but the 'gal' is used for geophysical exploration. 1 gal is equivalent to 0.01 m/s^2 or 1 cm/s^2. However, the unit gal is a huge unit compared to the changes in gravitational acceleration generated by differences in the Earth's subsurface masses. Because of the minimal magnitude of many

significant anomalies, the unit milligal (mGal) or microgal (μGal) is commonly employed in geophysical exploration and engineering geophysics (Telford et al., 1990; Blakely, 1996; Hinze et al., 2013).

The equation below defines the gravity effect on a point mass

$$U = \int_{r_1}^{r_2} \boldsymbol{F}_g \,.\, \partial \boldsymbol{r}, \tag{2.7}$$

where U is the gravitational potential and r_1 and r_2 are the distances. The gravitational potential (U) can be calculated by integrating the gravitational force ($\boldsymbol{F}_g$) between two sites separated by r_1 and r_2. The potential at a given point can be defined entirely by assuming that the potential is zero at infinity. The gravitational force acting on a unit mass (when moving a unit mass from r_1 to r_2) does the work $W_{(r_1,r_2)}$ as presented by

$$W_{(r_1,r_2)} = \int_{r_1}^{r_2} \boldsymbol{F}_g \,.\, d\boldsymbol{r}. \tag{2.8}$$

Using Newton's law of gravitation, we can present work as

$$W_{(r_1,r_2)} = G \int_{r_1}^{r_2} \frac{m}{r^2} d\boldsymbol{r} = Gm\left(\frac{1}{r_1} - \frac{1}{r_2}\right). \tag{2.9}$$

The potential difference is

$$\Delta U = W_{(r_1,r_2)} = \left[U_{(r_1)} - U_{(r_2)}\right] = Gm\left(\frac{1}{r_1} - \frac{1}{r_2}\right). \tag{2.10}$$

Assuming that r_2 is removed to infinity ($U_{(r_2)} = 0$), the gravity potential of a point mass can be generally expressed as:

$$U\,(r) = G\,\frac{m}{r} = G\int \frac{\partial m}{r}. \tag{2.11}$$

The gravitational potential is given in m^2/s^2 or gal·m. The acceleration (m/s^2) of any point mass towards m, Eq. 2.3, is given by $-dU\,/\,dr$. The derivative of U in any direction, in general, gives the acceleration of a point mass in that given direction. The equation below also presents the acceleration in the r direction (Parasnis, 1979).

$$\boldsymbol{a} = \frac{dU}{dr} = -\,G\,\frac{m}{r^2} \tag{2.12}$$

In the gravity survey, the gravimeter measures the vertical component of the target's gravitational influence (Δg_z) but the formula $G\,\frac{m}{r^2}$ yields the acceleration acting in line with two (observation and target points) masses (Δg_r) (Fig. 2-3). The geometry should be corrected since the Δg_z is being measured along the surface over the target. The Δg_z can be defined as

$$\Delta g_z = \Delta g_r \cos(\theta) = \Delta g_r\,\frac{z}{r}. \tag{2.13}$$

By knowing that $\vec{a} = \Delta g_r = G\,\frac{m}{r^2}$, the equation below can be generally derived.

$$\Delta g_z = G\,\frac{mz}{r^3} = G\,\frac{mz}{(x^2+z^2)^{3/2}} \qquad (2.14)$$

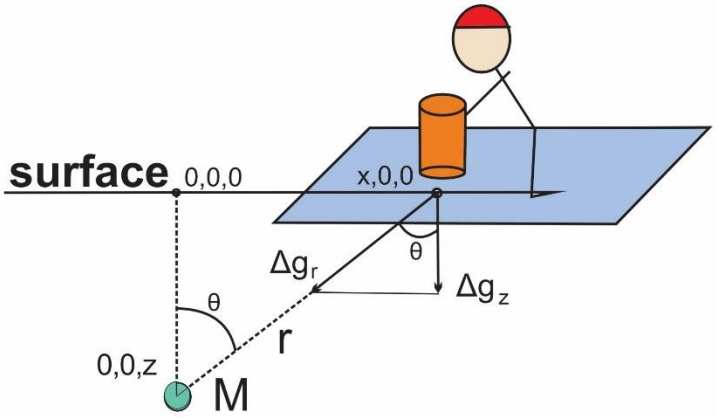

Figure 2-3. *Geometry of gravity measurements. The gravimeter (orange cylinder) measures the vertical component of the target's (green circle) gravitational influence ($\Delta \boldsymbol{g_z}$) (modified from https://gpg.geosci.xyz/_images/grav_diag.gif).*

In general, the gravity anomaly of any shape can be calculated by adding the attractions of all the body's mass elements. Figure 2-4 shows an example of a small prismatic body of density ρ, with sides of length δx', δy', and δz', located at x', y', and z'. This element's mass δm is expressed as

$$\delta m = \rho\ \delta x'\ \delta y'\ \delta z'. \qquad (2.15)$$

As a result, at a distance r, the body's attraction (δg) at a point outside the body (x, y, z) is calculated using the equation

$$\delta g = G\rho\ \frac{(z'-z)}{r^3}\,\delta x'\ \delta y'\ \delta z'. \qquad (2.16)$$

The gravity anomaly of the entire body (Δg) can be derived by adding all elements that comprise the body. Thus, by integrating the equation below, the attraction of bodies of regular geometry can be determined.

$$\Delta g = \iiint G\rho\ \frac{(z'-z)}{r^3}\,\delta x'\ \delta y'\ \delta z' \qquad (2.17)$$

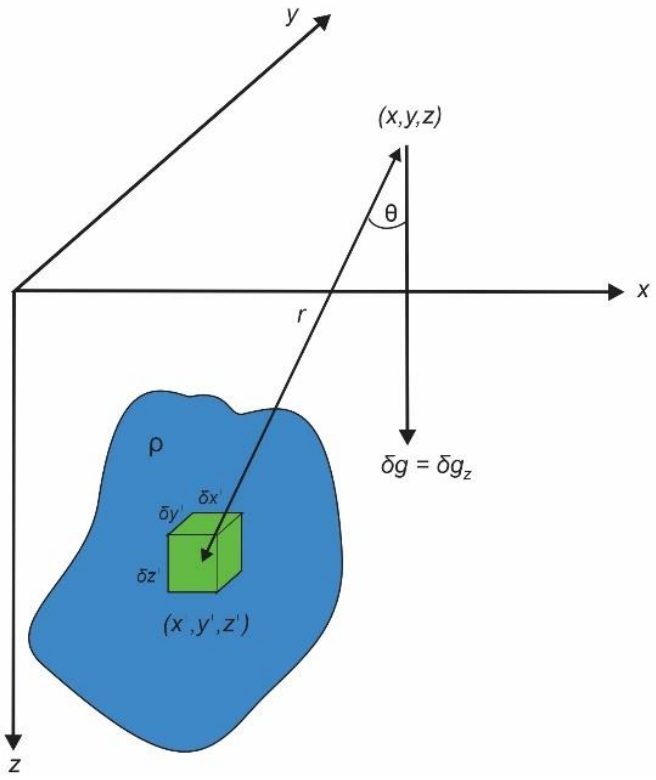

Figure 2-4. *Gravity anomaly of an irregularly shaped element of a mass. The green cube represents the small prismatic body. (modified from Kearey et al., 2002).*

Inversion of surface gravity data can recover the anomalous density feature (Oldenburg and Li, 2005). The gravity field's vertical component is represented by

$$g_z(\boldsymbol{r_0}) = G \int_v \rho\,(\boldsymbol{r}) \frac{z - z_0}{|\boldsymbol{r} - \boldsymbol{r_0}|^3}\, dv, \qquad (2.18)$$

where ρ is the density contrast, $\boldsymbol{r}$ is the target location and $\boldsymbol{r_0}$ is the observation location. v represents the volume of the anomalous mass, and G is the gravitational constant. More explanations of the theories about gravity potential and gravity inversion are presented in Appendix 1 and discussed comprehensively by earlier prominent authors (Oldenburg, 1974; Parasnis, 1979; Telford et al., 1990; Li and Oldenburg, 1998; Hinze et al., 2013). The acquired density or density contrast models from the inversion are used to characterize the subsurface geologic features or structures. The density values of common minerals and rocks are shown in Table 2-1.

Table 2-1. *Densities of common rocks and minerals (modified from Telford, 1990).*

Rock type	Average density (g/cm^3)	Mineral	Average density (g/cm^3)
Sediments (wet)		**Bauxite**	2.45
Overburden	1.92	**Limonite**	3.78
Soil	1.92	**Siderite**	3.83
Clay	2.21	**Rutile**	4.25
Gravel	2	**Manganite**	4.32
Sand	2	**Chromite**	4.36
Sandstone	2.35	**Ilmenite**	4.67
Shale	2.4	**Pyrolusite**	4.82
Limestone	2.55	**Magnetite**	5.12
Dolomite	2.7	**Franklinite**	5.12
Sedimentary rocks (average)	2.5	**Hematite**	5.18
Igneous Rocks		**Cuprite**	5.92
		Cassiterite	6.92
Rhyolite	2.52	**Wolframite**	7.32
Andesite	2.61	**Sphalerite**	3.72
Granite	2.64	**Malachite**	4
Granodiorite	2.73	**Chalcopyrite**	4.2
Porphyry	2.74	**Stagnate**	4.4
Quartz diorite	2.79	**Stibnite**	4.6
Diorite	2.85	**Pyrrhotite**	4.65
Lavas	2.9	**Molybdenite**	4.7
Diabase	2.91	**Marcasite**	4.85
Basalt	2.99	**Pyrite**	5
Gabbro	3.02	**Bornite**	5.1
Peridotite	3.15	**Chalcocite**	5.65
Acidic igneous rocks (average)	2.61	**Cobaltite**	6.1
Basic igneous rocks (average)	2.79	**Arsenopyrite**	6.1
Metamorphic Rocks		**Bismuththinite**	6.57
		Galena	7.5
Quartzite	2.6	**Cinnabar**	8.1
Schists	2.64	**Lignite**	1.19
Graywacke	2.65	**Soft coal**	1.32
Marble	2.75	**Anthracite**	1.5
Serpentine	2.78	**Chalk**	2.01
Slate	2.79	**Graphite**	2.15
Gneiss	2.8	**Rock salt**	2.22

Amphibolite	2.96	**Gypsum**	2.35
Eclogite	3.37	**Kaolinite**	2.53
Metamorphic rocks (average)	2.74	**Orthoclase**	2.53
		Quartz	2.65
		Calcite	2.65
		Anhydrite	2.93

The following portion briefly explains concepts and applications of gravity gradients (e.g., total horizontal derivative) (Cordell and Grauch, 1982; Nabighian et al., 2005). For example, the rate of change or the spatial derivative of g in the x-direction (HD_x) (Fig. 2-5) is expressed as

$$\mathrm{HDx} = \frac{\partial g}{\partial x}. \tag{2.19}$$

Furthermore, the horizontal gradient or the total horizontal derivative (THD) is defined as

$$\mathrm{THD} = \sqrt{\left(\frac{\partial g}{\partial x}\right)^2 + \left(\frac{\partial g}{\partial y}\right)^2}. \tag{2.20}$$

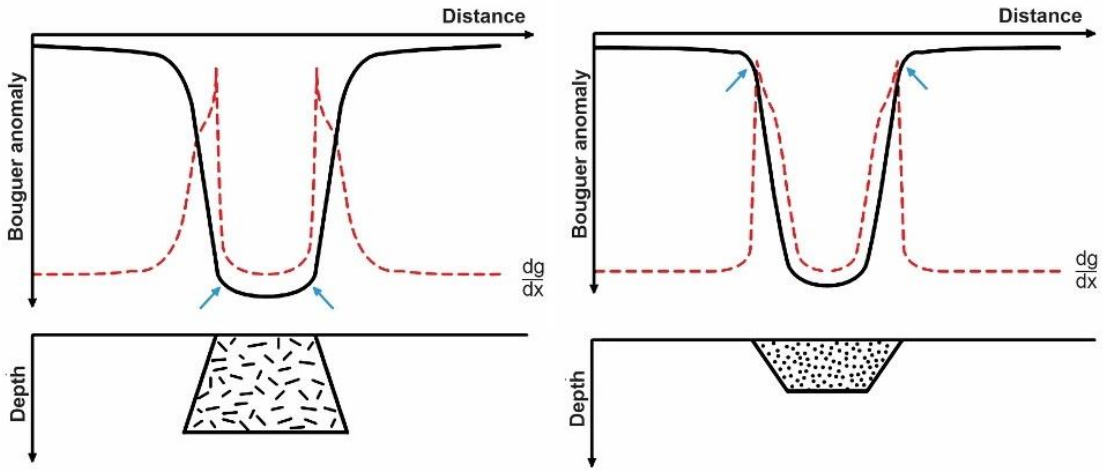

Figure 2-5. *Profiles of Bouguer anomalies across (left) a granite body and (right) a sedimentary basin. Arrows indicate the inflection points. The broken lines represent the gravity anomaly's horizontal derivative (modified from Kearey et al., 2002).*

These horizontal derivatives can delineate concealed subsurface density variations. The second horizontal derivative (2HD) determines the gradient's rate of change as expressed by

$$2\mathrm{HD} = \frac{\partial^2 g}{\partial x^2}. \tag{2.21}$$

The inflection points show the location of the gradient's highest rate of change. This type of processing can also distinguish the boundaries of the density contrast and the possible type of the anomalous subsurface body (e.g., sedimentary basin, igneous intrusion).

The second derivative of the vertical component is also helpful for interpreting gravity results (Evjen, 1936; Elkins, 1951; Tsuboi and Kato, 1952) (Fig. 2-6). The rate of change in gravity in the vertical direction (2VD) is represented by

$$2\text{VD} = \frac{\partial^2 g}{\partial z^2}. \tag{2.22}$$

The 2VD can be derived by using the Laplace equation

$$\frac{\partial^2 g}{\partial x^2} + \frac{\partial^2 g}{\partial y^2} + \frac{\partial^2 g}{\partial z^2} = 0 \tag{2.23}$$

for gravity as a potential field. The $\frac{\partial^2 g}{\partial z^2}$ can be computed easily because the $\frac{\partial^2 g}{\partial y^2}$ and $\frac{\partial^2 g}{\partial x^2}$ can be acquired from the Bouguer anomaly maps.

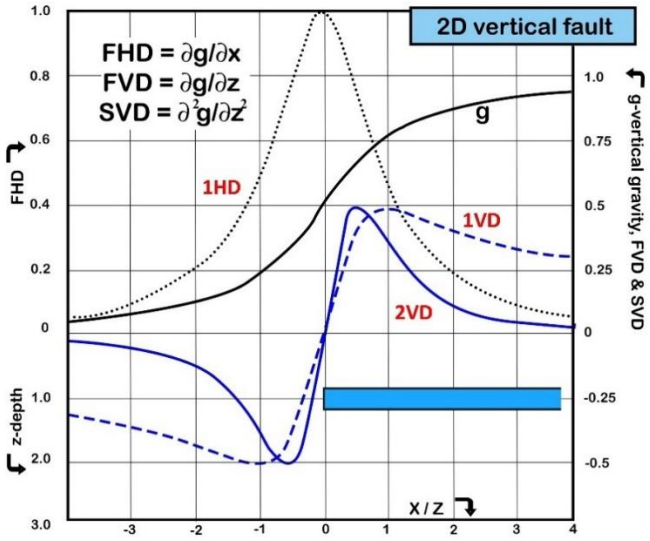

Figure 2-6. *Gravity anomaly profiles over an infinitely long and steep vertical contact (blue rectangle) representing geological units of different densities. g = vertical gravity; 1VD = first vertical derivative; 1HD = first horizontal derivative; 2VD = second vertical derivative (modified from Hinze et al., 2013).*

Derivative filters enhance a gravity anomaly field's higher-wavelength and shorter-wavelength components and identify source configurations. They are valuable in detecting subtle changes in the gravity field. Both vertical and horizontal derivatives are helpful. Vertical derivatives are useful for locating anomalies derived from shallow sources, while horizontal derivatives are primarily used for locating the edges of broad anomalous sources (Simpson et al., 1985; Hinze et al., 2013).

2.3 Regional Geologic and Tectonic Setting

The Philippine island arc system is a complex and tectonically active region. It is characterized by ophiolite accretion, arc magmatism, ocean basin closure, and other tectonic processes (Mitchell et al., 1986; Rangin, 1991; Yumul et al., 2008a; Aurelio et al., 2013). The Philippine archipelago consists of two general terranes: the Palawan-Mindoro Microcontinental Block and the Philippine Mobile Belt (PMB) (Mitchell et al., 1986; Rangin, 1991; Yumul et al., 2008a) (Fig. 2-7). The Palawan-Mindoro Microcontinental Block was once part of mainland Asia, while the PMB originated from the sub-equatorial regions (Taylor and Hayes, 1980; Holloway, 1981; Rangin et al., 1990; MGB, 2010) (Fig. 2-7). The PMB is an actively deforming zone between two oppositely-dipping subduction systems (Mitchell et al., 1986; Rangin, 1991; Yumul et al., 2008a; Aurelio et al., 2013). The eastern side of the PMB is bounded by the west-dipping East Luzon Trough and the Philippine Trench (e.g., Hamburger et al., 1983; Yumul et al., 2008a). Southeast-dipping subduction zones mark the archipelago's western side: Manila Trench, Negros Trench, Sulu Trench, and Cotabato Trench (e.g., Mitchell et al., 1986; Yumul et al., 2008a).

The bathymetric map of the Philippines shows very deep features (~8km to 9km) corresponding to the mentioned subduction zones (Fig. 2-8). Generally, the eastern side of the Philippines has a deeper bathymetry than the western flank. The left-lateral strike-slip Philippine Fault, which traverses the entire island arc system, accommodates the oblique convergence between the Philippine Sea Plate and Eurasian Plate (e.g., Barrier et al., 1991; Aurelio, 2000). The amalgamation of different terranes paved the way to form tectonic collages with diverse lithologic characteristics categorized into ophiolitic rocks, metamorphic rocks, magmatic arcs, and sedimentary basins (MGB, 2010). Ophiolitic and metamorphic basement rocks overprinted by relatively younger volcanic series and thick sedimentary basins define the Philippines' present geology.

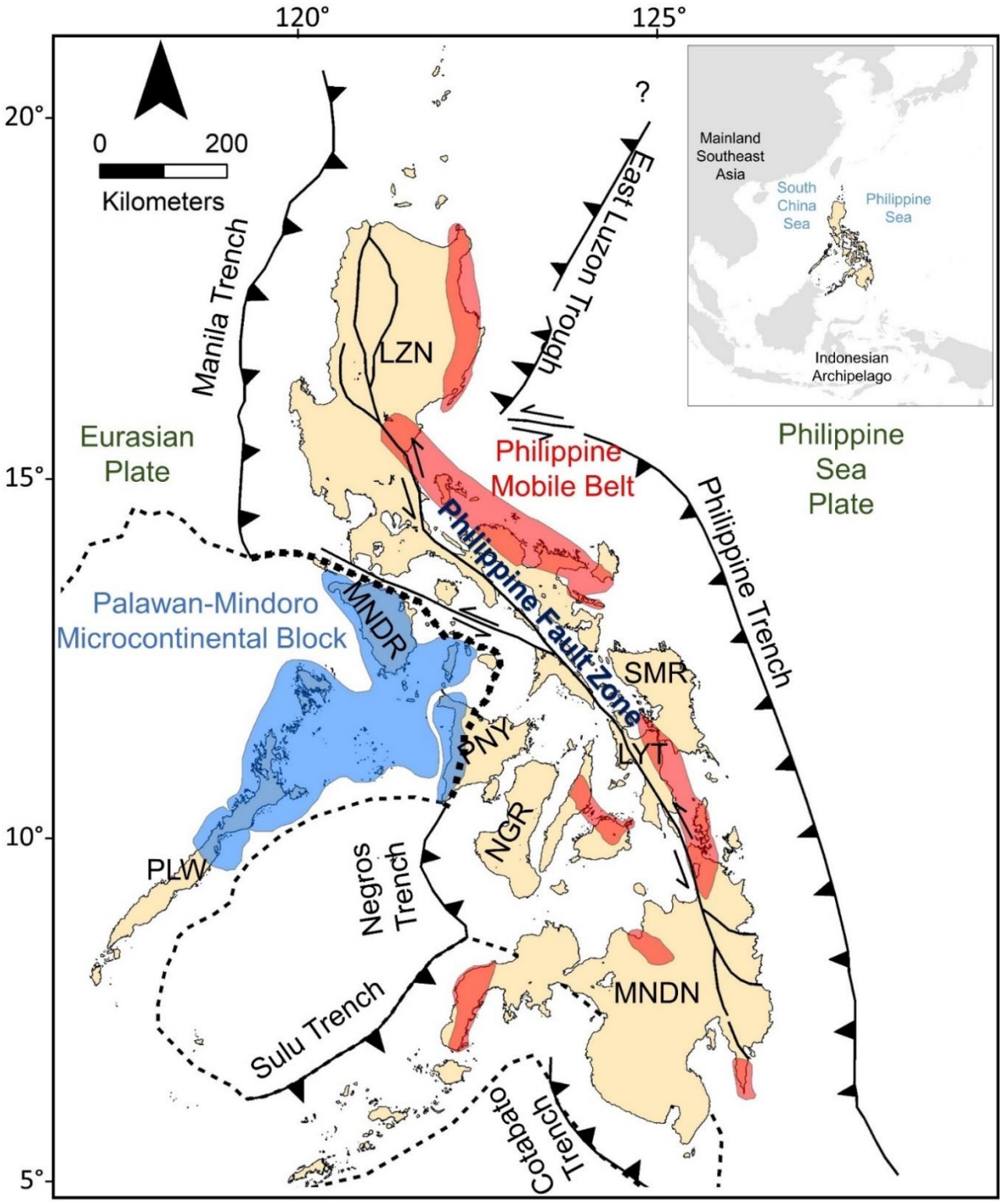

Figure 2-7. *General tectonic map of the Philippine island arc system (modified from Rangin, 1991; Yumul et al., 2008a, b). The continental Palawan-Mindoro Microcontinental Block and island arc Philippine Mobile Belt (PMB) characterize the Philippine Archipelago. Abbreviations represent the mentioned islands: LZN = Luzon, MNDR = Mindoro, PLW = Palawan, PNY = Panay, NGR = Negros, SMR = Samar, LYT = Leyte, MNDN = Mindanao. Red areas represent Cretaceous (island arc) metamorphic zones, while blue areas correspond to pre-Cretaceous (continental) metamorphic regions (modified from MGB, 2010). The inset map shows the location of the Philippines relative to Southeast Asia.*

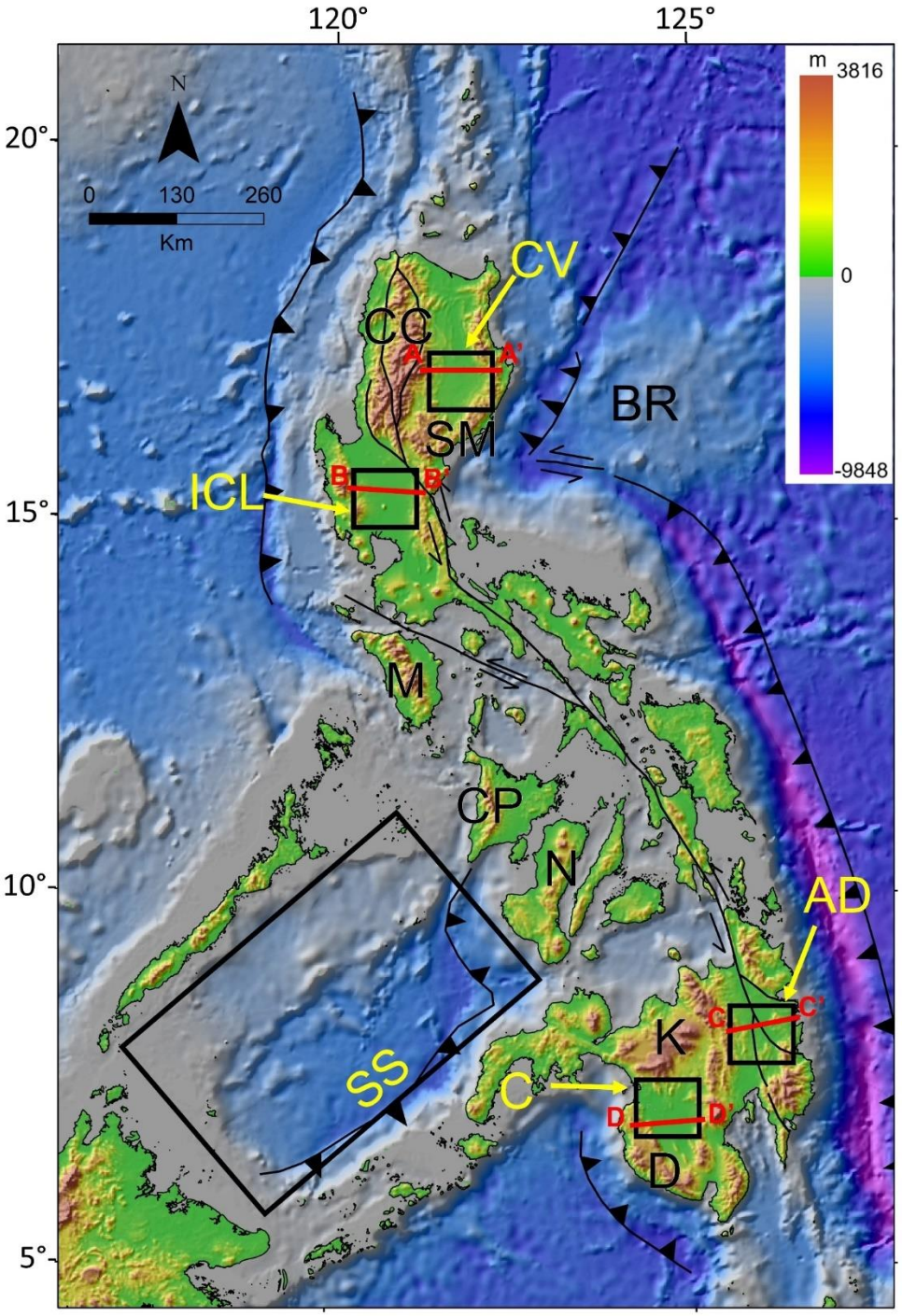

Figure 2-8. *Topographic and bathymetric map of the Philippines modified from GEBCO (2020) (https://download.gebco.net) showing major structural and tectonic features. The trenches surrounding the Philippine archipelago correlate with the deep bathymetric features. The topographic highs of Luzon Island include Central Cordillera (CC), Sierra Madre (SM), and Zambales Range (ZR). Katanglad Mountains (K) and Daguma Range (D) are the prominent elevated areas in Mindanao Island. Black-line boxes represent the locations of the specific areas where the 2-D radially averaged power spectrum technique (SS) and 3-D gravity inversion (CV, ICL, C, AD) were applied. CV = Cagayan Valley Basin, ICL = Ilocos-Central Luzon Basin, AD = Agusan-Davao Basin, C = Cotabato Basin, SS = Sulu Sea, BR = Benham Rise. A-A', B-B', C-C', and D-D' are section lines representing the geological cross sections presented in figures 2-17, 2-18, and 2-19.*

2.4 Methodology

The Philippines' isostatic anomaly digital grid was acquired from the World Gravity Map (WGM) of the Bureau Gravimetrique International (BGI) (2012). The BGI produced global gravity anomaly maps and digital grids considering an Earth model that accounts for the influence of most surface masses (e.g., atmosphere, land, oceans, lakes) (Balmino et al., 2012). Different corrections were applied to the gravity data to remove the non-geologic effects; three WGM anomaly maps were produced (i.e., surface free air, Bouguer, isostatic) by BGI taking into account the elevation data from ETOPO1 Global relief (Bonvalot et al., 2012). The gravity anomalies were computed based on the spherical geometry of the isostatic equilibrium (Airy-Heiskanen model). This computation removed the effects of deep isostatic roots and anti-roots (Balmino et al., 2012). Thus, the isostatic anomaly map shows the gravity anomalies corresponding to the upper crust's geologic features (Simpson et al., 1985; Lowrie and Fichtner, 2019). The isostatic anomaly grid has a gravity dataset with a 1-minute by 1-minute (1' by 1') spatial resolution (Balmino et al., 2012). The high-resolution isostatic anomaly digital grid of WGM was processed to reveal the Philippines' geologic structures and features from surface to upper crustal depths. Non-linear color zoning was used to generate the Philippines' isostatic anomaly map to efficiently represent the wide range of grid values (-280 to 200 mGal). The elevation data was downloaded from the 30-m Shuttle Radar Topographic Mission (SRTM) Digital Elevation Model (DEM). The bathymetric map of the Philippines was modified from the General Bathymetric Chart of the Oceans (GEBCO) 2020). The distribution of the general geologic groupings is outlined in the 'Geology of the Philippines' (e.g., Aurelio and Peña, 2002; MGB, 2010). ArcGIS software was used to register and overlay secondary data and visualize the features related to gravity anomaly. Geosoft Oasis Montaj software was utilized to process, filter, analyze, and generate gravity anomaly maps.

2.4.1 Grid Enhancement Processes

Upward continuation: In understanding deeper large-scale crustal features, gravity anomalies due to smaller local small structures are less important than regional anomalies. The regional gravity signals can be enhanced to focus on deeper features (Lowrie and Fichtner, 2019). Since deep and large bodies produced long-wavelength and broad anomalies, upward continuation was applied to smooth out near-surface effects (e.g., Nabighian et al., 2005). The isostatic gravity anomaly was continued upward to investigate the Philippines' density distribution according to depths. The digital grid was processed by applying an upward continuation filter at 5 and 20 km distances. The upward continuation estimates and emphasizes

the gravity anomaly at a minimum depth of half of the input filter (e.g., 5 km filter = 2.5 km minimum depth) (Jacobsen, 1987). The upward continuation was implemented to investigate the high-density ophiolitic basement rocks and low-gravity sedimentary basins at depth.

First Vertical derivative: The first vertical derivative (1VD) filter was applied to the free-air gravity anomaly (FAA) grid map to highlight the edges of gravity anomalies in the Sulu Sea. This grid enhancement process helped locate regional structures represented by density contrast boundaries. The first vertical derivative presents the rate of change of the gravity field in a vertical direction. The resolution of the short-wavelength anomalies is significantly enhanced, and the regional (long-wavelength) gravity field signal is attenuated when the first vertical derivative is applied (Nabighian et al., 2005). The shallow near-vertical contacts of the subsurface bodies in the Sulu Sea are represented by the zones corresponding to the zero-value. The resulting map was correlated with the Sulu Sea's upper crustal structures. The 1VD was only performed over the Sulu Sea to present an example of a supplementary way of deducing large-scale geologic structures and features, especially in remote areas with complex tectonics and scarce ground data.

2.4.2 Two-Dimensional (2-D) Radially Averaged Power Spectrum Analysis

The depth to the top of the interfaces with varying regional density contrast (e.g., Moho, basement rock) in the Sulu Sea was estimated using the 2-D radially-averaged power spectrum technique. Potential field data's power spectrum radial value can be obtained using a Fourier Transform (Spector and Grant, 1970; Mishra and Pedersen, 1982; Tselentis et al., 1988). Many studies have established the usefulness of the 2-D radially-averaged power spectrum analysis for estimating the Moho depth, crustal thickness, and basement rock interfaces (Gómez-Ortiz et al., 2005; Leseane et al., 2015; Kumar et al., 2016; Alemu et al., 2018; Kunnummal and Anand, 2019). In this study, the radial power spectra were prepared using the forward Fast Fourier Transform (FFT) function of the Geosoft software. The natural logarithms of the spectral values were plotted against the wavenumbers. A proportional average depth of the density contrast interface can be derived from the slope of each segment (e.g., Tselentis et al., 1988). The WGM2012 FAA grid in the Sulu Sea region delineated the estimated depths of the abrupt density discontinuities at deeper levels. The Sulu Sea was chosen as the representative area to apply the 2-D radially-averaged power spectrum analysis for characterizing the crustal features and estimating the Moho depth because of its complex tectonics (Murauchi et al., 1973; Kudrass et al., 1986; Rangin, 1989; Schlüter et al., 1996; Liu et al., 2014).

Firstly, the optimum sub-window size was identified by analyzing power spectra of different grid cell sizes of 0.5-degree by 0.5-degree (~ 55 km by 55 km), 1 degree by 1 degree (~110 km by 110 km), and 2 degrees by 2 degrees (~220 km by 220 km). Since the geophysical data available in the Sulu Sea are scarce, an initial estimate of the depth to Moho was obtained using the Crust 1.0 model (Laske et al., 2013) and some limited seismic reflection and refraction data (Murauchi et al., 1973).

The Crust 1.0 model presents a range of 18 to 23 km Moho depth over the Sulu Sea, while the seismic refraction measurements estimate a crustal thickness of around 11km along the NW Sulu Basin. By comparing the calculated depths of the first segment (at different sub-window sizes) using the 2-D spectral analysis and the initial estimate of Moho depths, a good correlation was obtained for a sub-window dimension of 1 degree by 1 degree. A total of 60 sub-windows having 50% overlap in all directions were generated. The spectral graph can be generally subdivided into three different slopes that correspond to the average depth of the interfaces. The first segment (lowest wavenumber) represents the deeper depth. The second segment corresponds to the shallower depth; the slope with the highest wavenumber is usually due to the shallow noise.

2.4.3 Three-Dimensional (3-D) Gravity Inversion

Several studies about the geology of the sedimentary basins of the Philippines have been published, focusing on drilling data and seismic profiles (e.g., Caagusan, 1978; Tamesis, 1981; Saldivar-Sali et al., 1986). These previous studies presented results and geologic cross-sections with higher resolution (e.g., basin thickness). However, since not all of the portions of the basins were assessed using seismic and drilling surveys, the wide-ranging coverage of the WGM2012 dataset can fill the gaps or areas without available ground data. The 3-D gravity inversion program is originally developed by Dr. Hideki Mizunaga (Appendix 2). The program is based on the theory of inverting surface gravity data to retrieve a 3-D distribution of density contrast (Li and Oldenburg, 1998). Using the Li and Oldenburg (1998) method, the Earth is modeled using a huge number of rectangular cells of constant density, and the final density distribution is generated by minimizing a model objective function while fitting the observed data. In the objective function, depth weighting was used to compensate for the natural decay of the kernels so that the inversion returns depth information. The coarseness of the 3-D inversion result presents a limitation for local and detailed interpretation. Nevertheless, these 3-D models provide supplementary information for a large-scale density estimate of the upper crustal zones.

The 3-D density contrast models of four large representative basins were estimated using a linear solution approach. The solution was determined using a linear relationship between the shape/dimension variation and density contrast. A large rectangular superblock was discretized into small rectangular blocks to enable the numerical solution of the inverse problem of the gravity data. A total of 638 gravity data points from the isostatic anomaly map of the WGM 2012 were used to generate a synthetic model of 8,000 blocks. The subsurface was divided into 50 by 40 by 4 in X, Y, and Y directions. The program employed iterations using a least-square solution to minimize the objective function (Haáz, 1953). An L2-norm regularization was used with varying smoothness factors to minimize the non-unique solution. This research performed several inversion processes using different smoothness factors.

The available geologic cross-sections were used to constrain the 3-D models. The smoothness factor that best matched the geologic cross-sections (Tamesis, 1981) based on drill hole and seismic reflection data was used for the 3-D gravity inversion. A parameter that minimizes the sum of the differences between the observed and calculated gravity anomalies (residual function) should be obtained to solve the inverse problem. The best values of the parameters were calculated by minimizing the sum of squares of the residuals between observed and calculated anomalies.

2.5 Results and Discussion

2.5.1 Gravity Signatures over the Philippine Island Arc System

The isostatic gravity anomaly map extracted from the WGM reveals the Philippines' regional geologic and tectonic features (Fig. 2-9). The PMB (red to pink; ~ 10 to 100 mGal) is generally surrounded by very low negative anomalies (blue; ~ 0 to -70 mGal) attributed to the deep trenches and troughs that bound the archipelago. Areas underlain by denser materials reflect more positive anomalies, while lower-density zones generate more negative signatures (Parasnis, 1979; Telford et al., 1990; Hinze et al., 2013; Lowrie and Fichtner, 2019).

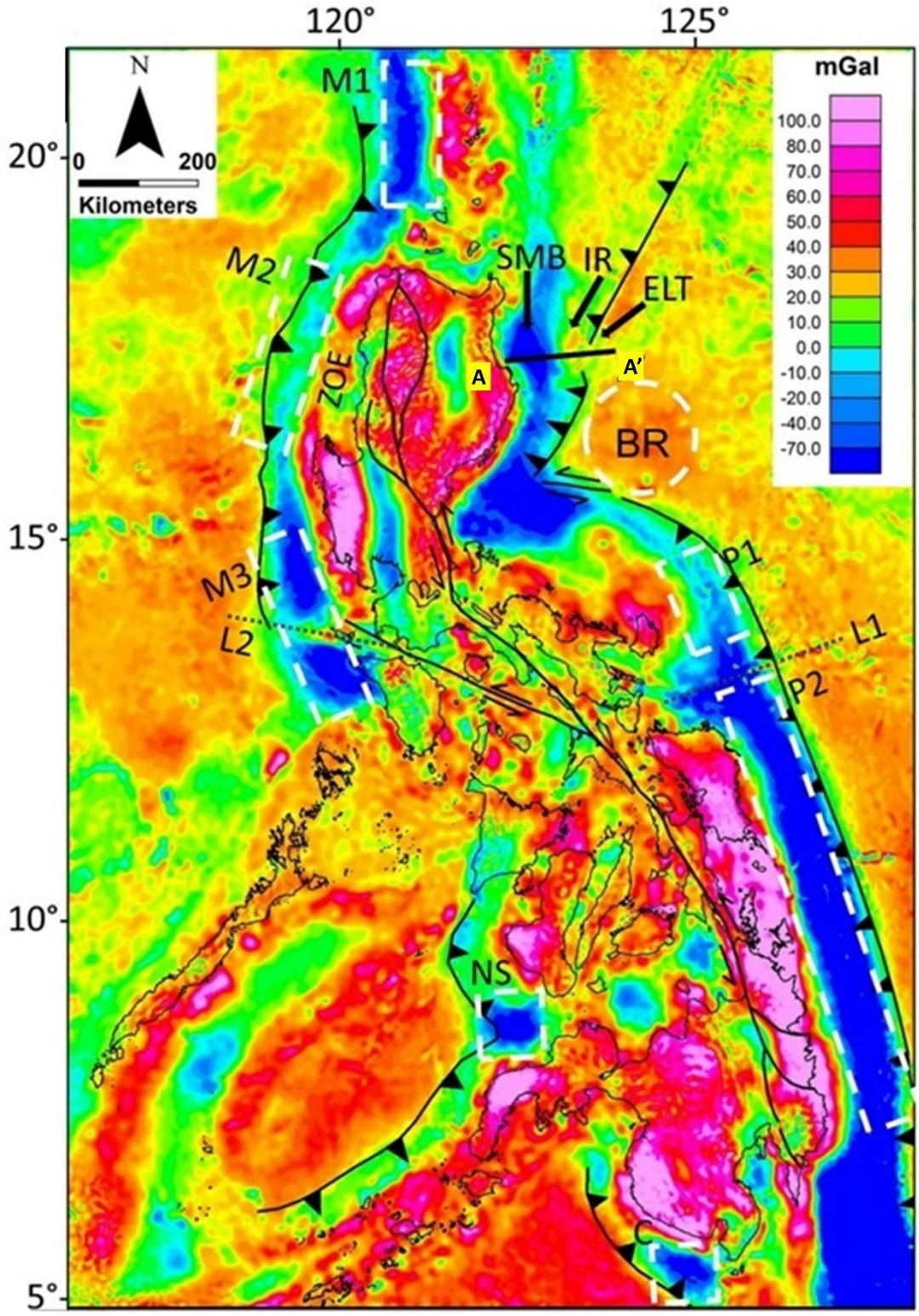

Figure 2-9. *Isostatic gravity anomaly map of the Philippines showing the Philippine Mobile Belt (PNB) bordered by negative anomalies corresponding to the deep trenches. Traces of significant structures (e.g., fault, trench) and features (e.g., Palawan-Mindoro Microcontinental Block, PNB) were overlaid on the map. SBM = Sierra Madre Basin, IR = Isabella Ridge, ELT = East Luzon Trough, BR = Benham Rise, P1 = northern Philippine Trench, P2 = southern Philippine Trench, M1 = northern Manila Trench, M2 = central Manila Trench, M3 = southern Manila Trench, ZOE = Zambales Ophiolite extension, NS = Negros and Sulu Trenches intersection, C = southern Cotabato Trench.*

The broad north-trending negative anomaly characterizes Luzon Island's eastern offshore area; it represents the East Luzon Trough (ELT) forearc basin. The very low negative anomaly zones (< -70 mGal) correspond to the thick accumulation of sediments, as confirmed by previous seismic and bathymetric surveys (Fig. 2-10). Lewis and Hayes (1983) defined the plate boundary along eastern Luzon as a young active zone that decreases its activity towards the north. They also noted that gravity signatures do not follow the ELT's trend, except for the low anomalies south of 17 deg latitude. This observation is consistent with the trace of the ELT gravity anomaly (which propagates to the northeast) that was delineated in the isostatic anomaly map (Fig. 3a). The discrepancy between the active tectonic zone and the ELT suggested that the ELT exemplifies a portion of past subduction episodes (Lewis and Hayes, 1983). The northern, very low gravity zone (< -70 mGal) was identified as the Sierra Madre Basin (SMB), with a maximum sediment thickness of 4.5 km (Lewis and Hayes, 1983). The remnant of the Oligocene subduction zone, the Isabella Ridge, was also delineated in the isostatic gravity anomaly map (Lewis and Hayes, 1983). Section A-A' on the map presents the pattern of the negative, positive, and moderate gravity anomalies. These anomalies represent Sierra Madre Basin (forearc basin), Isabella Ridge (subduction complex), and East Luzon Trough (trench), respectively (Fig. 2-10).

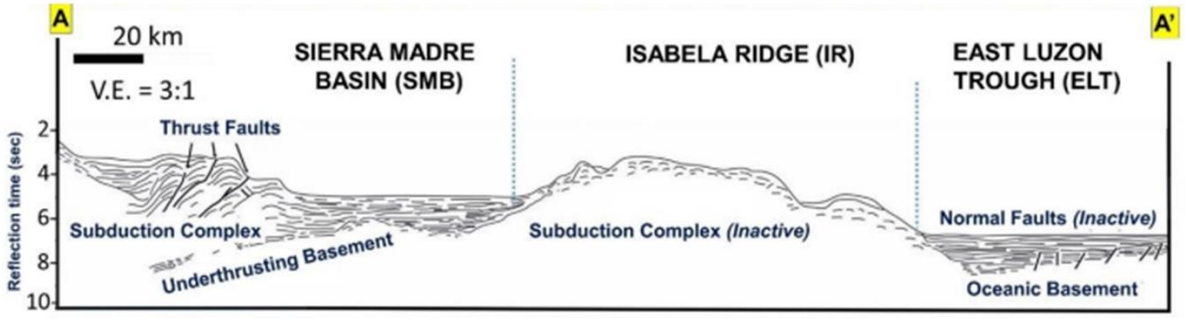

Figure 2-10 *Interpretation of seismic reflection profile across the SMB, IR, and ELT (modified from Hayes and Lewis, 1984). The location of the seismic reflection profile is marked by the A-A' in Figure 2-9.*

The Benham Rise, interpreted as a large igneous province (Barretto et al., 2020), is exemplified by the circular high gravity region on the gravity anomaly map (Fig. 2-9). To the south of the ELT, shallow negative gravity anomaly zones may indicate thick sediment accumulations, which defines the active tectonism along eastern Luzon (e.g., Lewis and Hayes, 1983). The gravity anomalies along the ELT agree with the known geology and tectonics delineated by previous studies (e.g., Lewis and Hayes, 1983; Barretto et al., 2020).

The Philippine Trench is described as a young subduction system with an accretionary prism that disappears towards the Mindanao area (Cardwell et al., 1980; Karig et al., 1986). The isostatic anomaly map showed varying gravity signatures along the Philippine Trench; the northern part (P1) has a higher gravity anomaly than the southern portion (P2). The very low negative gravity zone (<-70 mGal) along the southern part of the Philippine Trench system may correspond to very thick sediment accumulation along the forearc basin. The positive low (green) anomaly zones (0 to 20mGal) (P1 in Fig. 2-9) represent the elevated higher-density mantle rocks (seaward) and thinning of sedimentary deposits (landward) (e.g., Lewis and Hayes, 1983; Lowrie and Fichtner, 2019). The bathymetric anomalies defining the Philippine Trench do not coincide well with the low gravity anomalies indicating a heterogenous subduction zone morphology. Furthermore, an east-northeast linear gravity anomaly feature (L1) was also delineated on the gravity anomaly map, which may represent a structural boundary (lineament) between the P1 and P2 (Fig. 2-9). This linear anomaly can also be recognized in the bathymetric map presented in Figure 2-8.

The east-dipping Manila Trench shows non-uniform negative gravity anomalies that generally correspond to the variable thicknesses of sedimentary deposits overlying basement rocks. Hayes and Lewis (1984) reported that the Manila trench's forearc basins have a maximum sediment thickness of 4.5 km. They also suggested that the thickness variation in the forearc basin is due to sediment accumulation and the accretionary prism's local uplift rate. The distinct negative gravity values (< -40 mGal) on the northern (M1) and southern (M3) portions of the Manila Trench represent a balance between the local accumulation of sediments and the uplift rate of accretionary prisms (Fig. 2-9). In contrast, the absence of very low negative gravity anomaly values in the central part (M2) corresponds to the lower rate of local sediment accumulation relative to the rate of accretionary prism uplift (complex forearc) (Hayes and Lewis, 1984). The very low negative gravity anomalies (<-70 mGal) at the northern and southern portions of the Manila Trench correspond to the very thick sediment deposits; high sediment supply comes from the collision zones of Taiwan-Eurasia (north) and the Palawan-Mindoro Microcontinental Block (south) (Hayes and Lewis, 1984). Recent seismic reflection and bathymetry data confirm the deformational patterns in the forearc region of the Manila Trench (Armada et al., 2020b).

The gravity anomalies along the Manila Trench (i.e., M1, M2, M3) (Fig. 2-9) correlate well with the bathymetric and seismic data from earlier studies (e.g., Hayes and Lewis, 1984; Armada et al., 2020). However, the gravity anomaly map can recognize additional regional geologic and tectonic features. The very high and contiguous gravity anomaly along the

offshore western Luzon Island was interpreted as the extension of the Zambales Ophiolite Complex (Fig. 2-9). Furthermore, the gravity anomaly map shows that M3 is divided by a west-northwest linear gravity anomaly (L2) (Fig. 2-9). That can also be recognized in the bathymetric map (Fig. 2-8) and can be interpreted as a regional tectonic feature related to the Philippine Fault Zone.

The Negros, Sulu, and Cotabato Trenches have prominent gravity lows generally associated with thick low-density sediments. Based on the generally expected gravity anomaly signatures of trenches and the previously defined correlation between the processed isostatic gravity anomaly map and detailed ground surveys, the complex forearc basin system of these three trenches (i.e., Negros, Sulu, Cotabato) can be understood. The peculiar low gravity zones were noted at the intersection of Negros and Sulu Trenches (NS) and the southern part of the Cotabato Trench (C) (Fig. 2-9). Since there are no detailed studies about these three trenches, we can deduce that the very low gravity zones may suggest a very thick accumulation of sediments; these may indicate active local tectonics along the negative zones.

The isostatic gravity anomalies correlate with the subsurface geology, sedimentary basins, and basement rocks of the Philippines. The map reflects the variations of gravity fields caused by density differences of materials in the upper crust. Based on the lithologic classification from published works (e.g., Aurelio and Peña, 2002; MGB, 2010), regional groupings were overlaid on the gravity anomaly map (Fig. 2-11). The summary of the regional geologic groupings concerning the gravity anomaly map is presented in Table 2-2. Generally, negative gravity signatures represent the sedimentary basins (< 0 mGal), moderate gravity anomalies correspond to the metamorphic rocks (0 to 80 mGal), and very high gravity anomalies typify ophiolitic basement rocks (> 80 mGal).

Table 2-2. *Significant regional geologic features are delineated on the isostatic anomaly map of the Philippines.*

General Anomaly	Correlation	Location
Low gravity anomaly (< 0 mGal)	Sedimentary Rocks	Ilocos-Central Luzon Basin (ICL), Cagayan Valley Basin (CV), Mindoro Basin (M), Southern Luzon-Bicol Basin (SLB), Iloilo Basin (I), Visayan Sea Basin (VS), Samar Basin (S), Agusan-Davao Basin (AD), Cotabato Basin

Moderate gravity anomaly (0 to 80 mGal)	Metamorphic Rocks	Continental: Northern Palawan-Mindoro Block (NPM), Antique Range (AR) Island Arc: Eastern Luzon (EL), Southern Visayas (SV), Mindanao (M)
High gravity anomaly (> 80 mGal)	Ophiolitic Rocks	Western Luzon (Zambales Ophiolite Complex), Northeast Luzon (Ilocos Norte Ophiolite/ Peridotite), Eastern Luzon (Isabela Ophiolite), Southeastern Luzon (Cadig Ophiolite Complex, Lagonoy Ophiolite, Cagraray Peridotire, Pangarinan Peridotite), Mindoro (Amnay Ophiolite), Antique (Antique Ophiolite), Eastern Visayas-Mindanao (Dinagat Ophiolite), Central Mindanao (Awang Ultramafic Complex, Pantaron Ultramafic Complex), Western Mindanao (Polanco Ophiolite), Southeastern Mindanao (Pujada Ophiolite)

The gravity anomaly map also correlates well with the three principal basins of the Philippines, namely, Ilocos-Central Luzon Basin (ICL), Cagayan Valley Basin (CV), and Agusan-Davao Basin (AD) (Fig. 2-11a). These sedimentary basins have distinct and defined north-trending negative anomalies (< -20 mGal). The isostatic gravity anomaly map only shows negative gravity anomalies on significantly thick sedimentary formations. Correlated with the established geology (Aurelio and Peña, 2002; MGB, 2010), other portions of the basins do not show negative anomalies because of their shallow or very dense basement rocks; high gravity anomaly masks the gravity lows representing the sedimentary formations. Circular gravity lows were also delineated across the Bohol Sea, signifying a thick sediment accumulation. This feature was previously interpreted as the proto-Southeast Bohol Trench that bound the Western Visayan Block (Yumul et al., 2008b).

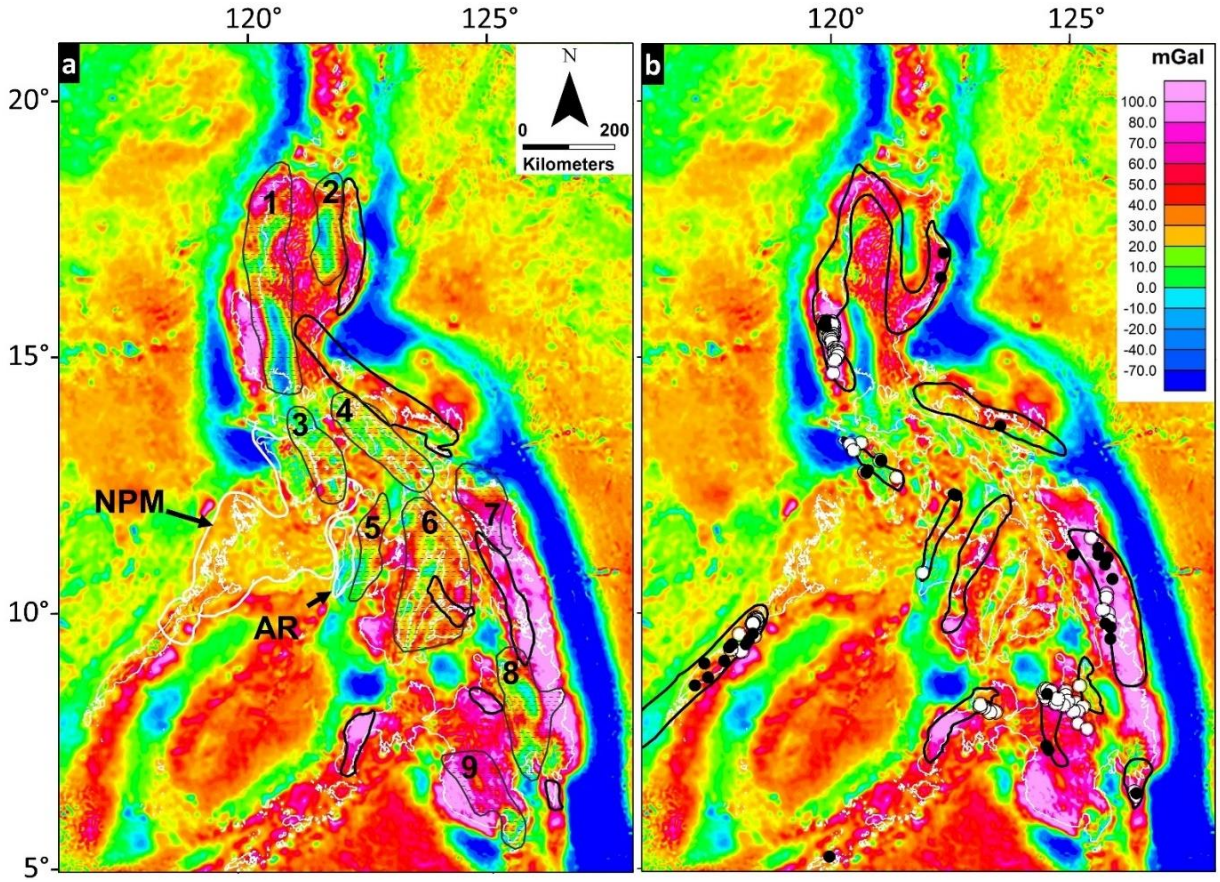

Figure 2-11. *Isostatic anomaly map of the Philippines showing the general distribution of (a) sedimentary basins (polygons with hachures), metamorphic rocks (heavy line polygons), and (b) ophiolitic rocks (modified from MGB, 2010). Numbers represent the sedimentary basins of PMB affinity: 1 = Ilocos-Central Luzon (ICL), 2 = Cagayan Valley (CV), 3 = Mindoro, 4 = Southern Luzon-Bicol, 5 = Iloilo, 6 = Visayan Sea, 7 = Samar, 8 = Agusan-Davao (AD), 9 = Cotabato (C). NPM = Northern Palawan-Mindoro block (white polygon), AR = Antique Range. Circles symbolize the occurrences of nickel (black) and chromite (white) deposits in the Philippines (MGB, 2010).*

The distribution of metamorphic rocks generally coincides with moderate gravity anomaly values (0 to 80 mGal) (Fig. 2-11a). MGB (2010) classified metamorphic rocks into Pre-Cretaceous (continental) and Cretaceous (island arc) metamorphic zones. Pre-Cretaceous metamorphic zones in the east-central Philippines (i.e., Northern Palawan-Mindoro, Antique Range) are represented by lower gravity anomalies (0 to 30 mGal). The Cretaceous metamorphic rocks, sparsely distributed in eastern Luzon, Visayas, and Mindanao islands, have higher gravity signatures (30 to 60 mGal). The Cretaceous zones are characterized by mafic-to-ultramafic rocks (Aurelio and Peña, 2002; MGB, 2010). The exception to the positive correlation between the moderate gravity signatures and metamorphic rocks are those areas that are dominantly underlain by ophiolitic rocks. Ophiolitic rocks' high gravity anomaly

signature masks the gravity lows representing the metamorphic regions. The documented metamorphosed ophiolitic rocks along eastern Luzon (Geary et al., 1988; Billedo, 1994) and eastern Mindanao (Pubellier et al., 1991; Quebral, 1994) are consistent with these observations.

The regional groupings of ophiolitic rocks, delineated by previous works (e.g., Aurelio and Peña, 2002; MGB, 2010), coincide well with areas having very high gravity anomalies (> 70mGal) (Fig. 2-11b). The occurrence of ophiolitic rocks, which serve as basement rocks of most islands, is extensive within the Philippines. Lower gravity anomalies are due to metamorphism in some ophiolitic zones (e.g., southeastern Luzon). The gravity anomaly map presents clusters of very high gravity zones identified as ophiolitic regions. These clustered regions have distinguishable massive outcrops of ultramafic rocks: northern Luzon (Ilocos Norte Ophiolite), western Luzon (Zambales Ophiolite Complex), eastern Luzon (Isabela-Aurora Ophiolite), southern Palawan (Palawan Ophiolite), Samar-eastern Mindanao (NE Leyte, Samar, SW Leyte, Dinagat, Surigao, Pujada ophiolites), Central Mindanao (Central Mindanao ophiolites), and western Mindanao (Zamboanga Ophiolite). These regions were described in McCabe et al. (1982), Schweller et al. (1984), Rangin et al. (1985), Mitchell et al. (1986), and MGB (2010). This gravity information is essential in constraining geologic boundaries in areas challenging to map due to inaccessibility. The massive occurrence of ultramafic rocks resulted in highly positive anomalies in these regions. These high positive anomalies have previously been reported for some Philippine ophiolites, such as the Southeast Bohol Ophiolite (Barretto et al., 2000) and the Zambales Ophiolite Complex (Salapare et al., 2015). Gravity-high anomalies related to ophiolites were also observed in some studies in the USA (Godfrey et al., 1997) and Oman (Manghnani and Coleman, 1981). Complete ophiolite suites were also reported in some areas (i.e., Zambales, Isabela, southern Palawan, Pujada). These wide-ranging and regional gravity signatures provide a better picture of the complex Philippine island arc system in correlation with available ground data.

2.5.2 Basement Rocks and Basins

The Philippines' upward continuation maps show that the very high gravity anomalies (> 75 mGal), associated with the dense features, are distributed in Luzon, southern Visayas islands, Mindanao, and southern Palawan. The 5 km upward continuation delineates areas underlain by very dense ophiolite rocks or may indicate the occurrence of massive magmatic arcs (Negros, Daguma Range). Very high (> 90 mGal) gravity anomaly signatures coincide with the well-known massive ophiolitic outcrops (e.g., Tamayo et al., 2004; Yumul, 2007). The

5 km upward continuation of gravity anomaly can be clustered into four regions: western Luzon, eastern Visayas-Mindanao, western Mindanao, and southern Palawan (Fig. 2-12a).

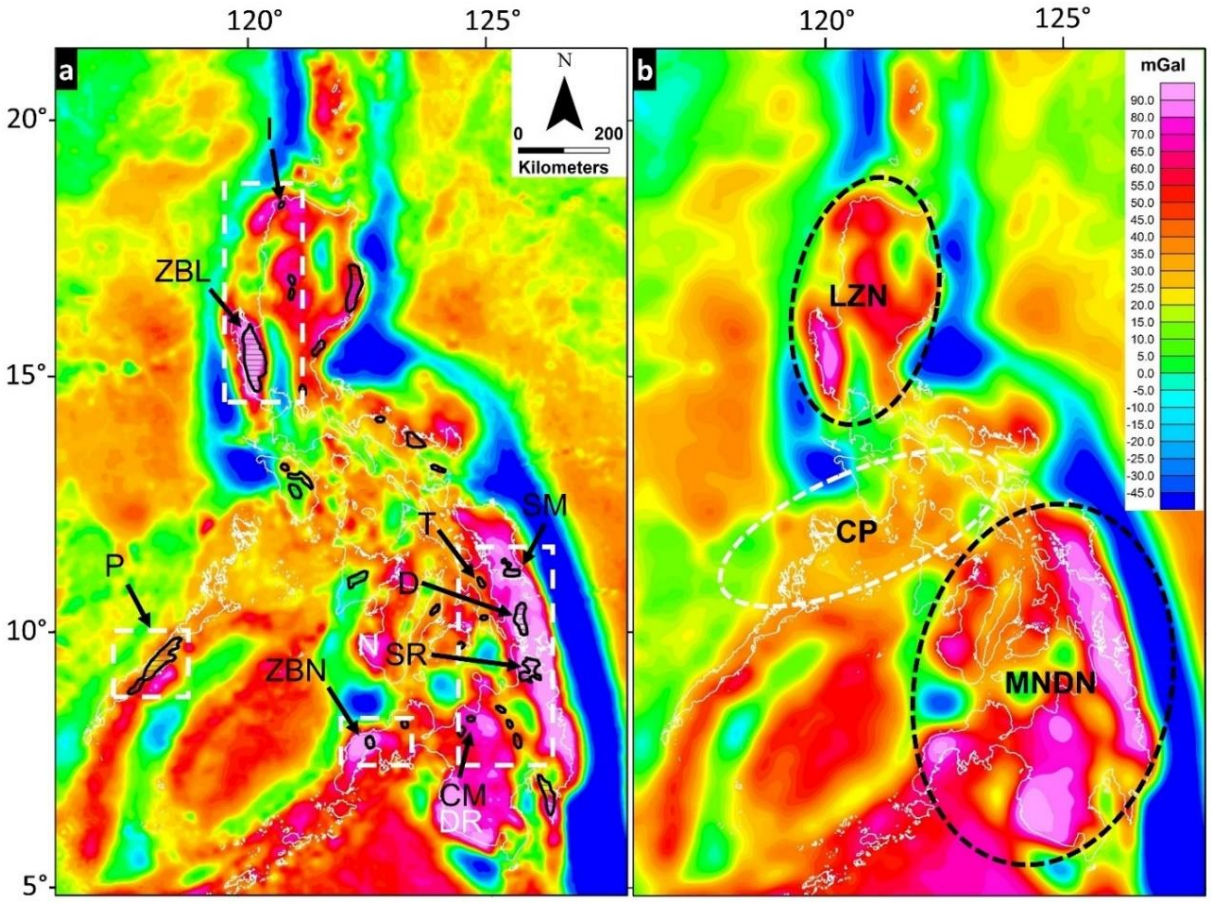

Figure 2-12. *Upward continued maps of the Philippines at 5 and 20 km representing minimum depths of (a) 2.5 and (b) 10 km, respectively. (a) Massive ophiolitic outcrops coincide with very high-gravity anomaly signatures (> 90mGal). Representative ophiolites and ophiolite complexes are labeled on the map: I = Ilocos Norte Ophiolite, ZBL = Zambales Ophiolite Complex, P = Palawan Ophiolite, ZBN = Zamboanga Ophiolite, T = Tacloban Ophiolite Complex, SM = Samar Ophiolite, D = Dinagat Ophiolite, SR = Samar Ophiolite, CM = Central Mindanao Ophiolite. White labels represent the massive magmatic arcs: N = Negros, DR = Daguma Range. White dashed polygons present the four major zones (> 90 mGal) that suggest thicker and more massive ophiolitic basement rocks. (b) Generally, the central Philippines has lower-gravity anomalies (20 to 35 mGal) than the rest of the archipelago (45 to 200 mGal). CP = Central Philippines, LZN = Luzon, MNDN = Mindanao.*

Very high gravity anomalies were recognized in western Luzon - representing the Zambales Ophiolite Complex (e.g., Abrajano and Pasteris, 1989; Yumul and Dimalanta, 1997), and offshore extension of Ilocos Norte Ophiolite northeast of Luzon (e.g., Arai et al., 1997; Pasco et al., 2019). These high gravity anomalies characterize the dense ultramafic rocks separated by the thick Ilocos-Central Luzon basin. In southern Palawan, the exceptionally high

gravity anomaly corresponds to the Palawan Ophiolite (e.g., Rammlmair et al., 1987; Aurelio et al., 2014) perceivable at the eastern offshore of central Palawan. High gravity signatures of Zamboanga Ophiolite (i.e., Polanco, Titay) (Yumul et al., 2004) are apparent in western Mindanao. Finally, the continuous very high gravity anomalies along the Leyte and Samar islands due to the Tacloban and Samar ophiolites (e.g., Balmater et al., 2015; Guotana et al., 2017) are very prominent on the 5 km upward continuation map (Fig. 2-12a). The same anomalies are also remarkable along the easternmost Mindanao due to the Dinagat and Surigao ophiolites (Yumul, 2007; MGB, 2010). Similar to the case in northern Luzon, the signatures of the very high anomaly zones in western Mindanao and northcentral Mindanao (Central Mindanao Ophiolite) are separated by the negative anomaly signature of the ~4.5 km thick Agusan Davao Basin (Ranneft et al., 1960). High gravity signatures of the massive Negros and Daguma magmatic arcs that persist at deeper levels may indicate dense ophiolitic basement rocks. Limited regional studies of southern Mindanao mentioned the occurrence of serpentinized peridotite as part of the Basement Complex of western Mindanao (e.g., Ranneft et al., 1960). After applying the 20 km upward continuation (Fig. 2-12b), the exceptionally high anomalies (> 90 mGal) are only recognizable in western Luzon and southwest Mindanao. These anomalies indicate that the signal sources are located at a deeper level. The persistence of the very high gravity anomaly values in southern Mindanao may suggest a massive and dense ophiolitic basement complex. It is also interesting to note that the central Philippines (CP) has generally lower gravity signatures (20 to 35 mGal) compared to the distinct very high gravity values (45 to 200 mGal) in Luzon and Mindanao (Fig. 2-12b). This occurrence is a significant indication of dissimilar major basement rocks (i.e., continental and oceanic origins) of the Philippine archipelago, revealed by their characteristic gravity signatures (e.g., Manalo et al., 2015).

In contrast to the high anomaly zones of dense and massive basement rocks, the sedimentary basins manifest a strong negative anomaly due to the mass deficiency of the underlying thick sedimentary rocks and quaternary alluvium. The gravity anomaly data from Luzon Island were separately presented to understand the range of gravity anomaly values corresponding to the sedimentary basin. Figure 2-13a shows Luzon Island's gravity signatures after the 5 km upward continuation filtering; negative gravity anomalies characterize the Philippines' two significant basins, i.e., Ilocos-Central Luzon Basin (ICL) and Cagayan Valley Basin (CV). The Oligo-Miocene magmatic belts generally separate the two basins along Central Cordillera (MGB, 2010) (Fig. 2-13b). The prominent north-trending negative anomalies (-15 to -37 mGal) remain until the 20 km upward continued depth (Fig. 2-13c). The

Ilocos-Central Luzon Basin (west) exemplified a larger negative anomaly zone than the Cagayan Valley Basin (east). The maximum thickness of the Oligocene to Pleistocene sedimentary deposits underlying the Ilocos-Central Luzon Basin (14 km) is thicker than the sedimentary sequence in Cagayan Valley Basin (10 km) (Tamesis, 1976; Bachman and Lewis, 1983). The portions dominated by very low anomalies (< 5 mGal) provided a general indication of where sediment accumulation is thickest within the basins. At a 10 km upward continuation, the lowest gravity anomalies were delineated in the central portion of the Cagayan Valley Basin and the southern part of the Ilocos-Central Luzon Basin. The 20 km upward continuation map shows the negative gravity anomaly diminished in the northern part of the Ilocos-Central Luzon Basin; it implies that the dense basement rock is shallower in the northern Ilocos Region than in south-central Luzon. These new regional processed data provided supplemental knowledge in understanding the Philippines' basins and basements concerning their gravity signatures.

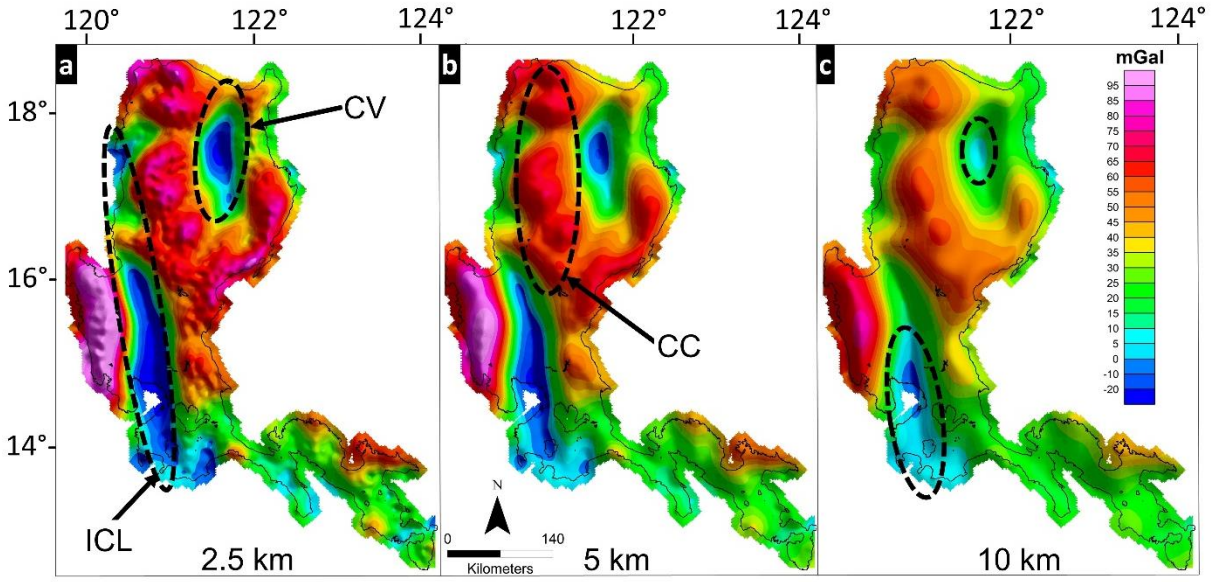

Figure 2-13. *Upward continued maps of Luzon Island at 5, 10, and 20 km representing minimum depths of (a) 2.5, (b) 5, and (c) 10 km, respectively. Magmatic belts separate Ilocos-Central Luzon Basin (ICL) and Cagayan Valley Basin (CV) along Central Cordillera (CC) (MGB, 2010). (c) Very low-gravity anomaly zones (< 5mGal) indicate portions of the basins with the thickest sediment accumulation (e.g., Tamesis, 1976; Bachman and Lewis, 1983).*

2.5.3 Crustal Features and Moho Depths in the Sulu Sea

Large-scale features in the Sulu Sea were characterized using the FAA grid data of the WGM 2012. The FAA gravity map of the Sulu Sea shows values that range from -86 to 85 mGal (Fig. 2-14a). This map reveals regional geologic features (with varying density) representing shallow and deep sources. The Sulu Sea has three distinct gravity features, which

will be the focus of this section. The very high gravity anomaly (> 60 mGal) of Cagayan Ridge subdivides the basin into two: NW Basin and SE Basin (Fig. 2-14a). This east-northeast-trending feature represents a submerged ridge of an extinct volcanic arc, which is generally composed of volcanic rocks (e.g., basalt, andesite) overlain by thick carbonate sediments (Kudrass et al., 1986; Rangin, 1989). Gravity low (< -24 mGal) represents the NW Basin, while moderate gravity anomalies (20 to 40 mGal) characterize the SE Basin. The NW Basin represents a suture zone that marks the collision between the Palawan Continental Block and Cagayan Ridge (Rangin and Silver, 1991). There are two prominent hypotheses for the origin of the SE Basin. The first hypothesis implies that the subduction of the Proto South China Sea (PSCS) triggered the Cagayan arc volcanism and 'SE Basin' back-arc formation. The counter hypothesis suggests that the SE Basin is a marginal basin that opened before the Cagayan arc volcanism (Rangin and Silver, 1991).

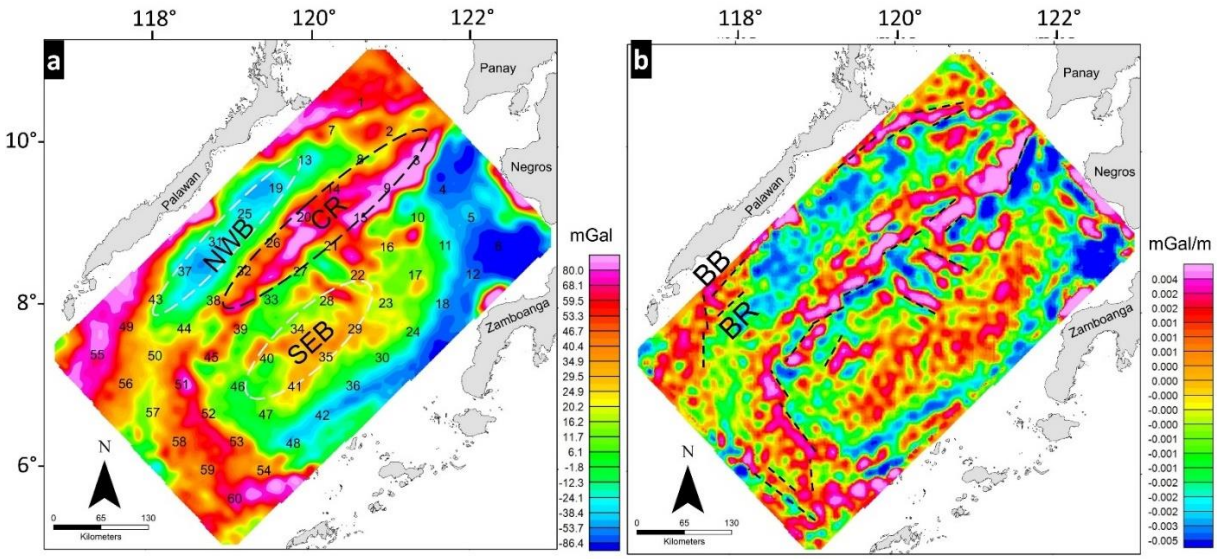

Figure 2-14. *a) FAA map of Sulu Sea showing the three major features: NWB = Northwest Basin, CR = Cagayan Ridge, SEB = Southeast Basin. The numbers represent the center of the sub-windows location for calculating the radially averaged power spectrum. b) The first vertical derivative map reveals the Sulu Sea's enhanced shallow features. Prominent lineaments (black dashed line) were traced to some large-scale structures (e.g., Rangin, 1989; Schlüter et al., 1996). BB = Balabac Basin, BR = Banggi Ridge.*

The first vertical derivative (1VD) map was prepared to delineate upper crustal geologic features in the Sulu Sea (Fig. 2-14b). The 1VD map generally presents how much the gravity potential changes in the vertical direction (e.g., Nabighian et al., 2005). Steep and semi-vertical features, where potential does not change, are represented by zero or near-zero values.

Prominent linear features and some large-scale structures (e.g., vertical fault, fold axis) identified by the previous studies (e.g., Rangin, 1989; Schlüter et al., 1996) were overlaid on the map. The 1VD map shows that anomalies are associated with shallow features that are dominantly related to the Cagayan Ridge.

Gravity anomaly features at the central part have a general NE-SW orientation. These structures are related to normal faults as delineated from the seismic and Seabeam data (Rangin, 1989). The southeast extension of the Cagayan Ridge fracture zones was also traced to the map's southwesternmost portion. These features imply the extension of Cagayan Ridge to the southwest, as represented by the similar rock types identified in the area (Rangin, 1989). The NW Basin and SE Basin are relatively quiet regarding 1VD features. However, some large-scale features bound the northern and southern NW Basin. The ENE-trending features in the northern part of the NW Basin are associated with the set of folds (Rangin, 1989).

In contrast, NE and NNW-trending features are attributed to the normal faults along Balabac Basin and Banggi Ridge (Rangin, 1989). Two NW-trending features were identified in the 1VD map adjacent to the SE Basin. The previous studies did not recognize these features; these areas can be sites of interest for future detailed studies. Generally, the good correlations present us with a supplementary way of deducing large-scale geologic structures and features, especially in remote areas without available ground data.

The result of the 2-D spectral analysis presented an estimated depth of Moho and basement rocks along the three prominent gravity high and low zones. Figure 2-15 shows representative examples of 2-D radially-averaged power spectral curves in the Sulu Sea. The 2-D radially-averaged power spectrum analysis revealed that the average depth to the top of the deeper segment ranges from 12 to 23 km (Fig. 2-16a). On the other hand, the average depth to the top of the shallow segment is within the range of 5 to 11 km (Fig. 2-16b). The deeper segment is associated with the Moho depth based on the 11 to 23 km depth range obtained from the Crust 1.0 model (Laske et al., 2013) and some available seismic reflection and refraction data (Murauchi et al., 1973). The gravity zone associated with the Cagayan Ridge can be attributed to a relatively shallow Moho (~14 to 16 km). The NW Basin is generally represented by deep Moho (~19 to 22km), while the SE Basin is dominantly characterized by very shallow Moho (~ 12 to 14 km) (Fig. 2-16a). The shallower segment is interpreted as the depth to the basement rock (5 to 11 km).

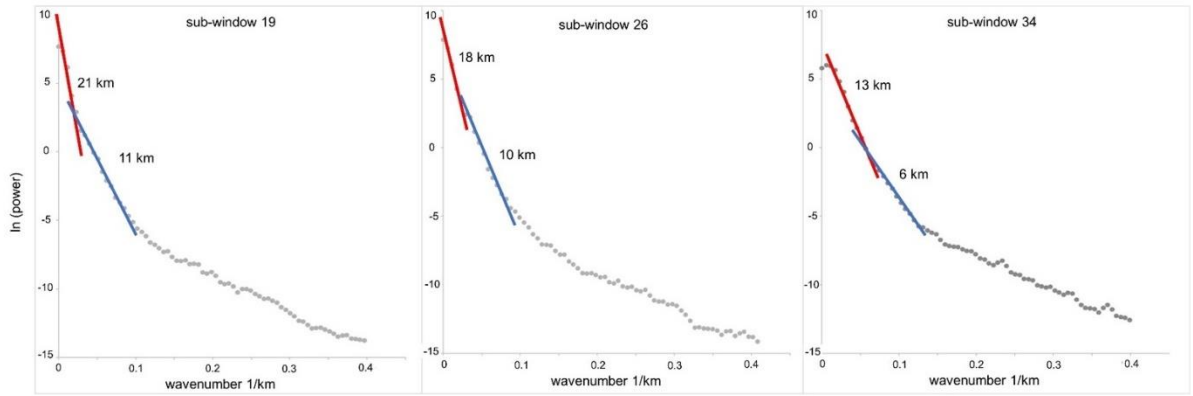

Figure 2-15. *Two-dimensional (2-D) radially averaged power spectral curves of some representative blocks extracted from 1-degree by 1-degree sub-windows of the FAA anomaly map in the Sulu Sea. See Figure 2-14(a) for the sub-window location.*

The depth to basement rock estimate was constrained by previous works (Murauchi et al., 1973; Rangin, 1989). Based on the seismic refraction and reflection study of Murauchi et al. (1973), the layer at a depth of 6km (SE Basin) to 10 km (NE Basin) may represent a volcanic basement or metasediments. The gravity zone associated with the NW Basin has a deep basement rock (north: 9 to 11 km, south: 7 to 9 km) (Fig. 2-16b). This occurrence can be attributed to the thickening of the sedimentary deposits (1 to 7.5 km) towards Palawan (Murauchi et al., 1973).

The SE Basin is dominantly characterized by basement rock with shallow depth to the north (5 to 7 km) and relatively deep (7 to 9 km) to the south. The shallow basement rock is due to a basement rock overlain by thin sedimentary deposits (Murauchi et al., 1973; Rangin, 1989). Generally, the southeastern side of the Cagayan Ridge has ~7.5km depth to basement rock. However, varying depths to the basement were noted on the northwestern side. Some portions in the north have very shallow basement rocks (5 to 7 km), while some southern parts have deeper basement rocks (8 to 9 km). That may be attributed to the difference in sedimentary thickness along these sides (Murauchi et al., 1973; Rangin, 1989).

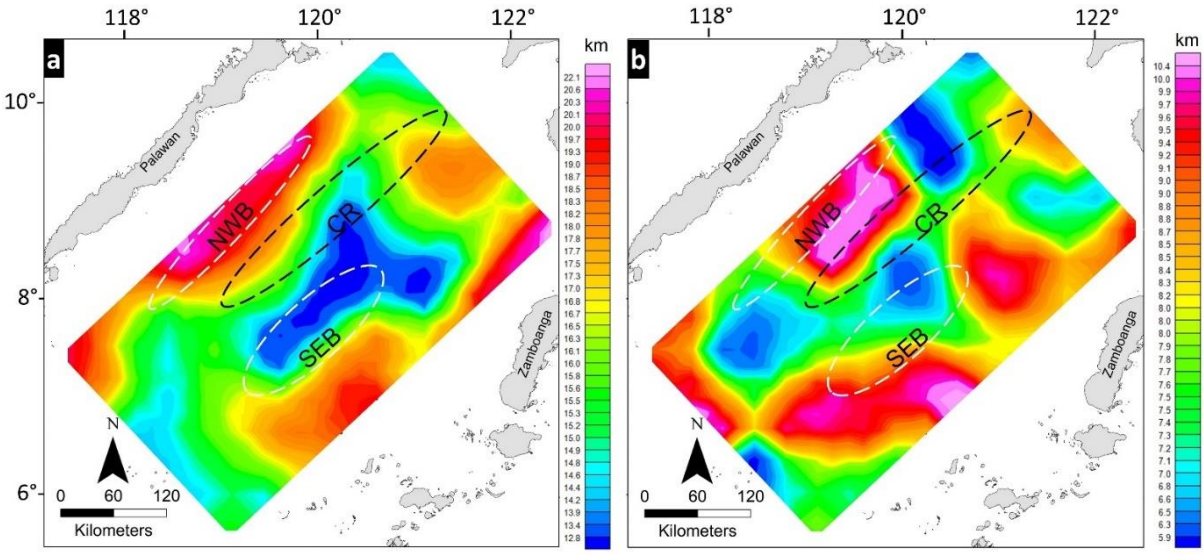

Figure 2-16 *Average (a) Moho and (b) basement depth maps calculated from radially averaged power spectrum technique. The maps overlay tracks of the three major features: NWB = Northwest Basin, CR = Cagayan Ridge, SEB = Southeast Basin.*

The three prominent FAA gravity anomalies discussed in this section are attributed to the depths of basement rock and Moho. However, based on the pattern and orientation of the depth maps, the FAA gravity anomaly associated with Cagayan Ridge and the two sub-basins: NW and SE basins, are predominantly controlled by Moho undulation. The new estimate of Moho depth and pattern, based on the 2-D spectral analysis along the Sulu Sea, supports the back-arc basin evolution hypothesis of the SE Basin (Rangin and Silver, 1991).

The deep Moho and basement rock (thicker sedimentary deposits) in NW Basin can be associated with the thickened crust due to the subduction/ collision of the Proto South China Sea (PSCS) (Rangin and Silver, 1991; Liu et al., 2014). This event triggered the volcanism of the Cagayan arc and the opening of the 'SE Basin' oceanic back-arc basin (shallow Moho and basement rock). Although the 2-D spectral analysis scope is limited within the Sulu Sea, the results still present the usefulness and applicability of the WGM 2012 dataset for large-scale mapping and reconnaissance surveys.

2.5.4 Three-Dimensional (3-D) Gravity Inversion in Sedimentary Basins

This section presents a general discussion of the results of 3-D gravity inversion in representative areas of major sedimentary basins in the Philippines. The result of the 3-D gravity inversion provides additional knowledge by presenting new 3-D density contrast models of the subsurface with extensive coverage (e.g., estimated thickness, morphology). The 3-D density contrast model of the Cagayan Valley Basin (CV) shows a low-density anomaly belt, which has a general trend NNW direction. This low-density zone corresponds to CV's low gravity anomaly of sedimentary basin features (Fig. 2-17a). Figure 2-17b shows a low-density zone characterized by deep extension at the northern part of the map (7 km depth). These features were not presented in the southern part of the map. The thick, low-density zones to the north were correlated to the upper Neogene to lower Neogene sedimentary deposits (Tamesis, 1981). Older and denser Cretaceous-Paleogene sedimentary rocks underlie these sedimentary deposits (Fig. 2-18e). On the contrary, the 3-D density of the Central Luzon Basin (CL) presents deeper and more extensive low-density zones, especially in the southern part of the map (Fig. 2-17c). Relatively thin low-density zones, representing thin sedimentary deposits, are recognized in the central part of the map (Fig. 2-17d). The southern part reveals the very thick Quaternary and Neogene deposits (>7 km) (Fig. 2-18f). The very dense zones for the CV and CL 3-D models represent the basement rocks of the sedimentary basins (e.g., ultramafic complexes, ophiolitic rocks) (e.g., Tamesis, 1981).

The Agusan-Davao Basin (AD) and Cotabato Basin (C) basin morphologies were also mapped using the 3-D gravity inversion results. Figures 2-19a and 2-19b show relatively thin and narrow low-density zones representing the Pliocene to Miocene sedimentary deposits. The AD is generally oriented NNW and thickens from south to north. The sedimentary basin thickness can be estimated at 3 to 5 km. Figures 2-19c and 2-19d show maps and sections of the Cotabato Basin that are dominantly influenced by positive density contrast. Higher density zones correspond to the very shallow basement rocks in the area. The very thin (2 to 3km) low-density zones are interpreted as Neogene sedimentary deposits distributed in the central and eastern parts of the maps (Fig. 2-19f). The low negative density contrast in the eastern part is attributed to the Quaternary pyroclastics in the area. The model's resolution is coarse due to the dataset's coarseness and the program's computational capacity. Nonetheless, using the 3-D gravity inversion results, the large-scale sedimentary thickness distribution and basin morphology can be mapped effectively and appropriately. Using the WGM2012 dataset for basin characterization and 3-D visualization presents a fast and efficient way of understanding the regional geology of vast areas of interest.

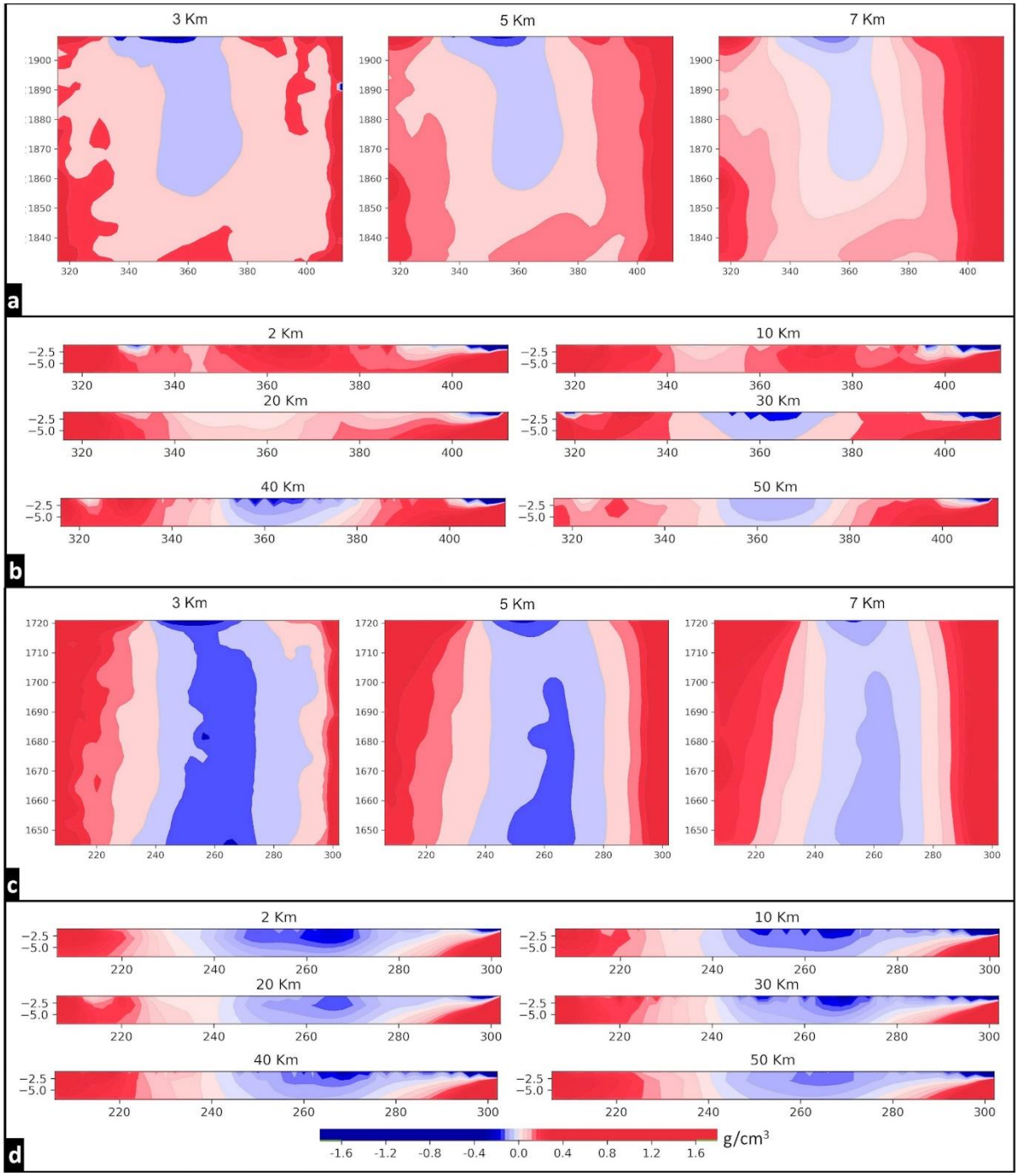

Figure 2-17. *(a) Horizontal (at 3, 5, and 7 km depths) and (b) vertical slices at the Y-axis (at 2, 10, 20, 30, 40, and 50 km distances from the southern edge of the map) of the Cagayan Valley Basin's (CV) 3-D density contrast model. The (c) horizontal and (d) vertical slices at the Y-axis of the 3-D density contrast model of the Central Luzon Basin (CL) present broader, deeper, and negative density contrast zones. Coordinates (a, c) are in WGS 84/ UTM Zone51 N (km).*

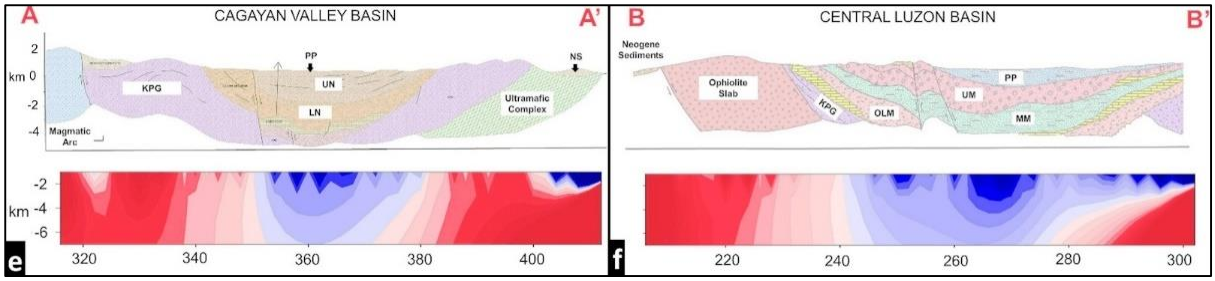

Figure 2-18. *Comparison of the geological cross sections (upper) and density contrast model (× 1.5 vertical exaggeration) resulting from the 3-D inversion (lower) for (e) Cagayan Valley Basin and (f) Central Luzon Basin. KPG = Cretaceous-Paleogene, LM = Lower Neogene, UN = Upper Neogene, OLM = Oligocene-Lower Miocene, MM = Middle Miocene, UM = Upper Miocene, PP = Plio-Pleistocene. The geological cross sections are modified from Tamesis (1981).*

2.6 Conclusion

Many parts of the Philippine island arc system still lack geopotential field studies; earlier gravity anomaly maps were only based on limited data points. The wide-ranging and complete gravity datasets from the WGM 2012 are very useful in understanding the Philippine archipelago's regional geologic and tectonic features by providing significant constraints in evaluating the structures from upper to lower crustal depths (e.g., basin, basement, Moho). The investigation of gravity anomalies in the Philippine island arc system presents negative gravity anomaly zones corresponding to the surrounding trenches that bound the PMB and thick sedimentary basins. Areas with moderate gravity anomalies are associated with metamorphic belts, and the very high gravity anomaly regions define the ophiolitic basement rocks. The upward continuation of the gravity data reveals a relatively low gravity (20 to 35 mGal) in the continental central Philippines compared to the gravity highs (45 to 200 mGal) of the island arc PMB. This study also presents a new estimate of the average Moho (12 to 22 km) and basement (5 to 11 km) depths along the Sulu Sea using the 2-D radially-averaged power spectrum analysis. The application of the 3-D gravity inversion in some significant sedimentary basins in the Philippines provides an efficient and effective way of characterizing interesting crustal density distribution and visualizing the regional subsurface density contrasts. With the availability and proven efficiency of the WGM 2012 data, these techniques can be applied for future structural and geologic explorations in the Philippines and other areas with similar geologic and tectonic settings.

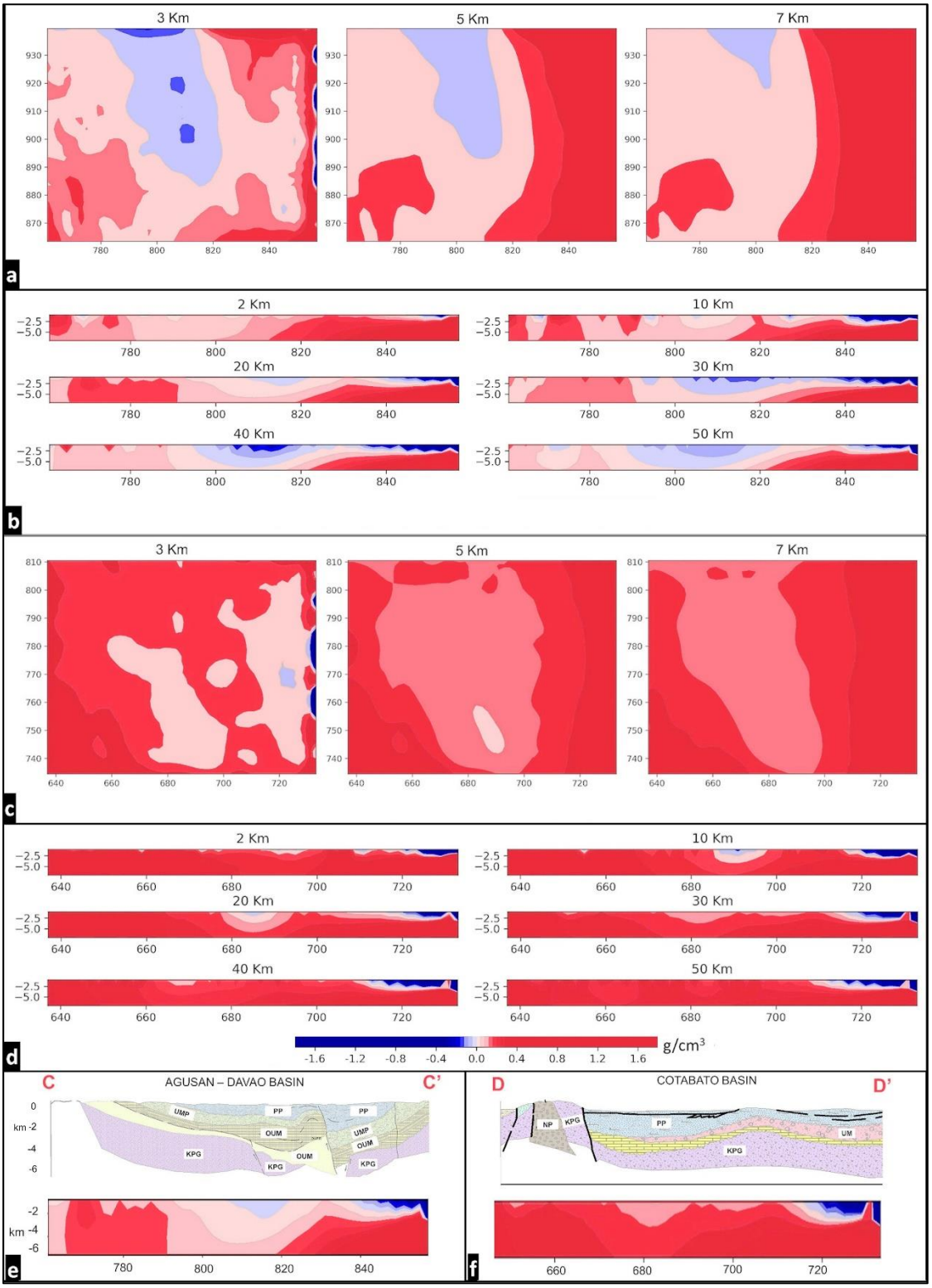

Figure 2-19. *a) Horizontal (3, 5, and 7 km depth) and b vertical slices at the Y-axis (2, 10, 20, 30, 40, and 50 km from the southern edge of the map) of the 3-D density contrast model in Agusan-Davao Basin (AD) and c, d Cotabato Basin (C). Coordinates (a, c) are in WGS 84/UTM Zone51 N (km). The comparison of the geological cross sections (upper) and density contrast model (× 1.5 vertical exaggeration) resulting from the 3-D inversion (lower) are presented for the e AD and f C. KPG = Cretaceous-Paleogene, NP = Neogene Pluton, OUM = Oligocene-Upper Miocene, UMP = Upper Miocene-Pliocene, UM = Upper Miocene, PP = Plio-Pleistocene. The geological cross sections are modified from Tamesis (1981).*

CHAPTER 3

Characterization of Potential Cu-Au Mineralization in Eastern Labo using Electrical Resistivity-Induced Polarization (ER-IP) and Very Low Frequency-Electromagnetics (VLF-EM) Methods

3.1 Introduction

The Philippines is considered one of the essential metallogenic regions in Southeast Asia due to its diverse and abundant ore deposits (Bryner, 1969; Santos, 1974; Hutchison and Taylor, 1978; Hagemann and Brown, 2000; Jimenez et al., 2002; Zhang et al., 2020) (Fig. 3-1). One of the common deposits in the Philippines is a porphyry-epithermal type. Extensive studies revealed the significance of porphyry-epithermal deposits in the Philippines (Divis, 1983; Mitchell and Balce, 1990; Arribas et al., 1995; Chang et al., 2011; Hedenquist et al., 2017; Braxton et al., 2018). Copper and gold mineralization in the Philippines is generally related to the porphyry copper system, where enormous porphyry districts may comprise high (to intermediate) sulfidation epithermal and skarn mineralization in hydrothermally altered rock units (Sillitoe, 2010). Gold mining in Bicol, specifically in the Camarines Norte, was the locals' main livelihood before the 1900s or even before the colonization of Spaniards in the 16th Century (Chaput, 1987; James and Fuchs, 1990). There are a few published studies about mineralization in Eastern Labo. For example, it was observed that the mineralization in Exiban occurs along and near faults, and some manifestations of massive pyrite are related to gold and quartz (between the contact of andesite and volcanic siltstones) (James and Fuchs, 1990). A high sulfidation of gold and copper mineralization was reported in the Nalesbitan area, Labo (Sillitoe et al., 1990). The consolidated report on the cooperative mineral exploration in the Bicol north area of (JICA, 2002) also presented the great potential of the Eastern Labo for further mineral exploration (Appendix 3). A low concentration of rare earth element (REE) was also revealed in a skarn deposit in eastern Labo (Gibaga et al., 2022). Areas adjacent to Mt. Labo have poor bedrock exposure due to the thick pyroclastic deposit and lush vegetation. Thus, mineral exploration in thick, overburdened areas receives less attention than in regions with exposed mineral deposits.

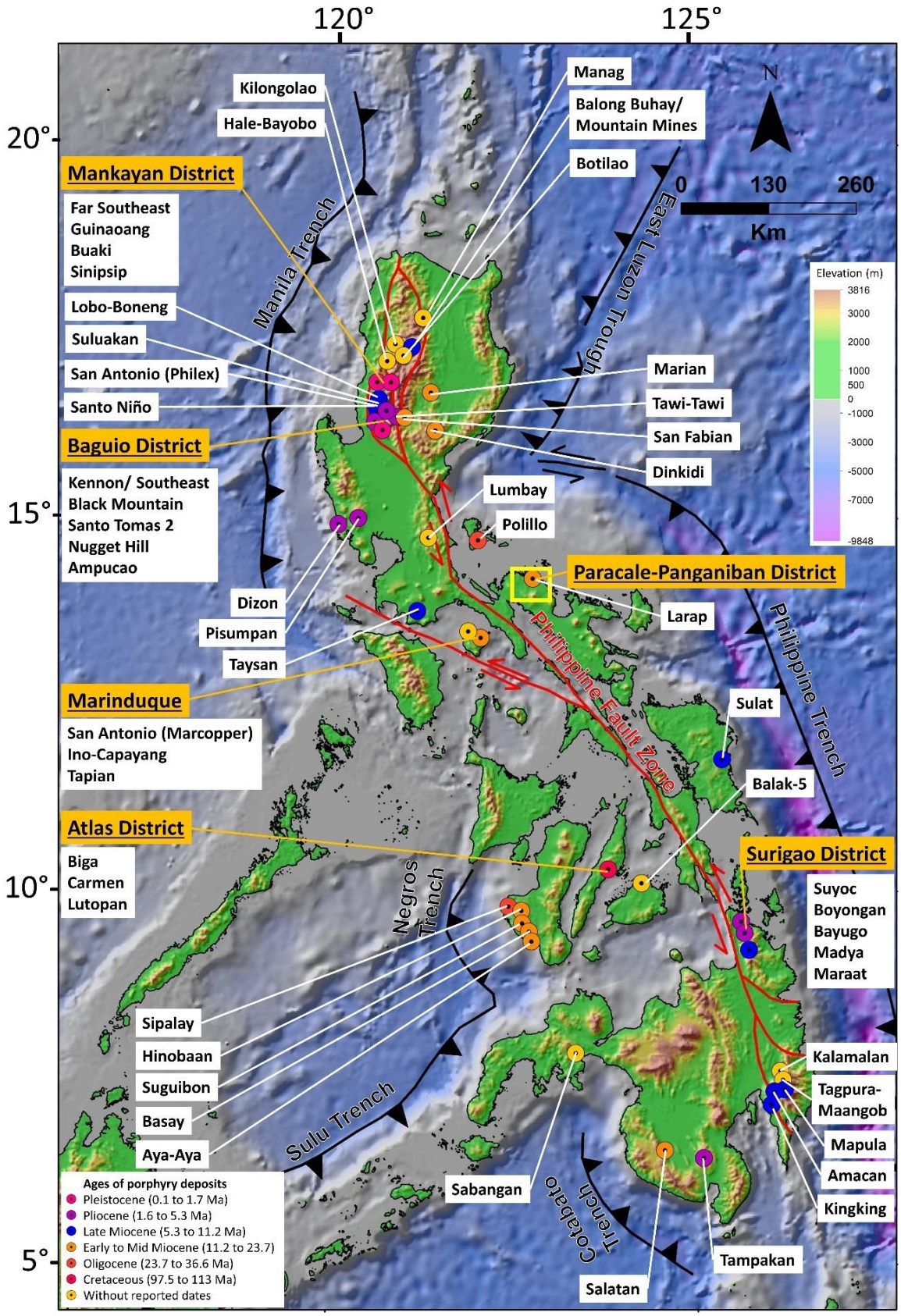

Figure 3-1. *Tectonic map showing the distribution of notable porphyry deposits in the Philippines (modified from Braxton et al., 2018, Zhang et al., 2020). The yellow box marks the location of the study area. Topographic and bathymetric maps are generated from GEBCO (https:// download.gebco.net).*

Intensive geochemical sampling, geological mapping, drilling, and other field survey procedures are frequently employed to search for buried mineral deposits. However, because of the vast exploration areas, it takes a lot of time and money to apply these approaches and find potential zones of mineralization. The exploration of sulfide minerals (e.g., pyrite, chalcopyrite) related to mineralization is remarkably effective when using electrical resistivity and induced polarization (ER-IP) techniques (Telford et al., 1990; Spitzer and Chouteau, 2003; Loke et al., 2013; Jang et al., 2014). Geological structures and features can be accurately delineated using 2-D ER-IP imaging surveys coupled with appropriate, fast, and stable automatic data inversion techniques (Degroot-Hedlin and Constable, 1990; Loke and Barker, 1996; Li and Oldenburg, 2000). This dissertation investigates the subsurface geophysical anomalies over a thick overburden using cost-effective and time-efficient electrical resistivity and induced polarization methods. This second part of this research presents new geophysical field data and yields new information about the local subsurface features to help search for promising targets for Cu-Au exploration in Eastern Labo, Bicol, Philippines.

3.2 Electrical Resistivity (ER), Induced Polarization (IP), and Very Low Frequency Electromagnetics (VLF-EM) Theories

3.2.1 Electrical Resistivity (ER)

Electric charge is a fundamental property of nature for electrical resistivity surveying, like time, mass, and length (Telford et al., 1990; Lowrie, 2007; Milsom and Eriksen, 2011). Coulomb's law states that

$$F = K \frac{Q_1 Q_2}{r^2}, \tag{3.1}$$

where r represents the distance between the two electric charges (Q_1 and Q_2) and K is a constant defined as $(4\pi\varepsilon_0)^{-1}$. The ε_0 is the permittivity constant approximately equal to $8.854187 \times 10^{-12}\ \frac{C^2}{Nm^2}$. The unit of charge is the coulomb (1C = 1A s): the amount of charge that travels through a location in an electrical circuit of one ampere (A) of electric current from one second (s). Eq. 3.1 expresses that the force of attraction or repulsion between two charged spheres is inversely proportional to the square of the distance between their centers and directly proportional to the product of their electric charges. This inverse-square law, Eq. 3.1, is similar to the law of universal gravitation in Eq. 2.1.

The electric field (E) of the charge is the force that another charge Q applies to a unit electric charge. We can thus derive the equation for the electric field (at distance r from charge Q) by setting $Q_1 = Q$ and $Q_2 = 1$:

$$E = \frac{Q}{4\pi\varepsilon_0 r^2}. \quad (3.2)$$

Moving a charged particle from one place in the field to another requires work. This work contributes to the system's potential energy. The electric potential (U) (the unit is joules per coulomb) is the potential energy of a unit charge (Q) at a given distance (r). Moving a distance (dr) against the field (E) modifies the potential by an amount dU:

$$dU = -Edr. \quad (3.3)$$

The above equation equates to work against E (Telford et al., 1990; Lowrie, 2007; Milsom and Eriksen, 2011). The electric potential (U) at a given distance (r) can be computed by combining the Eq. 3.3 and Eq. 3.2 and integrating:

$$U = -\int_{\infty}^{r} Edr \quad (3.4)$$

$$U = -\int_{\infty}^{r} \frac{Q}{4\pi\varepsilon_0 r^2} dr$$

resulting to

$$U = \frac{Q}{4\pi\varepsilon_0 r}. \quad (3.5)$$

The potential difference (volt is the unit) between two points is the energy required to move a unit charge from one point to another in the electric field of Q.

Ohm's law states that, in a conducting wire, the electric current (I) is proportional to the potential difference (V) across it:

$$V = IR, \quad (3.6)$$

where R represents the resistance (the unit is ohm) of the conductor, the resistance is related to the specific material's length (L) and inversely proportional to its cross-sectional area (A), and the proportionality constant - resistivity (ρ) (Fig. 3-2):

$$R = \rho\frac{L}{A}. \quad (3.7)$$

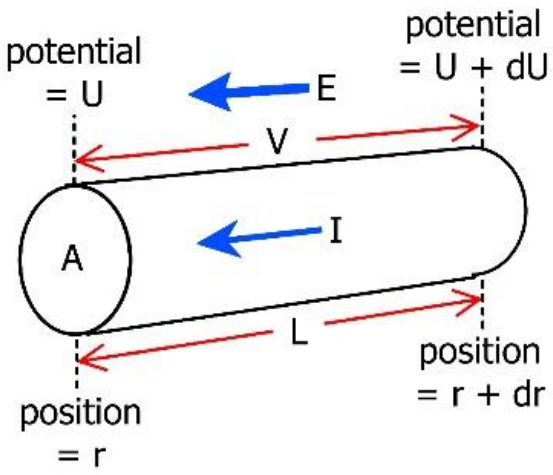

Figure 3-2. *Illustration of the parameters defining Ohm's law for a straight conductor (modified from Lowrie, 2007).*

Resistivity (the unit is ohm-m) is a material's intrinsic physical property that indicates its capacity to oppose the flow of charge. The following formula can be achieved after combining Eq. 3.6 and Eq. 3.7 and rearranging the terms.

$$\frac{V}{L} = \rho \frac{I}{A} \qquad (3.8)$$

The ratio $\frac{V}{L}$ on the left side of this equation represents the electric field (E) (rearranged Eq. 3.3), while the ratio $\frac{I}{A}$ is the current density (J). The combined and simplified formula

$$E = \rho J \qquad (3.9)$$

is convenient for calculating data given the potential difference (V) (represented by E) and electric current (I) (represented by J) and quantifying the results (ρ) in ER method.

The resistivity (ρ) of minerals (Table 3-1) and rocks (Table 3-2; Fig. 3-3) is the significant physical property determined by the ER method. The ER method has been widely used in mineral exploration and groundwater investigations due to the excellent correlation between electrical properties, geology, mineralogy, and fluid content (e.g., Parasnis, 1979; Telford et al., 1990; Kearey et al., 2002; Sharma and Baranwal, 2005). When a good conductor is found in rocks with greater resistivity, ER anomalies occur (e.g., clayey mineralized zone). Because the resistivity values of various rocks and minerals vary significantly, the contrast between the clayey mineralized zone and host rock is frequently large (Fig. 3-3). Metallic ores can have extremely low resistivity, but igneous rocks with no water can have very high resistivity (Table 3-1 and 3-2).

Table 3-1. *Electrical resistivity ranges of common minerals and their formula* (Telford et al., 1990).

Mineral	Formula	Resistivity Range (ohm-m)
Bismuthinite	Bi2s3	18 to 570
Covellite	CuS	3×10^{-7} to 8×10^{-5}
Chalcocite	CU2S	3×10^{-5} to 0.6
Chalcopyrite	CuFeS2	1.2×10^{-5} to 0.3
Bornite	Cu_5FeS_4	2.5×10^{-5} to 0.5
Pyrite	FeS_2	2.9×10^{-5} to 1.5
Pyrrhotite	Fe_nS_m	6.5×10^{-6} to 5×10^{-2}
Cinnabar	HgS	2×10^{7} (average)
Molybdenite	MoS_2	10^{-3} to 6×10^{2}
Galena	PbS	3×10^{-5} to 3×10^{2}
Millerite	NiS	3 x 10-^{7} (average)
Stannite	Cu_2FeSnS_2	10^{-3} to 6×10^{3}
Stibnite	Sb_2S_3	10^{5} to 10^{12}
Sphalerite	ZnS	1.5 to 10^{7}
Cobaltite	CoAsS	3.5×10^{-4} to x 10^{-1}
Arsenopyrite	FeAsS	2×10^{-5} to 15
Niccolite	NiAs	10^{-7} to 2×10^{-3}
Bauxite	Al_2O_2 - nH_2O	2×10^{2} to 6×10^{3}
Cuprite	Cu_2O	10^{-3} to 300
Chromite	$FeCr_2O_4$	1 to 10^{6}
Specularite	Fe_2O_3	6×10^{-3} (average)
Hematite	Fe_2O_3	3.5×10^{-3} to 10^{7}
Limonite	$2Fe_3O_3$ - $3H_2O$	10^{3} to 10^{7}
Magnetite	Fe_3O_4	5×10^{-5} to 5.7×10^{3}
Ilmenite	$FeTiO_3$	10^{-3} to 50
Wolframite	Fe, Mn, WO_4	10 to 10^{-5}
Pyrolusite	MnO_2	5×10^{-3} to 10
Quartz	SiO_2	4×10^{10} to 2×10^{14}
Cassiterite	SnO_2	4 x 10-^{4} to 10^{4}
Rutile	TiO_2	30 to 1000
Uraninite (pitchblende)	UO_2	1 to 200
Anhydrite	$CaSO_2$	10^{9} (average)
Calcite	$CaCo_3$	2×10^{12} (average)
Flouride	CaF_2	8×10^{13} (average)
Siderite	$Fe_2(CO3)_3$	70 (average)
Rock salt	NaCl	30 to 10^{13}
Sylvite	KCl	10^{11} to 10^{12}
Diamond	C	10 to 10^{14}

Table 3-2. *Electrical resistivity ranges of common rocks and sediments* (Telford et al., 1990).

Rock	Resistivity range (ohm-m)
Granite porphyry	4.5×10^3 (wet); 1.3×10^6 (dry)
Feldspar porphyry	4×10^3 (wet)
Syenite	10^2 to 10^6
Diorite porphyry	1.9×10^3 (wet); 2.8×10^4 (dry)
Porphyrite	10 to 5×10^4 (wet); 3.3×10^3 (dry)
Carbonized porphyry	2.5×10^4 (wet); 6×10^4 (dry)
Quartz diorite	2×10^4 to 2×10^6 (wet); 1.8×10^5 (dry)
Porphyry (various)	60 -10^4
Dacite	2×10^4 (wet)
Andesite	4.5×10^4 (wet); 1.7×10^2 (dry)
Diabase (various)	20 to 5×10^7
Lavas	10^2 to 5×10^4
Gabbro	10^3 to 10^6
Basalt	10 to 1.3×10^7 (dry)
Olivine norite	10^3 to 6×10^4 (wet)
Peridotite	3×10^3 (wet); 6.5×10^3 (dry)
Hornfels	8×10^3 (wet); 6×10^7 (dry)
Schists (calcareous and mica)	20 to 10^4
Tuffs	2×10^3 (wet); 10^5(dry)
Graphite schist	10 to 10^2
Slate (various)	6×10^2 to 4×10^7
Gneiss (various)	6.8×10^4 (wet); 3×10^6 (dry)
Marble	10^2 to 2.5×10^8 (dry)
Skarn	2.5×10^2 (wet); 2.5×10^8 (dry)
Quartzites (various)	10 to 2×10^8
Consolidated shales	20 to 2×10^3
Argillites	10 to 8×10^2
Conglomerates	2×10^3 to 10^4
Sandstones	1 to 6.4×10^8
Limestones	50 to 10^7
Dolomite	3.5×10^2 to 5×10^3
Unconsolidated wet clay	20
Marls	3 to 70
Clays	1 to 100
Oil sands	4 to 800

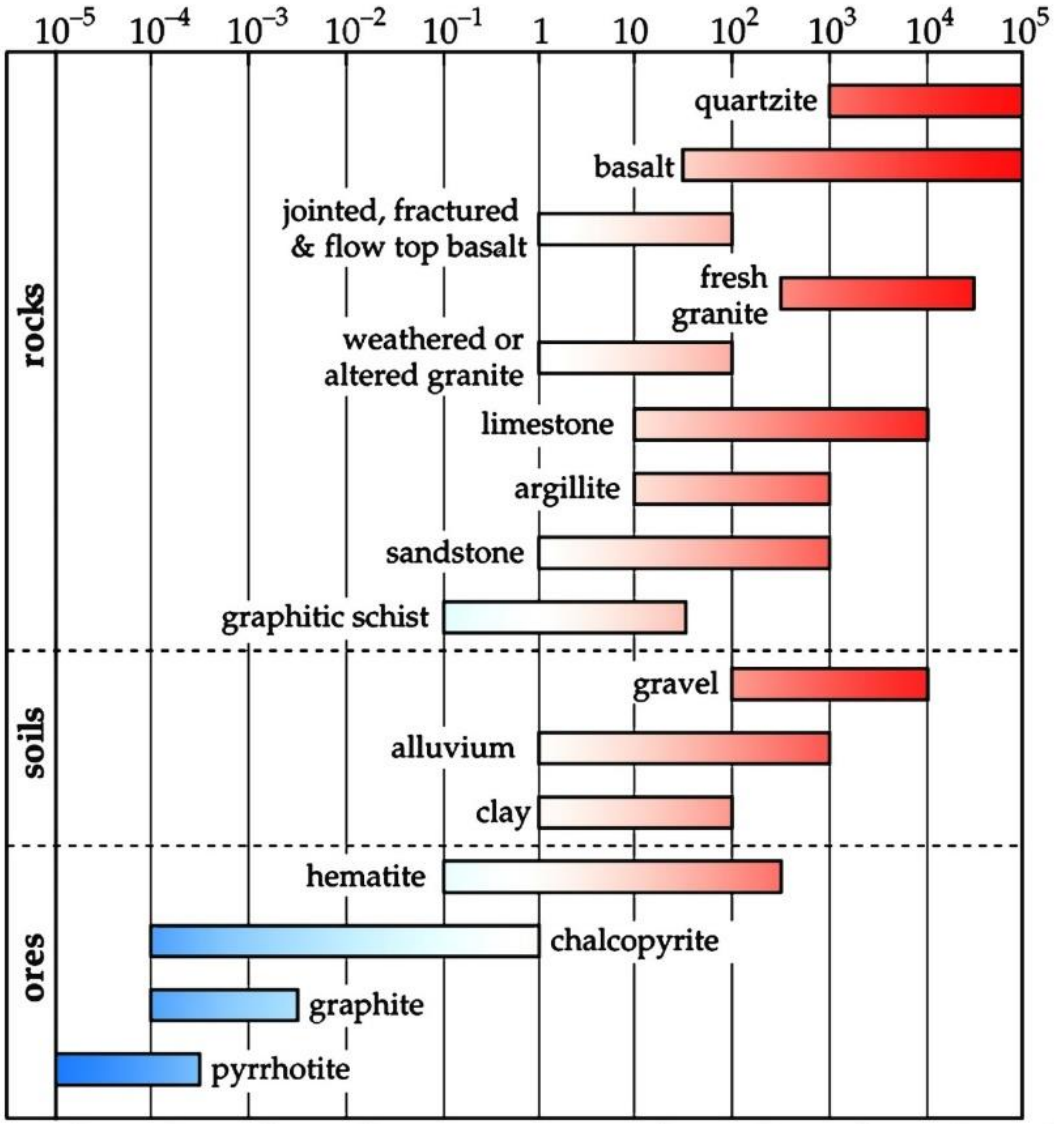

Figure 3-3. *Electrical resistivity ranges for some rocks, soils, and ores* (Telford et al., 1990; Ward, 1990; Lowrie, 2007). *The x-axis on the top represents the resistivity in ohm-m.*

In the ER field survey, electrodes are usually used to introduce current to the ground. Current (*I*) flows outward from the source electrode. The electric field lines (yellow lines) around a source (A) electrode are directed radially outward, whereas the field lines surrounding a sink electrode (B) are oriented radially inward (Fig. 3-4).

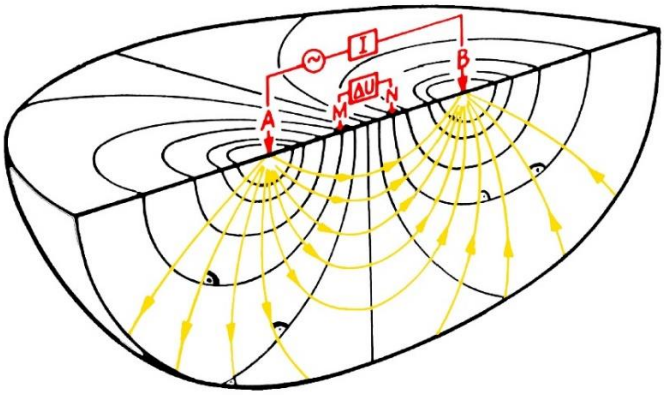

Figure 3-4. *ER measurement principle. Electric field lines around the source (A) and sink (B) electrodes are directed radially outward and inward, respectively (modified from Knödel et al., 2007).*

The equipotential surfaces are normal to the electric field lines and current flow. The current density can be defined as

$$J = \frac{I}{A} = \frac{I}{2\pi r^2}. \tag{3.10}$$

The surface area of a hemisphere with radius r is $2\pi r^2$ (Fig. 3-5).

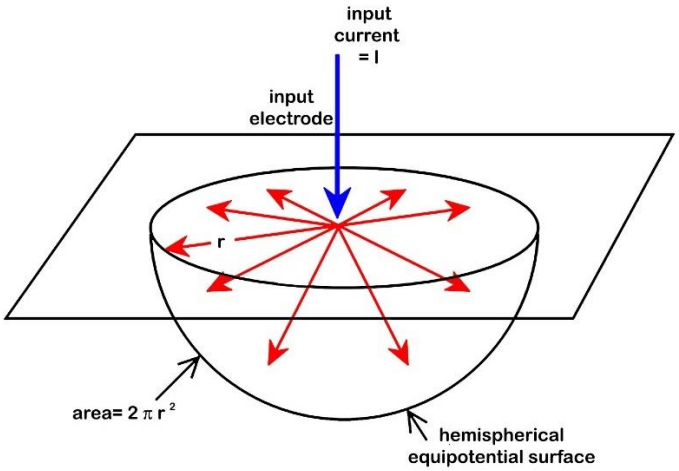

Figure 3-5. *Illustration of the electric field lines (red arrows) and equipotential surface around a single electrode (modified from Lowrie, 2007).*

Thus, the electric field (E) from Eq. 3.9 can be represented by the formula

$$E = \rho \frac{I}{2\pi r^2}. \tag{3.11}$$

The electric potential (U) at a given distance (r) can be obtained by substituting Eq. 3.11 in Eq. 3.3.

$$dU = -\rho \frac{I}{2\pi r^2} dr \tag{3.12}$$

and integration:

$$U = \rho \frac{I}{2\pi r}. \quad (3.13)$$

The typical four-electrode approach comprises an array of two current and two potential electrodes (Fig. 3-6).

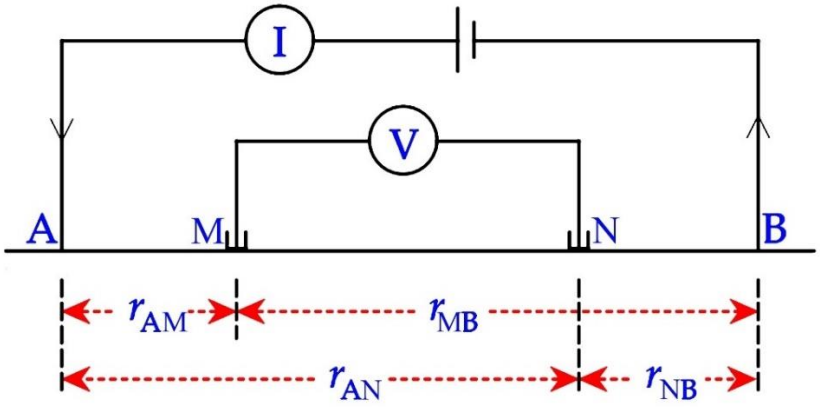

Figure 3-6. *Principle of the general four-electrode configuration for ER measurement. Current electrodes are represented by A and B, while potential electrodes are M and N.*

A (source) and B (sink) represents the current electrodes, while M and N are the potential electrodes. The potential at the electrode (M) due to the source (A) can be computed using the formula

$$U_{MA} = + \rho \frac{I}{2\pi r_{MA}}, \quad (3.14)$$

while the negative sign represents the potential due to the sink (B):

$$U_{MB} = - \rho \frac{I}{2\pi r_{MB}}. \quad (3.15)$$

Combining Eq. 3.14 and Eq. 3.15, the potential at electrode M based on the effects of source (A) and sink (B) electrodes can be derived as

$$U_M = \rho \frac{I}{2\pi} \left(\frac{1}{r_{MA}} - \frac{1}{r_{MB}} \right). \quad (3.16)$$

Using the exact derivation as Eq. 3.16, the potential at electrode N can be represented as

$$U_N = \rho \frac{I}{2\pi} \left(\frac{1}{r_{NA}} - \frac{1}{r_{NB}} \right). \quad (3.17)$$

The potential difference (V) measured by the voltmeter of the electrical resistivity instrument is equivalent to

$$V = \rho \frac{I}{2\pi} \left\{ \left(\frac{1}{r_{MA}} - \frac{1}{r_{MB}} \right) - \left(\frac{1}{r_{NA}} - \frac{1}{r_{NB}} \right) \right\}. \quad (3.18)$$

Therefore, rearranging Eq. 3.18 gives the formula for the apparent resistivity:

$$\rho_a = \frac{V}{I} 2\pi \left\{ \left(\frac{1}{r_{MA}} - \frac{1}{r_{MB}} \right) - \left(\frac{1}{r_{NA}} - \frac{1}{r_{NB}} \right) \right\}^{-1}. \quad (3.19)$$

The apparent resistivity of some typical arrays or geometries for ER survey is presented in Figure 3-7. The dipole-dipole (termed as "double dipole" in other literature) array was generally used in this research.

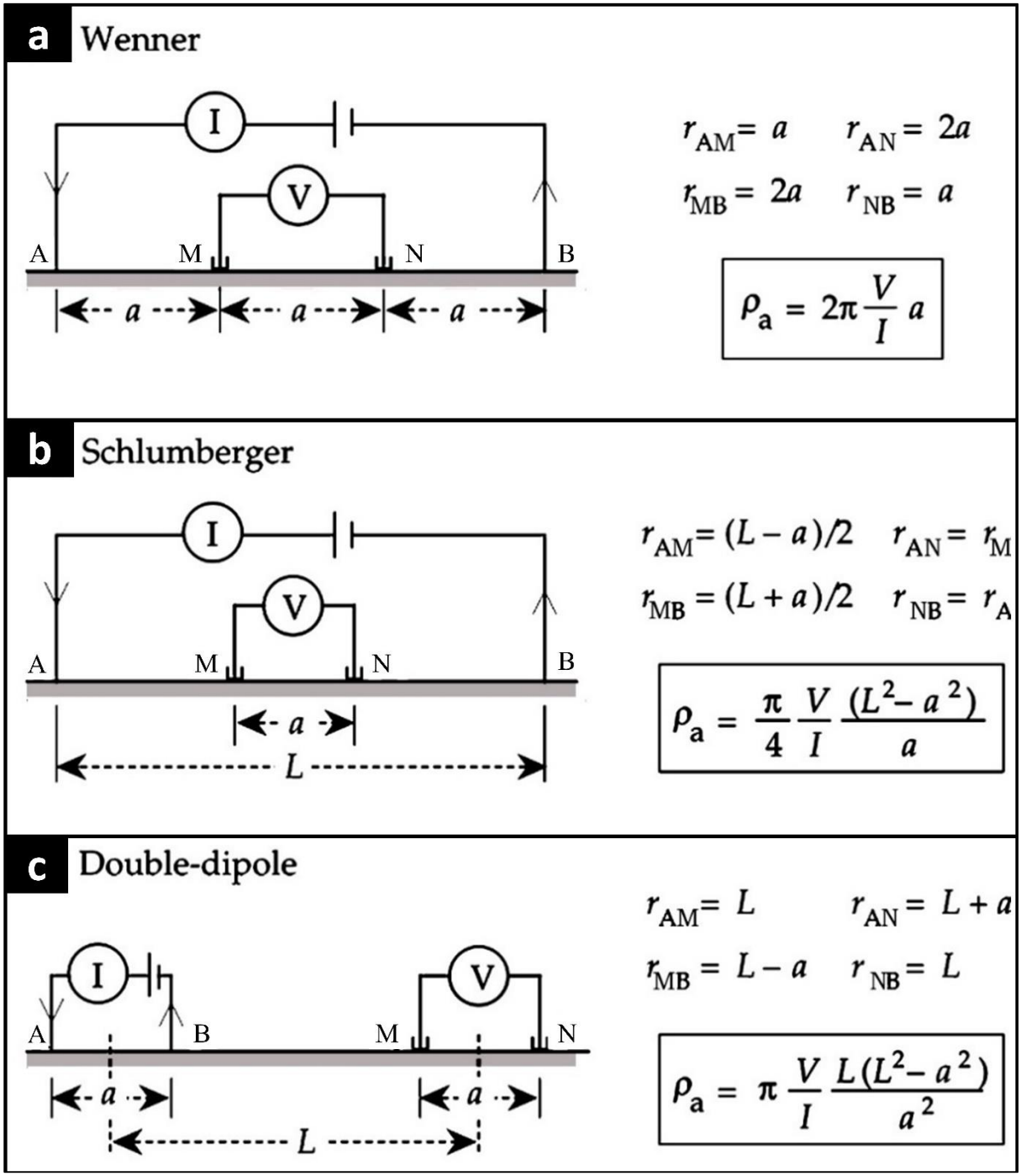

Figure 3-7. *(a) Wenner, (b) Schlumberger, and (c) dipole-dipole/ double dipole arrays present the typical configurations of current and potential electrodes for ER survey. The apparent resistivity can be computed using the formula on the right (modified from Lowrie, 2007).*

3.2.2 Induced Polarization (IP)

Induced polarization (IP) is generally defined as the accumulation of ionic charges represented by the gradual decline and increase of the voltage when the current is switched off and on, respectively (Telford et al., 1990; Lowrie, 2007) (Fig. 3-8). The membrane polarization and electrode polarization are the two mechanisms responsible for generating electric dipole moments (IP effects) within the rock. A four-electrode ER survey's positive and negative flow sequence may be alternated by intervals when the current is switched off. The inducing current appears box-like, while the voltage between the potential electrodes does not quickly drop to zero when the current is discontinued (Fig. 3-8b). This mechanism demonstrates how potentials collected during an ER survey may be connected to charges that accumulate when current is induced to flow. The physical attribute assessed in the IP method is chargeability.

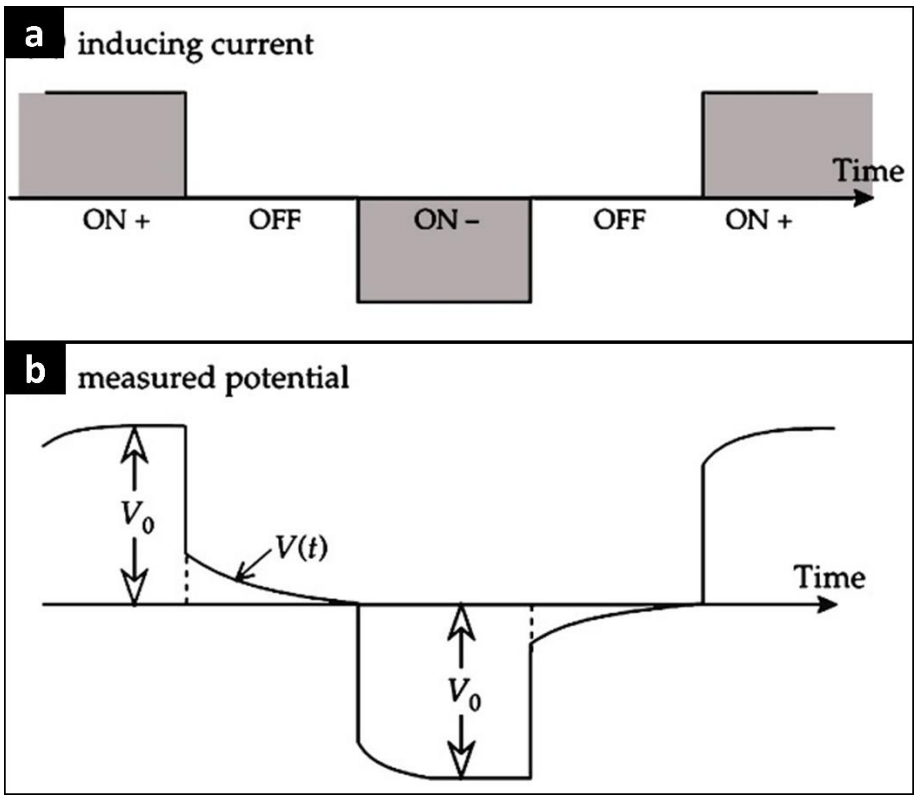

Figure 3-8. *Principles of the IP-related decay showing the inducing current and measured potential after the current is switched on and off (modified from Lowrie, 2007).*

Differences in the capacity of ions in pore fluids to travel through a porous rock cause membrane polarization (Fig. 3-9a). Minerals with a negative surface charge attract positive ions in the pore fluid. These positive ions build on the grain surface and spread into neighboring pores. This partially blocking effect selectively allows one ion to pass through. It results in

polarized ionic distribution by causing short accumulations of negative ions in the rock. It causes brief accumulations of negative ions in the rock, resulting in a polarized ionic distribution. Because clay minerals have tiny grain and pore diameters, the impact of induced polarization is most evident. Furthermore, high chargeability values can be attributed to clay grains with relatively high charges, which can adsorb ions on their surfaces.

When ore minerals (with metallic grains) are present, electrode polarization causes a high chargeability anomaly (Fig. 3-9b). Electrolytic and electronic conductions take place around and within the metallic grains. The flow of ions in the electrolyte is slower than the transport of electrons through the metallic grains. As a result, opposing charges build on the facing sides of a metallic grain, obstructing ionic transport through the pore fluid. After turning on the external current, an overvoltage accumulates for a short period. In contrast, after the current is turned off, the accumulated ions scatter, and the overvoltage steadily decays. The magnitude of the generated polarization effect (chargeability) is caused by the metallic content of the rock.

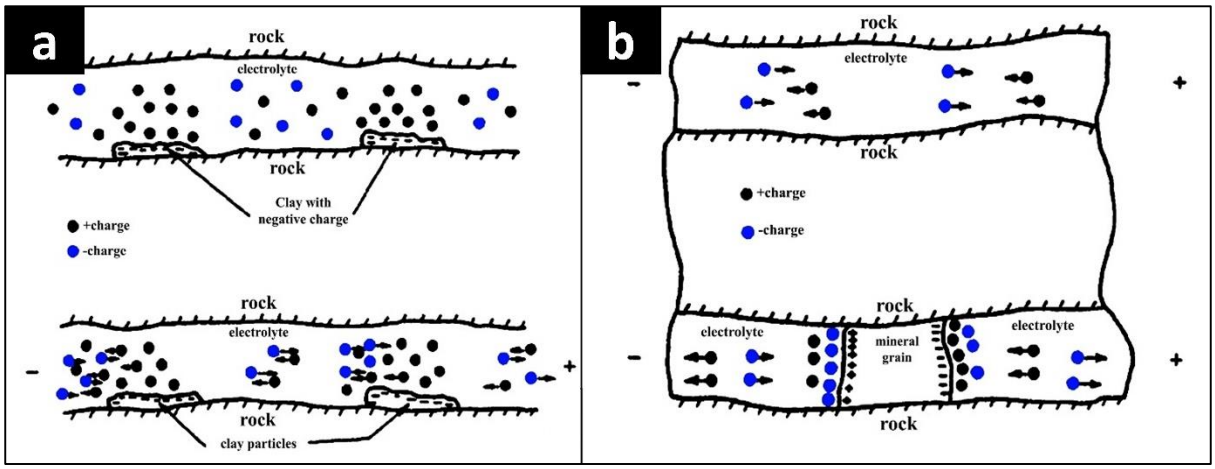

Figure 3-9. *General principles of IP effects. (a) Membrane polarization: the application of DC to a porous sandstone causes the (top) normal distribution of ions to be (below) polarized (b) Electrode polarization depends on the metallic content of the rock* (Telford et al., 1990).

In the field operation for the induced polarization (IP) survey, the steady-state voltage V_0 is recorded and compared to the amplitude of the decaying residual voltage $V(t)$ at time t after the current is switched off (Fig. 3-10). The ratio $V(t)/V_0$ is given as a percentage; it decays throughout the interval (e.g., 0.1 to 10s) between turning the current on and off. If the decay curve is sampled at several places, the shape and area under the curve may be determined

(Fig. 3-10d). The chargeability (M) is defined as the area under the decay curve given as a proportion of the steady-state voltage:

$$M = \frac{1}{V_0}\int_{t_1}^{t_2} V(t)dt. \qquad (3.20)$$

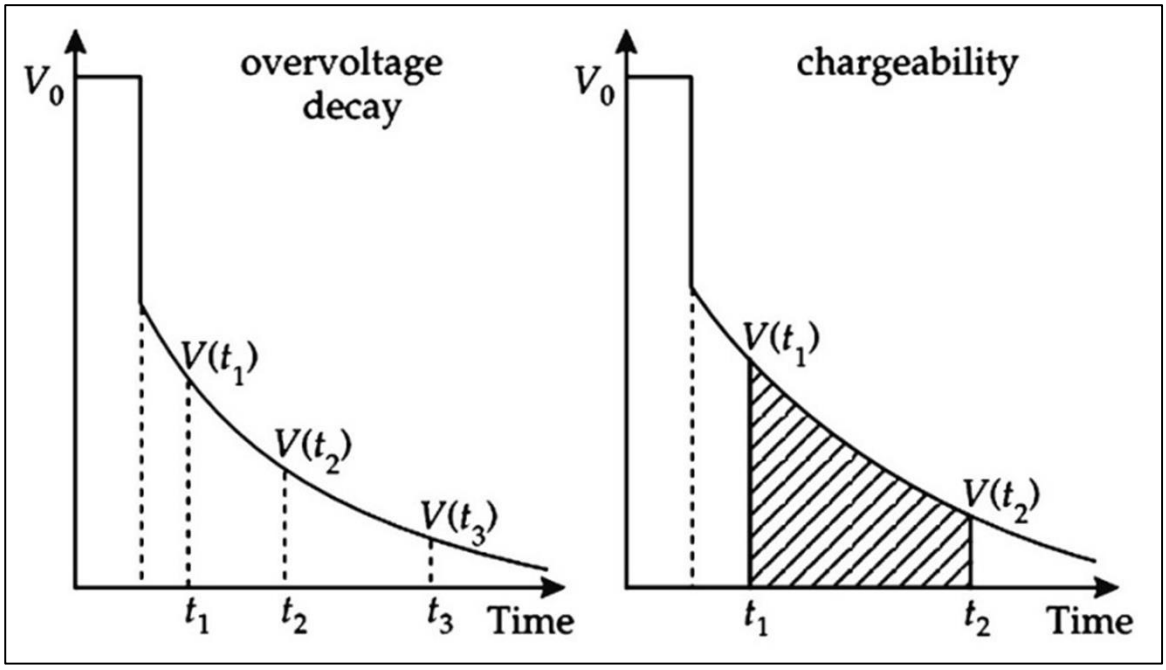

Figure 3-10 *The area under the decay curve is the chargeability (M) (modified from Lowrie, 2007).*

The significant physical property determined by the IP method is the chargeability of minerals (Table 3-3) and rocks (Table 3-4).

Table 3-3. *Chargeability values of some common minerals* (Telford et al., 1990).

Mineral	**Changeability (ms)**
Pyrite	13.4
Chalcocite	13.2
Copper	12.3
Graphite	11.2
Chalcopyrite	9.4
Bornite	6.3
Galena	3.7
Magnetite	2.2
Malachite	0.2
Hematite	0.0

Table 3-4. *Chargeability values of some common rocks and minerals (Telford et al., 1990).*

Material	Changeability (ms)
20% sulfides	2000 to 3000
8-20% sufides	1000 to 2000
2-8% sulfides	500 to 1000
Volcanic tuffs	300 to 800
Sandstone, siltstone	100 to 500
Dense volcanic rocks	100 to 500
Shale	50 to 100
Granite, grandodiorite	10 to 50
Limestone, dolomite	10 to 20

Various array types (e.g., Wenner, dipole-dipole) can be used in Electrical Resistivity Imaging (ERI) or Electrical Resistivity Tomography (ERT) for measuring apparent resistivity and chargeability. For example, when using a dipole-dipole array, the apparent resistivity and chargeability obtained in each measurement are plotted below the array's midpoint at the intersection of two lines inclined at 45 degrees. (Fig. 3.11).

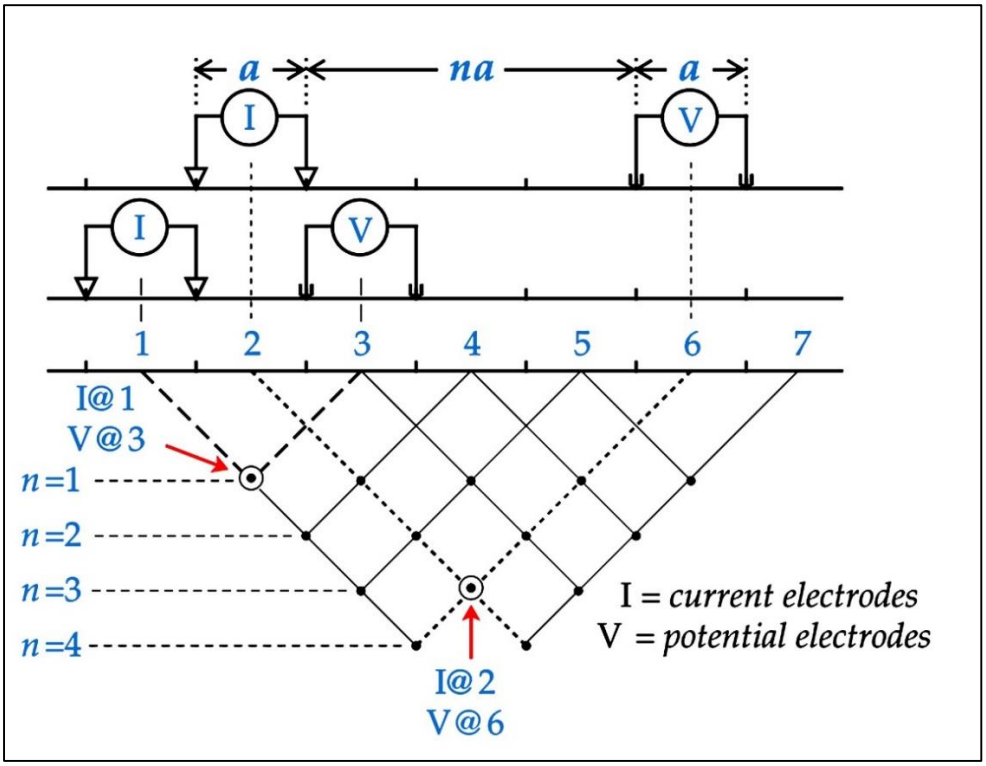

Figure 3-11. *The intersection of 45 degrees lines extending from the mid-points of the transmitter and receiver pairs is the location of the data point of a dipole-dipole array pseudo-section (modified from Lowrie, 2007).*

Before the field survey, the array is typically designed using a laptop or PC and then downloaded to the resistivity instrument. This resistivity imaging approach employs numerous electrodes linked by a multicore wire. Typically, electrodes for 2-D surveys are placed along a straight line and separated by a set distance. The ER apparatus automatically collects data according to the designed array, resulting in apparent resistivity and chargeability pseudo-sections (Fig 3.12). After that, the apparent resistivity and chargeability are inverted to get the true resistivity and IP sections (Fig 3.12).

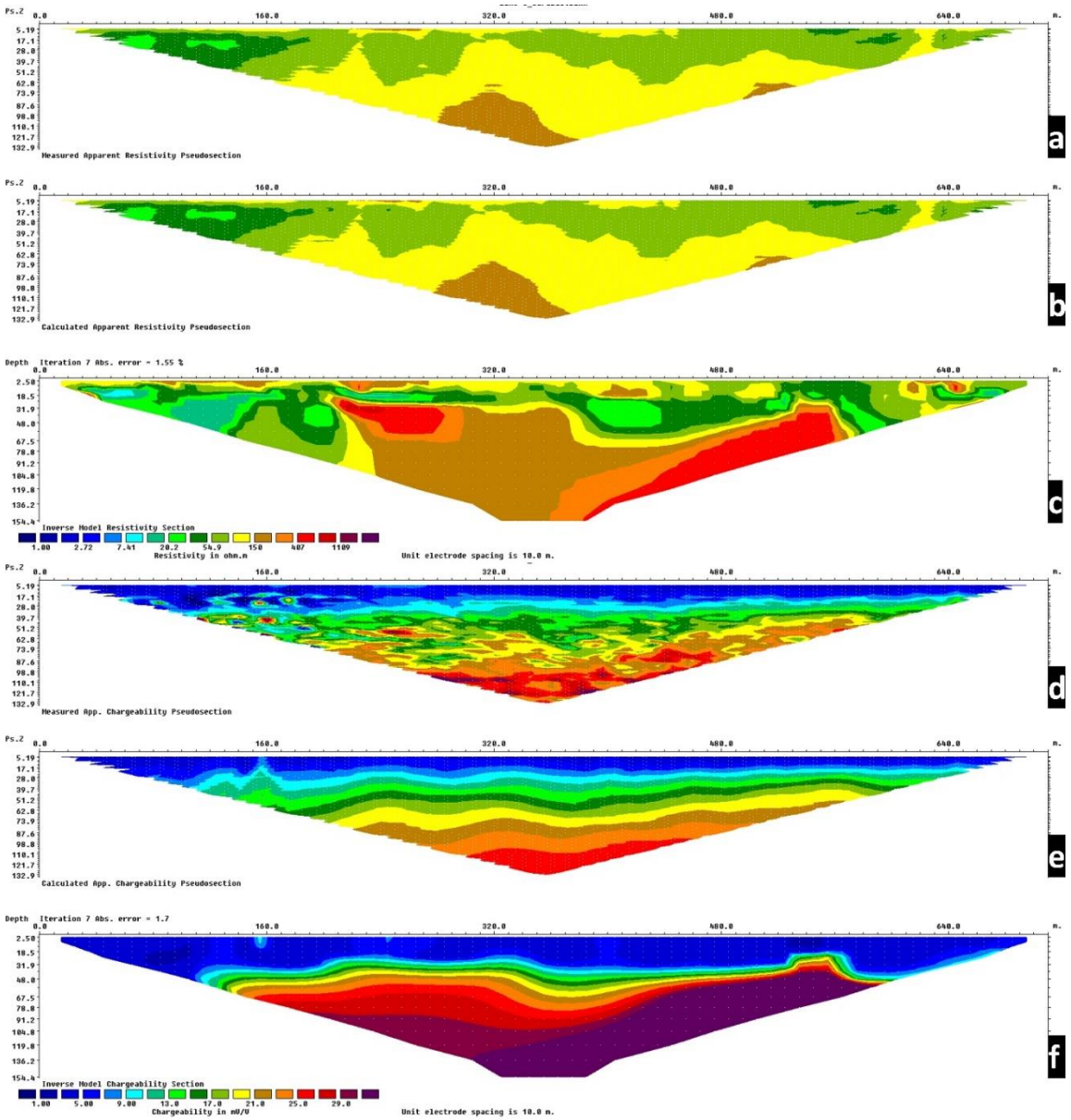

Figure 3-12. *Examples of (a) measured and (b) calculated apparent resistivity pseudo sections with their corresponding (c) inverted resistivity model section. The sections below are examples of (d)measured and (e) calculated apparent chargeability pseudo sections with their corresponding (f) inverted chargeability model section. The electrode spacing is 10 m for this example, and the RMS errors are shown on the upper left side of the inverted models.*

3.2.3 Very Low Frequency-Electromagnetics (VLF-EM)

Very low frequency (VLF) is an Electromagnetic (EM) surveying method that employs electromagnetic radiation created in the low-frequency range of about 15-25 kHz by powerful radio dipole transmitters. These dipole transmitters are used in long-distance communications and navigation systems. The VLF emitters can be found thousands of kilometers from the survey region. At great distances from the source, the electromagnetic field is planar and horizontal (Fig. 3-13). The electric component E is in a vertical plane, and the magnetic component H is in a horizontal plane at right angles to the direction of propagation. The magnetic vector cuts a conductor that strikes in the transmitter's direction, and the generated eddy currents form a secondary electromagnetic field. The VLF instrument is tiny and light, comprising three coils with axes at right angles that can detect signals from any direction. Signals from two transmitters (i.e., NWC and JJI) are read concurrently during the field investigation. The VLF-EM data is selected based on signal quality. Traverses are usually executed in a straight line over the survey area with specified data point separation (15 m for this study).

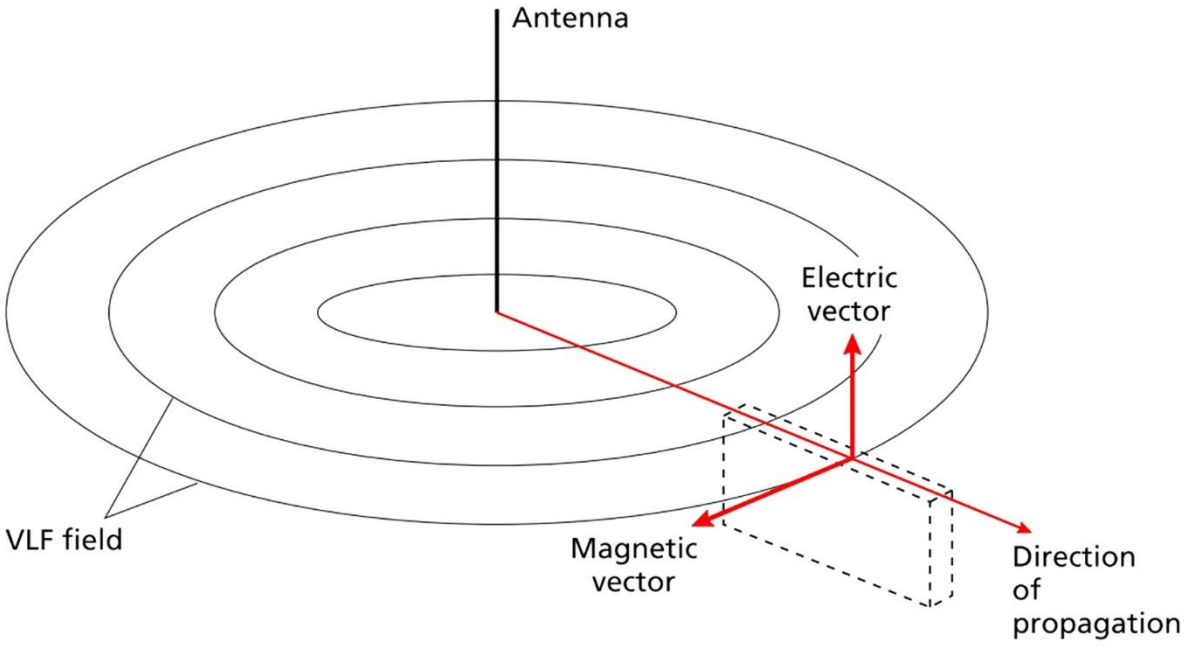

Figure 3-13. *The VLF method's guiding principle. Dashed lines depict a tabular conductor striking the antenna and being cut by the magnetic vector of the electromagnetic field. (modified from Keary, 2002).*

Several approaches for interpreting VLF-EM data have been developed. Fraser (Fraser, 1969) and Karous-Hjelt (Karous and Hjelt, 1983) filters are the most often used processing techniques for qualitative interpretation. The Fraser filter (Fraser, 1969) is sensitive to the magnetic polarization ellipse's tilt angle (real component). The Fraser filter computes horizontal gradients and smoothes the data to produce maximum values over conductors, which may be contoured. On each set of four sequential data points (i.e., f1, f2, f3, and f4), the Fraser filtering formula, Eq. 3.21, is applied, and the resulting value (F_{2_3}) is plotted halfway between f2 and f3.

$$F_{2\_3} = (f_1 + f_2) - (f_3 + f_4) \tag{3.21}$$

An apparent current density pseudo-section can be generated by filtering the in-phase data using the Karous and Hjelt filter (Karous and Hjelt, 1983). The current density pseudo-section represents the apparent current concentrations at various depths. Lower apparent current density values correspond to greater resistivity values, and high apparent current density values correspond to low resistivity (i.e., clayey or fractured mineralized zone). The most basic form of the Karous-Hjelt filter is

$$\frac{\Delta z}{2\pi} I_a\left(\Delta x/_2\right) = -0.205H_{-2} + 0.323H_{-1} - 1.446H_0 + 1.446H_1 - 0.323H_2 + 0.205H_3 I_{a_{(x/2)}}, \tag{3.22}$$

where Δz represents the estimated thickness of the current sheet, I_a is the current density, and x is the distance between the data points and the depth of the current sheet. The normalized vertical magnetic field anomaly for each of the six data points is represented by H_{-2} through H_3.

The Karous and Hjelt filter displays the depth of various current concentrations, which might indicate the spatial distribution of subsurface geological features (e,g., faults and mineralized zones) (Ogilvy and Lee, 1991). The finite Karous-Hjelt filter method is a more extended and rigorous version of the Fraser filter. The Karous-Hjelt filter, on the other hand, is developed directly from the magnetic fields associated with the subsurface current flow (Karous and Hjelt, 1983).

A typical VLF-EM survey orientation is shown in Figure 3-14. The survey lines are roughly perpendicular to the magnetic field and at right angles to the geological strike of the conductor. Conductive inhomogeneity causes secondary fields produced by the induced current to be overlaid on the primary field. This mechanism produces an elliptically polarized field (Fig. 3-15).

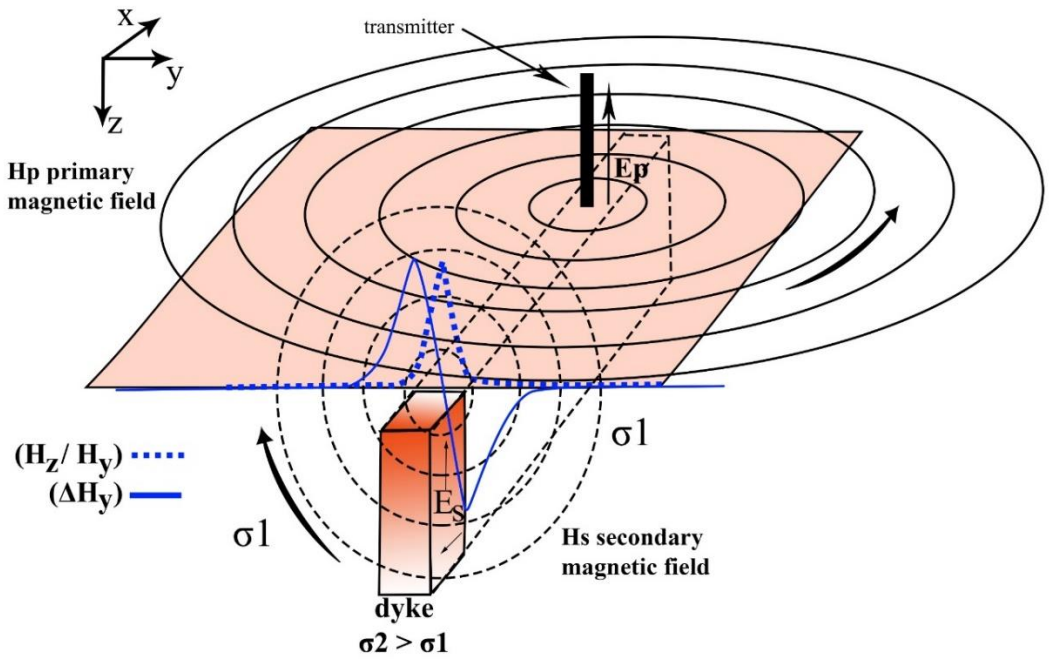

Figure 3-14. *The principle of a typical VLF-EM survey design.*

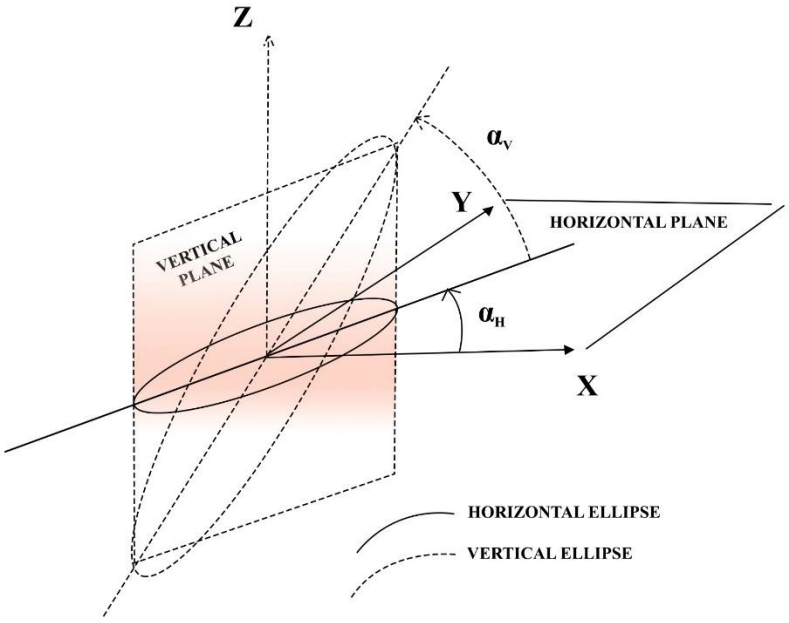

Figure 3-15. *Magnetic field ellipses in vertical and horizontal planes (e.g., Telford et al., 1990; Lowrie, 2007).*

Equation 3.23 is used to compute the tilt angle (inclination of the main axis of the polarization ellipse)

$$\tan\alpha = \pm\frac{2\left(H_z/H_y\right)\cos\Delta\emptyset}{1-\left(H_z/H_y\right)^2}, \qquad (3.23)$$

while Equation 3.24 is used to calculate the ellipticity (ratio of the minor to the major axis of the ellipse).

$$\varepsilon = \frac{H_z H_y \sin \Delta\emptyset}{{H_1}^2} \quad (3.24)$$

$\Delta\emptyset$ represents the phase difference:

$$\Delta\emptyset = \emptyset z - \emptyset y. \quad (3.25)$$

H_1 is represented by the formula

$$H_1 = \left| H_z e^{i\Delta\emptyset} \sin\alpha + H_y \cos\alpha \right|, \quad (3.26)$$

where $\emptyset z$ and $\emptyset y$ are the phases of the vertical and horizontal magnetic field components, respectively. H_z (vertical) and H_y (horizontal) characterize the total magnetic field components. The real and quadrature components of the tipper can be roughly represented by the tangent of the tilt angle and ellipticity, respectively. The two types of anomalies that are usually investigated are real anomalies (A_r)

$$A_r = \tan\alpha \times 100\%, \quad (3.27)$$

and the imaginary anomalies (A_i)

$$A_i = \varepsilon \times 100\%. \quad (3.28)$$

3.3 Geologic, Tectonic and Metallogenic Setting

The study area is classified under the Ancient Southeastern Luzon Arc stratigraphic grouping, specifically within the Quezon-Camarines Norte Block (MGB, 2010). Previous studies revealed that southeastern Luzon, including the Paracale-Panganiban mineral district, experienced complex tectonic and structural evolution (MGB, 2010; Yumul et al., 2020). Low-grade metamorphism (e.g., greenschist) of the volcanic and sedimentary cover of the ophiolitic rocks, which are extensively scattered throughout the Ancient Southeastern Luzon Arc, provides evidence of large-scale tectonic processes. (Geary et al., 1988; Geary and Kay, 1989; Dimalanta et al., 2020). The study area is located in the southern part of the Larap porphyry deposit (Paracale-Panganiban mineral district). The mineral district is bounded by the west-dipping Philippine Trench and the left-lateral strike-slip Philippine Fault to the east and west, respectively (Barrier et al., 1991; Aurelio, 2000). (Fig 3-1).

The Paracale-Panganiban mineral district and its vicinity are generally underlain by thirteen geologic units (Fig. 3-16 and Fig 3-17). The oldest Jurassic Malaguit Schist is composed of Amphibolite schist and greenschist distributed in the northern portion of the study area (Miranda and Caleon, 1979). Thrust against the Malaguit Schist is the Cretaceous Cadig Ophiolite Complex, composed of serpentinized peridotite and gabbro (MGB, 2010). This Ophiolite Complex was reported in the coastal areas of Paracale and Jose Panganiban. The late Cretaceous Tigbinan Formation was named for the greywacke-spilite-chert sequence exposed in the eastern part of the study area (Miranda and Caleon, 1979). Tumbaga Formation (Eocene) is characterized by two members: the lower clastic member (composed of conglomerate, arkose, shale, and wacke) and the upper calcareous member (limestone, marl, shale). This formation was noted along the river; some floats were observed during the field survey (Fig 3-18a). Conformably overlying the Tumbaga Formation is the Oligocene Larap Volcanic Complex. It is initially named for the andesite, andesitic flow breccia, and tuff in Larap, Panganiban (Meek, 1941). The Early Miocene Bosigon Formation is characterized by the lower member (conglomerate, sandstone, shale, limestone) and upper member (basalt, volcanic wacke, tuff breccia, chert, limestone) in Labo (MGB, 2010). Unconformably overlying the Bosigon Formation is the Sta. Elena Formation (Late Miocene) (Miranda and Caleon, 1979). It comprises conglomerate, sandstone, siltstone, shale, and limestone reported in the eastern side of the study area (MGB, 2010). Viñas Formation (Pliocene) comprises sandstone, mudstone, conglomerate, and limestone (Corby et al., 1951). Macogon Formation has an age of Pliocene; it consists of pyroclastic rocks, shale, and basalt flow and hosts the Nalesbitan epithermal gold deposit (Miranda and Caleon, 1979). Bagacay Andesite (Pliocene) is part of the Bicol Volcanic Arc Complex, composed of hornblende andesite and volcanic breccia (Meek, 1941). Labo Volcanic Complex is the youngest formation observed in the study area (Fig. 3-18b). It has an age of Pleistocene and is composed of interlayered andesite, dacite, and basalt flows; it is intercalated with tuff and other pyroclastics distributed in the southern part of the study area (Miranda and Caleon, 1979). The partial melting of the Philippine Sea Plate subducting along the Philippine Trench resulted in lava flows and pyroclastic deposition (from Mt. Labo), causing the formation of the Labo Volcanic Complex (MGB, 2010).

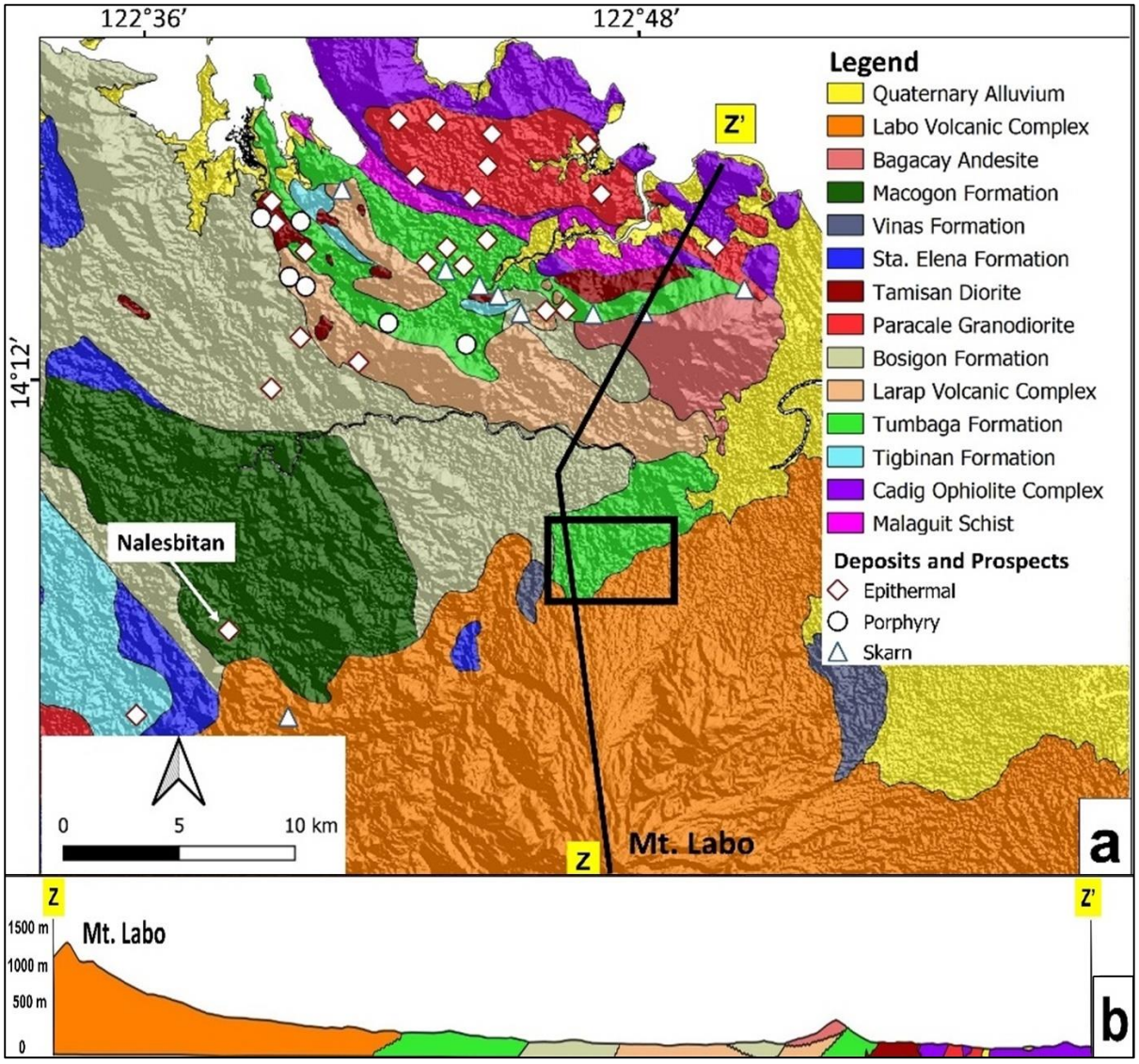

Figure 3-16. *(a) Geologic map and (b) cross-section of the Paracale-Panganiban Mineral District and its vicinity showing the locations of prospects and deposits related to epithermal, porphyry, and skarn mineralization (modified from Mitchell and Balce, 1990; MGB, 2010).*

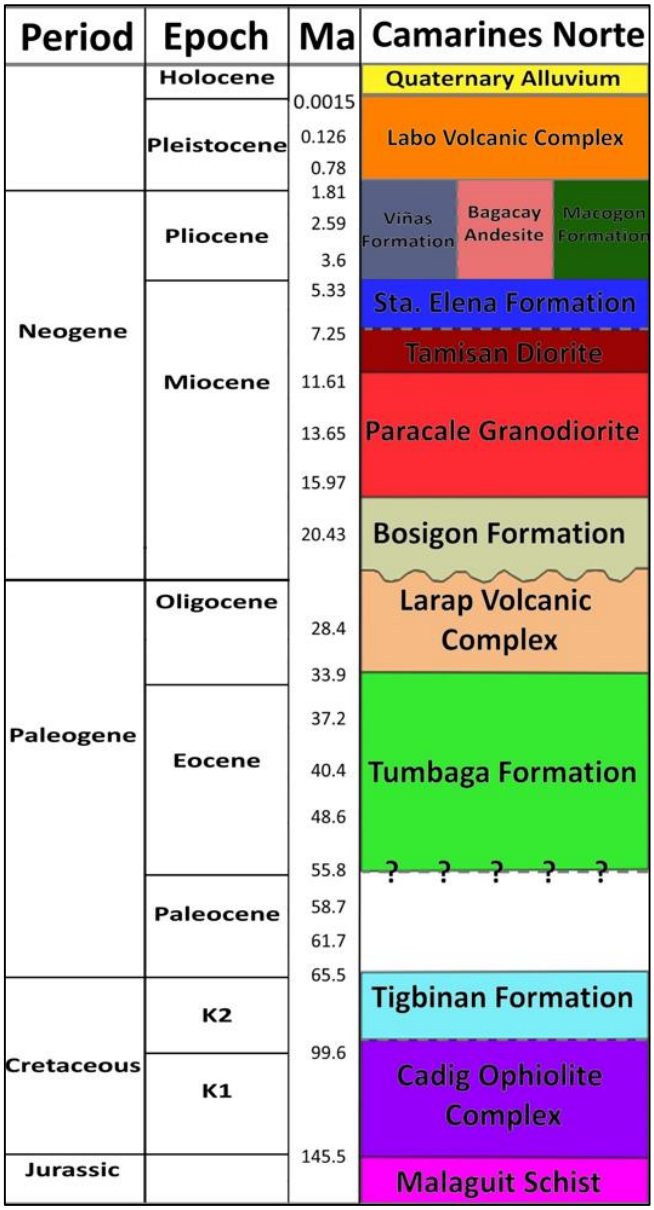

Figure 3-17. *Stratigraphic column of the Paracale-Panganiban Mineral District and its vicinity (modified from MGB, 2010).*

The Paracale Granodiorite (Early to Middle Miocene) is a medium- to coarse-grained plutonic rock composed of albite-oligoclase, orthoclase, biotite, and quartz (Meek, 1941). It intrudes the serpentinized peridotite in the Paracale-Panganiban mining district and is associated with the gold mineralization in the area. The other intrusive rock that underlies the study area is the Tamisan Diorite, which has an age of early Late Miocene (MGB, 2010). Among the reported rock units, only three formations were encountered (and interpreted from the ER-IP data) in the main study area: the Tumbaga Formation, the Labo Volcanic Complex, and the Tamisan Diorite (or other intrusive rock).

Figure 3-18. *Outcrops of (a) the thick pyroclastic deposit of the Labo Volcanic Complex and (b) the upper calcareous member (limestone) of the Tumbaga Formation observed in the study area.*

3.4 Methodology

3.4.1 Pre-fieldwork preparation

The ER-IP study in the Labo, Camarines Norte commenced with collating and assimilating existing geological, structural, and Remote Sensing (RS) data using Geographic Information System (GIS) techniques. Before going to the field, comprehensive analysis using RS and GIS techniques covering the study area at its vicinity was implemented using different free satellite datasets (e.g., Landsat, Sentinel-1, Sentinel-2). Basic GIS concepts and some examples of RS data processing used in this research are presented in the Appendix section. Advanced Spaceborne Thermal Emission and Reflection (ASTER) RS data were downloaded from the METI AIST Data Archive System (MADAS) website (https://gbank.gsj.jp/madas/map/index.html); Landsat, Digital Elevation Model (DEM), and Sentinel-2 RS data were downloaded from earth explorer website (https://earthexplorer.usgs.gov/); political boundaries and other spatial data were downloaded from Database of Global Administrative Areas (GDAM) website (https://gadm.org/index.html). RS datasets of Labo and its vicinity were downloaded to have an initial overview of the study area's geographic information (e.g., location, accessibility, land cover, and geology). Other remote sensing studies (e.g., hillshade analysis) were implemented before the field survey (Fig. 3-19). Appendix 4 shows some base maps created in preparation for the field survey. Since this research focuses on the ER-IP survey, representative results of the RS analysis in this study area are presented in Appendix 5.

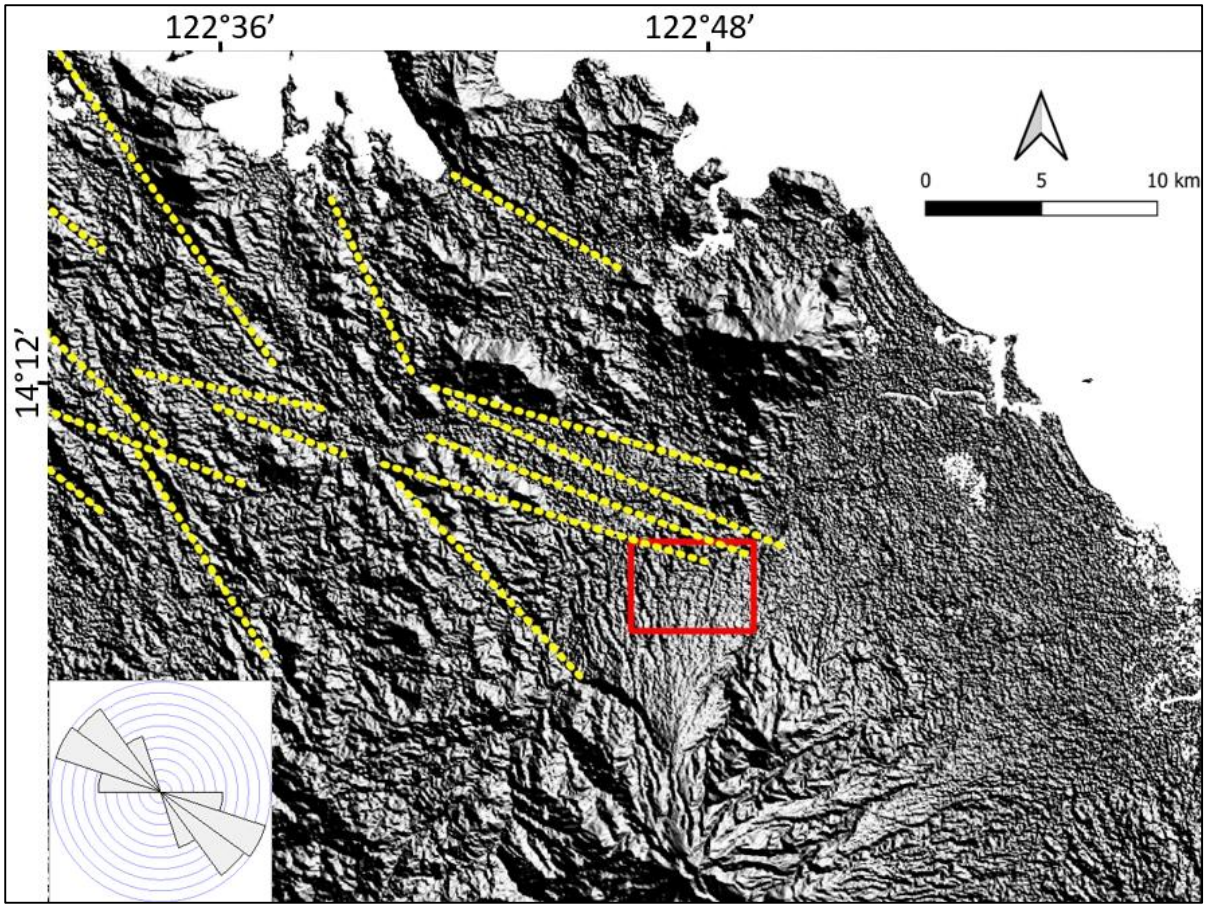

Figure 3-19. *Dominant east-northwest trending lineaments delineated from the DEM hillshade analysis (yellow dotted lines). The azimuth of the light is 45 degrees. The red box marks the location of the specific study area.*

The pre-geophysical and geological data gathering had long and tedious procedures due to restrictions because of the COVID-19 pandemic. The initial planning and coordination stages were done in the quarantine facility thru calls and online meetings because of the strict quarantine protocol in the Philippines (after arrival from Japan). The actual pre-fieldwork preparation started with the lay-outing and printing of base maps (e.g., topographic, geologic, structural) for the field survey and face-to-face meeting with the survey team (e.g., geologists) in the MGB office. Planning and preparation stages were conducted before going to the study area to ensure the security and safety of the field team. Courtesy calls were done before the field survey to get official approval from the local government unit (LGU) and obtain permission from the residents and landowners to sample/survey the specific study area. Since the study area is located in a remote region, the team ensured the survey area was safe from armed conflicts and other field hazards. It was also essential to test the instruments to make sure its good condition before going to the study area and conducting the field survey.

The succeeding field survey component, consisting of the geological mapping and geophysical surveys (e.g., VLF-EM, ER-IP), was undertaken with the help of the MGB Central Office (CO) and Regional Offices (RO). Two phases of field survey were implemented for this research. The first phase is the reconnaissance survey (2021), and the second is the detailed ER-IP survey (2022). COVID -19 testing and isolation were done before going to the study area for the field survey. Concerning planning and fieldwork stages, academic institutions (e.g., Exploration Geophysics Laboratory-Kyushu University) and government sectors (e.g., Mines and Geosciences Bureau) were also requested to provide inputs to share the geoscientific knowledge and experience in the conduct of the research.

3.4.2 Very Low Frequency Electromagnetics (VLF-EM) Survey

The Very Low Frequency Electromagnetics (VLF-EM) survey, together with the geological mapping, was part of the reconnaissance stage of this research. The first week of the reconnaissance survey was employed to establish local contacts and obtain permissions from the residents and landowners to sample/survey an area of interest. For the geological survey, representative rock samples were collected (if possible), and preliminary analysis (e.g., megascopic) was implemented in a regional study area before narrowing down to a specific target area. This reconnaissance phase was implemented to ensure that the area is suitable for the planned ER-IP geophysical survey. The implementation of the reconnaissance geophysical surveys started with the field design and area preparation (e.g., set up grid, clear vegetation). The VLF-EM data acquisition took more time than field mapping and rock sampling due to the difficulty of data acquisition (e.g., rough terrain) in some areas (Fig 3-20).

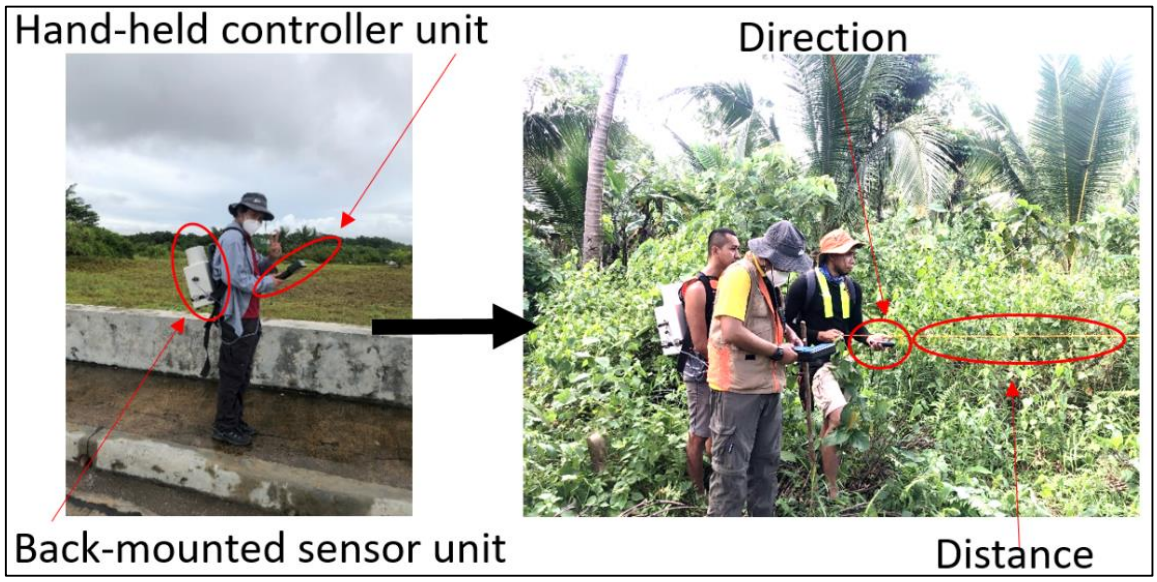

Figure 3-20.*Field survey using the VLF-EM instrument.*

VLF-EM data were acquired using IRIS instruments' T-VLF radio wave receiver (Fig 3-20). Tilt mode, which solely measures magnetic components, was selected for the field survey. The VLF-EM approach operates in the low-frequency range (15 to 25 kHz) and helps define vertical and dipping conductors (Paál, 1968; Paterson and Ronka, 1971; Phillips and Richards, 1975; McNeill and Labson, 1991; Ogilvy and Lee, 1991; Goldman and Neubauer, 1994). The implemented VLF-EM survey for this research used two VLF transmitters in Exmouth, Western Australia (NWC) and Ebino, Japan (JJI), with frequencies of 19.8 kHz and 22.2 kHz, respectively. Despite the distance between the transmitters, a strong primary field was available in the study area. The delineated regional structure has an approximate E-W strike. Therefore, the six VLF lines were orientated north-south (Fig. 3-21). VLF-EM surveys were conducted in the study area's northern (next to the specified lineaments) and southern (with thick overburden) parts. A 15 m distance separates the measurement stations of the VLF-EM lines. The acquired data were processed using Fraser and Karous-Hjelt filters (Fraser, 1969; Karous and Hjelt, 1983; Ogilvy and Lee, 1991).

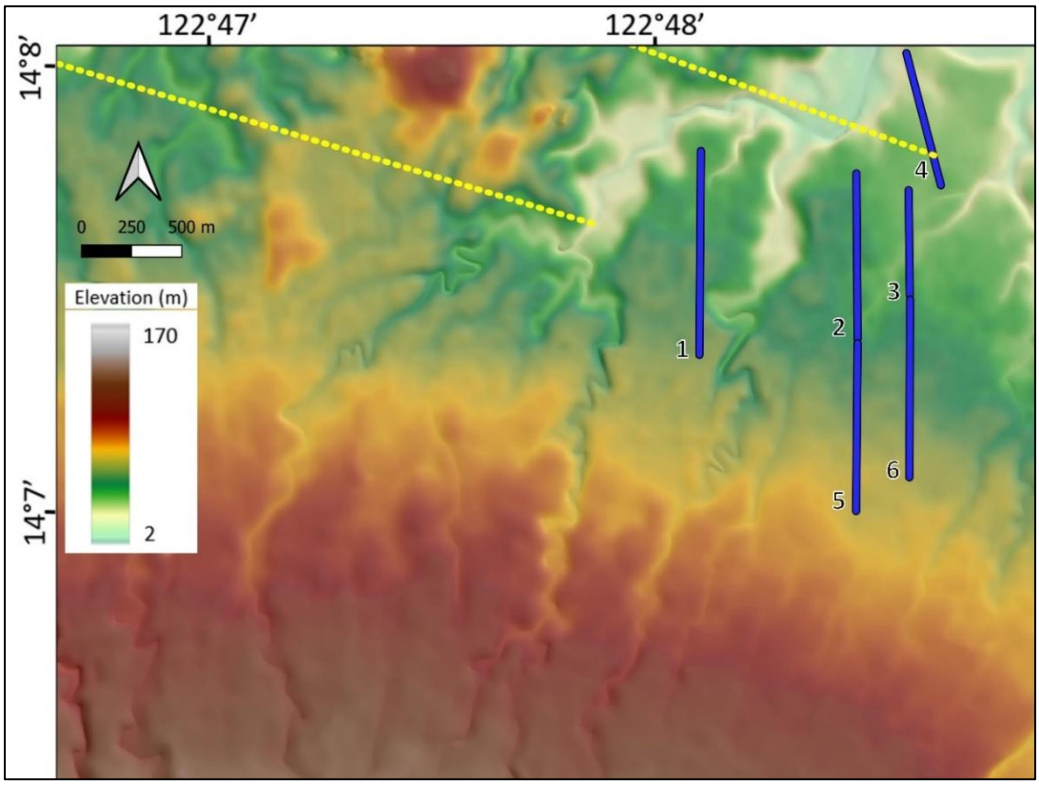

Figure 3-21. *Locations of the six VLF-EM profile lines. The dotted yellow lines represent the interpreted lineaments from the DEM hillshade analysis. The elevation data were downloaded from the 30-m Shuttle Radar Topographic Mission (SRTM) Digital Elevation Model (DEM) (https://www2.jpl.nasa.gov/srtm/cbanddataproducts.html).*

3.4.3 Electrical Resistivity-Induced Polarization (ER-IP) Survey

The electrical resistivity and time-domain induced polarization (ER-IP) data were gathered simultaneously using the IRIS Syscal Pro Switch 72 instrument (Fig. 3-22). Iris Instruments provided the specs of the resistivity imaging system (http://www.iris-instruments.com/syscal-prosw.html). The Syscal Pro system is a multinode resistivity and induced polarization imaging device that may be used for environmental and engineering geophysical research. This equipment can do up to ten measurements at once. It measures 31cm by 23cm by 31cm and weighs 11kg. Its transmitter has a maximum output voltage of 1000V and a maximum current of 2.5A. The receiver has pulse lengths of 0.2s, 0.5s, 1s, 2s, 4s, or 8s, an input impedance of 100Mohm, and an accuracy of 0.2%. The device includes power line noise rejection at 50 and 60 Hz as well as SP linear drift correction. The electrical resistivity tomography (ERT) survey was implemented using a dipole-dipole array with an electrode separation of 10 m. The dipole-dipole array was chosen because it offers relatively strong horizontal resolution, good depth of investigation, and low electromagnetic coupling (Sasaki, 1992; Neyamadpour et al., 2010; Loke, 2012).

The data were collected along sixteen profile lines (710m length), with north-south and east-west orientations (Appendix 6). One ER-IP survey per day was implemented due to the rough topography and weather conditions on some days of the survey. Outcrop observation and sampling were also done if possible. The ER-IP data acquisition took more time than the geologic mapping and VLF-EM survey because of the difficulty (~ 1 hour) of setting up the field survey and the long (~4 hours) data acquisition time.

Figure 3-22. *Photo of the Syscal Pro Switch 72 instrument and accessories (e.g., wire) used in the ER-IP survey.*

The north-south-oriented profiles were designed almost perpendicular to the ENE-ESE lineaments delineated using the hillshade analysis; the lineaments may indicate regional geologic structures related to potential mineralization in the area (Fig. 3-23). Several ER-IP data are needed to produce more reliable 2-D and 3-D subsurface models (e.g., to constrain the location of potential mineralized zones) in the study area. The 2-D sections were collated and inverted to produce pseudo-3D ER and IP models. The continuity of the subsurface geo-electric layers interpreted from Profiles A-A' to J-J' was validated by running east-west-oriented ER-IP profiles (i.e., K-K', M-M'). The 3D inversion of ER and IP data was also done to confirm the continuity of the anomalous zones and provide a better picture of the changes in resistivity and chargeability with depth. Profiles O-O' and P-P' were used to calibrate the ER-IP values with their corresponding mineralization potential.

The last part of the field survey involved data processing and preliminary geophysical data analysis. Before returning to the MGB office, initial interpretations were made to delineate and highlight the location of the geophysical anomaly and its correlation with the subsurface structures. The ER-IP data were kept within the excellent range, and bad data points were removed before undertaking the 2-D inversion. Measured data were filtered to exclude negative and very high apparent resistivity (1 to 3,000 ohm-m) values (outliers). The data points with minimal current (< 0.5 mA) and voltage (<0.1 mV) were also exterminated from the dataset. These outliers could have relatively changed the response in anomalous zones related to mineralization.

The resistivity and chargeability of the model blocks were calculated using the RES2DINV program (Loke, 2012). The L1 norm (robust) inversion method was used because the subsurface mineralized features are expected to be separated by relatively sharp boundaries, and the Gauss-Newton optimization technique was employed to solve the least-squares equation (Loke et al., 2003; Loke, 2012). An initial damping factor of 0.15 was chosen to account for the noise caused by the surface heterogeneities in the data. During the inversion process, minimum and maximum damping factors are fixed at 0.020 and 5.0. The root-mean-squared (RMS) error measures the difference between the measured and calculated apparent resistivity values. Since the model with the lowest RMS error may not necessarily be the optimal model from a geological perspective, the inversion iterations were terminated when the RMS error value did not change significantly (< 5%) (Loke, 2022). The 3-D inversion of ER and IP data was performed using ResIPy ((Blanchy et al., 2020)). Iteration is a computational operation that is repeated in order to achieve increasingly closer approximations to a problem's solution. The purpose of ER-IP inversion is to produce a model, which is a

mathematically idealized representation of a portion of the Earth that provides results that are comparable to the observed data. In all optimization methods, an initial model is iteratively updated to reduce the discrepancy between the model response and the observed data values.

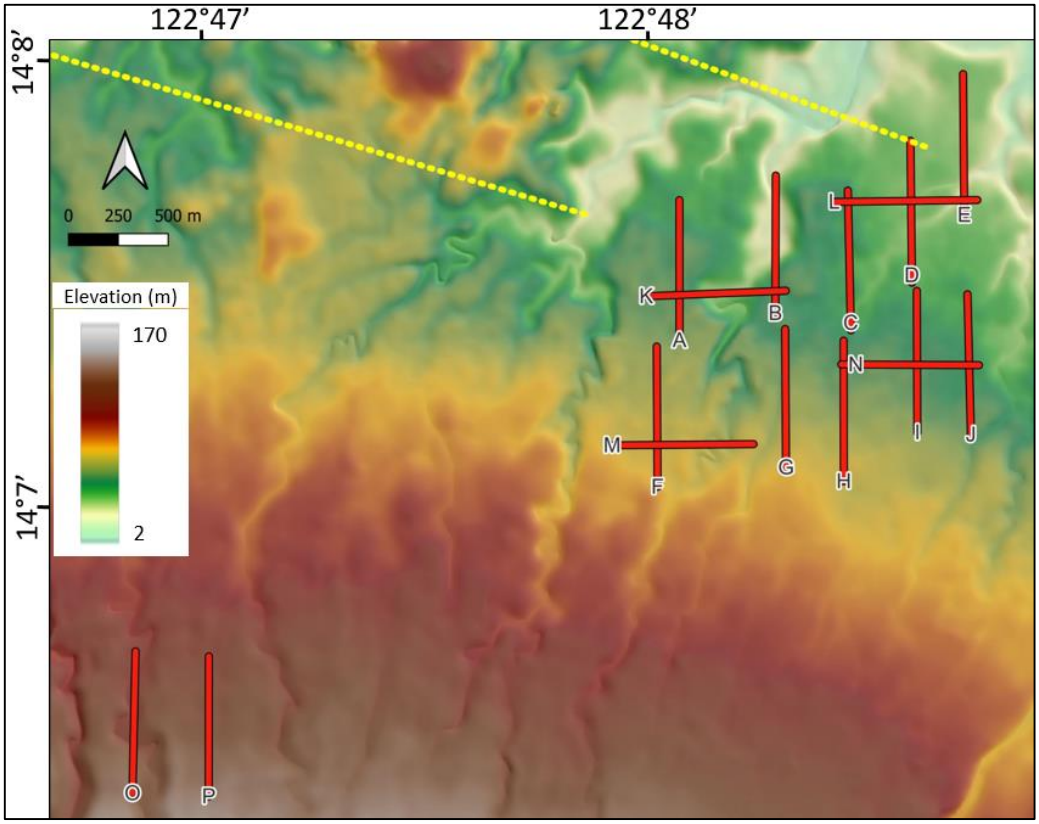

Figure 3-23. *Fourteen ER-IP profiles are located in the main study area (northeast), and two are in the calibration area (southwest). The dotted yellow lines represent the interpreted lineaments from the DEM hillshade analysis. The elevation data were downloaded from the 30-m Shuttle Radar Topographic Mission (SRTM) Digital Elevation Model (DEM) (https://www2.jpl.nasa.gov/srtm/cbanddataproducts.html).*

3.5 Results and Discussion

3.5.1 Very Low Frequency Electromagnetics (VLF-EM)

Figures 3-24 to 3-29 show the VLF-EM responses for all six profile lines (Profiles 1 to 6). The Fraser derivative graphs and the apparent current density subsurface distributions (derived from the Karous-Hjelt filtering technique) were discussed for each VLF-EM profile. The results along each profile are reported based on the distance from the section's starting point (the southern part of the profile). The x-axis represents the distance from the starting point. The y-axis is the phase component (in %) in figures 3-24a to 3-29a; it is the pseudo depth in figures 3-24b to 3-29b.

3.5.1.1 VLF-EM Profile 1

Profile 1 is located in the northeastermost part of the study area. It is oriented north-south and has a total length of 735 m. VLF-EM Profile 1 is parallel and adjacent (~50m) to ER-IP Profile A (Figure 3-24). The zero cross-over of the in-phase component and the high positive Fraser peak depict a high conductivity fractured zone on the southern and northern parts of the section at around 150 m and 570 m, respectively. The Karous-Hjelt filter of profile VLF-EM Profile 1 shows high current density (blue color) portions with positive Fraser peaks. The anomaly persists until the 30 to 40 m-depth. The high current density was interpreted as the clayey pyroclastic lithology of the Labo Volcanic Complex (overburden). This high conductivity zone was also observed in Profile A. Furthermore, the boundary between the blue and red zones could be attributed to a geologic structure correlated with the sharp, linear, and vertical anomaly in ER-IP Profile A-A' (Figure 3-32). The other high current density zone at the 570 m mark can also be associated with the relatively low resistivity zones at the northern portion of Profile A-A'.

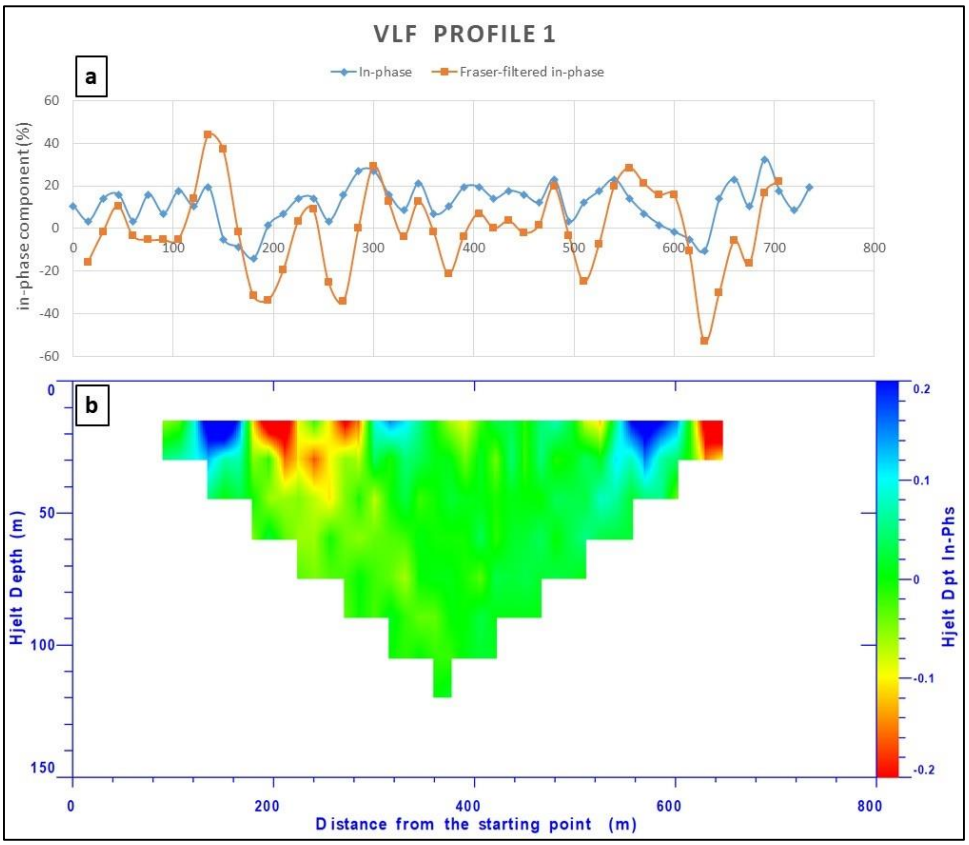

Figure 3-24. *VLF-EM response along Profile 1: (a) observed in-phase components and its Fraser derivative and (b) Karous-Hjelt current density section.*

3.5.1.2 VLF-EM Profile 2

The results of the VLF-EM survey in the northern central part of the study area are presented in VLF-EM Profile 2 (865-m length). It trends in the north and is located on the same site as ER-IP Profile C-C'. The in-phase component has minor zero crossovers on the 100 m, 300 m, and 550 m marks (Figure 3-25). The Fraser positive peaks were noted at 310 m and 550 m from the beginning of the section. These zones were identified as the high current density regions associated with the relatively low resistivity regions of the overburden, as shown in Profile C-C'.

Furthermore, the continuation of the high current density signature at around 40 m-depth (at the 550m mark) can be attributed to the low resistivity zone (Zone C) of the underlying Tumbaga Formation at the southern portion ER-IP Profile C-C'. This linear feature could indicate a geologic structure (e.g., fractured zone) that may influence this section's high concentration of sulfide minerals (i.e., high chargeability). This portion is a good location for drilling, assuming that the conductive fractured zone is related to mineralization. The poor conductivity zones (red patches) are attributed to the dry overburden.

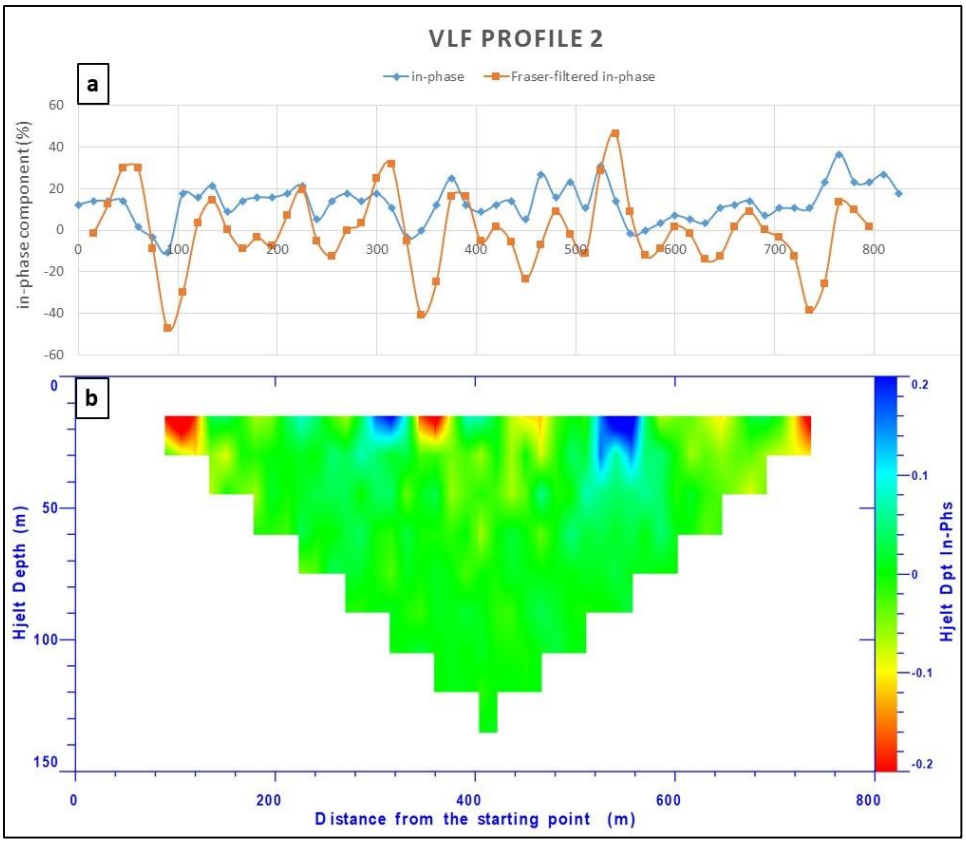

Figure 3-25. *VLF-EM response along Profile 2: (a) observed in-phase components and its Fraser derivative and (b) Karous-Hjelt current density section.*

3.5.1.3 VLF-EM Profile 3

Profile 3 is relatively short (525 m) because of the very steep river cliff encountered during the survey. Profile 3 has a north-south orientation and is located on the eastern side of VLF-EM Profile 2 (Fig. 3-26). This profile is also parallel and near (~50 m) the ER-IP Profile D-D'. The in-phase component crossover the zero at the 1230m and 1290 m mark, presenting a substantial positive Fraser peak. The Karous-Hjelt section shows a high current density zone at 1155 m and 1230 m marks. This anomalous zone can be observed at a depth of around 60m. Correlating with the ER-IP Profile D-D', these high current density areas are attributed to the relatively low resistivity portion of Zone A and Zone H. There were no observed linear vertical features on the ER-IP model sections. However, the continuity of the relatively low resistivity zones at the 280 m (in the ER-IP model) mark warrants a further investigation of this site for a potential structure-related anomaly. The red regions to the south of the profile represent the poor conductivity zones characterized by the thick overburden at the central portion of Profile C-C'.

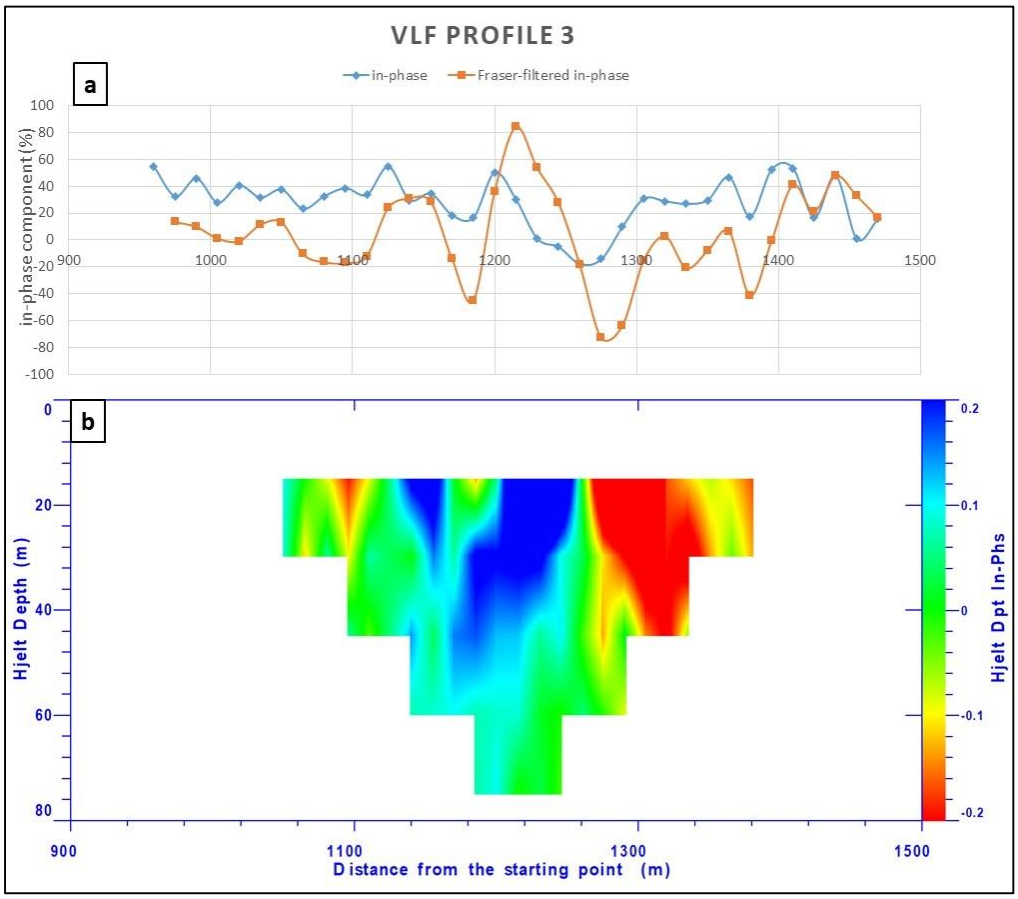

Figure 3-26. *VLF-EM response along Profile 3: (a) observed in-phase components and its Fraser derivative and (b) Karous-Hjelt current density section.*

3.5.1.4 VLF-EM Profile 4

VLF-EM Profile 4 is located in the farthest northeastern part of the study and has an NNW-SSE orientation. Figure 3-27 shows the results of the VLF-EM survey showing the anomalous zones up to the depth of 30 m. The zero crossovers were observed at the 135 m and 240 m marks. High positive Fraser peaks are present on four prominent locations in the profile (i.e., 120 m, 240 m, 420 m, 555 m) representing the high current density zones. On the other hand, the central portion of the area (red), with a very low negative Fraser peak, corresponds to a vast poor conductivity zone. The extensive high anomaly on the southernmost part of the Karous-Hjelt current density section is on the location of the trace of the lineament, which was delineated using the remote sensing analysis (Figure 3-19). This information supports the interpretation that the high current density areas in the section are related to an excellent conductive fractured zone with a WNW-ESE strike direction. Minor and shallow high current density anomalous zones were also noted on the northwestern side of the profile, indicating a shallow clayey tuffaceous layer of Labo Volcanic Complex (overburden).

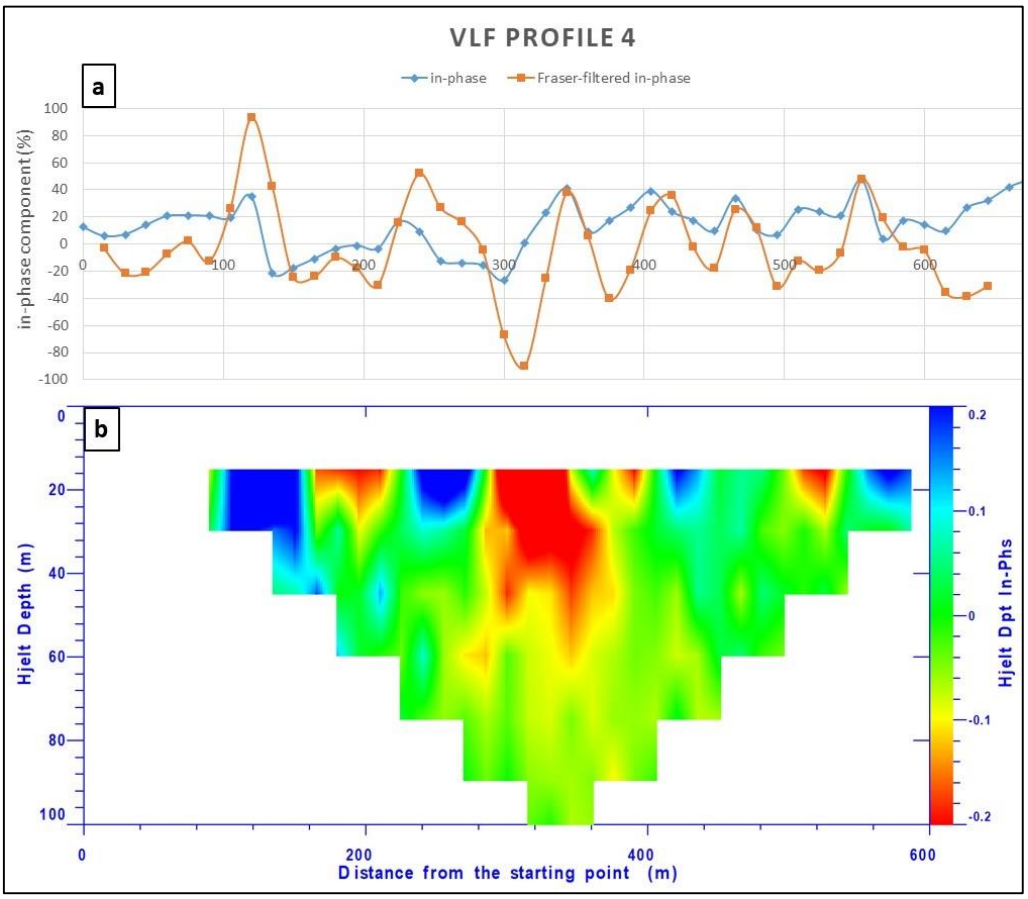

Figure 3-27. *VLF-EM response along Profile 4: (a) observed in-phase components and its Fraser derivative and (b) Karous-Hjelt current density section.*

3.5.1.5 VLF-EM Profile 5

Profile 5 is situated on a relatively elevated terrain in the southern part of the study area. The profile (with a total length of 825 m) is oriented north-south and about 20 m east of ER-IP Profile H-H'. The in-phase component behaves quieter on the southern part of the profile than on the northern side (Fig. 3-28). Furthermore, the positive peaks (after subjecting to the Fraser derivative) are not evident in the profile. Some minor high current density zones can be observed at 285 m and 720 m marks. These shallow anomalous zones are also reflected in the Karous-Hjelt current density section. The red zones are considered poor conductivity zones attributed to the dry rocks/soils, while the blue regions can be due to the relatively low to moderate resistivity clay lenses within the overburden. No lineament was delineated using the remote sensing technique, and thick pyroclastic deposits were noted in the ER-IP Profile H-H'. This thick pyroclastic overburden could be why the anomalous zones on the K-H current density section are not persistent at greater depths. A homogenous non-conductive subsurface (indicative of an absence of mineralized zones) generally define in this section.

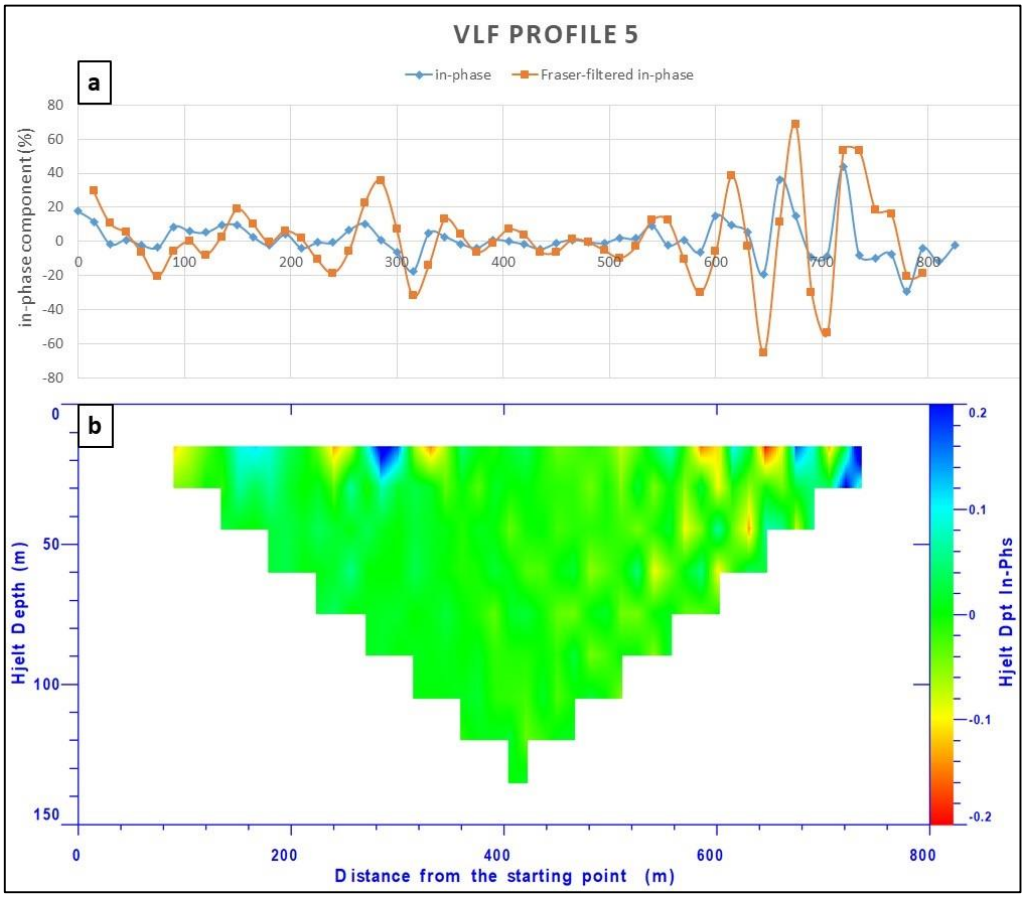

Figure 3-28. *VLF-EM response along Profile 5: (a) observed in-phase components and its Fraser derivative and (b) Karous-Hjelt current density section.*

3.5.1.6 VLF-EM Profile 6

Profile 6 runs from south to north and has a total length of 705 m. This profile shows the subsurface lateral conductivity variation at the study area's southeastern side and is located 80 m west of the ER-IP Profile C-C'. The in-phase component has no zero crossovers indicating a relatively homogenous subsurface (Fig. 3-29). Some minor Fraser-positive peaks were identified at 645 m and 745 m marks. These zones were identified as the minor high current density regions associated with the overburden's shallow, slightly clayey composition. The high current density signature is limited up to around 30-m depth; thus, a feature attributed to a significant geologic structure (e.g., fractured zone) is not likely to be present. The thick (~ 40 m) Labo Volcanic Complex was delineated in the ER-IP Profile I-I', indicating that the shallow anomalous current density zones (blue and red zones) are due to the manifestation of overburden alone. The poor conductivity zones (red patches) are attributed to the dry overburden. The homogeneity of VLF-EM and ER-IP results suggests that this portion of the study area is not a good location for exploratory drilling for potential mineralization.

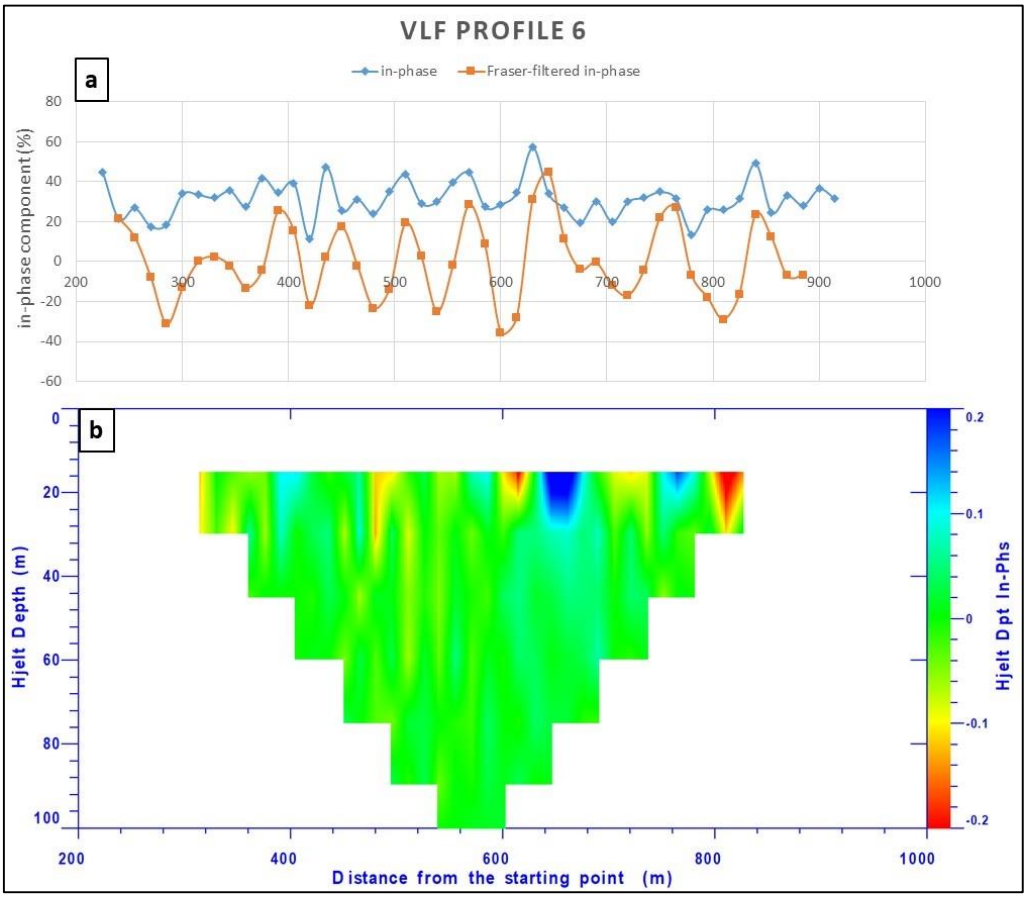

Figure 3-29. *VLF-EM response along Profile 6: (a) observed in-phase components and its Fraser derivative and (b) Karous-Hjelt current density section.*

3.5.2 Electrical Resistivity-Induced Polarization (ER-IP)

Figures 3-32 to 3-47 show the 2-D ER-IP inverted models for all sixteen profile lines (Profiles A-A' to P-P') generated from this research. Figures 3-32 to 3-41 represent the north-trending profiles, while Figures 3-42 to 3-45 illustrate the east-west oriented profiles. Figures 3-46 and 3-47 present the two sections in the calibration area. The root-mean-square (RMS) errors between the measured and computed values for the resistivity and IP data were shown at the upper left side of the 2-D profiles. The average depth of investigation based on the generated inverted models is around 150 m. The x-axis represents the distance from the starting point, while the y-axis is the elevation in meters. Figures 3-53 to 3-56 represent the 3-D ER-IP inverted models and their corresponding depth slices. These 3-D models were generated to understand better the geometry related to mineralization potential in the study area.

3.5.2.1 2-D Electrical Resistivity and Induced Polarization (ER-IP) models

Characterizing the underlying lithology in the inverted ER-IP model sections uses the range of resistivity and chargeability values. The derived models are constrained by correlating the ER-IP models with some drilling information to support the interpretations of the subsurface geology (Fig. 3-30). Photographs of representative core samples displaying mineralization occurrence in the calibration area are shown in Figure 3-31. The three main resistivity and chargeability ranges utilized to categorize the related mineralization and subsurface lithology in the corresponding models are shown in Table 3-5. The resistivity and chargeability ranges shown in Table 3-5 were combined to identify eight subsurface lithologies, which may correspond to the potential mineralization in the study area (Table 3-6). Borehole data from adjacent drill holes were used as a reference in deducing the lithologic units. The letters (i.e., A to H) in Figures 3-32 to 3-47 represent the zones of deduced subsurface lithology.

Table 3-5. *Ranges of electrical resistivity and chargeability values utilized to characterize the underlying lithology.*

Range	Resistivity (ohm-m)	Chargeability (mV/V)
Low	< 15	< 15
Moderate	15 to 100	15 to 25
High	> 100	> 25

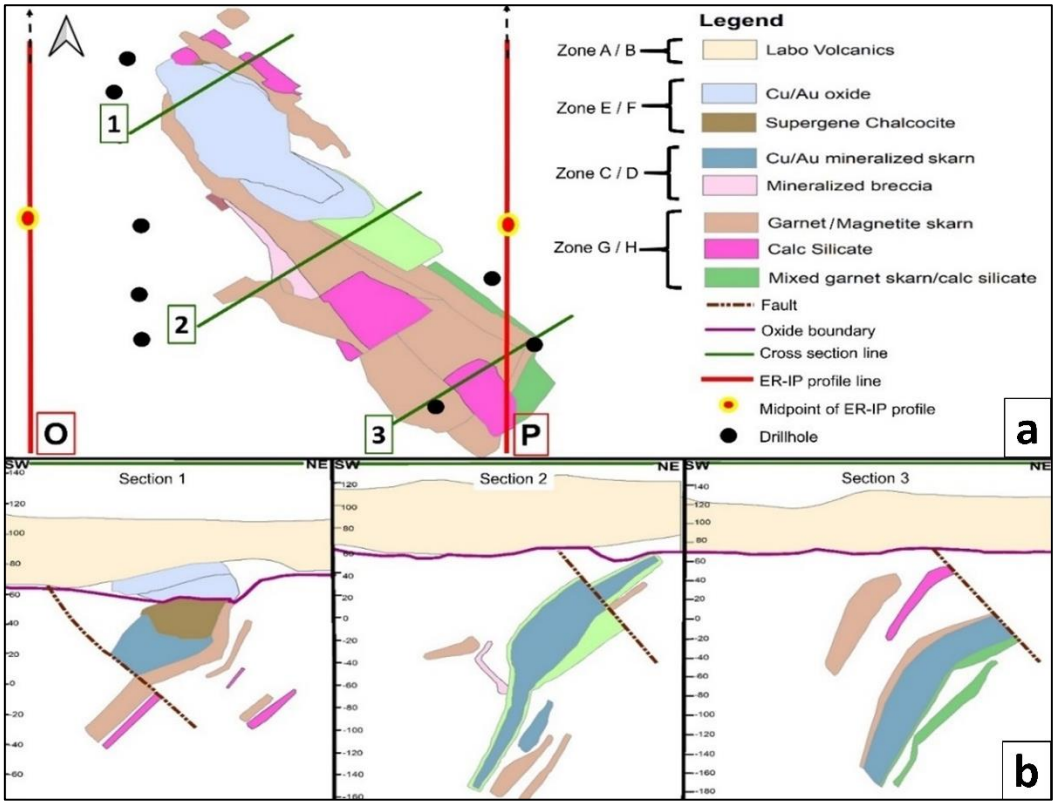

Figure 3-30. *(c) Plan and (d) section views of the mineralized zones in the calibration area from borehole data (modified from Gordon et al., 2016).*

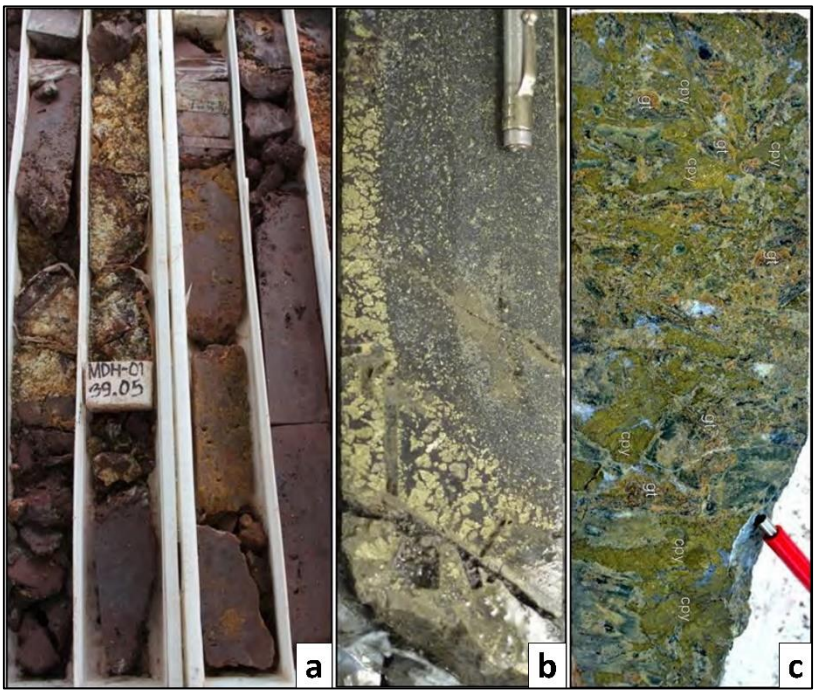

Figure 3-31. *Representative core samples show mineralization occurrence in the calibration area (Gordon et al., 2016). (a) The oxidized hematite-rich mineralization represents Zone E / F, while the (b) high-grade chalcopyrite magnetite skarn and (c) garnet (gt) skarn with high-grade chalcopyrite (cpy) mineralization characterize the Zone C / D.*

Table 3-6. *Deduced lithologic units representing the resistivity/chargeability zones identified based on the combination of the generalized resistivity and chargeability ranges.*

Zone	Resistivity (ohm-m)	Chargeability (mV/V)	Deduced lithology
A	moderate to high (shallower depth)	low	Labo Volcanic Complex (overburden): tuff and other pyroclastics; interlayered andesite, dacite, and minor basalt flows; 30 to 50 m thickness
B	low (shallower depth)	low	Clayey layers (lenses) within Labo Volcanic Complex
C	moderate	high	Tumbaga Formation: lower clastic member (e.g., sandstone); upper calcareous member (e.g., limestone); high concentration of disseminated sulfide minerals (e.g., pyrite, chalcopyrite)
D	high	high	Tumbaga Formation (or plutonic rock): Highly silicified with disseminated sulfide minerals (e.g., pyrite, chalcopyrite)
E	low	moderate to high	Oxide zone: Concentrated sulfide minerals along clayey, weathered, fractured portions; weathered ferruginous clay (e.g., native copper mineralization)
F	low (deeper depth)	low	Oxide zone: Hematite-rich zone (replacement of magnetite by hematite)
G	high	low	Tamisan Diorite: quartz diorite (may represent other plutonic rocks)
H	moderate to high	low	Tumbaga Formation: lower clastic member (e.g., sandstone); upper calcareous member (e.g., limestone); deficient (to none) concentration of disseminated sulfide minerals

3.5.2.1.1 ER-IP Profile A-A'

Profile A-A' has a south-north orientation and is located northwest of the study area. The model sections show four distinct anomalous resistivity and chargeability zones characterized by the change in lithology and mineralization potential (Fig. 3-32). The topmost layer (Zone A) has a thickness of around 20 to 40 m. The thickest (40m) part is the southernmost side and between the 400 to 500-m mark. Mark 240 m and the northern portion of the profile presents the thinnest layer. Zone A is characterized by generally moderate resistivity (15 to 350 ohm-m) and low chargeability (< 15 mV/V) in the resistivity and IP model sections, respectively. Within the Labo Volcanic Complex (Zone A), low resistivity zones (<15 ohm-m) (Zone B) were observed in the southern portion of the model section (60 m and 100 m marks) corresponding to clay lenses (e.g., weathered argillaceous tuffs).

Underlying the Labo Volcanic Complex layer (Zone A) are the zones of higher resistivity and chargeability (Zone C and D). This underlying lithology is identified as the Eocene Tumbaga Formation (MGB, 2004). The moderate resistivity with a high chargeability zone on the southern portion of the profile is represented by Zone C. The moderate resistivity is attributed to the highly indurated clastic rocks of the Tumbaga Formation. High chargeability indicates an anomalous concentration of disseminated sulfides (e.g., chalcopyrite, pyrite).
On the other hand, Zone D presents high resistivity and high chargeability anomalies. Zone D was noted on the northern portion of the model section. The anomalous zone may correspond to highly silicified rock (high resistivity) with disseminated sulfides (high chargeability). The depth to the surface of Zone C and D are around 110 m and 80m, respectively.

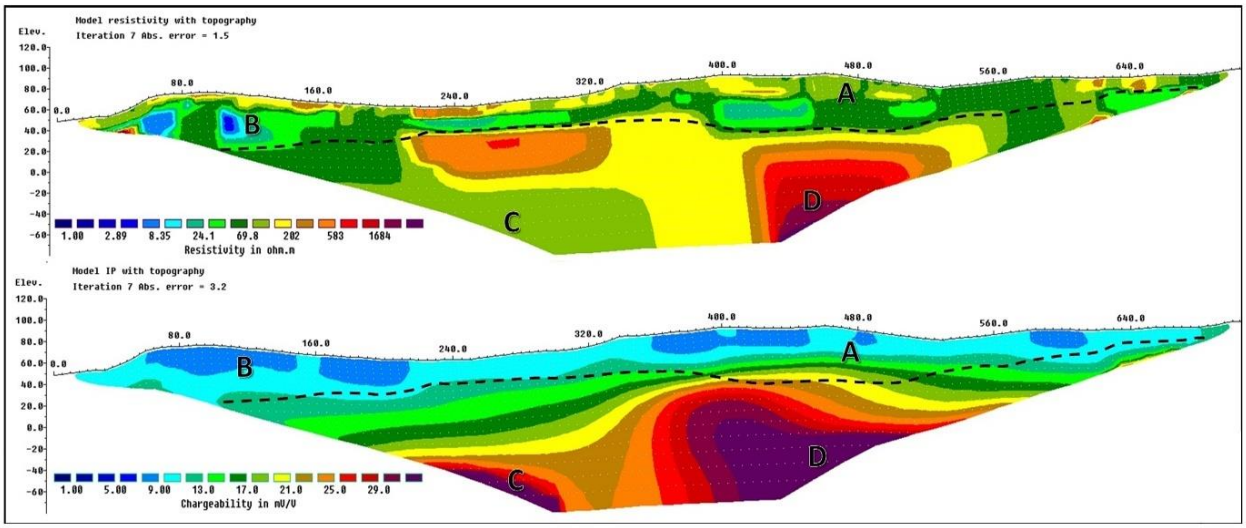

Figure 3-32. *2-D resistivity and induced polarization inverted model sections of Profile A-A'.*

3.5.2.1.2 ER-IP Profile B-B'

Profile B-B' presents the results of the ERT and IP surveys in the northern part of the study area (east of Profile A-A') (Fig. 3-33). It trends in a north direction, and the southern portion of the profile is located on a creek area. Zone A is represented by moderate to high resistivity values (> 15 ohm-m) and a low chargeability layer (< 15 mV/V). The Labo Volcanic Complex layer (Zone A) thickness in this section is generally uniform (~20 m). It has patches of low resistivity values in the profile's southern part (70 m mark). This Zone B is interpreted as pyroclastic rocks dominantly composed of clay minerals.

Moderate resistivity zones and moderate to high chargeability zones generally underlie Zone A. Some anomalous low resistivity zones in the profile's southern portion (130 m mark) indicate a fractured and weathered (clayey) zone. Its moderate chargeability anomaly may indicate sulfide (e.g., pyrite) occurrence. Zone C is the only identified distinct zone in this profile. Unlike Zone C in Profile A-A, these moderate resistivity (15 to 350 ohm-m) and high chargeability (>25 mV/V) anomalies are located in the central portion of the model profile. Furthermore, the cross-sectional area of Zone C in this profile is considerably bigger than Profile A-A'. This immense occurrence indicates more massive potential mineralization. It is also interesting to note that shallow small-scale mining activities have been reported in this area. Based on the IP 2-D model, the depth to the surface of this anomaly (Zone C) on the 370 m mark is around 60 m.

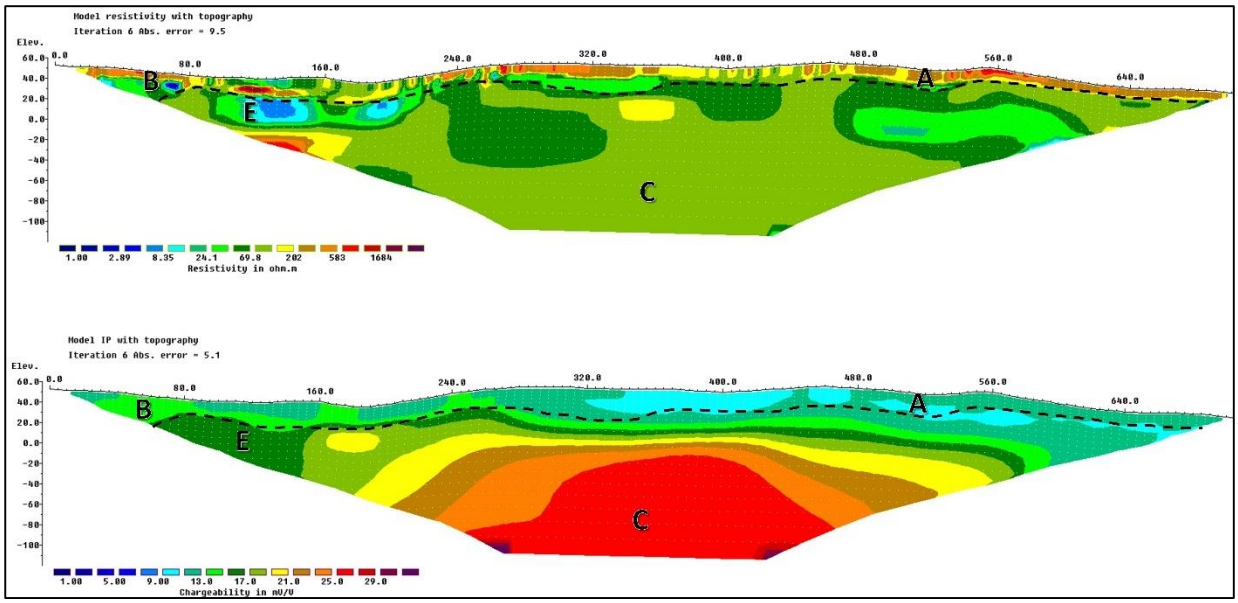

Figure 3-33. *2-D resistivity and induced polarization inverted model sections of Profile B-B'.*

3.5.2.1.3 ER-IP Profile C-C'

Profile C-C' has a north-south orientation and is located on the eastern side of Profile B-B' (Fig. 3-34). The thickness of Zone A generally increases from south (10 m thickness) to north (40 m thickness). Mark 120 m has the thinnest interpreted overburden (Labo volcaniclastics). Moderate to high resistivity (> 15 ohm-m) and low chargeability (< 15 mV/V) values define Zone A. A high resistivity zone was noted on the northern portion of the 2-D resistivity model, indicating resistive igneous rocks (e.g., andesite, basalt flows) within the overburden. It is also interesting to note that there are no low resistivity regions; this implies an absence of a clayey pyroclastic layer.

Below the monotonous Zone A are Zone C and Zone H. Zone C is confined on the northern side, as depicted on the 2-D IP model. This anomalous zone (15 to 350 ohm-m and >25 mV/V) is centered on the 420 m mark and located on a relatively elevated point (~ 60 masl). Sharp linear (90 degrees) boundary can also be noted on the IP and resistivity model sections that may indicate a geological structure (e.g., fault). That may suggest fault-controlled mineralization in the study area. Zone H underlies the southern side of the profile; this is the typical background signature of the Tumbaga Formation without disseminated sulfide. Zone H has moderate resistivity (15 to 350 ohm-m) and chargeability (15 to 25 mV/V) signatures. Some patches of low resistivity zones on the southern side of the 2-D resistivity model profile. These anomalous spots may indicate minor mineralized areas related to fracturing or weathering (presence of clay alteration minerals).

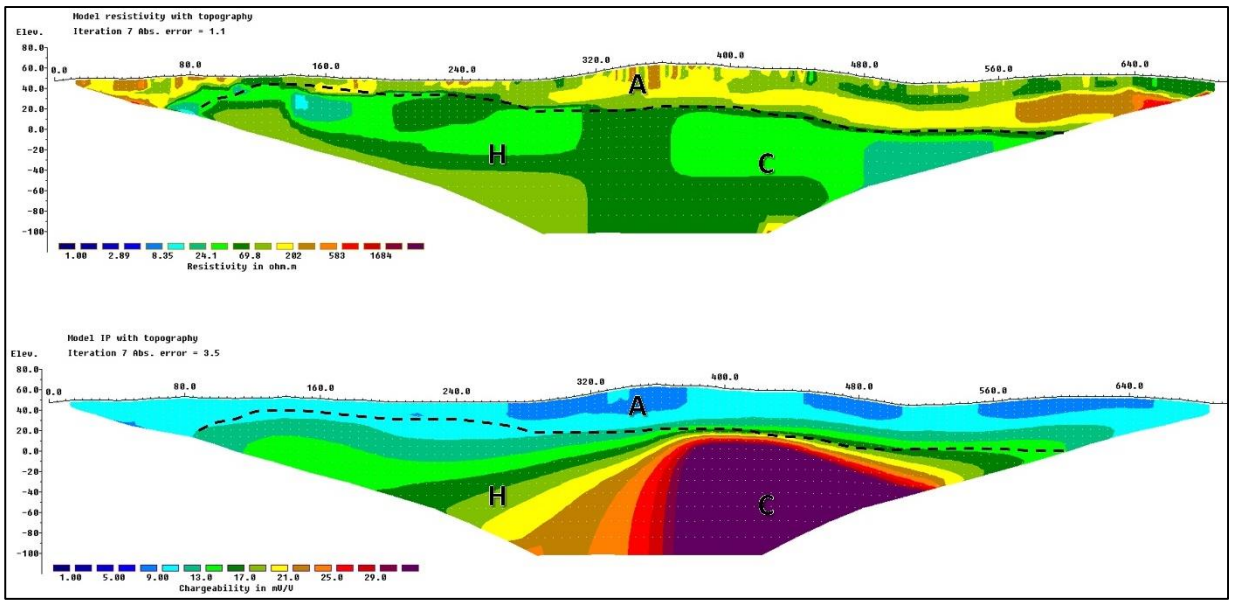

Figure 3-34. *2-D resistivity and induced polarization inverted model sections of Profile C-C'.*

3.5.2.1.4 ER-IP Profile D-D'

Profile D-D is located in the northern part of the study area (east of Profile C-C') and has a north-south orientation. Figure 4-35 shows the results of the ER-IP survey. The top overburden (Labo volcaniclastics) is designated as Zone A. This zone is represented by moderate to high resistivity values (> 15 ohm-m) and a low chargeability layer (< 15 mV/V) with variable thickness from 20 m (e.g., at 500 m mark) to 60 m (e.g., 370 m mark). Zone A generally thins out from south to north. Profile B-B' does not present a low resistivity zone within the top layer of the 2-D resistivity model section. That indicates an absence of clayey tuffaceous layers of the Labo Volcanic Complex on the northeastern side of the study area.

The underlying layer is characterized by the Zone C and H of the Tumbaga Formation. Moderate resistivity (15 to 350 ohm-m) and chargeability (15 to 25 mV/V) values represent Zone H. Tumbaga Formation comprises of lower clastic member (e.g., conglomerate) and upper calcareous member (e.g., limestone). The southern part of the profile is categorized as Zone H (between 0 m to 400 m marks). This zone implies barren rocks of the Tumbaga Formation (e.g., clastic member). On the other hand, the northern side of the 2-D IP model shows an anomalous high chargeability region (>25 mV/V), termed Zone C. This circular anomaly is interpreted as the Tumbaga Formation with a higher concentration of disseminated sulfides (e.g., chalcopyrite and magnetite mineralization). The depth to the surface of the low-resistivity anomaly at the 500 m and 590 m marks are around 50 m and 20 m, respectively.

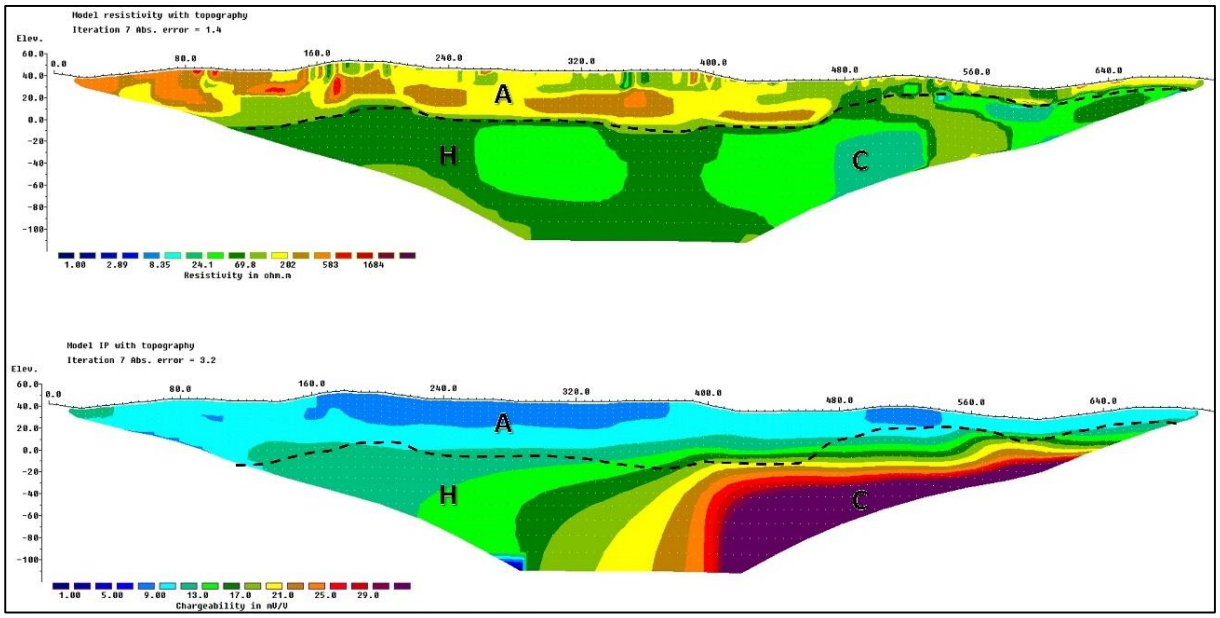

Figure 3-35. *2-D resistivity and induced polarization inverted model sections of Profile D-D'.*

3.5.2.1.5 ER-IP Profile E-E'

The north-south Profile E-E' is located on the northeasternmost side of the study area. The 2-D resistivity profile is generally characterized by three distinct geoelectric zones (i.e., A, C, G) (Fig. 3-36). These zones have corresponding characteristic chargeability values. The first layer (Zone A) is defined by moderate resistivity (15 to 100 ohm-m) and low chargeability (< 15 mV/V) and is interpreted as the Labo Volcanic Complex. Low resistivity zones are also absent in this profile, indicating a semi-uniform (without clayey lithology) composition of the Labo Volcanics overburden.

The second zone (Zone C) below overburden has a relatively lower resistivity and high chargeability. From the 2-D chargeability model profile, relatively more minor anomalous chargeability zones can be observed centered at 190 m and 580 m marks. The relatively minute occurrence of high chargeability zones indicates a diminishing mineralization potential east of the study area. The third zone (Zone G) represents very high resistivity (> 100 ohm-m) and low chargeability values. That can be interpreted as a massive, intrusive rock (Tamisan Diorite?) reported in the study area's vicinity. The mineralization (skarn) represented by Zone C can be attributed to the hydrothermal alteration caused by the interpreted intrusive rock. The previous reports from mining companies about the local mineralization in the area and the calibration of ER-IP data (Fig. 3-30) support this interpretation.

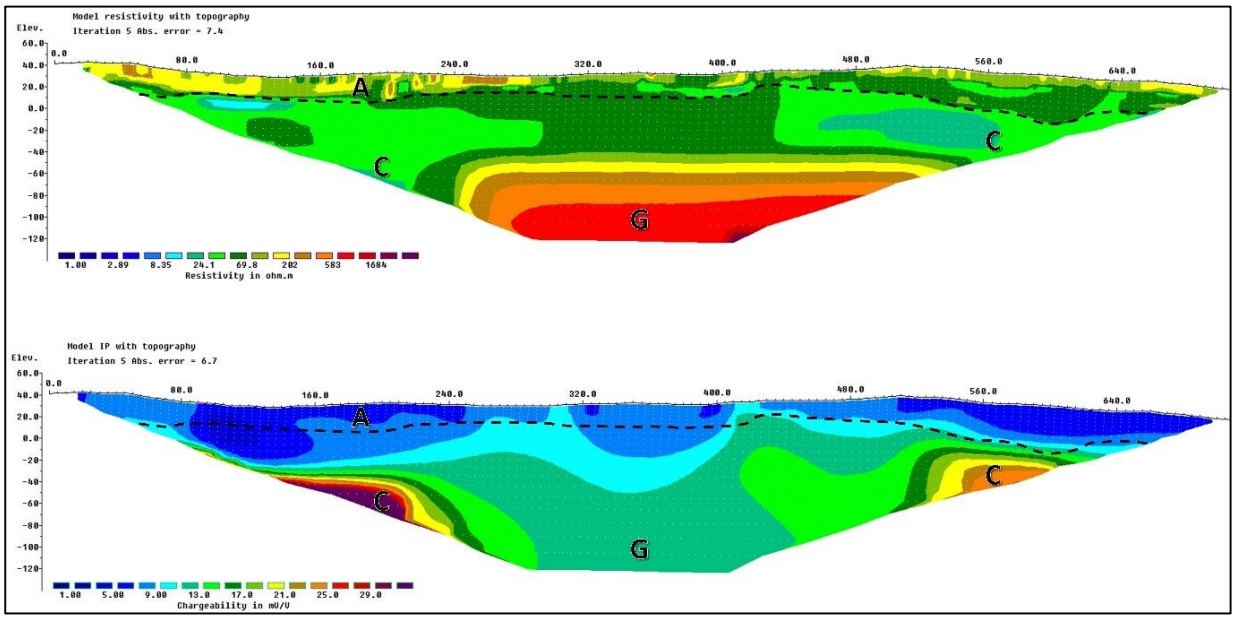

Figure 3-36. *2-D resistivity and induced polarization inverted model sections of Profile E-E'.*

3.5.2.1.6 ER-IP Profile F-F’

The resistivity and IP inverted models for Profile F-F’ was prepared to show the subsurface resistivity and chargeability variations on the southeastern side of the study area (Fig. 3-37). The profile has a north-south orientation and is situated on a relatively elevated topography (~ 70 to 80 masl). Profile F-F’ shows a moderate to high (>15 ohm-m) geoelectric layer overlaying a relatively lower resistivity (green portion). Low resistivity patches were not observed within Zone A, indicating an absence of clayey lithology of the Labo Volcanic Complex. The thickness of the overburden is uniform (~20 m) along the profile.

Zone H represents the non-mineralized Tumbaga Formation with moderate resistivity (15 to 100 ohm-m) and chargeability (15 to 25 mV/V). A circular anomaly (Zone E) characterized by low resistivity (<15 ohm-m) and high chargeability (>25 mV/V) is observed within the Zone H. Zone E was noted at the 200 m mark with an approximate depth of 20 m. This anomalous zone is interpreted as a highly oxidized and mineralized portion of the Tumbaga Formation. Relatively low resistivity and high chargeability values were observed on the southern side of the 2-D resistivity and IP model profiles, respectively. This occurrence indicates a possible presence of localized mineralized regions. Zone G represents the bottommost anomalous region, interpreted as the very resistive intrusive rock, and has an estimated depth of 90 m. The decrease of the observed high chargeability zones in this profile offers insight into the mineral potential decrease in the study area's southern portion.

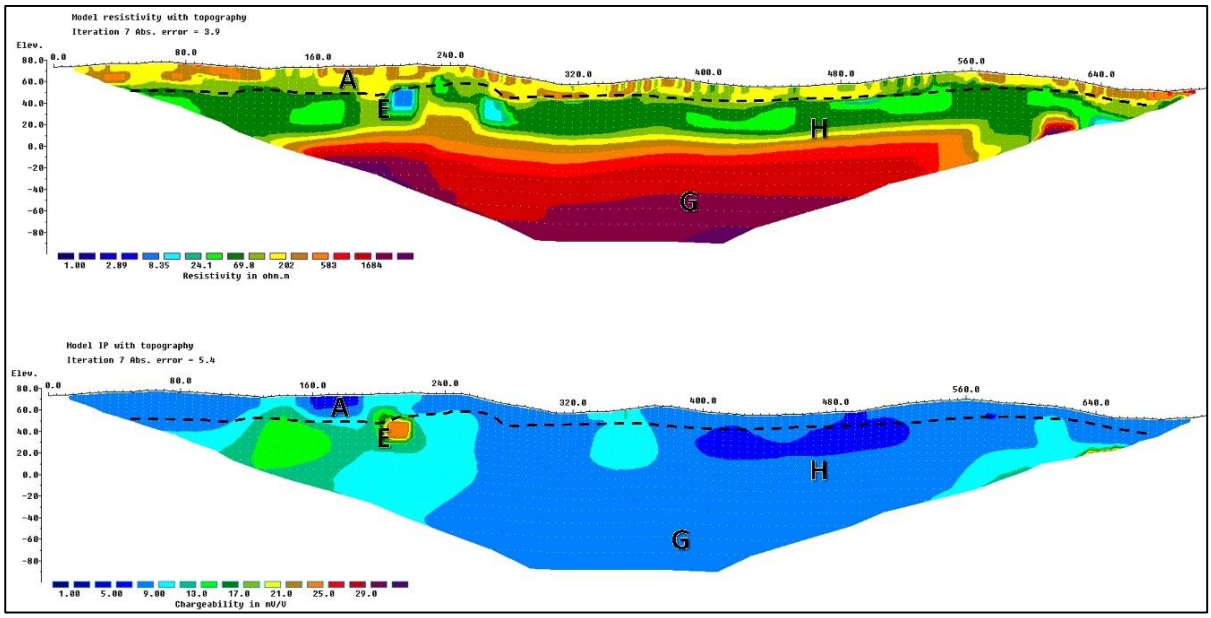

Figure 3-37. *2-D resistivity and induced polarization inverted model sections of Profile F-F’.*

3.5.2.1.7 ER-IP Profile G-G'

The north-south Profile G-G' is located on the southeastern side of the study area (east of Profile F-F'). Three geoelectric zones (i.e., A, H, G) generally characterized the 2-D resistivity model (Fig. 3-38). A small anomalous resistivity zone (Zone E) is also observed within Zone H. Zone a defined as the first layer represented by moderate resistivity (15 to 100 ohm-m) and low chargeability (<15 mV/V). This topmost layer is identified as the overburden composed of the Labo Volcanic Complex (e.g., pyroclastic rocks) with thicknesses ranging from 20 to 40m. Low resistivity zones are also absent in this profile, indicating a homogenous (without clayey lithology) composition.

Below the overburden are several zones corresponding to their characteristic resistivity and chargeability values. The second zone (Zone H) has relatively lower resistivity (15 to 100 ohm-m) and variable high chargeability interpreted as Tumbaga Formation. Small anomalous chargeability zones (Zone E) can be observed on the 2-D chargeability model profile at 40 m depth on the 140 m mark. The minor manifestation of high chargeability zones indicates a lessening mineralization potential to the south of the study area. Zone G represents high resistivity (> 100 ohm-m) and low chargeability values. That can be interpreted as Tamisan Diorite (intrusive rock). The depth to the surface of the intrusive rock (at the 330 m mark) is estimated to be 100 m. Mineralization due to hydrothermal alteration could be related to this interpreted intrusive rock (Zone G).

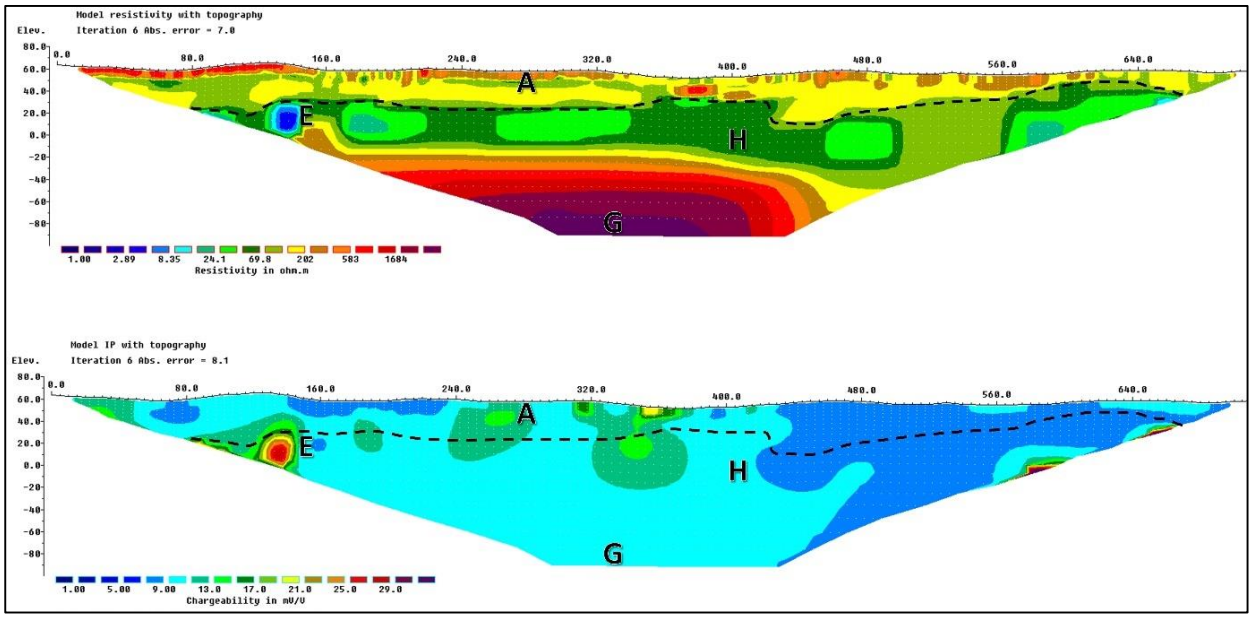

Figure 3-38. *2-D resistivity and induced polarization inverted model sections of Profile G-G'.*

3.5.2.1.8 ER-IP Profile H-H'

Profile H-H' is a north-south trending profile characterized by two geoelectric zones (Fig. 3-39). This profile is located in the south-central portion of the study area. The first zone (Zone A) is represented by moderate to high resistivity values (>15 ohm-m). The 2-D model presents a thick (~ 40 m) overburden with interbedded high and moderate resistivity layers. These layers are interpreted as interlayered volcaniclastic lithology of the Labo Volcanic Complex (e.g., tuffs, dacite flows) (MGB, 2004). The lower resistivity sandwiched in Zone A can be attributed to the more clayey tuffaceous part of the overburden. The delineation of Zone A is also manifested in the 2-D IP resistivity model. The presence of very low chargeability values (< 9 mV/V) generally separates Zone A (overburden) and Zone H (Tumbaga Formation).

The underlying layer is interpreted as the Tumbaga Formation, characterized by the lower clastic member (e.g., conglomerate) and upper calcareous member (e.g., limestone). Zone H has moderate resistivity (15 to 350 ohm-m) and chargeability (15 to 25 mV/V) values. The top layer (24 to 202 ohm-m) of Zone H has relatively lower resistivity than the bottom layer (> 202 ohm-m). The depth to the surface of the lower-resistivity layer and the higher-resistivity layer is around 40 m and 100 m, respectively. However, the IP anomaly distribution is inconsistent with the boundary of Zone H's top and bottom layers. This occurrence indicates a variable chargeability distribution (and sulfide occurrence) in Tumbaga Formation. The northern side of the 2-D IP model shows an anomalous small moderate chargeability region (>15 mV/V).

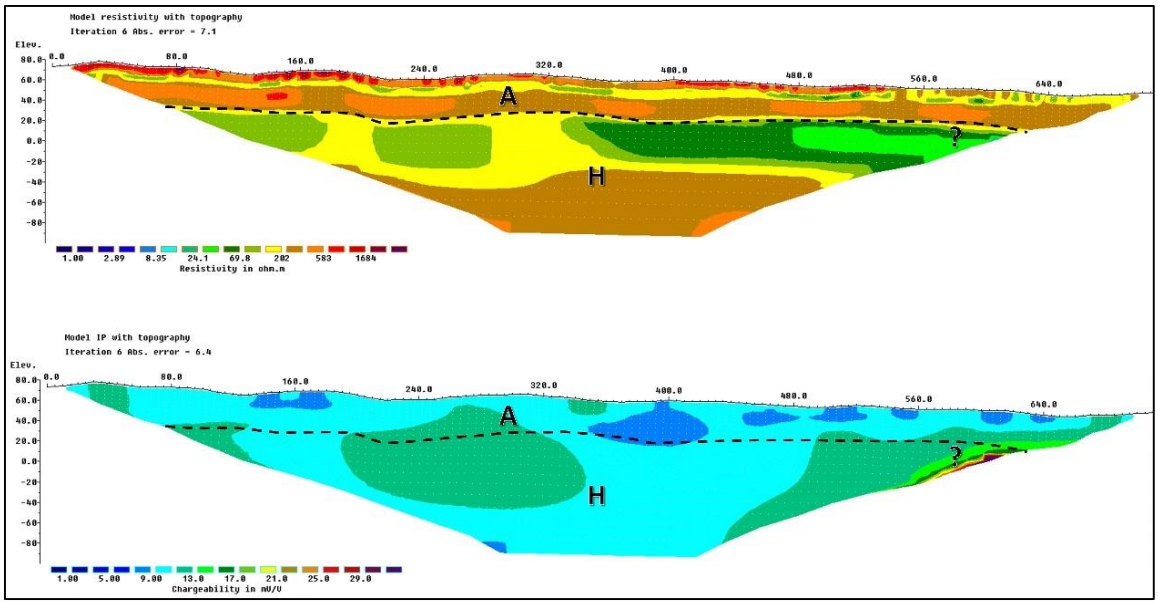

Figure 3-39. *2-D resistivity and induced polarization inverted model sections of Profile H-H'.*

3.5.2.1.9 ER-IP Profile I-I'

Figure 3-40 shows the resistivity and chargeability distributions along the vertical sections crossing Profile I-I'. These 2-D models (i.e., resistivity, chargeability) present an electrical characterization of the southeast of the study area (east of Profile H-H'). The 2-D resistivity model delineates the bottom boundary of the overburden (Labo Volcanic Complex). Zone A is outlined by an abrupt vertical resistivity change (from higher to lower resistivity). It has a thickness of around 30 to 40 m. The uppermost layer generally has very high resistivity values (> 350 ohm-m), while the lower layer has a moderate resistivity signature (~ 200 to 350 ohm-m).

Below Zone A are Zones H and G. The complex resistivity behavior of Zone A suggests heterogeneity of the underlying layers. The relatively high resistivity values observed in the southern part of the resistivity model would indicate the presence of intrusive rock. This anomaly (Zone G) probably relates to Tamisan Diorite at greater depth. The northern side of the profile has moderate resistivity signatures attributed to the barren Tumbaga Formation. Zone H has no anomalous chargeability distribution except for a relatively higher chargeability zone patch at the 290 m mark. This anomaly may indicate the presence of clayey zones because the chargeability signature is not high (>25 mV/V) to be considered sulfide-bearing rocks. Furthermore, the patch of low resistivity close to this anomalous chargeability zone may support this notion. Among the north-south trending profiles, Profile I-I' has the lowest mineralization potential based on the corresponding resistivity and chargeability values.

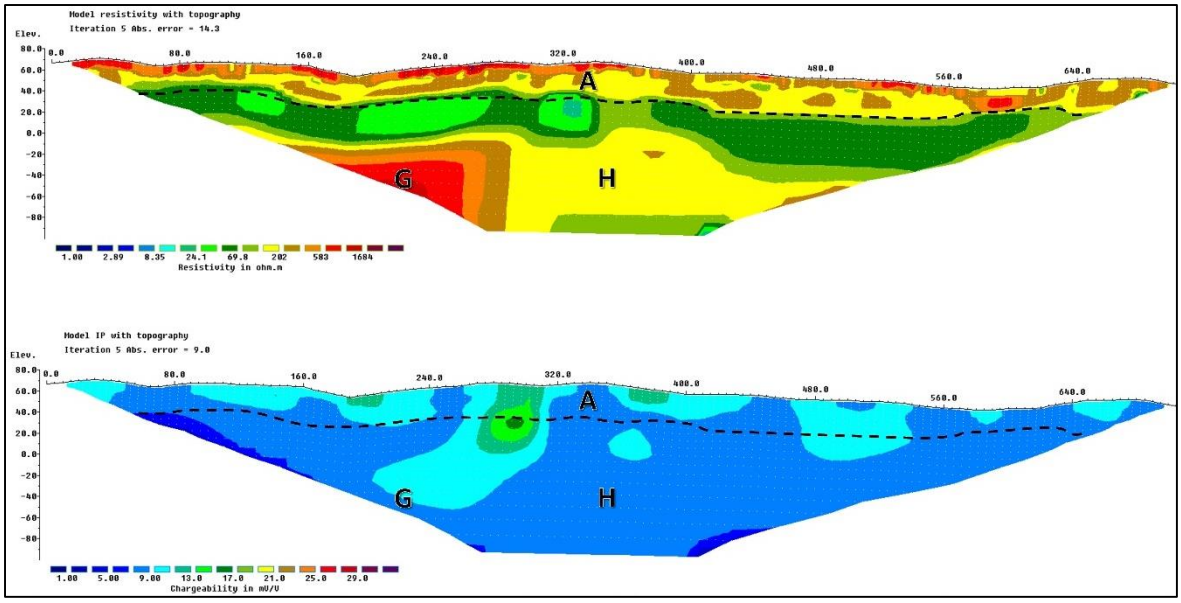

Figure 3-40. *2-D resistivity and induced polarization inverted model sections of Profile I-I'.*

3.5.2.1.10 ER-IP Profile J-J'

Profile J-J' shows the results of the ER-IP surveys in the farthest southeast portion of the study area (Fig. 3-41). It trends in a north direction and has an elevation of around 60 to 65 masl. Zone A is represented by moderate to high resistivity (> 15 ohm-m) and a low chargeability layer (< 15 mV/V). The Labo Volcanic Complex layer (Zone A) thickness in this section varies from 15 to 35 m. Patches of low resistivity values are not present in this section, but thin high resistivity strata are evident, representing the dry soil cover. The 2-D IP model shows a uniform chargeability distribution in Zone A, except for relatively lower IP values at around 60 m, 300 m, and 650 m marks.

For the lower region, Zone H and G were observed. High resistivity and low chargeability anomalies represent Zone G. These anomalies may correspond to the area underlain by the intrusive rock (Tamisan Diorite). Zone H is north of Zone G, with moderate resistivity and low chargeability values characterized by the barren Tumbaga Formation. Zone H exhibits varying resistivity values with a generally uniform chargeability signature. The upper layer of Zone H has a relatively lower resistivity characteristic than the lower layer. Based on the uniform low chargeability signature, this Zone H can be interpreted to have a scarce (to none) concentration of sulfide minerals, thus, low mineralization potential. Within Zone H, the low resistivity zone (< 15 ohm-m) at the 200 m mark is inferred to be a localized clayey lithology of the Tumbaga Formation. To further investigate the lateral continuity of the mineral potential in the study area, east-west-trending 2-D resistivity, and chargeability models were prepared and analyzed.

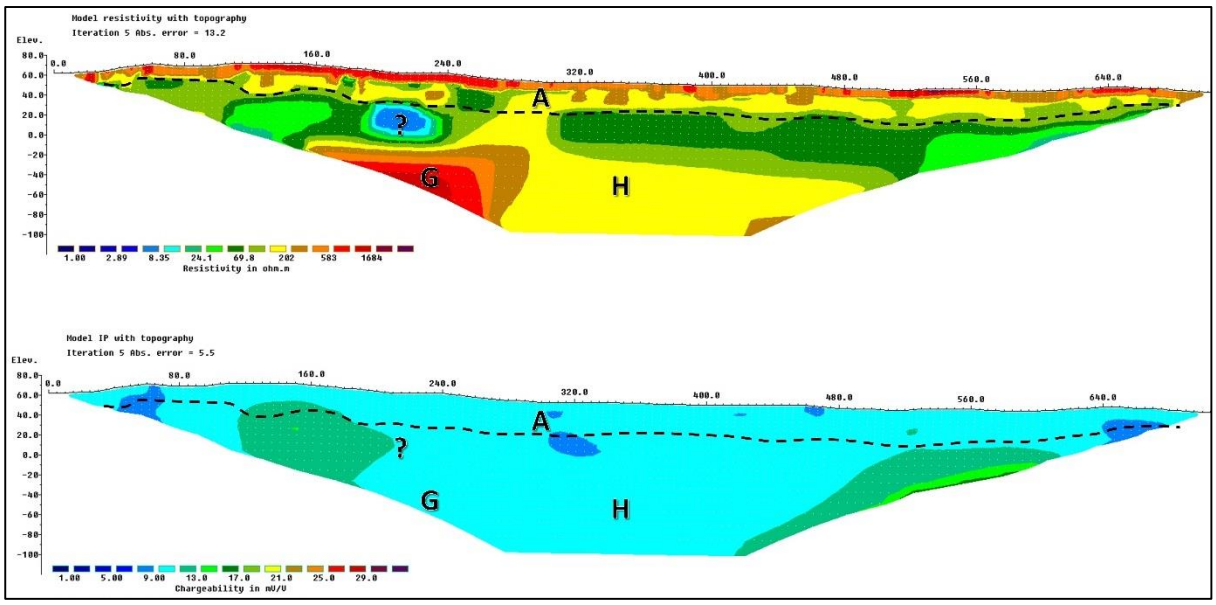

Figure 3-41. *2-D resistivity and induced polarization inverted model sections of Profile J-J'.*

3.5.2.1.11 ER-IP Profile K-K'

Profile K-K' has an east-west orientation located on the northwestern side of the study area (Fig. 3-42). The uppermost layer (Zone A) is interpreted as the pyroclastic overburden (Labo Volcano Complex). The thickness of Zone A generally decreases from the west (45 m thickness) to the east (20 m thickness). Mark 100 m has the thickest interpreted overburden. Moderate to high resistivity (> 15 ohm-m) and low chargeability (< 15 mV/V) values characterize Zone A. A low resistivity zone (Zone B), with a corresponding high chargeability signature, was noted on the eastern portion of the 2-D model, indicating clayey pyroclastic deposits (e.g., fine-grained tuff) within the overburden. The anomalous low resistivity patches are noted in the 100m and 130 m marks at 30 m and 20 m depths, respectively.

Within the lower layer, the moderate resistivity (15 to 350 ohm-m) and high chargeability (> 25 mV/V) zones were interpreted as Tumbaga Formation with a high concentration of disseminated sulfides (Zone C). These anomalous high chargeability regions were observed in the 160 m mark and between 420 m to 610 m marks. The average depth to the surface of these areas of interest is 30 m. Very high resistivity and moderate chargeability signatures were noted on the central part of the 2-D resistivity section. This layer is interpreted as a sill of intrusive rock (possibly Tamisan Diorite). This concordant igneous structure (sill) was noted between 190 m to 320 m marks with an average depth of 25 m. The concentration of disseminated sulfides (high chargeability) can be attributed to the hydrothermal alteration and mineralization brought by the interpreted intrusive rock (high resistivity) in the section.

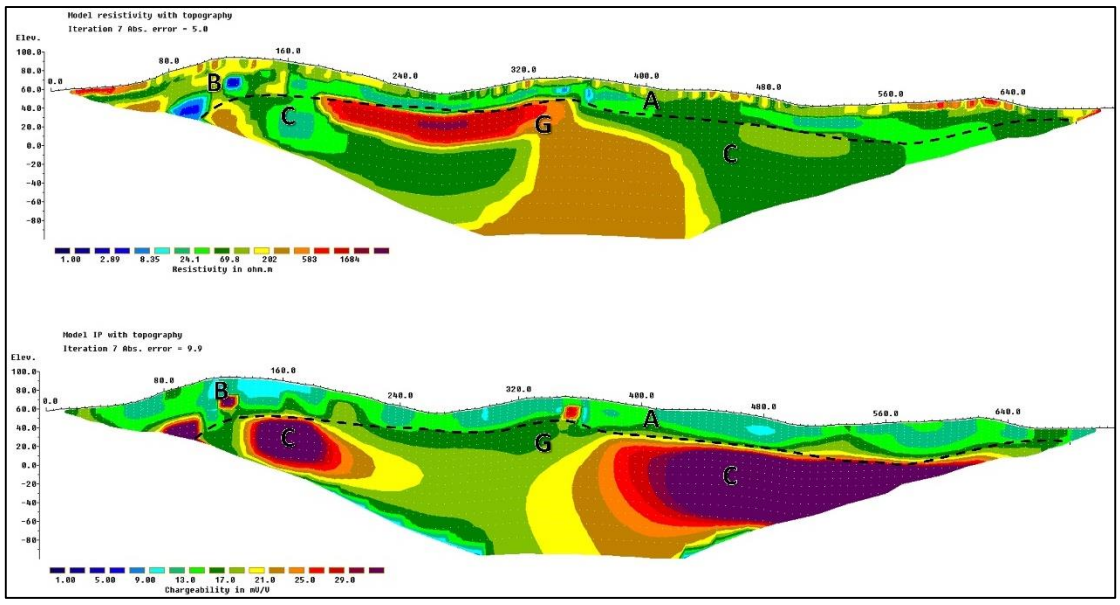

Figure 3-42. *2-D resistivity and induced polarization inverted model sections of Profile K-K'.*

3.5.2.1.12 ER-IP Profile L-L'

The east-west oriented Profile L-L' is located on the northeastern side of the study area. The 2-D resistivity profile is generally characterized by four distinct geoelectric zones (i.e., A, C, D, E) (Fig. 3-43). These anomalous zones have corresponding chargeability values. The first layer is defined by moderate resistivity (15 to 350 ohm-m) and low chargeability (< 15 mV/V), interpreted as the Labo Volcanic Complex (Zone A). This section's overburden thickness (Zone A) varies from 10 to 45 m; it thickens from west to east. Low resistivity zones are also absent in this profile, indicating a semi-homogenous composition of the Labo Volcanics overburden (without clayey lithology).

At greater depths, a relatively low resistivity marks the lower boundary of Zone A. Zone C has moderate resistivity (15 to 350 ohm-m) and high chargeability (> 25 mV/V), indicating a higher concentration of sulfide minerals in the Tumbaga Formation. The chargeability values gradually increase to the eastern side of the profile. A high resistivity anomaly with corresponding high chargeability was noted at the deeper portion (Zone D) of the 2-D resistivity model profile. This signature indicates a highly silicified rock (due to high resistivity) with disseminated sulfide minerals (due to high chargeability). It is worth noting that highly resistive intrusive rocks were interpreted in the adjacent profiles within the study area. Zone E is represented by low resistivity and high chargeability anomaly. This behavior is typical for an oxide zone with native copper mineralization (e.g., black ferruginous clay), which was reported in some mining areas.

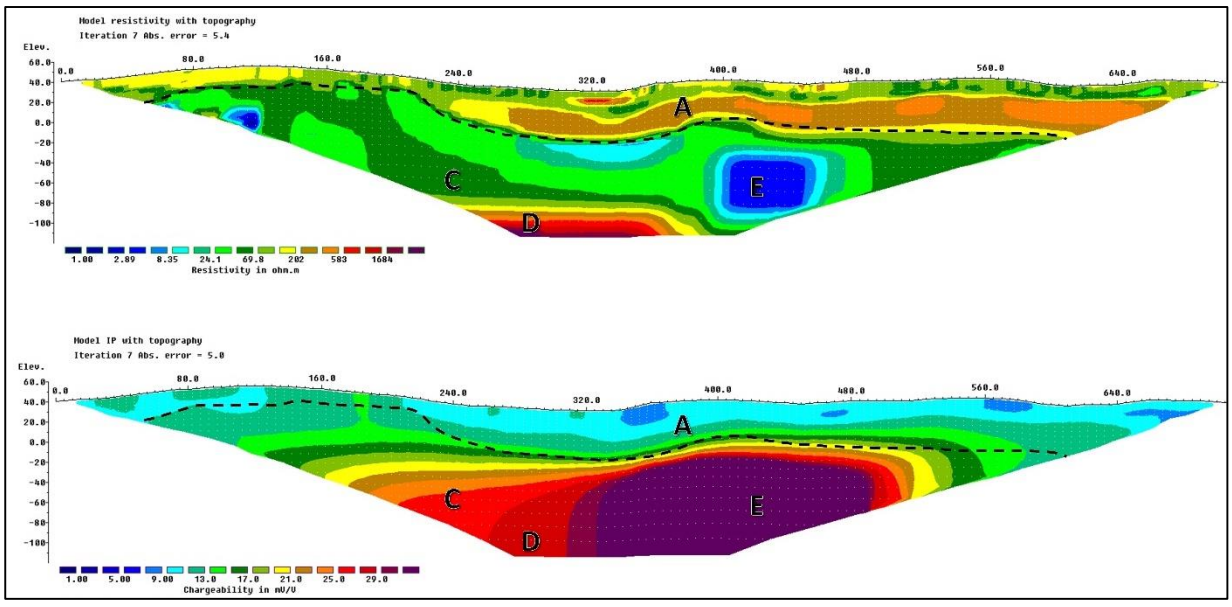

Figure 3-43. *2-D resistivity and induced polarization inverted model sections of Profile L-L'.*

3.5.2.1.13 ER-IP Profile M-M'

Two geoelectric layers characterize the east-west trending profile in the southwestern part of the study area (e.g., Zone A, Zone H) (Fig. 3-44). The first zone generally represents moderate resistivity values (15 to 350 ohm-m) with some high resistivity signatures (350 to 100 ohm-m) patches. This zone has consistently low chargeability (< 15 mV/V). This top layer is interpreted as Zone A, characterized by the pyroclastic deposits of the Labo Volcanic Complex. Zone A's thickness is uniform at around 20 m. The absence of low resistivity (clayey) regions indicates a relatively homogenous overburden composition.

Zone H, interpreted as the barren Tumbaga Formation, is also characterized by moderate resistivity (15 to 350 ohm-m) and low chargeability (< 15 mV/V) values. The upper geoelectric layer of Zone H has a relatively low resistivity signature (69 to 202 ohm-m) and a thickness of around 40 to 45 m. The depth to the surface of the lower, more resistive layer of Zone H is 60 to 80 m. The difference in resistivity signatures can be attributed to the clay content and degree of induration of the Tumbaga Formation. Furthermore, it can also be observed that there is a horizontal discontinuity of the chargeability values roughly located at 210 m from the first electrode. These relatively high chargeability and low resistivity zones are located at the approximate intersection between Profile F-F' and Profile H-H', where a small anomalous zone was interpreted as a highly oxidized and mineralized portion of the Tumbaga Formation. This interpretation could also be related to the chargeability discontinuity in this profile. This zone can be a potential area of interest within this profile for further exploration.

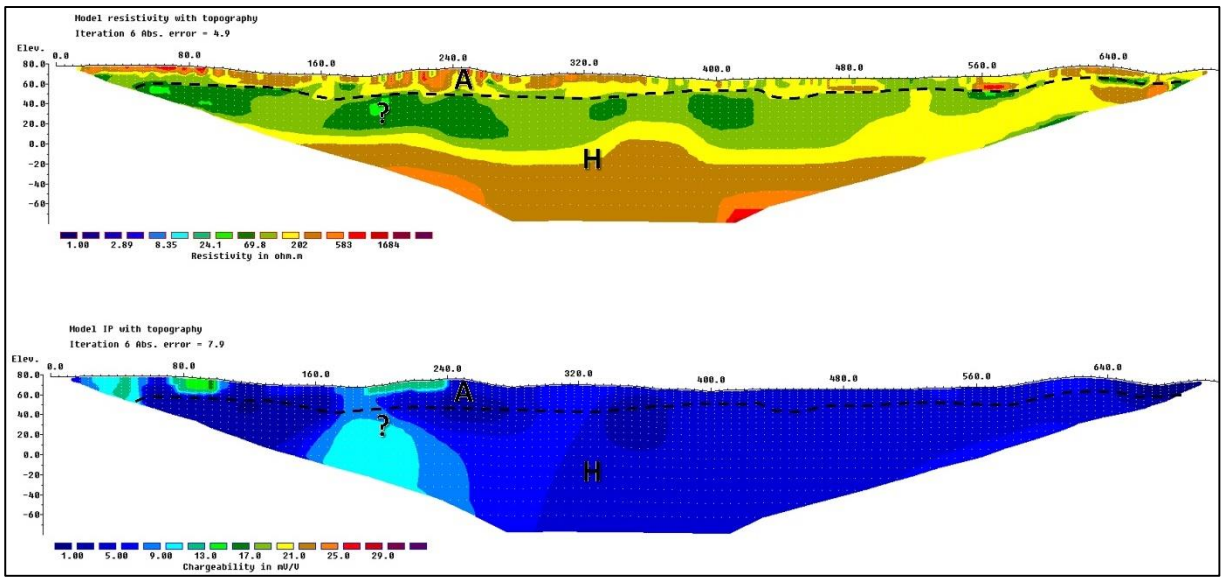

Figure 3-44. *2-D resistivity and induced polarization inverted model sections of Profile M-M'.*

3.5.2.1.14 ER-IP Profile N-N'

In profile N-N', three distinct resistive zones were interpreted (Fig. 3-45). This profile is located on the southeastern side of the study area and is oriented east-west. The 2-D resistivity model shows a moderate to high (15 to 350 ohm-m) geoelectric layer overlaying a relatively lower resistivity layer (green portion). Low resistivity patches were not observed within Zone A, indicating an absence of clayey lithology of the overburden (Labo Volcanic Complex). The thickness of the overburden varies from 30 to 20 m; it thins out from west to east.

Below Zone A, a high resistivity anomaly zone (> 350 ohm-m) with a low chargeability signature occurs from 240 to 340 m along the profile. This anomaly is represented by Zone B and interpreted as an intrusive rock (probably Tamisan Diorite). The depth to the surface of Zone B is around 100 m. Moderate resistivity (15 to 350 ohm-m) and low chargeability (< 15 mV/V) values represent Zone H. This zone is interpreted as Tumbaga Formation without a significant concentration of sulfide minerals. The anomalously high chargeability zones were not observed in the 2-D IP models section indicating an absence of mineral potential in this area. The rough estimate of the spatial distribution of the mineral potential is also reflected in individual interpretations of the resistivity and IP model profiles. The analysis of these east-west sections (Profile K-K' to Profile M-M') also elucidates the lateral continuity of the anomalous zones and strengthens the notion that the potential mineralized zones are concentrated on the northern and eastern sides of the study area.

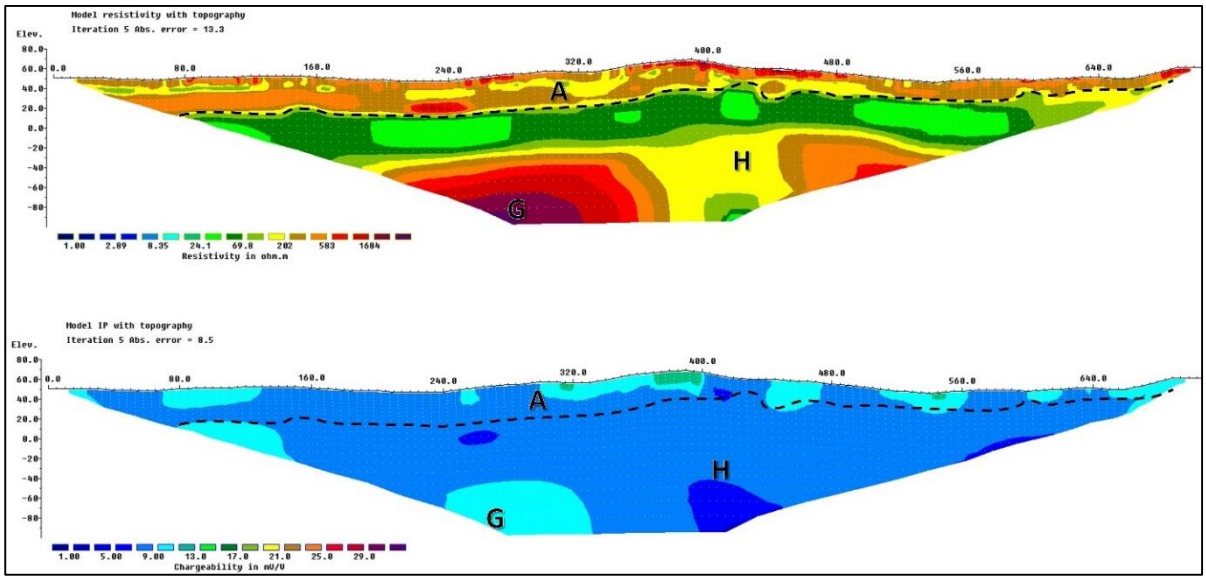

Figure 3-45. *2-D resistivity and induced polarization inverted model sections of Profile N-N'.*

3.5.2.1.15 ER-IP Profile O-O'

Profile O-O' has a north-south orientation and is located on the western side of the calibration area (Fig. 3-46). The uppermost layer (Zone A) represents the Labo Volcano Complex (pyroclastic overburden). The thickness of Zone A generally decreases from south (45 m thickness) to north (20 m thickness). Mark 100 m has the thickest interpreted overburden. Moderate to high resistivity and low chargeability (< 15 mV/V) values characterize Zone A.

The lower layer is characterized by low to moderate resistivity signatures with varying chargeability values. Black lines represent the approximate drill holes from the publicly released drilling report of Mt. Labo Exploration and Development Company (Gordon et al., 2016). Please note that the distance of the drillings from the model sections is from 20 to 80 m. Within the lower layer, the moderate resistivity (15 to 350 ohm-m) and high chargeability (> 25 mV/V) zones were interpreted as Tumbaga Formation with a high concentration of disseminated sulfides (Zone C). Relatively high concentrations of Gold (0.4 ppm), Iron (6.4 %), and Copper (1.6 %) were reported from the depth of 104 m of the drill core MDH-068. (Appendix 7). A low resistivity zone (Zone E), with a corresponding high chargeability signature, was noted on the southern portion of the 2-D resistivity and IP models. These anomalous zones indicate distinctive ferruginous clay deposits (e.g., native copper mineralization) within the oxidized zone. The potential mineralized zones are noted at the 160m and 330 m marks at a depth of around 20 m. Very low chargeability and resistivity anomalies were also noted at the central part of the section (Zone F). This zone is interpreted as a hematite-rich zone with very low chargeability characteristics.

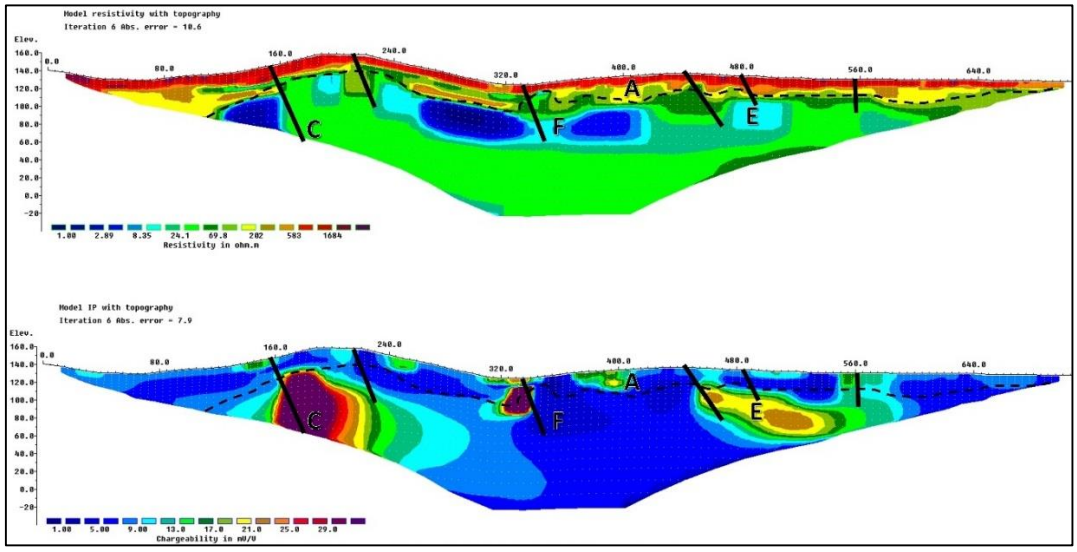

Figure 3-46. *2-D resistivity and induced polarization inverted model sections of Profile O-O'.*

3.5.2.1.16 ER-IP Profile P-P'

Profile P-P' shows the results of the ER-IP surveys in the eastern portion of the calibration area (Fig. 3-47). It trends north and has a varying elevation of around 120 to 160 masl. Zone A generally represents moderate to high resistivity and low chargeability layer (< 15 mV/V). The Labo Volcanic Complex layer (Zone A) thickness in this section varies from 40 to 65 m. Patches of low resistivity values are present in this section representing clayey pyroclastic deposits. A thick high resistivity stratum is also evident in the southern area.

The 2-D IP model shows a variable chargeability distribution in the bottom layer (i.e., Zone E, Zone H). High IP values were noted at around 240 m and 340 m marks which presents potential zones of mineralization. A fault structure was interpreted at the 160 m mark due to the linear and vertical anomaly shown in the 2-D resistivity model section. The Mt. Labo Exploration and Development Company (Gordon et al., 2016) also reported a fault structure around this area. Zone E represents massive sulfides along clayey fractured areas or native copper mineralization. For example, this anomaly was reflected by the high concentration of gold (0.2 to 2.6 ppm), iron (4.3 to 62.5 %), and copper (0.6 to 2.4 %) in drill hole 057 at a depth of 89.5 m to 279.8 m (Appendix 7). Please note that drilling exploration is concentrated only at the southern part of the profile; the distance of the drillings from the model sections is from 15 to 65 m. Zone E was interpreted at depths 40 to 120 m based on the 2-D resistivity and IP models. Zone H was delineated at the 240 m and 410 m marks at a depth of around 80 m; it represents Tumbaga Formation without disseminated sulfide concentration.

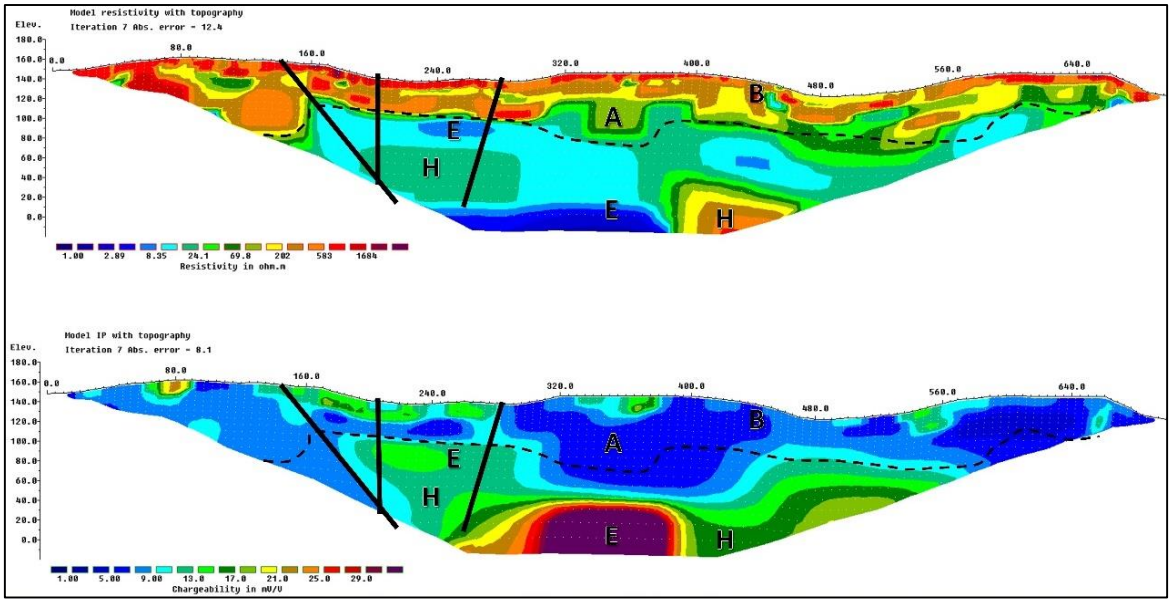

Figure 3-47. *2-D resistivity and induced polarization inverted model sections of Profile P-P'.*

Based on the sixteen 2-D ER-IP models (Fig. 3-32 to 3-47), the majority of the potential mineralized zones are represented by moderate resistivity (15 to 100 ohm-m) and high chargeability regions (> 25 mV/V) (Zone C). Zones C and D occurrences in the northern profiles (Fig. 3-32 to 3-36) are persistent at the end portion (beyond the 380 m mark) of the 2-D model sections. These two zones have variable depths (30 to 120 m) from the ground surface depending on the thickness of the overburden (Labo Volcanic Complex) (Table 3-7). Some model sections (e.g., Profile F-F', Profile G-G') show patches of low resistivity (< 15 ohm-m) anomaly with corresponding highly chargeable zones (>25 mV/V) (Zone E), which may indicate concentrated sulfide minerals along clayey and weathered, fractured zones. Zone E is generally distributed at the southwestern side of the study area at around 210 and 135 meters from the starting point of Profile F-F' and Profile G-G', respectively. These highly chargeable with low resistivity zones generally occurs at a relatively shallower depth of around 20 to 30 m.

Table 3-7 was prepared to characterize the location of the mineral potential in the study area. It summarizes the distribution of potential mineralized zones in the study area. The name of the profiles and the corresponding zones are shown in the table. Column 3 presents the distances from the starting point of the profile to the center of the anomalous zone; column 4 shows the depth to the surface of the zone.

Table 3-7 *Estimated distances and depths of the potential zones of mineralization.*

Profile name	**Zone name**	**Distance from the starting point of the profile to the center of the zone (m)**	**Depth to the surface of the zone (m)**
A-A'	C, D	270, 440	100, 60
B-B'	C	380	60
C-C'	C	430	50
D-D'	C	510	60
E-E'	C, C	190, 580	80,70
F-F'	E	210	20
G-G'	E	135	30
K-K'	C, C	160, 510	40, 30
L-L'	C, D, E	240, 290, 430	80, 120, 60
O-O'	C, F, E	90, 360, 490	40, 40, 30
P-P'	E, E	250, 350	40, 100

3.5.2.2 3-D Electrical Resistivity and Induced Polarization (ER-IP) models

3-D ER-IP inversions were implemented in the two blocks representing the high-mineralized (northern potion) and low-mineralized (southern potion) potential regions delineated from the results of the 2-D ER-IP investigations. Figure 3-48 shows the location of the blocks and examples of 3-D ER models.

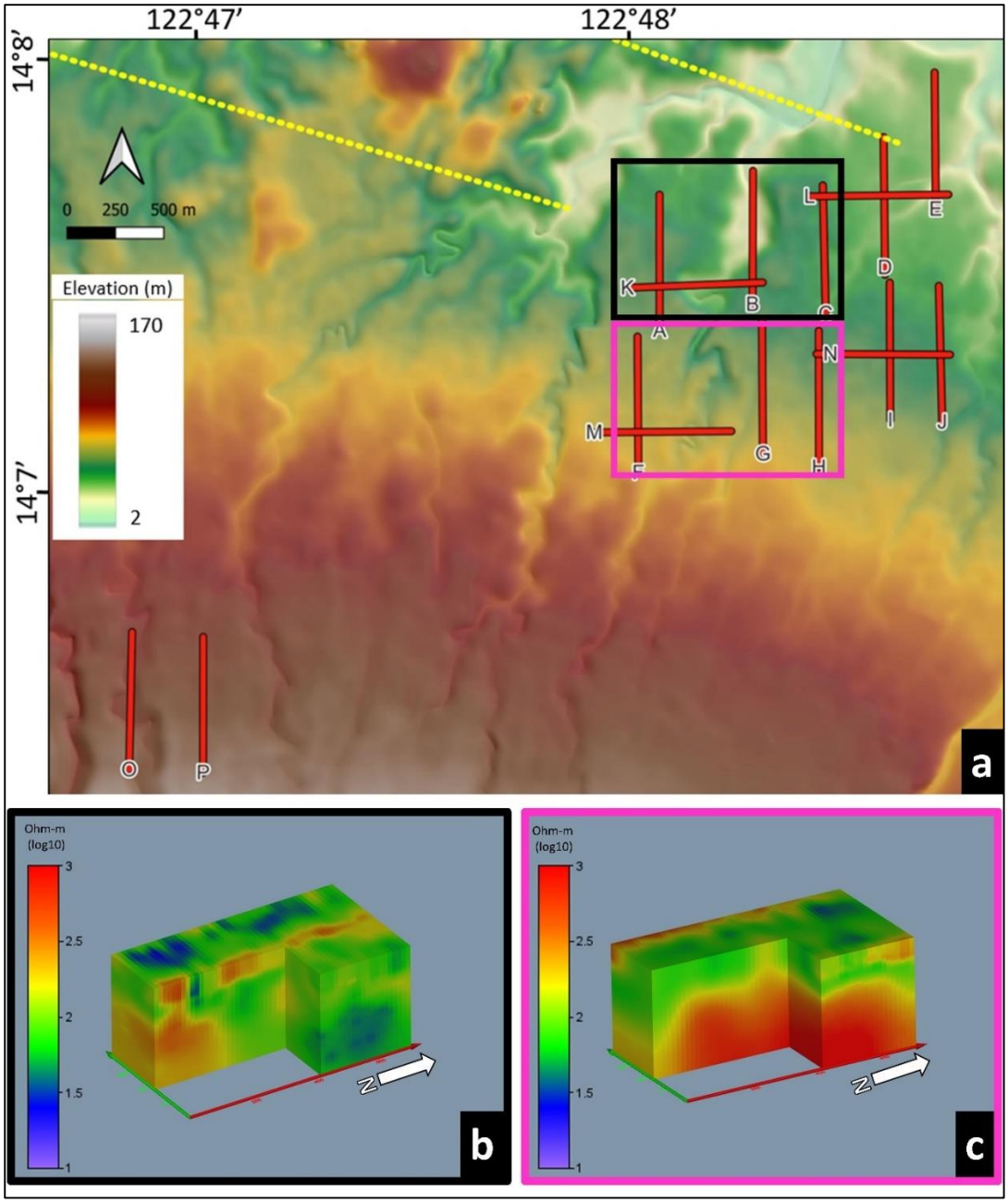

Figure 3-48. *(a) Location of the two blocks used in the 3-D inversion of ER-IP data. The (b) northern block (block box) indicates a more mineralization potential region compared to the (c) southern block (pink box) based on the initial results of the 2-D ER-IP inversion.*

The 3-D ER and IP models help understand the geometry of the potential mineralized zones by showing the 3-D spatial distribution of the promising zones (e.g., high chargeability). The individual interpretations of the 2-D ER and IP models were compared with the results of the 3-D ER-IP inversions (Fig. 3-49 to 3-52). The difference between the subsurface ER and IP anomalies in the northern and southern blocks was also noted based on the horizontal planes showing the resistivity and chargeability distributions (Fig. 3-53 to 3-56). The horizontal slices delineated the different zones corresponding to their anomalous resistivity and chargeability values. Although the fully 3-D ER survey is known to produce more accurate findings than 2-D surveys, the 3-D ER survey was not done due to the unavailability of specialized instruments and the very high survey cost. Instead, 3-D ER-IP models were generated from the combined parallel 2-D survey lines (Yi et al., 2001; Loke, 2012). Unlike the 2-D inversion, the inversion of 3-D ER and IP data uses 3-D mesh, allowing the 3-D variation (x, y, and z directions) of the ER and IP values during each iteration. The mesh spacing is fine on the surface and becomes larger as the distance increases from the electrodes. The growth factor 10 was chosen for the mesh; this means that the elements at the boundary are ten times as big as those at the surface (Blanchy et al., 2020). The solutions usually converged in 5 to 8 iterations.

The subsurface resistivity values from the result of the 3-D inversion were compared with the preceding 2-D inverted models. The features and thickness of the overburden (Labo Volcanic Complex) were reflected in the 3-D models. Also, the underlying anomalous zones are clearly shown in the 3-D ER and IP models (Fig. 3-49 to 3-52). The ER anomalies of the 3-D model in the northern block are complex. The overburden is thin, with patches of low-resistivity lenses representing Zone B. At shallower depth, the ER anomaly along the 2-D Profile A-A' is lower than the areas along B-B' (Fig. 3-49). At the deeper portion, the southwestern side of the 3-D model has higher ER anomaly than the northeastern side.

In contrast with the complex ER anomalies of the northern block, the southern block has simple resistivity distribution and thick overburden (Fig. 3-50). This resistivity signature is expected because the southern block is close to Mt. Labo, which has thick pyroclastic deposits. The shallower depth generally presents moderate to high ER anomalies, while the deeper depth shows a uniform high ER anomaly. The 3-D IP model in the northern block presents subsurface inhomogeneity (Fig. 3-51). The shallower portion has low to high chargeability values, while the deeper portion has moderate to high IP anomalies. On the other hand, the IP anomalies in the southern block are plain and lower than the northern block (Fig. 3-52). Generally, the 3-D resistivity and chargeability distributions are consistent with the 2-D ER-IP models.

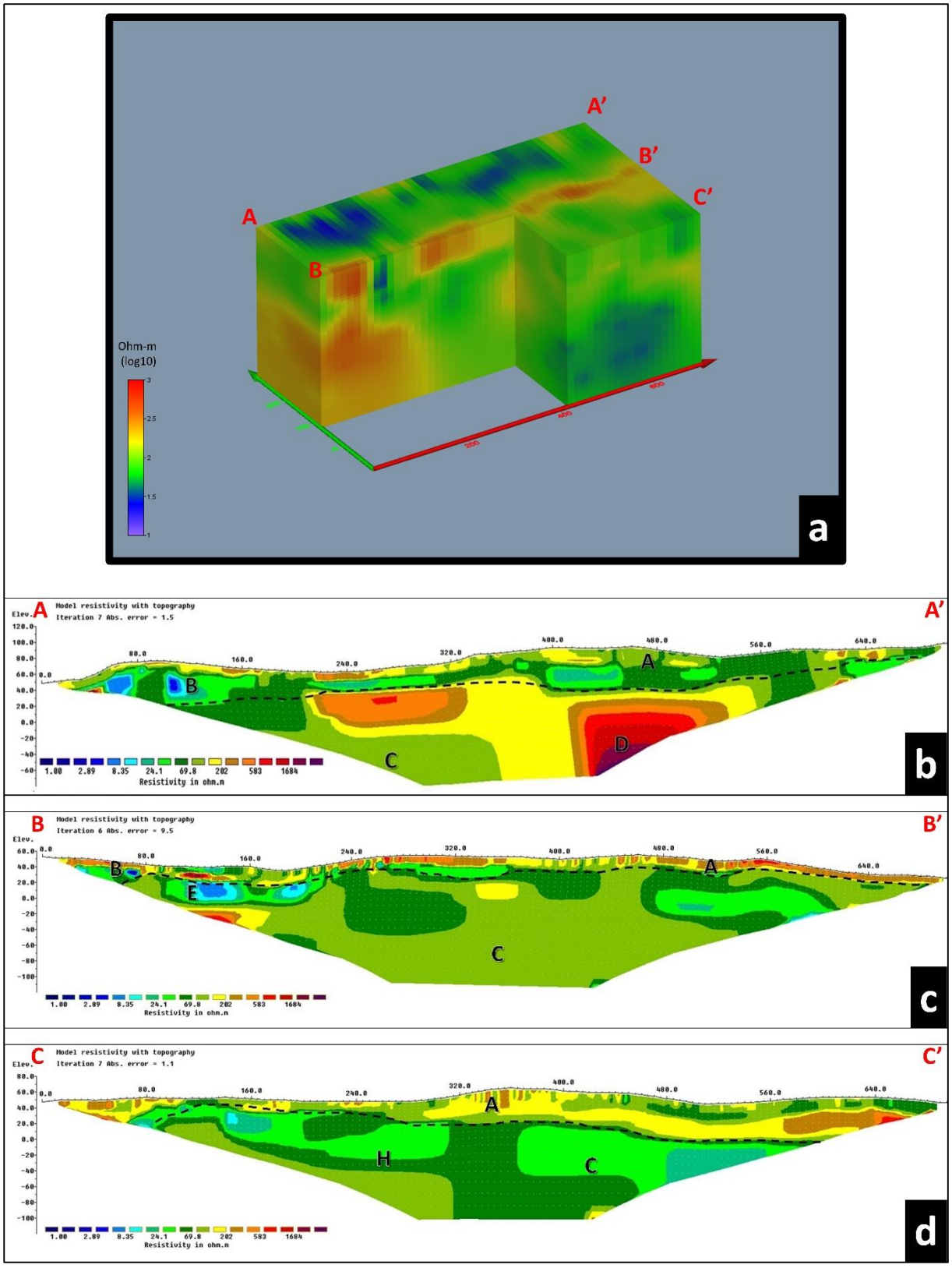

Figure 3-49. *Comparison of the (a) 3-D and (b, c, d) 2-D (A-A', B-B', C-C') ER inverted models in the northern block of the study area.*

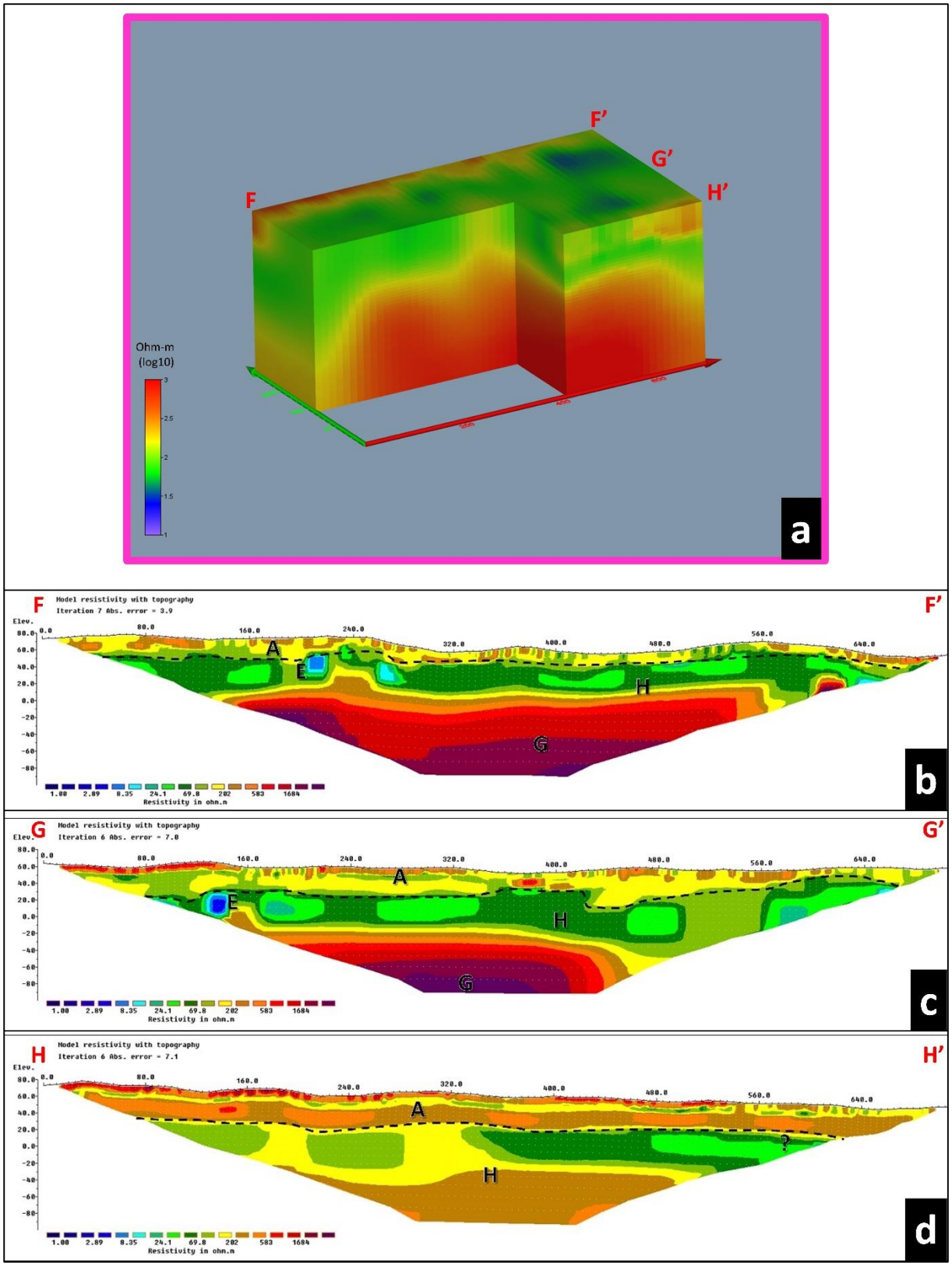

Figure 3-50. *Comparison of the (a) 3-D and (b, c, d) 2-D (F-F', G-G', H-H') ER inverted models in the southern block of the study area.*

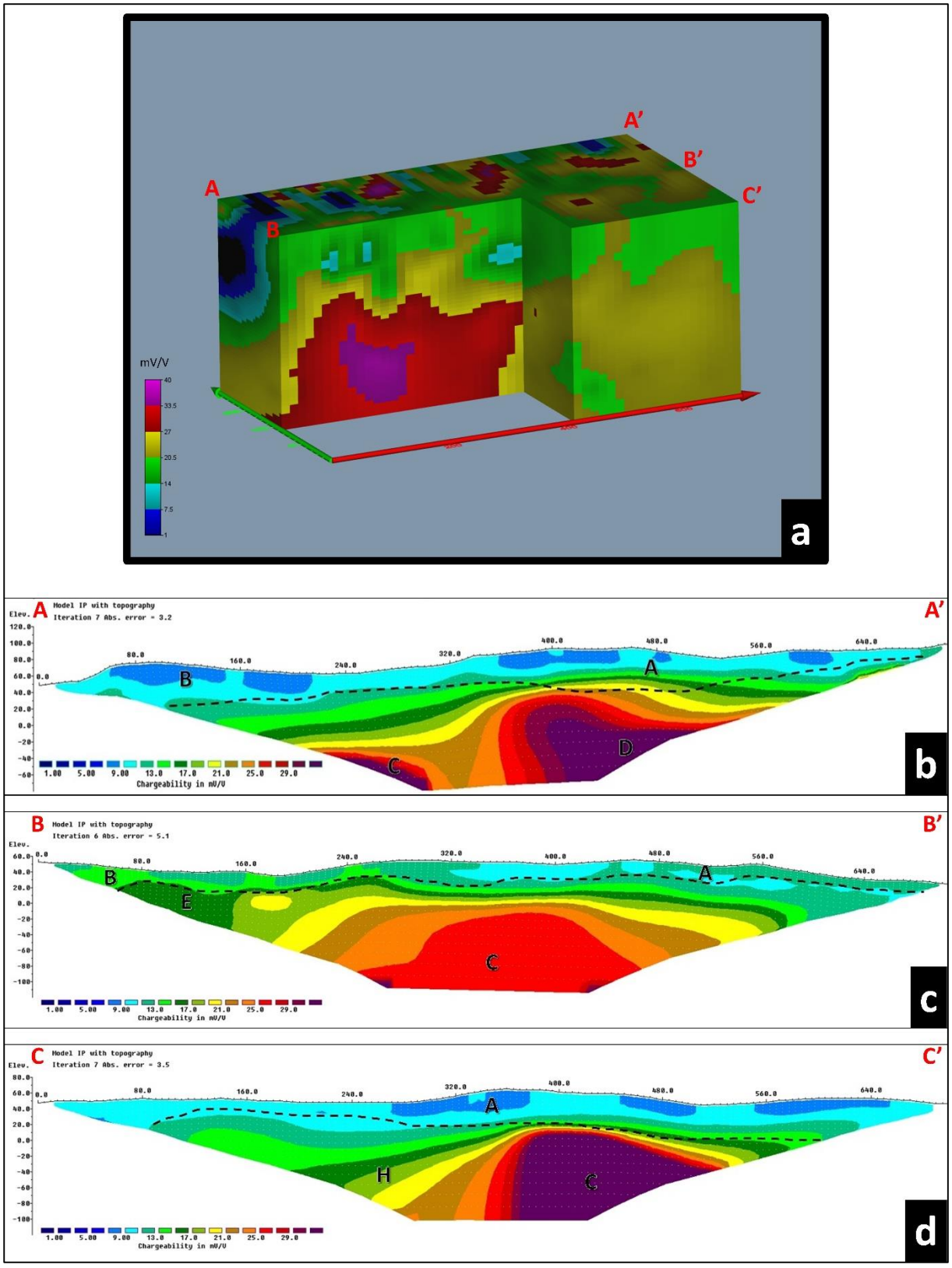

Figure 3-51. *Comparison of the (a) 3-D and (b, c, d) 2-D (A-A', B-B', C-C') IP inverted models in the northern block of the study area.*

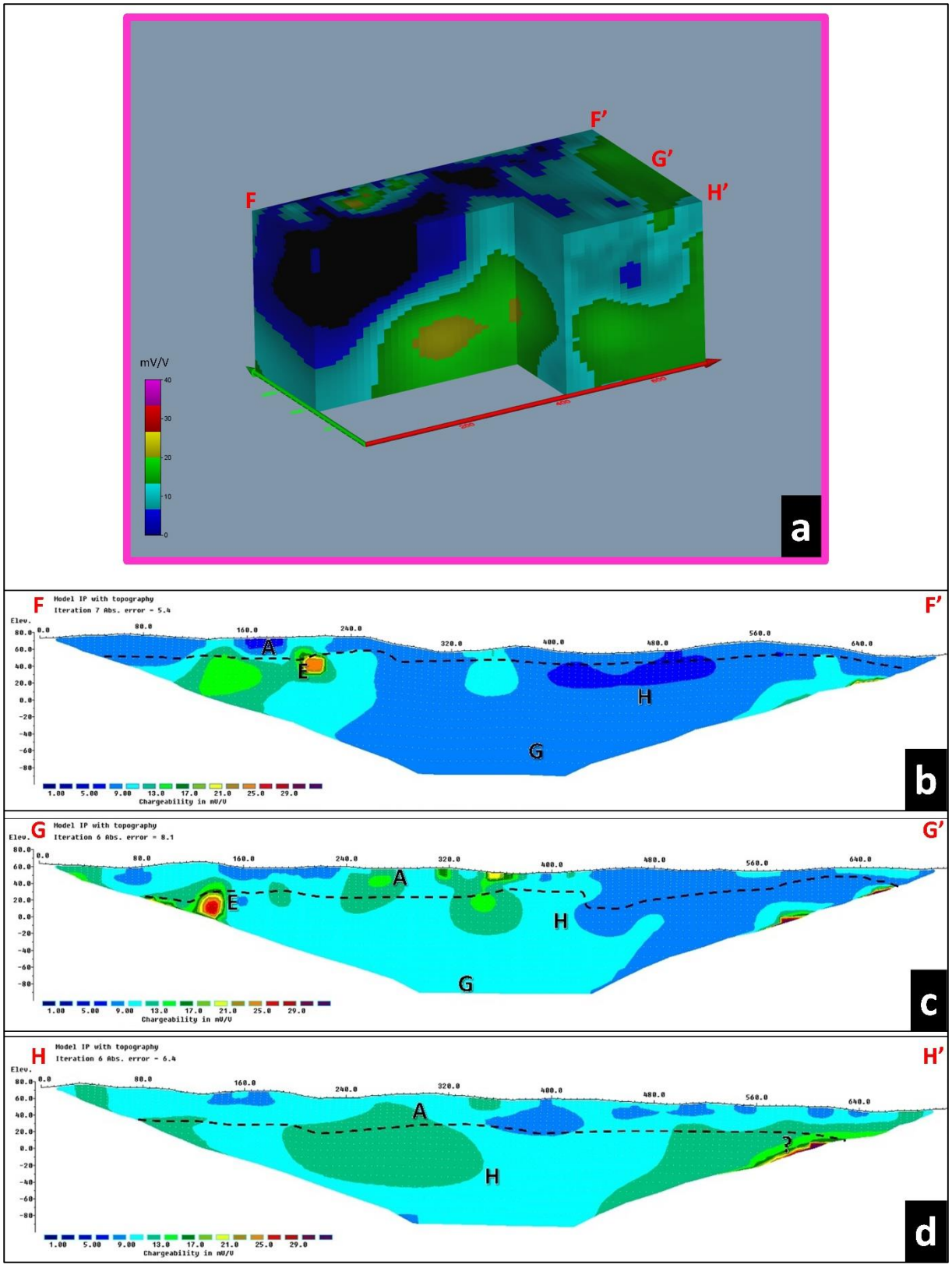

Figure 3-52. *Comparison of the (a) 3-D and (b, c, d) 2-D (F-F', G-G', H-H') IP inverted models in the southern block of the study area.*

Figures 3-53 to 3-56 depict the depth slices of both the resistivity and chargeability signatures for the northern and southern blocks at 50, 0, -50, -100, and -150 m depths. The majority of the area is characterized by background resistivity values (around 100 ohm-m) and relatively low chargeability (around 20 mV/V). Some high ER and IP zones appear until -100 m elevation. The 3-D ER-IP model is discussed in detail by showing the horizontal slices at various depths.

The horizontal planes representing the resistivity distribution in the northern block are represented in Figure 3-53. Zones A and B are apparent at the 50 m elevation representing the resistivity variation within the Labo Volcanic Complex. The low ER zones characterize the clayey lenses of the pyroclastic overburden. At the 0 m elevation, Zones A and B are not evident. Instead, this may represent the upper portion of the Tumbaga Formation as delineated from the 2-D ER-IP models. The high resistivity zone at the southern part of the model continues from east to west (Profile A-A' to C-C'). Also, the high resistivity zones are vertically consistent up to -100 m elevation. Figure 3-54 shows the IP depth slices in the northern block. Zone C represents the intermediate resistivity (15 to 350 ohm-m) with high chargeability (>25 mV/V) values delineated at the elevation of -50 to -100 m (white dashed line). High IP anomaly, which corresponds to a high concentration of disseminated sulfide minerals, are extensive in zones dominated by moderate to high resistivity. These are consistent with the interpretation and calibration of the 2-D ER-IP anomalies. The 3-D visualization also effectively presents the continuity of the ER and IP anomalous zones related to mineralization potential.

The resistivity (Fig. 3-55) and chargeability Fig. 3-56) depth slices in the southern block clearly demonstrate that moderate to high resistivity (> 100 ohm-m) and low chargeability (< 15mV/V) dominate the southern part of the study area. The horizontal slices at 50 and 0m elevation show a variable resistivity distribution. However, the resistivity increases with depth from -50 m up to -100 m elevation characterizing Zone G (based on the 2-D ER-IP model investigation). Zone G becomes broader as the depth increases. Based on the low chargeability values in the 3-D IP model slices, the sulfide mineralization potential is not promising in the southern block. Zone G has very low chargeability (<15 mV/V), extending from 50 m elevation to -100 m elevation. However, a relatively high chargeability zone was noted on the northern side of the 3-D ER-RP model at -100 m depth, which may indicate an area of interest with considerable sulfide mineral concentration (e.g., pyrite, chalcopyrite).

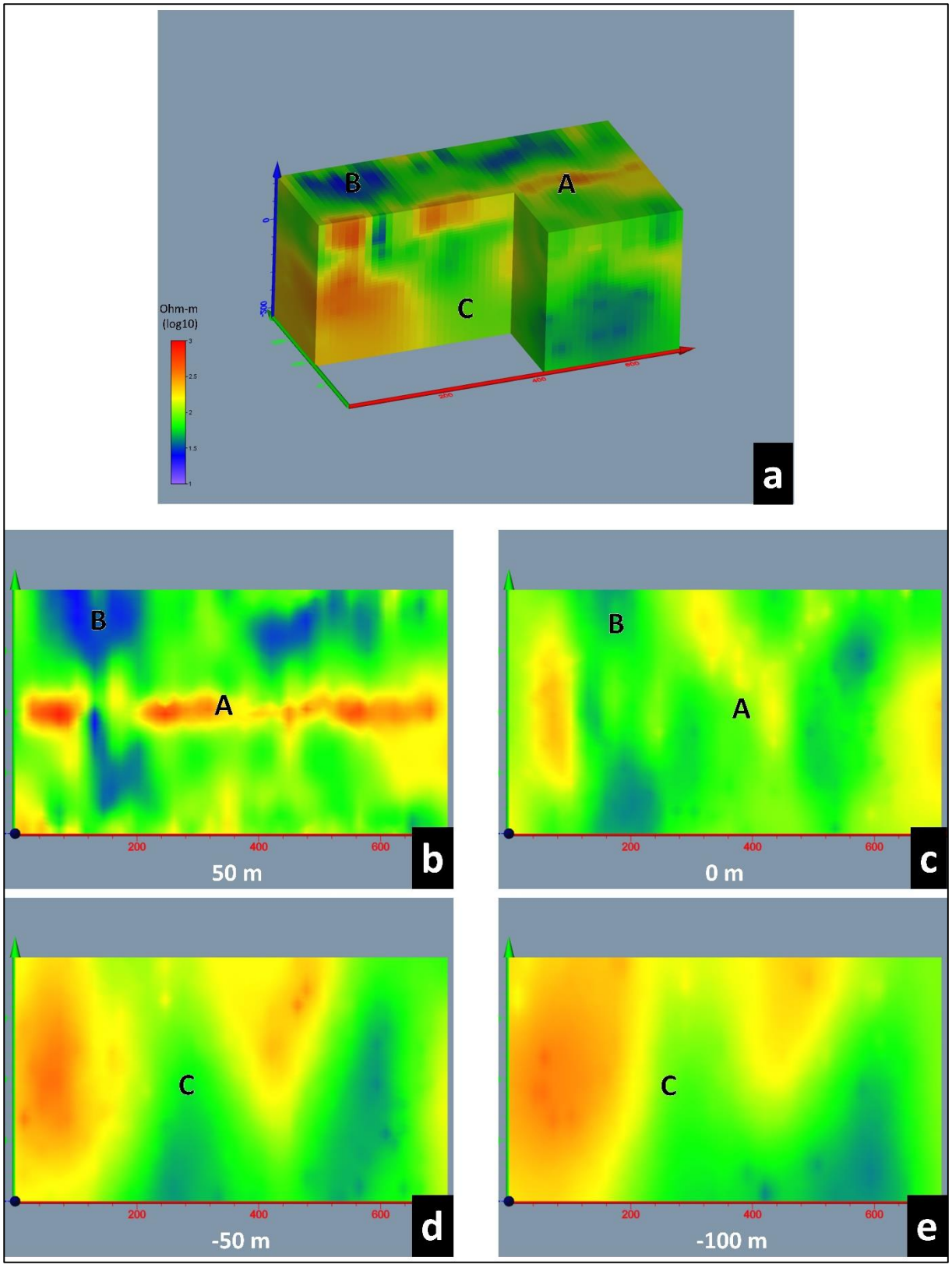

Figure 3-53. *Horizontal slices of the 3-D inverted ER model of the northern block at elevations of 50, 0, -50 and -100 m. The letters represent the zones of deduced subsurface lithological units.*

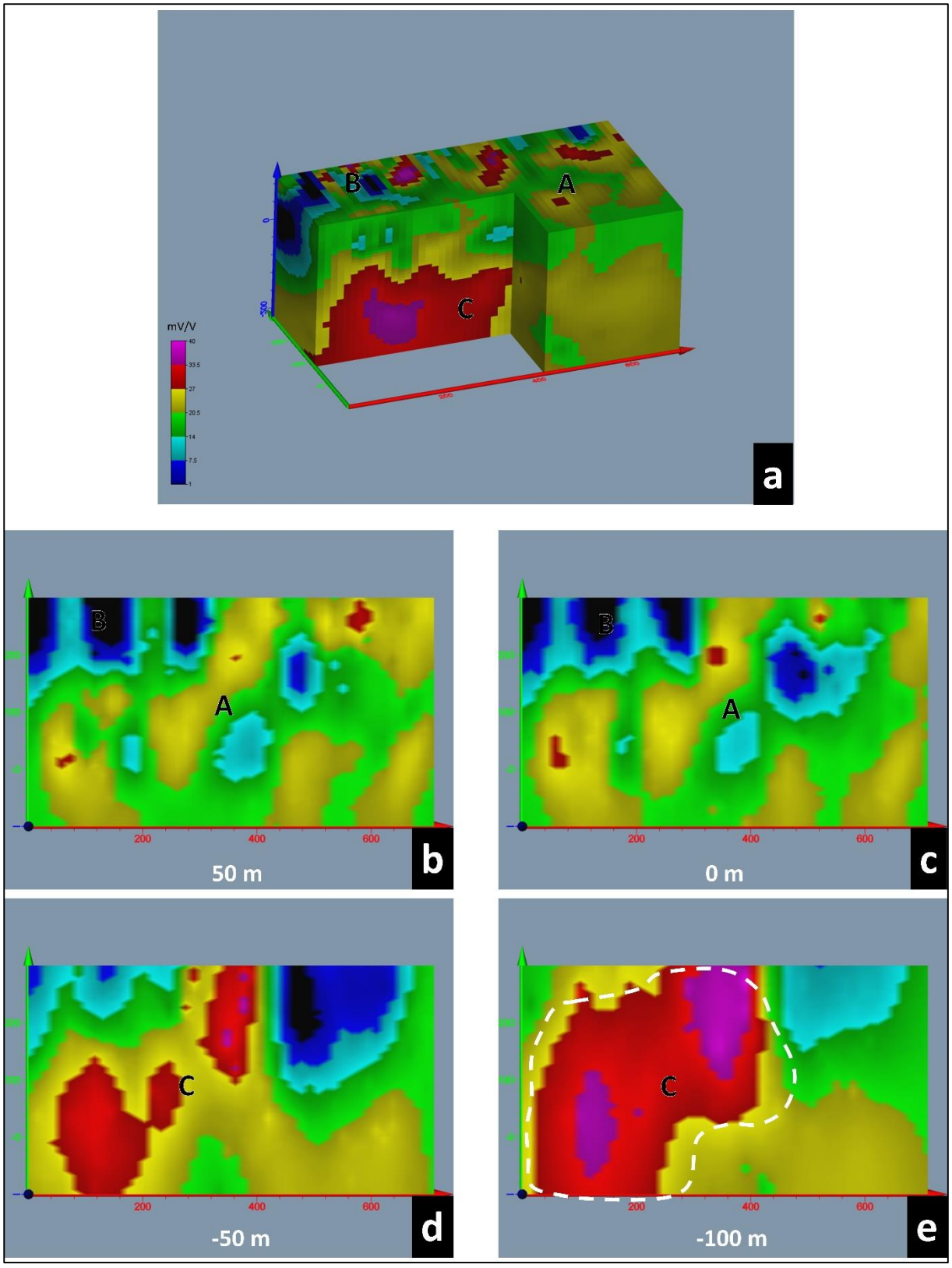

Figure 3-54. *Horizontal slices of the 3-D inverted IP model of the northern block at elevations of 50, 0, -50 and -100 m. The letters represent the zones of deduced subsurface lithological units.*

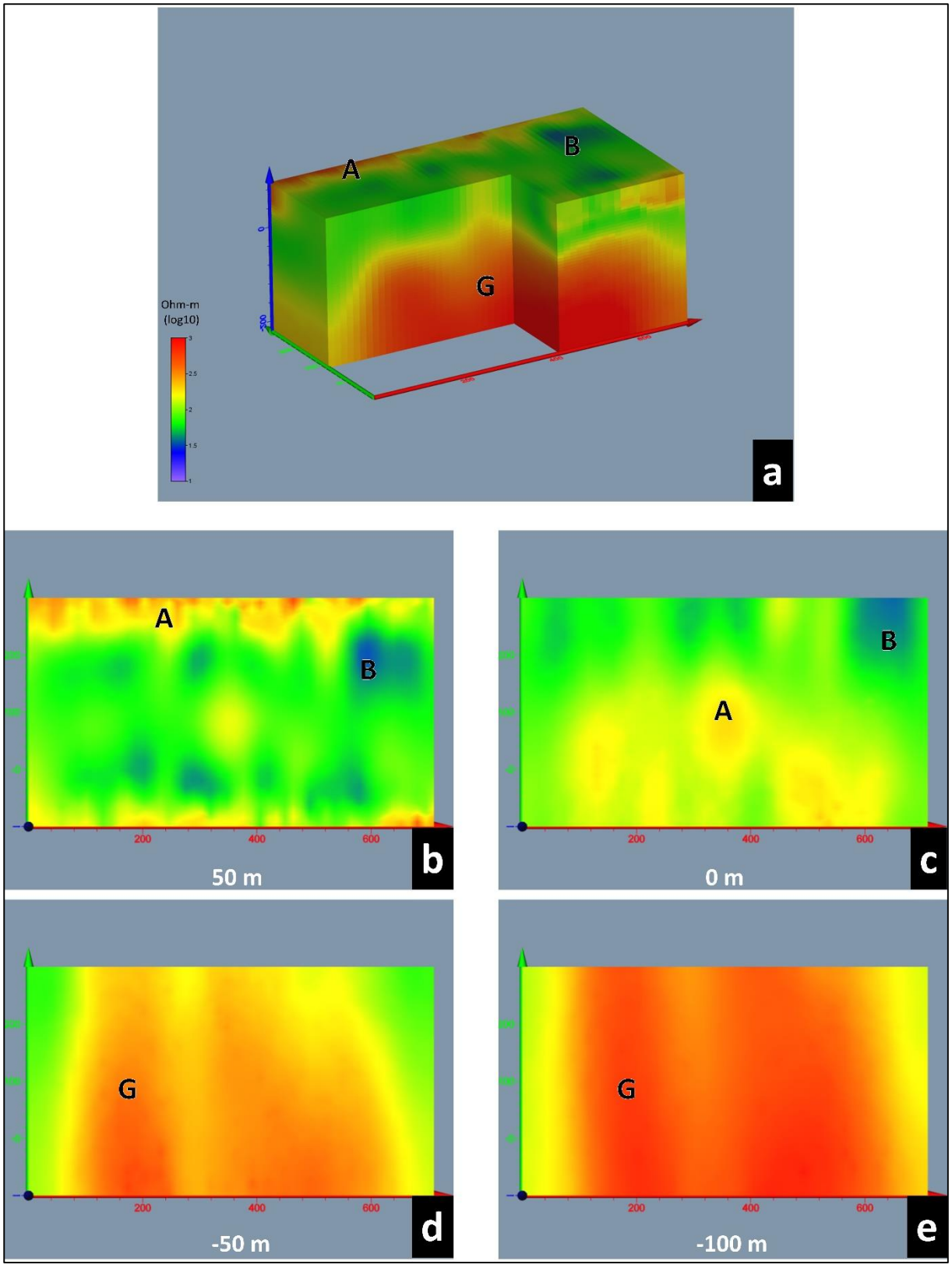

Figure 3-55. *Horizontal slices of the 3-D inverted ER model of the southern block at elevations of 50, 0, -50 and -100 m. The letters represent the zones of deduced subsurface lithological units.*

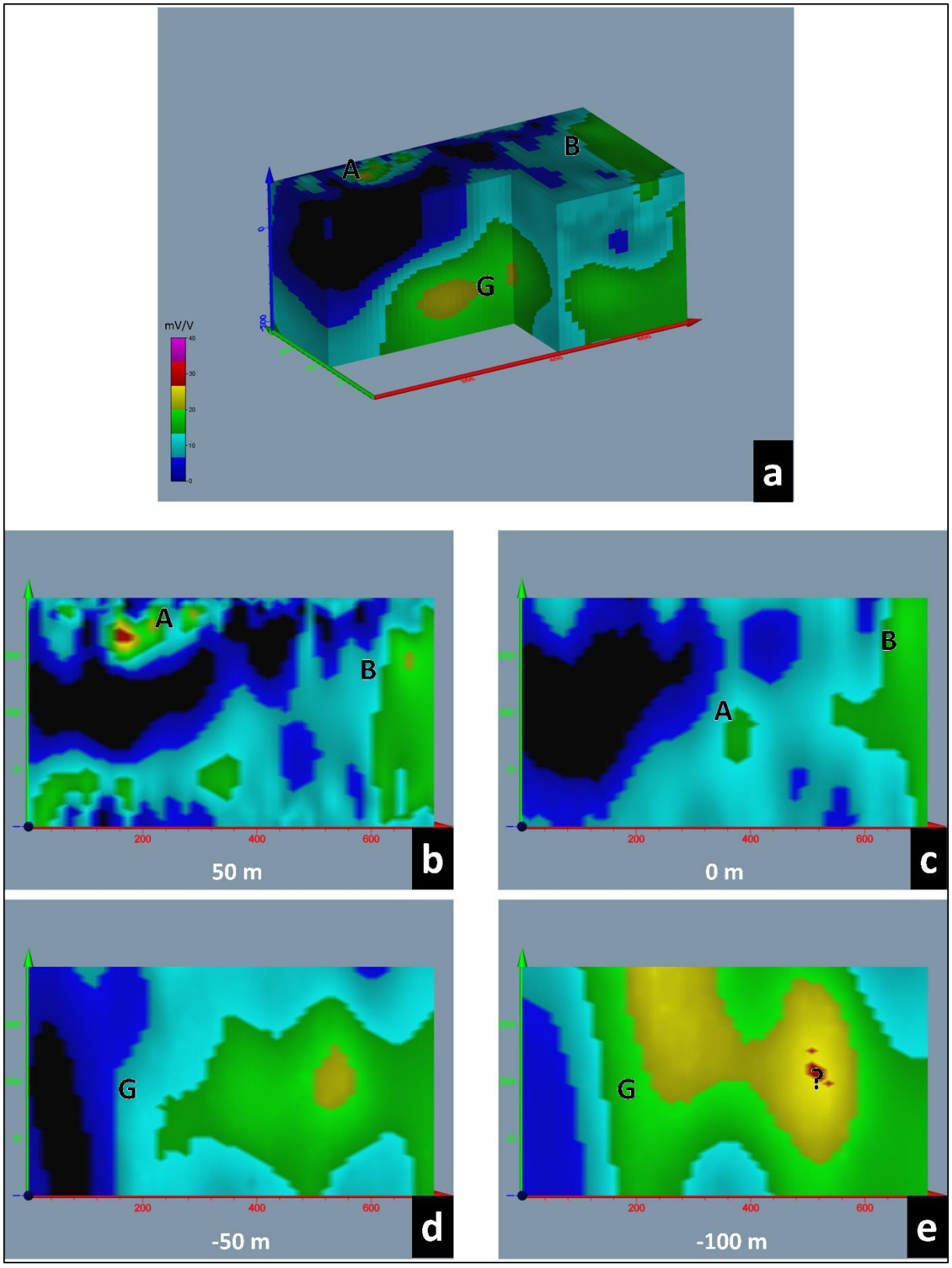

Figure 3-56. *Horizontal slices of the 3-D inverted IP model of the southern block at elevations of 50, 0, -50 and -100 m. The letters represent the zones of deduced subsurface lithological units.*

The 3-D ER-IP models provide prominent features and geometry of the potentially mineralized zones. These models allow the delineation of anomalous zones of interest in the study area (Zone C). The isosurface of the high chargeability zones (25 mV/V) was plotted on the 3D chargeability model in the northern block (Fig. 5-37a). The 25 mV/V-isosurface was also presented with the 3-D resistivity model to asses the 3-D geometry of the zone of interest with its corresponding resistivity values (Fig. 5-37b). The 3-D model shows that the high chargeable zone generally coincides with moderate (Zone C) to high (Zone D) resistivity zones. The high chargeability (25 mV/V) isosurface presented that the distribution of the anomalous Zone C is concentrated on the northern block's central portion at around 50 m. The high chargeability isosurface plot also revealed the anticlinal feature, which could be related to a mineralization structure. From the geological and geophysical information, the characteristics of the anomalous zones may suggest structure-related mineralization (e.g., faults, folds). This type of mineralization localization is common in epithermal-porphyry-type deposits (e.g., Sillitoe, 2010; Evrard et al., 2018).

The 3-D inversion of the resistivity and IP data demonstrated and confirmed that the two distinct high chargeable zones dominantly cause the anomaly (e.g., Zones C and D). The two highly chargeable zones have variable resistivity (> 100 ohm-m) values and extend to the elevation of -100 m. Zones C and D were also visible on the 2-D ER-IP models (e.g., Fig. 3-49), and the connection of these two zones was apparent at the elevation of -100m (Fig. 3-54). It is also evident that Zone C is the most extensive anomaly, representing the promising zone of mineralization in the study area. This manifestation explains the appearance of one huge, highly fractured mineralized feature (Zone C) on the conceptual model (Fig. 3-58).

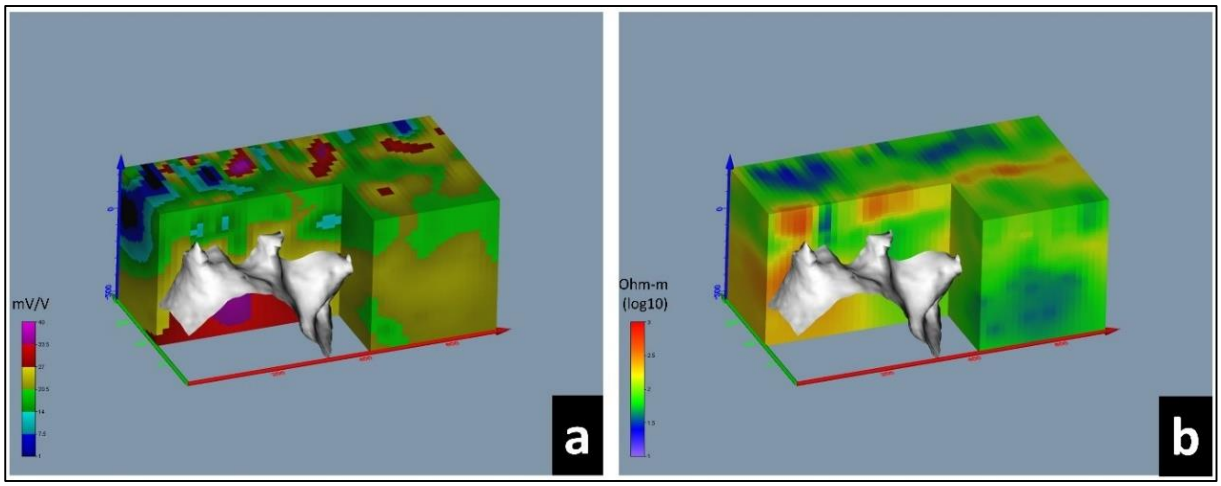

Figure 3-57. *High chargeability isosurface (25 mV/V) plotted together with the 3-D (a) IP and (b) ER models.*

3.6 Combined Geophysical Interpretation

The schematic conceptual model based on geological and geophysical information is shown in Figure 3-58. Faults, which may be attributed to the mineralization, were interpreted from the VLF-EM results and the 2-D and 3-D resistivity models. Some conductive clay lenses of the Labo Volcanic Complex were also demarcated from the Karous-Hjelt current density section of VLF-EM data. Based on the 2D and 3D ER-IP models, the topmost layer (Zone A) has a variable thickness of around 10 to 45 m. The thickest part can be observed at the southern side of the study area (near the Mt. Labo Crater). This interpreted thickness is in accord with the reported thickness of the Labo Volcanic Complex (MGB, 2010). The 2-D resistivity and IP models present a clear boundary between the overburden and underlying lithology; the geophysical signatures (ER-IP values) of the younger Pleistocene Labo Volcanic Complex (overburden) are distinctive from older Eocene Tumbaga formation.

Zone A is generally characterized by moderate to high resistivity (> 15 ohm-m) and low chargeability (< 15 mV/V) values in the resistivity and IP model sections, respectively. Within Zone A, low resistivity zones (<15 ohm-m) (Zone B) were observed in some model sections corresponding to clay lenses (e.g., weathered argillaceous tuffs) of the Labo Volcanic Complex (overburden). Zones C to H underlies the Labo Volcanic Complex. The boundary between Zone A and the lower zones (e.g., Zone C, Zone H) is defined by the abrupt change of resistivity and, to some extent, changeability.

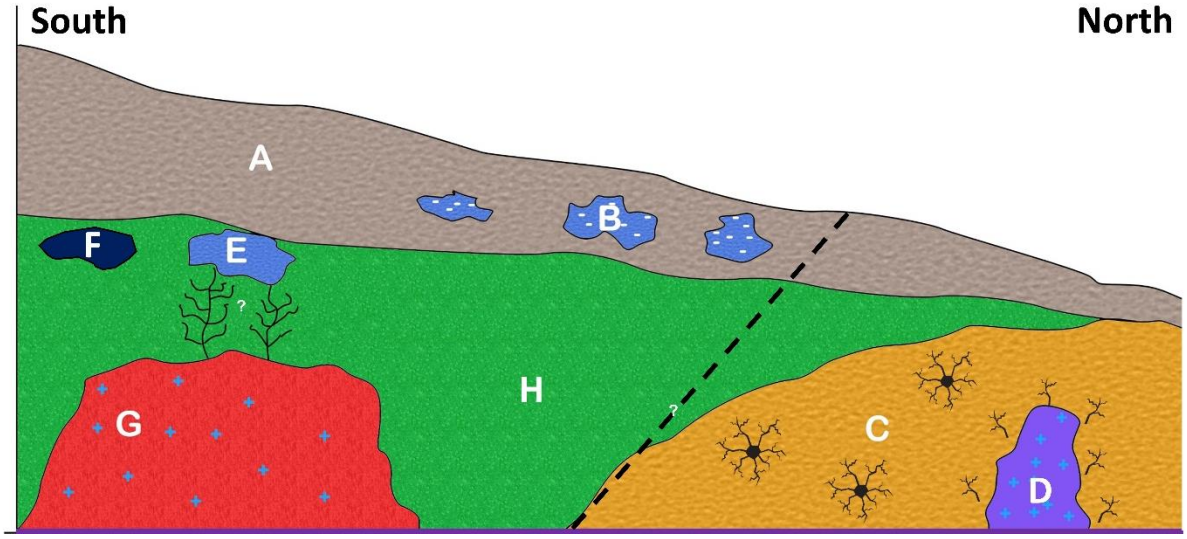

Figure 3-58. *A schematic section of the western part of the study area presenting a conceptual model of the spatial distribution of mineralization concerning the geological and geophysical data. White letters represent the deduced zones from ER-IP models. Note that Zone F is a special classification based on the anomaly observed at Profile O-O' in the calibration area only; this zone was not recognized in the main study area.*

The potential mineralized zones are represented by Zone C to F (Table 3-6). Zone C is defined as regions with moderate resistivity (15 to 100 ohm-m) and high chargeability (> 25 mV/V). It is interpreted as the Tumbaga Formation with a high concentration of disseminated sulfides (e.g., chalcopyrite, pyrite), which may indicate a potential zone of mineralization. Low resistivity and high changeability zones within Tumbaga Formation can be characterized by more clayey, fractured, and conductive zones of mineralized regions (Telford et al., 1990; Lowrie, 2007). For example, in Profile D-D, relatively low resistivity values (13 ohm-m) were noted within Zone C at different locations and depths (Fig. 3-35). This section interprets these lenses as prospective zones of mineralization (e.g., Cu-Au deposits). Another example is the low resistivity zone (question mark on the models) in Profile J-J' (Fig. 3-41). It presents a promising area for further investigation since it may indicate massive sulfides along localized clayey fractures. When it comes to unusually high IP distribution in the southern area, the anomalous changeability zones in Profile H-H' are ambiguously inferred as Tumbaga Formation with a higher concentration of disseminated sulfides (e.g., pyrite), but at least they could be prospective zones of mineralization in this section (Fig. 3-39). Also, the exceptionally high chargeability (> 25 mV/V) zone in Profile L-L' could be attributed to a massive sulfide or native copper mineralization; the very low resistivity (< 3 ohm-m) values could be due to the clayey characteristic of the mineral deposit (Fig. 3-43). Unlike the other sections, Profile L-L' shows a remarkable resistivity and chargeability heterogeneity that may indicate potential mineralized zones. However, some sections present minimal and unusual occurrences of high chargeability zone in Zone C, which could be attributed to random noise (e.g., telluric noise).

Zone C is distributed in the study area's northern portions (Profile A-A' to E-E') and the calibration area's western side (Profile O-O'). It is also interesting to note that (during the field survey) there are reported shallow small-scale mining activities along Profile C-C' in the past. Zone D has distinct high resistivity (>100 ohm-m) and high chargeability (> 25 mV/V) anomalies. Zone D was noted at Profile A-A'. This anomalous zone may correspond to highly silicified rock (high resistivity) with disseminated sulfides (high chargeability). Zone E is defined by low resistivity (< 15 ohm-m) with a corresponding high chargeability signature (> 25 mV/V). This anomaly has a generally small and circular appearance. Zone E could indicate distinctive ferruginous clay deposits (e.g., native copper mineralization) within the oxidized zone of the mineralized regions. The potential mineralized zones with type E signature are noted in Profile F-F', G-G', L-L', O-O', and P-P'. Zone F is represented by very low resistivity (< 15 ohm-m) and very low chargeability (< 5 mV/V) anomalies below the overburden. This zone is a special classification based on only the anomaly observed in Profile O-O' in the

calibration area. This distinct signature is interpreted as a hematite-rich zone with very low chargeability characteristics. Replacement of magnetite by hematite is one oxidation and supergene alteration reported in the calibration area (Gordon et al., 2016). The low resistivity may correspond to the shallow clayey features of the oxide zone with high copper and gold content.

Zones G and H are regions without potential copper and gold mineralization. Zone G is represented by very high resistivity (>100 ohm-m) and low chargeability (< 5 mV/V) values. That can be interpreted as a massive, intrusive rock (e.g., Tamisan Diorite) reported in the study area's vicinity (MGB 2010). Zone G was observed at deeper depths (>85 m) in Profiles F-F', G-G', I-I', and J-J'. Zone H is characterized by moderate to high resistivity (>15 ohm-m) and low to moderate chargeability (< 25 mV/V) values. All of the profile has an ER-IP signature that corresponds to Zone H. Some ER-IP model sections were not marked by Zone H to emphasize the potential zones of mineralization (because the sections will become crowded with labels). Zone H indicates barren rocks of the Tumbaga Formation with very low (to none) concentration of sulfide minerals, thus low copper and gold mineralization potential.

The ER-IP results were correlated and calibrated to validate the range of resistivity and chargeability values and their corresponding interpreted lithological units. ERT surveys were conducted in an area with known mineralization to calibrate and enhance the findings of the ER-IP data interpretation. The ER-IP surveys were performed next to eight drillholes positioned southeast of the main study area (Fig. 3-30). The survey lines were placed in a safe and secure location to acquire accurate subsurface information about the mineralized zones. As a result, the instrument readings (ER-IP data) were correlated with subsurface mineralization information (Appendix 7) to gain geologic knowledge of the subsurface and narrow the range of values of the categorized zones (lithologic units). The drilling logs were projected onto the ER-IP model sections. This way, the resistivity and chargeability signatures can be compared with the location and characteristics of the mineralization. The distance from the drill holes to the model section lines ranges from 20 m to 80 m. These distances could have presented a bias in the reliability of the borehole information when the drill log information was used to correlate the location and depth of the anomalous zones. Nonetheless, this drill log information was very valuable in constraining the interpretation and validation of the subsurface lithology.

Most Cu-Au mineralization was reported in magnetite skarn, garnet skarn, and oxidized supergene deposits associated with sulfide minerals such as chalcopyrite, pyrite, arsenopyrite, and covellite (Gordon et al., 2016). The ER-IP anomalous zones in the main study area do not necessarily specify a skarn type of mineralization. However, since the mineralized bodies in

the calibration area are associated with sulfide minerals, an estimate of copper and gold potential could be realized from the ER-IP calibration. Average grades of about 1.7 % Cu and 1.9 g/t Au were reported for the mineralized magnetite skarn in the calibration area; the grades of copper and gold are also economically significant in garnet skarn (Gordon et al., 2016). The mineralized skarn represents Zone C with moderate resistivity (15 to 100 ohm-m) and high chargeability (> 25 mV/V) values (Fig. 3-30). The oxidized supergene deposit (~ 20 to 30m thick) is distributed at the upper portion of the skarn; it underlies the Labo volcanic complex (overburden) (Gordon et al., 2016). These strongly oxidized and highly weathered regions were correlated to Zone E with corresponding low resistivity (< 15 ohm-m) and high chargeability (> 25 mV/V) signatures (Fig. 3-30). These relative geophysical signatures (e.g., resistivity, chargeability) related to the interpreted zones (Zone A to H) are consistent with other published studies (Zonge et al., 2005; Park et al., 2009; Sultan et al., 2009; Han et al., 2016; Sono et al., 2021).

The subsurface ER-IP data effectively identified potential zones for Cu-Au exploration based on the spatial distribution of the anomalous zones (e.g., Zone C). The promising regions that merit more detailed exploration (e.g., drilling) were delineated on the north-western side of the study area. That is due to the extensive occurrence of high chargeability zones and relatively low resistivity anomalies of Zone C. The 2-D and 3-D IP models clearly show that the study area is dominated by higher chargeability zones on the northern side (Fig. 3-32 to 3-36) compared with the southern side (Fig. 3-37 to 3-41). Examination of the IP models perpendicular (Fig. 3-42 to 3-45) to the north-south trending profiles confirms the continuity of the highly chargeable zones (e.g., the presence of disseminated sulfide minerals).

The 3-D ER-IP inversion models are consistent with the 2-D interpretations. It is clear that Zone C is the most widespread and, as such, has been designated as the most promising zone of mineralization in the study area. However, a lesser mineralization potential is most likely present in the southern part of the study area. This notion is due to Zone-E's minor occurrence at the shallower portion of the 2-D and 3-D models. The geophysical signatures in the 3-D models were also comparable to the values validated by drill holes in the calibration area. Overall, the 2-D and 3-D ER-IP images and the VLF-EM results help establish the boundaries of the overburdened and potentially mineralized zones. 3-D visualization effectively defines the spatial distribution of the promising zones of mineralization in the study area.

3.7 Conclusion and Exploration Implications

ER-IP surveys were conducted to characterize the potential Cu-Au mineralization across an area overlain by thick pyroclastic deposits in Eastern Labo (south of the Paracale-Panganiban mineral district), Bicol, Philippines. The interpretation of the resistivity and chargeability distribution in the study area generated significant findings that characterized the underlying lithology into eight zones. Zones from C to F represent potential mineralized regions generally defined by relatively high chargeability and variable resistivity. The non-mineralized zones are characterized by Zones A and B (overburden) and Zones G and H (underlying lithology). The available borehole data in the calibration area validated these subsurface lithological features.

The analysis of these east-west sections (Profile K-K' to Profile M-M') also elucidates the lateral continuity of the anomalous zones and strengthens the notion that the potential mineralized zones are concentrated on the northern and eastern sides of the study area. Pseudo-3-D resistivity and IP models were generated to understand better the continuity of the anomalous features and geologic structures related to the mineralization potential. With the 2-D and 3-D information, it can be established that the regional geologic structure (NW-SE lineament) affects the mineralization potential in the study area. The geometry of these anomalies related to mineral potential was strongly recognized from the 3-D resistivity and IP models in support of the individual interpretation of 2-D resistivity and IP models.

The new subsurface information generated from the cost-effective and time-efficient ER-IP surveys successfully delineated the promising prospects for Cu-Au exploration in the study area. Due to the extensive occurrence of high chargeability zones and relatively low resistivity anomalies, the prospective sites for further detailed investigation (e.g., drilling and other detailed geophysical surveys) were established on the northwestern side of the study area (Zone C). Identifying ER-IP signatures corresponding to potentially mineralized zones enable targeting new promising areas for more in-depth and detailed geophysical and geological surveys. This technique can be applied in other mining districts concealed by thick overburden.

CHAPTER 4
General Conclusion

4.1 Introduction

This study contributed novel information to the geoscience, geophysics, and mining community by collating, generating, and publishing new geophysical data in the Philippine island arc system. This research yielded maps and models disseminated to the geoscience community and other stakeholders by making them available to the public (published in academic journals). The published manuscripts offered new data and interpretations of the geology, tectonics, and mineral potentials in the Philippine island arc system using gravity and electrical resistivity-induced polarization (ER-IP) methods.

The first part of this study investigated the gravity anomalies in the Philippine island arc system and identified regional geologic and tectonic features (e.g., structures, sedimentary basins, and basement rocks), including those which may not have been previously delineated on gravity anomaly maps using the isostatic and free-air anomaly grids from World Gravity Map (WGM). The second part of this research presented the ER-IP and VLF-EM surveys to investigate the mineralization potential over a thick overburden in Eastern Labo, Camarines Norte, Philippines. Detailed geophysical data (i.e., ER-IP, VLF-EM) were generated to identify the geophysical signatures of the potential mineralized regions. The distribution of the potential Cu-Au mineralization was delineated and a subsurface model characterizing the depth, thickness, and extent of the mineralized zones in the study area was proposed. This research yielded new information about the local subsurface features that help locate promising targets for Cu-Au exploration in Eastern Labo, Camarines Norte, Philippines. The combination of the geophysical investigation (e.g., ER-IP, VLF-EM) for mineral resources exploration reduces the ambiguity of the interpretation of the potentially mineralized zones. The conceptual model shows the promising zones from the combined geophysical and geological information.

4.2 Gravity Data Analysis of the Philippine Island Arc System

Many areas of the Philippine island arc system still lack geopotential field research, and previous gravity anomaly maps were based on a small number of data points. The WGM 2012 gravity data are extremely valuable in understanding the regional geologic and tectonic characteristics of the Philippine archipelago by giving meaningful new interpretations and assessments of structures from upper to lower crustal depths (e.g., basin,

basement, Moho). The study of gravity anomalies in the Philippine island arc system reveals negative gravity anomaly zones that correspond to the surrounding trenches that border the PMB and thick sedimentary basins. Metamorphic belts are linked with moderate gravity anomalies, whereas ophiolitic basement rocks are defined by very high gravity anomalies. The upward continuation of gravity data indicates a comparatively low gravity anomaly (20 to 35 mGal) in the continental central Philippines compared to the island arc PMB's gravity highs (45 to 200 mGal). This dissertation also gives a new estimate of the average Moho (12 to 22 km) and basement (5 to 11 km) depths along the Sulu Sea using the 2-D radially-averaged power spectrum analysis. The use of 3-D gravity inversion in major sedimentary basins in the Philippines provides a quick and easy technique to characterize significant crustal density distributions and visualize regional subsurface density differences. These methodologies may be used for future structural and geologic studies in the Philippines and other places with comparable geologic and tectonic settings, thanks to the availability and demonstrated the efficiency of WGM 2012 data.

4.3 ER-IP and VLF-EM Surveys in Eastern Labo, Philippines

ER-IP and VLF-EM studies were carried out in Eastern Labo (south of the Paracale-Panganiban mining sector), Bicol, Philippines, to assess the possible Cu-Au mineralization overlain by thick pyroclastic deposits. The analysis of the resistivity and chargeability distribution in the research region yielded essential results that classified the underlying lithology into eight zones. Zones C–F depict potentially mineralized zones that are distinguished by relatively high chargeability and varied resistivity. Zones A and B (overburden) and Zones G and H (underlying lithology) are the non-mineralized zones. These subsurface lithological properties were confirmed using borehole data from the calibration area. The east-west section analysis (Profile K-K' to Profile M-M') also highlights the lateral continuity of the anomalous zones and supports the hypothesis that possible mineralized zones are focused on the northern and eastern edges of the research region. To better comprehend the continuity of the anomalous features and geologic structures associated with the mineralization potential, pseudo-3-D resistivity and IP models were created. The VLF-EM and 2-D and 3-D ER-IP data show that the regional geologic structure (NW-SE lineament) influences the mineralization potential in the study area. The geometry of these potential mineral anomalies was well identified by the 3-D resistivity and IP models, which supported the individual interpretation of the 2-D resistivity and IP models.

The new subsurface information derived from the cost-effective and time-efficient geophysical surveys (e.g., VLF-EM, ER-IP) effectively identified prospective Cu-Au exploration targets in the study area. Because of the widespread occurrence of high chargeability zones and relatively low resistivity anomalies, suitable areas for further comprehensive examination (e.g., drilling and other detailed geophysical surveys) were identified on the study area's northern flank (Zone C). Identifying ER-IP signals associated with possibly mineralized zones allows for the identification of new viable regions for further in-depth and thorough geophysical and geological assessments. This strategy can be used in other mining districts that are hidden by thick overburden.

4.4 Further Studies for the Future

Sites of interest for future geologic and tectonic studies were identified due to the peculiar gravity anomalies (e.g., in the Sulu Sea and representative major sedimentary basins) in the Philippine island arc system. Further detailed studies in Eastern Labo can also be focused on delineating the location of the mineralized zones and calculating the volume of ore reserves, if possible. In addition, the mechanism and genesis of the mineralization need to be further investigated. Despite the Paracale-Panganiban Mining District's endowment of epithermal-porphyry mineral deposits, tectonic influences on magma localization and dense geochemical studies have yet to be thoroughly investigated. Furthermore, thorough mineralogical and structural studies of the deposit were not possible due to the limited drill cores and surface exposures of the mineralized zones in the study area. A better knowledge of these factors would significantly improve the conceptual model of the study area.

The geophysical methods and techniques (e.g., gravity, electrical resistivity, induced polarization) learned from this study will be shared with the geoscience community in the Philippines, particularly with the technical personnel of the Mines and Geosciences Bureau (MGB). A project with a similar geophysical approach (after establishing the methodology for the geophysical surveys from this study) will be employed in proposed mineral reservation areas in the Philippines. This recommended project for the geological and geophysical exploration of mineral resources in proposed mineral reservation areas will not just open new geoscientific discoveries. It can also give way to the prosperous mining industry and economic development in the Philippines and other countries.

References

Abrajano TA, and **Pasteris JD** (1989) Zambales ophiolite, Philippines - II. Sulfide petrology of the critical zone of the Acoje Massif. *Contributions to Mineralogy and Petrology 103:64–77*. https://doi.org/10.1007/BF00371365

Alemu T, **Abdelsalam MG**, **Dawit EL**, **Atnafu B**, and **Mickus KL** (2018) The Paleozoic – Mesozoic Mekele Sedimentary Basin in Ethiopia: An example of an exhumed IntraCONtinental Sag (ICONS) basin. *Journal of African Earth Sciences 143:40–58*. https://doi.org/10.1016/j.jafrearsci.2018.03.010

Arabelos DN, and **Tscherning CC** (2010) A comparison of recent Earth gravitational models with emphasis on their contribution in refining the gravity and geoid at continental or regional scale. *Journal of Geodesy 84:643–660*. https://doi.org/10.1007/s00190-010-0397-z

Arai S, **Kadoshima K**, **Manjoorsa M V.**, **David CP**, and **Kida M** (1997) Chemistry of detrital chromian spinels as an insight into petrological characteristics of their source peridotites: an example from the Ilocos Norte ophiolite, northern Luzon, Philippines. *Journal of Mineralogy, Petrology and Economic Geology 92:137–141*. https://doi.org/10.2465/ganko.92.137

Armada L, **Dimalanta C**, **Parcutela N**, **Austria R**, **Padrones J**, **Payot B**, **Queaño K**, and **Yumul G** (2020a) Bouguer Anomaly of Central Cebu, Philippines. *Journal of Maps 16:577–584*. https://doi.org/10.1080/17445647.2020.1791270

Armada LT, **Dimalanta CB**, **Yumul GP**, and **Tamayo RA** (2009) Georesistivity Signature of Crystalline Rocks in the Romblon Island Group, Philippines. *Philippine Journal of Science 138:191–204*

Armada LT, **Hsu S-K**, **Dimalanta CB**, **Yumul Jr. GP**, **Doo W-B**, and **Yeh Y-C** (2020b) Forearc structures and deformation along the Manila Trench. *Journal of Asian Earth Sciences: X 4:100036*. https://doi.org/10.1016/j.jaesx.2020.100036

Arribas A, **Hedenquist JW**, **Itaya T**, **Okada T**, **Concepcion RA**, and **Garcia JS** (1995) Contemporaneous formation of adjacent porphyry and epithermal Cu-Au deposits over 300 ka in northern Luzon, Philippines. *Geology 23:337–340*. https://doi.org/10.1130/0091-7613(1995)023<0337:CFOAPA>2.3.CO;2

Aurelio MA (2000) Shear partitioning in the Philippines: Constraints from the Philippine fault and global positioning system data. *Island Arc 9:584–597*. https://doi.org/10.1111/j.1440-1738.2000.00304.x

Aurelio MA, **Forbes MT**, **Taguibao KJL**, **Savella RB**, **Bacud JA**, **Franke D**, **Pubellier M**, **Savva D**, **Meresse F**, **Steuer S**, and **Carranza CD** (2014) Middle to Late Cenozoic tectonic events in south and central Palawan (Philippines) and their implications to the evolution of the south-eastern margin of South China Sea: Evidence from onshore structural and offshore seismic data. *Marine and Petroleum Geology 58:658–673*. https://doi.org/10.1016/j.marpetgeo.2013.12.002

Aurelio MA, and **Peña RE** (2002) Geology and Mineral Resources of the Philippines - Volume 1: Geology. Department of Environment and Natural Resources – Mines and Geosciences Bureau, Philippines

Aurelio MA, **Peña RE**, and **Taguibao KJL** (2013) Sculpting the Philippine Archipelago since the Cretaceous through rifting, oceanic spreading, subduction, obduction, collision and strike-slip faulting: Contribution to IGMA5000. *Journal of Asian Earth Sciences 72:102–107*. https://doi.org/10.1016/j.jseaes.2012.10.007

Bachman SB, and **Lewis SD** (1983) Evolution of a Forearc Basin, Luzon Central Valley, Philippines. *AAPG Bulletin 67:1143–1162*. https://doi.org/10.1306/03B5B718-16D1-11D7-8645000102C1865D

Balmater HG, **Manalo PC**, **Faustino-Eslava D V.**, **Queaño KL**, **Dimalanta CB**, **Guotana JMR**, **Ramos NT**, **Payot BD**, and **Yumul GP** (2015) Paleomagnetism of the Samar Ophiolite: Implications for the Cretaceous sub-equatorial position of the Philippine island arc. *Tectonophysics 664:214–224*. https://doi.org/10.1016/j.tecto.2015.09.024

Balmino G, **Vales N**, **Bonvalot S**, and **Briais A** (2012) Spherical harmonic modeling to ultra-high degree of Bouguer and isostatic anomalies. *Journal of Geodesy 86:499–520*. https://doi.org/10.1007/s00190-011-0533-4

Barretto J, **Wood R**, and **Milsom J** (2020) Benham Rise unveiled: Morphology and structure of an Eocene large igneous province in the West Philippine Basin. *Marine Geology 419:106052*. https://doi.org/10.1016/j.margeo.2019.106052

Barretto JAL, **Dimalanta CB**, and **Yumul GP** (2000) Gravity variations along the Southeast Bohol ophiolite complex (SEBOC), Central Philippines: Implications on ophiolite emplacement. *Island Arc 9:575–583*. https://doi.org/10.1111/j.1440-1738.2000.00303.x

Barrier E, **Huchon P**, and **Aurelio M** (1991) Philippine Fault: a key for Philippine kinematics. *Geology 19:32–35*. https://doi.org/10.1130/0091-7613(1991)019<0032:PFAKFP>2.3.CO;2

Billedo E (1994) Geologie de la sierra madre septentrionale et de l'archipel de polillo (ceinture mobile est philippine): implications geodynamiques. (Doctoral dissertation, Nice)

Blakely RJ (1996) Potential theory in gravity and magnetic applications. Cambridge University Press, Cambridge

Blanchy G, **Saneiyan S**, **Boyd J**, **McLachlan P**, and **Binley A** (2020) ResIPy, an intuitive open source software for complex geoelectrical inversion/modeling. *Computers and Geosciences 137:104423*. https://doi.org/10.1016/j.cageo.2020.104423

Bonvalot S, **Balmino G**, **Brias A**, **Kuhn M**, **Peyrefitte A**, **Vales N**, **Biancale R**, **Gabalda G**, **Moreaux G**, **Reinquin F**, and **Sarrailh M** (2012) World Gravity Map. Bureau Gravimetrique International (BGI), map, CGMW-BGI-CNES-IRD Ed., Paris 1:8

Braitenberg C, **Mariani P**, **Ebbing J**, and **Sprlak M** (2011) The enigmatic Chad lineament revisited with global gravity and gravity-gradient fields. *Geological Society Special Publication 357:329–341*. https://doi.org/10.1144/SP357.18

Braxton DP, **Cooke DR**, **Ignacio AM**, and **Waters PJ** (2018) Geology of the Boyongan and Bayugo porphyry Cu-Au deposits: An emerging porphyry district in northeast Mindanao, Philippines. *Economic Geology 113:83–131*. https://doi.org/10.5382/econgeo.2018.4545

Bromley CJ (1981) Baslay-Dauin Resistivity Surveys-VES Interpretation

Bromley CJ, and **Espanola OS** (1982) Resistivity Methods Applied To Geothermal Exploration in the Philippines. In: Pacific Geothermal Conference. pp 447–452

Bryner L (1969) Ore deposits of the Philippines their geology. *Economic Geology 64:644–666*. https://doi.org/10.2113/gsecongeo.64.6.644

Bureau Gravimetrique International (BGI) (2012) WGM2012 Global Model. https://bgi.obs-mip.fr/data-products/grids-and-models/wgm2012-global-model/

Bureau of Mines and Geosciences (BMG) (1994) Geologic Map of Daet Quadrangle (1:50,000)

Caagusan NL (1978) Source material, compaction history and hydrocarbon occurrence in the Cagayan Valley Basin, Luzon, Philippines. In: Offshore South East Asia Conference (Southeast Asia Petroleum Exploration Society, SEAPEX Program), [Proceedings]. p 19 p

Camacho AG, **Fernández J**, **Charco M**, **Tiampo KF**, and **Jentzsch G** (2007) Interpretation of 1992–1994 Gravity Changes around Mayon Volcano, Philippines, Using Point Sources. In:

Deformation and Gravity Change: Indicators of Isostasy, Tectonics, Volcanism, and Climate Change. Birkhäuser Basel, Basel, pp 733–749

Cardenas MB, **Zamora PB**, **Siringan FP**, **Lapus MR**, **Rodolfo RS**, **Jacinto GS**, **San Diego-McGlone ML**, **Villanoy CL**, **Cabrera O**, and **Senal MI** (2010) Linking regional sources and pathways for submarine groundwater discharge at a reef by electrical resistivity tomography, 222 Rn, and salinity measurements. *Geophysical Research Letters 37:n/a-n/a*. https://doi.org/10.1029/2010GL044066

Cardwell RK, **Isacks BL**, and **Karig DE** (1980) The spatial distribution of earthquakes, focal mechanism solutions, and subducted lithosphere in the Philippine and northeastern Indonesian Islands. *The tectonic and geologic evolution of Southeast Asian seas and islands Part 1 23:1–35*. https://doi.org/10.1029/gm023p0001

Casulla MAA, **Mizunaga H**, **Tanaka T**, and **Dimalanta CB** (2022) Imaging crustal features and Moho depths through enhancements and inversion of gravity data from the Philippine island arc system. *Progress in Earth and Planetary Science 9:16*. https://doi.org/10.1186/s40645-022-00473-8

Casulla MAA, **Mizunaga H**, **Tanaka T**, and **Torres A** (2020) Subsurface Characterization using Geophysical and Hydrochemical Data: An Application to Groundwater Resources Management in Pampanga, Philippines. In: International Symposium on Earth Science and Technology. pp 162–168

Chang Z, **Hedenquist JW**, **White NC**, **Cooke DR**, **Roach M**, **Deyell CL**, **Garcia J**, **Gemmell JB**, **McKnight S**, and **Cuison AL** (2011) Exploration tools for linked porphyry and epithermal deposits: Example from the Mankayan intrusion-centered Cu-Au district, Luzon, Philippines. *Economic Geology 106:1365–1398*. https://doi.org/10.2113/econgeo.106.8.1365

Chaput D (1987) The miner warriors of the Philippines. *Philippine Studies 35:51–70*. https://doi.org/https://www.jstor.org/stable/42632984

Claerbout JF, and **Muir F** (1973) ROBUST MODELING WITH ERRATIC DATA. *GEOPHYSICS 38:826–844*. https://doi.org/10.1190/1.1440378

Constable SC, **Parker RL**, and **Constable CG** (1987) Occam's inversion: A practical algorithm for generating smooth models from electromagnetic sounding data. *GEOPHYSICS 52:289–300*. https://doi.org/10.1190/1.1442303

Corby GW, **Kleinpell RM**, **Popenoe WP**, **Merchant R**, **William H**, **Teves J**, **Grey R**, **Daleon B**, **Mamaclay F**, **Villongco A**, **Herrera M**, **Guillen J**, **Hollister JS**, **Johnson HN**, **Billings MH**, **Fryxell EM**, **Taylor EF**, and **Nelson CN** (1951) Geology and oil Possibilities of the Philippines. *Bureau of Mines, DANR Technical Bulletin Vol 21:365*

Cordell L, and **Grauch VJS** (1982) Mapping basement magnetization zones from aeromagnetic data in the San Juan Basin, New Mexico. In: SEG Technical Program Expanded Abstracts 1982. Society of Exploration Geophysicists, pp 246–247

David S, **Stephan JF**, **Delteil J**, **Müller C**, **Butterlin J**, **Bellon H**, and **Billedo E** (1997) Geology and tectonic history of Southeastern Luzon, Philippines. *Journal of Asian Earth Sciences 15:435–452*. https://doi.org/10.1016/S0743-9547(97)00027-5

Degroot-Hedlin C, and **Constable S** (1990) Occam's inversion to generate smooth, two-dimensional models from magnetotelluric data. *Geophysics 55:1613–1624*. https://doi.org/10.1190/1.1442813

Delfin FG, **Castro CC**, **Zaide MC**, **Clemente VC**, **de Jesus RG**, **Seastres JS**, **Layugan DB**, **Rodriguez RC**, and **PNOC-EDC** (1984) Mt. Apo Geothermal Project: First Stage Exploration. 71

Department of Environment and Natural Resources (DENR) (2016) Mandate, Vision and Mission. https://www.denr.gov.ph/index.php/about-us/mission-vision

Dey A, and **Morrison HF** (1979) Resistivity modeling for arbitrarily shaped three-dimensional structures. *GEOPHYSICS 44:753–780*. https://doi.org/10.1190/1.1440975

Dimalanta CB (1993) Geologic interpretation of gravity anomalies over the Baguio Mineral District. *Journal of the Geological Society of the Philippines 21–34*

Dimalanta CB, **Faustino-Eslava D V.**, **Gabo-Ratio JAS**, **Marquez EJ**, **Padrones JT**, **Payot BD**, **Queaño KL**, **Ramos NT**, and **Yumul GP** (2020) Characterization of the proto-Philippine Sea Plate: Evidence from the emplaced oceanic lithospheric fragments along eastern Philippines. *Geoscience Frontiers 11:3–21*. https://doi.org/10.1016/j.gsf.2019.01.005

Dimalanta CB, **Ramos EGL**, **Yumul GP**, and **Bellon H** (2009) New features from the Romblon Island Group: Key to understanding the arc-continent collision in Central Philippines. *Tectonophysics 479:120–129*. https://doi.org/10.1016/j.tecto.2009.02.015

Dimalanta CB, and **Yumul GP** (2004) Crustal thickening in an active margin setting (Philippines): The whys and the hows. *Episodes 27:260–264*. https://doi.org/10.18814/epiiugs/2004/v27i4/004

Divis AF (1983) The geology and geochemistry of Philippine porphyry copper deposits. *The tectonic and geologic evolution of Southeast Asian seas and islands Part 2 27:173–216*. https://doi.org/10.1029/gm027p0173

Ducut JD, **Alipio M**, **Go PJ**, **Concepcion II R**, **Vicerra RR**, **Bandala A**, and **Dadios E** (2022) A Review of Electrical Resistivity Tomography Applications in Underground Imaging and Object Detection. *Displays 73:102208*. https://doi.org/10.1016/j.displa.2022.102208

Elkins TA (1951) The Second Derivative Method of Gravity Interpretation. *Geophysics 16:29–50*. https://doi.org/10.1190/1.1437648

Ellis RG, and **Oldenburg DW** (1994) Applied geophysical inversion. *Geophysical Journal International 116:5–11*. https://doi.org/10.1111/j.1365-246X.1994.tb02122.x

Evjen HM (1936) The Place of The Vertical Gradient in Gravitational Interpretations. *Geophysics 1:127–136*. https://doi.org/10.1190/1.1437067

Evrard M, **Dumont G**, **Hermans T**, **Chouteau M**, **Francis O**, **Pirard E**, and **Nguyen F** (2018) Geophysical investigation of the Pb–Zn deposit of Lontzen–Poppelsberg, Belgium. *Minerals 8:1–22*. https://doi.org/10.3390/min8060233

Farquharson CG, and **Oldenburg DW** (1998) Non-linear inversion using general measures of data misfit and model structure. *Geophysical Journal International 134:213–227*. https://doi.org/10.1046/j.1365-246x.1998.00555.x

Fikos I, **Vargemezis G**, **Zlotnicki J**, **Puertollano JR**, **Alanis PB**, **Pigtain RC**, **Villacorte EU**, **Malipot GA**, and **Sasai Y** (2012) Electrical resistivity tomography study of Taal volcano hydrothermal system, Philippines. *Bulletin of Volcanology 74:1821–1831*. https://doi.org/10.1007/s00445-012-0638-5

Fraser DC (1969) Contouring of VLF-EM Data. *Geophysics 34:958–967*. https://doi.org/10.1190/1.1440065

Frost JE (1965) Controls of ore deposition for the Larap mineral deposits, Camarines Norte, Philippines. Stanford University

Gabo JAS, **Dimalanta CB**, **Yumul GP**, **Faustino-Eslava D V.**, and **Imai A** (2015) Terrane boundary geophysical signatures in Northwest Panay, Philippines: Results from gravity, seismic refraction and electrical resistivity investigations. *Terrestrial, Atmospheric and Oceanic Sciences 26:663–678*. https://doi.org/10.3319/TAO.2015.05.11.03(TC)

Geary EE, **Harrison TM**, and **Heizler M** (1988) Diverse ages and origins of basement complexes, Luzon, Philippines. *Geology 16:341*. https://doi.org/10.1130/0091-7613(1988)016<0341:DAAOOB>2.3.CO;2

Geary EE, and **Kay RW** (1989) Identification of an early cretaceous ophiolite in the Camarines Norte-Calaguas Islands basement complex, eastern Luzon, Philippines. *Tectonophysics 168:109–126*. https://doi.org/10.1016/0040-1951(89)90371-5

GEBCO Compilation Group (2020) GEBCO 2020 grid (gridded bathymetry data download). https://doi.org/10.5285/a29c5465-b138-234d-e053-6c86abc040b9

Gibaga CRL, **Samaniego JO**, **Tanciongco AM**, **Quierrez RNM**, **Montano MO**, **Gervasio JHC**, **Reyes RCG**, and **Peralta MJ V.** (2022) The rare earth element (REE) potential of the Philippines. *Journal of Geochemical Exploration 242:107082*. https://doi.org/10.1016/j.gexplo.2022.107082

Godfrey NJ, **Beaudoin BC**, and **Klemperer SL** (1997) Ophiolitic basement to the Great Valley forearc basin, California, from seismic and gravity data: Implications for crustal growth at the North American continental margin. *Geological Society of America Bulletin 109:1536–1562*. https://doi.org/10.1130/0016-7606(1997)109<1536:OBTTGV>2.3.CO;2

Goldman M, and **Neubauer FM** (1994) Groundwater exploration using integrated geophysical techniques. *Surveys in Geophysics 15:331–361*. https://doi.org/10.1007/BF00665814

Gómez-Ortiz D, **Tejero-López R**, **Babín-Vich R**, and **Rivas-Ponce A** (2005) Crustal density structure in the Spanish Central System derived from gravity data analysis (Central Spain). *Tectonophysics 403:131–149*. https://doi.org/10.1016/j.tecto.2005.04.006

Gordon D, **Reynolds N**, **Green A**, **Moormann C**, **Frew R**, **McIntyre J**, **Brett A**, **Epps J**, and **Morgan D** (2016) Rtg Mining Inc Mabilo Project National Instrument 43-101 TECHNICAL REPORT

Guotana JMR, **Payot BD**, **Dimalanta CB**, **Ramos NT**, **Faustino-Eslava D V.**, **Queaño KL**, and **Yumul GP** (2017) Petrological and geochemical characteristics of the Samar Ophiolite ultramafic section: implications on the origins of the ophiolites in Samar and Leyte islands, Philippines. *International Geology Review 00:1–17*. https://doi.org/10.1080/00206814.2017.1336944

Haáz IB (1953) Relations between the potential of the attraction of the mass contained in a finite rectangular prism and its first and second derivatives. *Geophysical Transactions II 7:57–66*

Hagemann SG, and **Brown PE** (2000) Exploration for Epithermal Gold Deposits. In: Gold in 2000. Society of Economic Geologists, pp 245–277

Hamburger MW, **Cardwell RK**, and **Isacks BL** (1983) Seismotectonics of the northern Philippine island arc. *The tectonic and geologic evolution of Southeast Asian seas and islands Part 2 27:1–22*. https://doi.org/10.1029/gm027p0001

Han MH, **Shin SW**, **Park S**, **Cho SJ**, and **Kim JH** (2016) Induced polarization imaging applied to exploration for low-sulfidation epithermal Au-Ag deposits, Seongsan mineralized district, South Korea. *Journal of Geophysics and Engineering 13:817*. https://doi.org/10.1088/1742-2132/13/5/817

Hayes DE, and **Lewis SD** (1984) A geophysical study of the Manila Trench, Luzon, Philippines. 1. Crustal structure, gravity, and regional tectonic evolution. *Journal of Geophysical Research 89:9171–9195*. https://doi.org/10.1029/JB089iB11p09171

Hayes DE, and **Lewis SD** (1985) Structure and tectonics of the Manila trench system, Western Luzon, Philippines. *Energy 10:263–279*. https://doi.org/10.1016/0360-5442(85)90046-5

Hedenquist JW, **Arribas R. A**, and **Aoki M** (2017) Zonation of Sulfate and Sulfide Minerals and Isotopic Composition in the Far Southeast Porphyry and Lepanto Epithermal Cu–Au Deposits, Philippines. *Resource Geology 67:174–196*. https://doi.org/10.1111/rge.12127

Hinze WJ, **Von Frese RRB**, and **Saad AH** (2013) Gravity and Magnetic Exploration: Principles, Practices, and Applications. Cambridge University Press, New York

Holloway NH (1981) The North Palawan block, Philippines: its relation to the Asian Mainland and its role in the evolution of the South China Sea. *Bulletin of the Geological Society of Malaysia 14:19–58*. https://doi.org/10.7186/bgsm14198102

Hutchison CS, and **Taylor D** (1978) Metallogenesis in SE Asia. *Journal of the Geological Society 135:407–428*. https://doi.org/10.1144/gsjgs.135.4.0407

Inman JR (1975) RESISTIVITY INVERSION WITH RIDGE REGRESSION. *GEOPHYSICS 40:798–817*. https://doi.org/10.1190/1.1440569

Jacobsen BH (1987) Case for Upward Continuation As a Standard Separation Filter for Potential-Field Maps. *Geophysics 52:1138–1148*. https://doi.org/10.1190/1.1442378

James LP, and **Fuchs WA** (1990) Exploration of the Exciban gold-copper-tellurium vein system, Camarines Norte, Philippines. *Journal of Geochemical Exploration 35:363–385*. https://doi.org/10.1016/0375-6742(90)90044-B

Jang H, **Park S**, and **Kim HJ** (2014) A simple inversion of induced-polarization data collected in the Haenam area of Korea. *Journal of Geophysics and Engineering 11:015011*. https://doi.org/10.1088/1742-2132/11/1/015011

Japan International Cooperation Agency (JICA) (2002) Report on the Cooperative Mineral Exploration in the Bicol North Area, the Republic of the Philippines, Consolidated Report

Jentzsch G, **Punongbayan RS**, **Schreiber U**, **Seeber G**, **Völksen C**, and **Weise A** (2001) Mayon volcano, Philippines: change of monitoring strategy after microgravity and GPS measurements from 1992 to 1996. *Journal of Volcanology and Geothermal Research 109:219–234*. https://doi.org/10.1016/S0377-0273(00)00313-9

Jimenez FA, **Yumul GP**, **Maglambayan VB**, and **Tamayo RA** (2002) Shallow to near-surface, vein-type epithermal gold mineralization at Lalab in the Sibutad gold deposit, Zamboanga del Norte, Mindanao, Philippines. *Journal of Asian Earth Sciences 21:119–133.* https://doi.org/10.1016/S1367-9120(02)00024-X

Karig DE, **Sarewitz DR**, and **Haeck GD** (1986) Role of strike-slip faulting in the evolution of allochthonous terranes in the Philippines. *Geology 14:852*. https://doi.org/10.1130/0091-7613(1986)14<852:ROSFIT>2.0.CO;2

Karous M, and **Hjelt SE** (1983) Linear Filtering of VLF Dip-Angle Measurements*. *Geophysical Prospecting 31:782–794*. https://doi.org/10.1111/j.1365-2478.1983.tb01085.x

Kearey P, **Brooks M**, and **Hill I** (2002) An Introduction to Geophysical Exploration, 3rd edn. Blackwell Science

Knödel K, **Lange G**, and **Voigt H-J** (2007) Environmental Geology. Springer Berlin Heidelberg, Berlin, Heidelberg

Komazawa M, **Pantig J**, and **Listanco EL** (2014) Caldera Structure Inferred from Gravity Basement around Bulusan Volcano, Southern Luzon, Philippines. *Journal of Geography (Chigaku Zasshi) 123:133–142*. https://doi.org/10.5026/jgeography.123.133

Kudrass HR, **Wiedicke M**, **Cepek P**, **Kreuzer H**, and **Müller P** (1986) Mesozoic and Cainozoic rocks dredged from the South China Sea (Reed Bank area) and the Sulu Sea and their significance for plate-tectonic reconstructions. *Marine and Petroleum Geology 3:19–30*.

https://doi.org/10.1016/0264-8172(86)90053-X

Kumar A, **S. Roy PN**, and **Das LK** (2016) Vertical density contrast and mapping of basement, Conrad and Moho morphologies through 2D spectral analysis of gravity data in and around Odisha, India. *Journal of Asian Earth Sciences 124:181–190*. https://doi.org/10.1016/j.jseaes.2016.05.002

Kunnummal P, and **Anand SP** (2019) Qualitative appraisal of high resolution satellite derived free air gravity anomalies over the Maldive Ridge and adjoining ocean basins, western Indian Ocean. *Journal of Asian Earth Sciences 169:199–209*. https://doi.org/10.1016/j.jseaes.2018.08.008

Laske G, **Masters G**, **Ma Z**, and **Pasyanos M** (2013) Update on CRUST1.0---A 1-degree global model of Earth's crust. *Geophys Res Abstracts 15:EGU General Assembly 2013-2658*

Lejay P (1938) The General Characters of the Gravity in the Philippines. *Nat Appl Sci Bull 6:223–285*

Leseane K, **Atekwana EA**, **Mickus KL**, **Abdelsalam MG**, **Shemang EM**, and **Atekwana EA** (2015) Thermal perturbations beneath the incipient Okavango Rift Zone, northwest Botswana. *Journal of Geophysical Research: Solid Earth 120:1210–1228*. https://doi.org/10.1002/2014JB011029

Lewis SD, and **Hayes DE** (1983) The Tectonics of Northward Propagating Subduction Along Eastern Luzon, Philippine Islands. *Washington DC American Geophysical Union Geophysical Monograph Series 27:57–78*. https://doi.org/10.1029/gm027p0057

Lewis SD, and **Hayes DE** (1984) A geophysical study of the Manila Trench, Luzon, Philippines: 2. Fore arc basin structural and stratigraphic evolution. *Journal of Geophysical Research 89:9196*. https://doi.org/10.1029/JB089iB11p09196

Li Y, and **Oldenburg DW** (2000) 3-D inversion of induced polarization data. *Geophysics 65:1931–1945*. https://doi.org/10.1190/1.1444877

Li Y, and **Oldenburg DW** (1998) 3-D inversion of gravity data. *Geophysics 63:109–119*. https://doi.org/10.1190/1.1444302

Lines LR, and **Treitel S** (1984) A REVIEW OF LEAST-SQUARES INVERSION AND ITS APPLICATION TO GEOPHYSICAL PROBLEMS*. *Geophysical Prospecting 32:159–186*. https://doi.org/10.1111/j.1365-2478.1984.tb00726.x

Liu W, **Li C**, **Zhou Z**, and **Fairhead JD** (2012) Tectonics of the Philippines and ambient regions from geophysical inversions. In: AGU Fall Meeting Abstracts. p 2671

Liu WN, **Li CF**, **Li J**, **Fairhead D**, and **Zhou Z** (2014) Deep structures of the Palawan and Sulu Sea and their implications for opening of the South China Sea. *Marine and Petroleum Geology 58:721–735*. https://doi.org/10.1016/j.marpetgeo.2014.06.005

Loke MH (2012) Tutorial: 2D and 3D electrical imaging surveys. Geotomo Software, Malaysia

Loke MH, **Acworth I**, and **Dahlin T** (2003) A comparison of smooth and blocky inversion methods in 2D electrical imaging surveys. *Exploration Geophysics 34:182–187*. https://doi.org/10.1071/EG03182

Loke MH, and **Barker RD** (1996) Rapid least-squares inversion of apparent resistivity pseudosections by a quasi-Newton method. *Geophysical Prospecting 44:131–152*. https://doi.org/10.1111/j.1365-2478.1996.tb00142.x

Loke MH, **Chambers JE**, **Rucker DF**, **Kuras O**, and **Wilkinson PB** (2013) Recent developments in the direct-current geoelectrical imaging method. *Journal of Applied Geophysics 95:135–156*. https://doi.org/10.1016/j.jappgeo.2013.02.017

Los Banos CF, **Layugan DB**, **Maneja FC**, and **Apuada NA** (1996) Geophysical model of Mt. Labo geothermal field, southeastern Luzon, Philippines. *Transactions - Geothermal Resources Council 20:689–696*

Los Baños CF, **Rigor DM**, **Layugan DB**, and **Bayrante LF** (2010) The Resistivity Model of the Mindanao Geothermal Project, South Central Mindanao, Philippines. In: World Geothermal Congress 2010. pp 1–6

Lowrie W (2007) Fundamentals of geophysics, Second. Cambridge University Press, Cambridge

Lowrie W, and **Fichtner A** (2019) Fundamentals of Geophysics. Cambridge University Press

Majumdar TJ, and **Bhattacharyya R** (2005) Bathymetry prediction model from high-resolution satellite gravity as applied over a part of the eastern Indian offshore. *Current Science 89:1754–1759*

Manalo PC, **Dimalanta CB**, **Faustino-Eslava D V.**, **Ramos NT**, **Queaño KL**, and **Yumul GP** (2015) Crustal thickness variation from a continental to an island arc terrane: Clues from the gravity signatures of the Central Philippines. *Journal of Asian Earth Sciences 104:205–214*. https://doi.org/10.1016/j.jseaes.2014.08.031

Manghnani MH, and **Coleman RG** (1981) Gravity profiles across the Samail Ophiolite, Oman. *Journal of Geophysical Research: Solid Earth 86:2509–2525*. https://doi.org/10.1029/JB086iB04p02509

McCabe R, **Almasco J**, and **Diegor W** (1982) Geologic and paleomagnetic evidence for a possible Miocene collision in western Panay, central Philippines. *Geology 10:325–329*. https://doi.org/10.1130/0091-7613(1982)10<325:GAPEFA>2.0.CO;2

McNeill JD, and **Labson VF** (1991) 7. Geological Mapping Using VLF Radio Fields. In: Electromagnetic Methods in Applied Geophysics. Society of Exploration Geophysicists, pp 521–640

Meek WB (1941) The geology of the Paracale-Jose Panganiban mining district of Camarines Norte, Luzon, Philippine Islands. Quezon City, Philippines

Milsom J, **Ali JR**, and **Queano KL** (2006) Peculiar geometry of northern Luzon, Philippines: Implications for regional tectonics of new gravity and paleomagnetic data. *Tectonics 25:1–14*. https://doi.org/10.1029/2005TC001930

Milsom J, and **Eriksen A** (2011) Field Geophysics, 4th edn. John Wiley & Sons, Chichester

Mines and Geosciences Bureau (MGB) (2022) Mission, Vision and Thrust. https://mgb.gov.ph/about-us/mandate-and-functions

Mines and Geosciences Bureau (MGB) (2014) Groundwater Assessment of Southwestern Portion of Bohol Island Through Geo-resistivity Survey. Quezon City, Philippines

Mines and Geosciences Bureau (MGB) (2017) Groundwater Resource Assessment of Bohol Province. Quezon City, Philippines

Mines and Geosciences Bureau (MGB) (2010) Geology of the Philippines, 2nd ed. Mines and Geosciences Bureau; Department of Environment and Natural Resources, North Avenue, Quezon City, Philippines

Miranda FE, and **Caleon PE** (1979) Geology and mineral resources of Camarines Norte and part of Quezon Province. Quezon City, Philippines

Mishra D., and **Pedersen LB** (1982) Statistical analysis of potential fields from subsurface reliefs. *Geoexploration 19:247–265*. https://doi.org/10.1016/0016-7142(82)90030-8

Mitchell AHG, and **Balce GR** (1990) Geological features of some epithermal gold systems, Philippines. *Journal of Geochemical Exploration 35:241–296*. https://doi.org/10.1016/0375-6742(90)90041-8

Mitchell AHG, **Hernandez F**, and **Dela Cruz AP** (1986) Cenozoic evolution of the Philippine Archipelago. *Journal of Southeast Asian Earth Sciences 1:3–22*. https://doi.org/10.1016/0743-9547(86)90003-6

Monasterial JL (2015) Microgravity Survey in 2009-2010 Around Bacman Geothermal Field, Philippines - Gravity Corrections and Interpretations. In: UNU-GTP Orkustofnun, Grensasvegur

Murauchi S, **Ludwig WJ**, **Den N**, **Hotta H**, **Asanuma T**, **Yoshii T**, **Kubotera A**, and **Hagiwara K** (1973) Structure of the Sulu Sea and the Celebes Sea. *Journal of Geophysical Research 78:3437–3447*. https://doi.org/10.1029/jb078i017p03437

Nabighian MN, **Grauch VJS**, **Hansen RO**, **LaFehr TR**, **Li Y**, **Peirce JW**, **Phillips JD**, and **Ruder ME** (2005) The historical development of the magnetic method in exploration. *Geophysics 70:33ND-61ND*. https://doi.org/10.1190/1.2133784

Neyamadpour A, **Wan Abdullah WAT**, **Taib S**, and **Neyamadpour B** (2010) Comparison of Wenner and dipole-dipole arrays in the study of an underground three-dimensional cavity. *Journal of Geophysics and Engineering 7:30–40*. https://doi.org/10.1088/1742-2132/7/1/003

Ogilvy RD, and **Lee AC** (1991) Interpretation of VLF-EM In-phase Data using Current Density Pseudosections. *Geophysical Prospecting 39:567–580*. https://doi.org/10.1111/j.1365-2478.1991.tb00328.x

Oldenburg DW (1974) The Inversion and Interpretation of Gravity Anomalies. *Geophysics 39:526–536*. https://doi.org/10.1190/1.1440444

Oldenburg DW, and **Li Y** (2005) 5. Inversion for Applied Geophysics: A Tutorial. In: Near-Surface Geophysics. Society of Exploration Geophysicists, pp 89–150

Paál G (1968) Very low frequency measurements in northern Sweden. *Geoexploration 6:141–149*. https://doi.org/10.1016/0016-7142(68)90009-4

Pal SK, **Majumdar TJ**, **Pathak VK**, **Narayan S**, **Kumar U**, and **Goswami OP** (2016) Utilization of high-resolution EGM2008 gravity data for geological exploration over the Singhbhum-Orissa Craton, India. *Geocarto International 31:783–802*. https://doi.org/10.1080/10106049.2015.1076064

Palattao MVB, **Nohay CM**, **Vargas EP**, **Reyes RY**, **Singayan AA**, and **Rosa AD** (2015) Implementation of the Borehole Disposal Project for Disused Sealed Radioactive Sources in the Philippines. In: Safety and Security of Radioactive Sources: Maintaining Continuous Global Control of Sources throughout Their Life Cycle. p 406

Parasnis DS (1979) Principles of Applied Geophysics. Springer Netherlands, Dordrecht

Parcutela NE, **Austria RSP**, **Dimalanta CB**, **Armada LT**, and **Yumul GP** (2022) Arc-crustal compression and its effects on the underlying mantle geometry as elucidated from the potential field signatures of the buckled Cretaceous Cebu lithosphere, Philippines. *Tectonophysics 831:229341*. https://doi.org/10.1016/j.tecto.2022.229341

Park JO, **You YJ**, and **Kim HJ** (2009) Electrical resistivity surveys for gold-bearing veins in the Yongjang mine, Korea. *Journal of Geophysics and Engineering 6:73–81*. https://doi.org/10.1088/1742-2132/6/1/008

Pasco JA, **Dycoco JMA**, **Valera GT V.**, **Payot BD**, **Pillejera JDB**, **Uy FAAE**, **Armada LT**, and **Dimalanta CB** (2019) Petrogenesis of ultramafic-mafic clasts in the Dos Hermanos Mélange, Ilocos Norte: Insights to the evolution of western Luzon, Philippines. *Journal of Asian Earth*

Sciences 184:104004. https://doi.org/10.1016/j.jseaes.2019.104004

Paterson NR, and **Ronka V** (1971) Five years of surveying with the Very Low Frequency—Electromagnetics method. *Geoexploration 9:7–26*. https://doi.org/10.1016/0016-7142(71)90085-8

Pavlis NK, **Holmes SA**, **Kenyon SC**, and **Factor JK** (2008) An Earth Gravitational Model to degree 2160: EGM2008. General Assembly of the European Geosciences Union

Pavlis NK, **Holmes SA**, **Kenyon SC**, and **Factor JK** (2012) The development and evaluation of the Earth Gravitational Model 2008 (EGM2008). *Journal of Geophysical Research: Solid Earth 117:1–38*. https://doi.org/10.1029/2011JB008916

Pelton WH, and **Smith PK** (1976) Mapping Porphyry Copper Deposits in the Philippines with IP. *Geophysics 41:106–122*. https://doi.org/10.1190/1.1440594

Phillips WJ, and **Richards WE** (1975) Study of the effectiveness of the VLF method for the location of narrow-mineralized fault zones. *Geoexploration 13:215–226*. https://doi.org/10.1016/0016-7142(75)90024-1

Pubellier M, **Quebral R**, **Rangin C**, **Deffontaines B**, **Muller C**, **Butterlin J**, and **Manzano J** (1991) The Mindanao collision zone: a soft collision event within a continuous Neogene strike-slip setting. *Journal of Southeast Asian Earth Sciences 6:239–248*. https://doi.org/10.1016/0743-9547(91)90070-E

Quebral R (1994) Tectonique du segment méridional de la faille Philippine, Mindanao oriental, Philippines: passage d'une zone de collision à une zone de décrochement. (Doctoral dissertation, Paris)

Racasa E, **Lloren R**, **Manglicmot M**, **Jago-On KAB**, **Balangue MIRD**, **Taniguchi M**, and **Siringan FP** (2018) Lacustrine groundwater discharge in southern Laguna de Bay, Philippines. In: The Water-Energy-Food Nexus. Springer, Singapore, pp 87–100

Rammlmair D, **Raschka H**, and **Steiner L** (1987) Systematics of chromitite occurrences in Central Palawan, Philippines. *Mineralium Deposita 22:190–197*. https://doi.org/10.1007/BF00206609

Rangin C (1991) The Philippine Mobile Belt: a complex plate boundary. *Journal of Southeast Asian Earth Sciences 6:209–220*. https://doi.org/10.1016/0743-9547(91)90068-9

Rangin C (1989) The Sulu Sea, a back-arc basin setting within a Neogene collision zone. *Tectonophysics 161:119–141*. https://doi.org/10.1016/0040-1951(89)90307-7

Rangin C, **Dahrin D**, **Quebral R**, **Bader AG**, **Cadet JP**, **Caglarcan G**, **Deffontaines B**, **Deplus C**, **Corpus EG**, **Hall R**, **Hello Y**, **Malod J**, **Lallemand S**, **Layugan DB**, **Louat R**, **Morales R**, **Pankow K**, … **Yudho T** (1996) Collision and strike-slip faulting in the northern Molucca Sea (the Philippines and Indonesia): Preliminary results of a morphotectonic study. *Geological Society Special Publication 106:29–46*. https://doi.org/10.1144/GSL.SP.1996.106.01.04

Rangin C, **Jolivet L**, and **Pubellier M** (1990) A simple model for the tectonic evolution of Southeast Asia and Indonesia region for the past 43 m.y. *Bulletin de la Société Géologique de France VI:889–905*. https://doi.org/10.2113/gssgfbull.vi.6.889

Rangin C, and **Silver EA** (1991) Neogene tectonic evolution of the Celebes-Sulu basins: new insights from Leg 124 drilling. *Proc, scientific results, ODP, Leg 124, Celebes and Sulu Seas 124:51–63*. https://doi.org/10.2973/odp.proc.sr.124.122.1991

Rangin C, **Stephan JF**, and **Müller C** (1985) Middle Oligocene oceanic crust of South China Sea jammed into Mindoro collision zone (Philippines). *Geology 13:425–428*. https://doi.org/10.1130/0091-7613(1985)13<425:MOOCOS>2.0.CO;2

Ranneft TSM, **Hopkin RM**, **Froelich AJ**, and **Gwinn JW** (1960) Reconnaissance Geology and Oil

Possibilities of Mindanao. *AAPG Bulletin 44:iii*. https://doi.org/10.1306/0BDA6014-16BD-11D7-8645000102C1865D

Reynolds J. (1997) An Introduction to Applied and Environmental Geophysics. John Wiley and Sons, Inc., Chichester

Rigor DM, **Layugan DB**, and **Los Banos CF** (1998) Magnetotelluric and Gravity Measurements in the Northern Negros Geothermal Field, Central Philippines. In: Asian Geothermal Energy'98, Symposium on "Current and Future Geothermal Energy Development in Asia. pp 115–124

Salapare RC, **Dimalanta CB**, **Ramos NT**, **Manalo PC**, **Faustino-Eslava D V.**, **Queaño KL**, and **Yumul GP** (2015) Upper crustal structure beneath the Zambales Ophiolite Complex, Luzon, Philippines inferred from integrated gravity, magnetic and geological data. *Geophysical Journal International 201:1522–1533*. https://doi.org/10.1093/gji/ggv094

Saldivar-Sali A, **Madrid AP**, **Reyes Jr RA**, and **Flower LG** (1986) Tectonic Setting and Petroleum Possibilities of Philippine Sedimentary Basins. *Transactions of the Fourth Circum-Pacific Energy and Mineral Resources Conference 223–242*

San Andres RB, and **Pedersen JR** (1993) Monitoring the Bulalo geothermal reservoir, Philippines, using precision gravity data. *Geothermics 22:395–402*. https://doi.org/10.1016/0375-6505(93)90027-K

Santos G (1974) Mineral Distribution and Geological Features of the Philippines. In: Metallogenetische und Geochemische Provinzen / Metallogenetic and Geochemical Provinces. Springer Vienna, Vienna, pp 89–105

Sasaki Y (1992) Resolution of Resistivity Tomography Inferred From Numerical Simulation. *Geophysical Prospecting 40:453–463*. https://doi.org/10.1111/j.1365-2478.1992.tb00536.x

Schlüter HU, **Hinz K**, and **Block M** (1996) Tectono-stratigraphic terranes and detachment faulting of the South China Sea and Sulu Sea. *Marine Geology 130:39–78*. https://doi.org/10.1016/0025-3227(95)00137-9

Schweller WJ, **Roth PH**, **Karig DE**, and **Bachman SB** (1984) Sedimentation history and biostratigraphy of ophiolite-related Tertiary sediments, Luzon, Philippines. *Geological Society of America Bulletin 95:1333–1342*. https://doi.org/10.1130/0016-7606(1984)95<1333:SHABOO>2.0.CO;2

Sharma SP, and **Baranwal VC** (2005) Delineation of groundwater-bearing fracture zones in a hard rock area integrating very low frequency electromagnetic and resistivity data. *Journal of Applied Geophysics 57:155–166*. https://doi.org/10.1016/j.jappgeo.2004.10.003

Sillitoe RH (2010) Porphyry Copper Systems. *Economic Geology 105:3–41*. https://doi.org/10.2113/gsecongeo.105.1.3

Sillitoe RH, **Angeles CA**, **Comia GM**, **Antioquia EC**, and **Abeya RB** (1990) An acid-sulphate-type lode gold deposit at Nalesbitan, Luzon, Philippines. *Journal of Geochemical Exploration 35:387–411*. https://doi.org/10.1016/0375-6742(90)90045-C

Silvester PP, and **Ferrari. RL** (1996) Finite elements for electrical engineers. Cambridge university press

Simpson RW, **Jachens RC**, **Saltus RW**, and **Blakely RJ** (1985) A New Isostatic Residual Gravity Map of the Conterminous United States. In: 1985 SEG Annual Meeting, SEG 1985. pp 197–198

Smith PK (1978) Report on Resistivity Survey (Dipole-Dipole) Mambucal, Negros Occidental

Sonido EP (1981) The State of Gravity Works in the Philippines. *J Geol Soc Phil 35:37–50*

Sono P, **Nthaba B**, **Shemang EM**, **Kgosidintsi B**, and **Seane T** (2021) An integrated use of induced

polarization and electrical resistivity imaging methods to delineate zones of potential gold mineralization in the Phitshane Molopo area, Southeast Botswana. *Journal of African Earth Sciences 174:104060*. https://doi.org/10.1016/j.jafrearsci.2020.104060

Spector A, and **Grant FS** (1970) Statistical Models for Interpreting Aeromagnetic Data. *Geophysics 35:293–302*. https://doi.org/10.1190/1.1440092

Spitzer K, and **Chouteau M** (2003) A dc resistivity and IP borehole survey at the Casa Berardi gold mine in northwestern Quebec. *Geophysics 68:453–463*. https://doi.org/10.1190/1.1567221

Steffen R, **Steffen H**, and **Jentzsch G** (2011) A three-dimensional Moho depth model for the Tien Shan from EGM2008 gravity data. *Tectonics 30:1–19*. https://doi.org/10.1029/2011TC002886

Sultan SA, **Mansour SA**, **Santos FM**, and **Helaly AS** (2009) Geophysical exploration for gold and associated minerals, case study: Wadi El Beida area, South Eastern Desert, Egypt. *Journal of Geophysics and Engineering 6:345–356*. https://doi.org/10.1088/1742-2132/6/4/002

Tamayo RA, **Maury RC**, **Yumul GP**, **Polvé M**, **Cotten J**, **Dimantala CB**, and **Olaguera FO** (2004) Subduction-related magmatic imprint of most Philippine ophiolites: implications on the early geodynamic evolution of the Philippine archipelago. *Bull Geol Soc France 175:443–460*. https://doi.org/10.2113/175.5.443

Tamesis EV (1981) Hydrocarbon Potential of Philippine Basins. *Energy 6:1179–1206*. https://doi.org/10.1016/0360-5442(81)90032-3

Tamesis E V. (1976) The Cagayan Valley basin: a second exploration cycle is warranted. In: SEAPEX Program, offshore South East Asia Conference

Taniguchi M, **Burnett WC**, **Dulaiova H**, **Siringan F**, **Foronda J**, **Wattayakorn G**, **Rungsupa S**, **Kontar EA**, and **Ishitobi T** (2008) Groundwater Discharge as an Important Land-Sea Pathway into Manila Bay, Philippines. *Journal of Coastal Research 1:15–24*. https://doi.org/10.2112/06-0636.1

Taylor B, and **Hayes DE** (1980) The tectonic evolution of the South China Basin. *The tectonic and geologic evolution of Southeast Asian seas and islands Part 1 23:89–104*. https://doi.org/10.1029/gm023p0089

Telford WM, **Geldart LP**, and **Sheriff RE** (1990) Applied Geophysics. Cambridge University Press, Cambridge

Teodoro CF (1970) General Characteristics of Gravity in the Island of Luzon, Philippines. *Journal of the Geological Society of the Philippines 24:20–26*

Tiampo KF, **Fernández J**, **Hayes T**, and **Jentzsch G** (2007) Modeling of Stress Changes at Mayon Volcano, Philippines. *Pure and Applied Geophysics 164:819–835*. https://doi.org/10.1007/s00024-007-0189-4

Tselentis G-A, **Drakopoulos J**, and **Dimitriadis K** (1988) A spectral approach to moho depths estimation from gravity measurements in Epirus (NW Greece). *Journal of Physics of the Earth 36:255–266*. https://doi.org/10.4294/jpe1952.36.255

Tsuboi C, and **Kato M** (1952) The First and Second Vertical Derivatives of Gravity. *Journal of Physics of the Earth 1:95–96*. https://doi.org/10.4294/jpe1952.1.95

Vaish J, and **Pal SK** (2015) Geological mapping of Jharia Coalfield, India using GRACE EGM2008 gravity data: a vertical derivative approach. *Geocarto International 30:388–401*. https://doi.org/10.1080/10106049.2014.905637

Vajda P, **Prutkin I**, **Tenzer R**, and **Jentzsch G** (2012) Inversion of temporal gravity changes by the method of local corrections: A case study from Mayon volcano, Philippines. *Journal of Volcanology and Geothermal Research 241–242:13–20*.

https://doi.org/10.1016/j.jvolgeores.2012.06.020

Ward S. (1990) Geotechnical and Environmental Geophysics. SEG, 8801 South Yale Suite 500 Tulsa OK 74137 USA

Wolke R, and **Schwetlick H** (1988) Iteratively Reweighted Least Squares: Algorithms, Convergence Analysis, and Numerical Comparisons. *SIAM Journal on Scientific and Statistical Computing 9:907–921*. https://doi.org/10.1137/0909062

Yi M-J, **Kim J-H**, **Song Y**, **Cho S-J**, **Chung S-H**, and **Suh J-H** (2001) Three-dimensional imaging of subsurface structures using resistivity data. *Geophysical Prospecting 49:483–497*. https://doi.org/10.1046/j.1365-2478.2001.00269.x

Yokoyama I, **Alcaraz A**, and **Peña O** (1975) Gravimetric studies of Taal Volcano, philippines. *Bulletin Volcanologique 39:479–489*. https://doi.org/10.1007/BF02597268

Yumul GP (2007) Westward younging disposition of Philippine ophiolites and its implication for arc evolution. *Island Arc 16:306–317*. https://doi.org/10.1111/j.1440-1738.2007.00573.x

Yumul GP, and **Dimalanta CB** (1997) Geology of the Southern Zambales Ophiolite Complex, (Philippines): Juxtaposed terranes of diverse origin. *Journal of Asian Earth Sciences 15:413–421*. https://doi.org/10.1016/S0743-9547(97)00019-6

Yumul GP, **Dimalanta CB**, **Gabo-Ratio JAS**, **Armada LT**, **Queaño KL**, and **Jabagat KD** (2020a) Mineralization parameters and exploration targeting for gold – copper deposits in the Baguio (Luzon) and Pacific Cordillera (Mindanao) Mineral Districts, Philippines: A review. *Journal of Asian Earth Sciences 191:104232*. https://doi.org/10.1016/j.jseaes.2020.104232

Yumul GP, **Dimalanta CB**, and **Jumawan FT** (2000) Geology of the southern Zambales Ophiolite Complex, Luzon, Philippines. *Island Arc 9:542–555*. https://doi.org/10.1111/j.1440-1738.2000.00300.x

Yumul GP, **Dimalanta CB**, **Maglambayan VB**, and **Marquez EJ** (2008a) Tectonic setting of a composite terrane: A review of the Philippine island arc system. *Geosciences Journal 12:7–17*. https://doi.org/10.1007/s12303-008-0002-0

Yumul GP, **Dimalanta CB**, **Tamayo RA**, and **Barretto JAL** (2008b) Contrasting morphological trends of islands in Central Philippines: Speculation on their origin. *Island Arc 9:627–637*. https://doi.org/10.1111/j.1440-1738.2000.00307.x

Yumul GP, **Dimalanta CB**, **Tamayo RA**, **Maury RC**, **Bellon H**, **Polvé M**, **Maglambayan VB**, **Querubin CL**, and **Cotten J** (2004) Geology of the Zamboanga Peninsula, Mindanao, Philippines: An enigmatic South China continental fragment? *Geological Society Special Publication 226:289–312*. https://doi.org/10.1144/GSL.SP.2004.226.01.16

Yumul GP, **Queaño KL**, **Padrones JT**, **Dimalanta CB**, and **Andal EA** (2020b) Adakitic Paracale Granodiorite in southeastern Luzon, Philippines: A peek at a Proto-Philippine Sea Plate-related magmatic arc. *Journal of Asian Earth Sciences: X 4:100035*. https://doi.org/10.1016/j.jaesx.2020.100035

Zhang Y, **Tian J**, **Hollings P**, **Gong L**, **Alburo I**, **Berador AE**, **Francisco DG**, **Li J**, and **Chen H** (2020) Mesozoic porphyry Cu–Au mineralization and associated adakite-like magmatism in the Philippines: insights from the giant Atlas deposit. *Mineralium Deposita 55:881–900*. https://doi.org/10.1007/s00126-019-00907-2

Zonge K, **Wynn J**, and **Urquhart S** (2005) 9. Resistivity, Induced Polarization, and Complex Resistivity. In: Near-Surface Geophysics. Society of Exploration Geophysicists, pp 265–300

Appendix 1: Inverse Theory

The basic inverse theory described in this section is generally adapted from Loke (2012). Geophysical inversion aims to create a model that produces results comparable to the observed data. The model is a mathematically idealized depiction of a part of the earth. The model has a collection of parameters representing the physical quantities to be estimated from the observable data. For a given set of model parameters, the model response is the synthetic data that may be generated from the mathematical connections that define the model. All inversion approaches simply attempt to find a model for the subsurface whose response agrees with the observed data within specified constraints and boundaries. The observed data can be represented by certain measured values (e.g., apparent resistivity, acceleration due to gravity). On the other hand, the model parameters in the cell-based technique are the model cells' physical properties (e.g., resistivity, chargeability, density). The finite-difference or finite-element approaches provide the mathematical link between the model parameters and the model response for the 2-D and 3-D resistivity models (e.g., Dey and Morrison, 1979; Silvester and Ferrari., 1996; Loke, 2015).

An initial model is iteratively updated to decrease the discrepancy between the model response and the observed data values when using the optimization technique. The observed data and model response may be expressed as a column vector $\boldsymbol{y}$, and $\boldsymbol{f}$, respectively.

$$\boldsymbol{y} = col(y_1, y_2, \dots, y_m) \quad \text{(A1)}$$

$$\boldsymbol{f} = col(f_1, f_2, \dots, f_m) \quad \text{(A2)}$$

The m represents the number of measurements. The model parameters can be expressed as vector $\boldsymbol{q}$.

$$\boldsymbol{q} = col(q_1, q_2, \dots, q_n) \quad \text{(A3)}$$

The n represents the number of model parameters. The vector $\boldsymbol{g}$ signifies the difference between the observed data ($\boldsymbol{y}$) and the model response ($\boldsymbol{f}$).

$$\boldsymbol{g} = \boldsymbol{y} - \boldsymbol{f} \quad \text{(A4)}$$

The initial model is updated in the least-squares optimization approach so that the sum of squares error E of the difference between the model response and the observed data values is minimized.

$$E = \boldsymbol{g}^T \boldsymbol{g} = \sum_{i=1}^{n} g_i^{\mathbf{2}} \quad \text{(A5)}$$

The Gauss-Newton equation is used to compute the change in model parameters that should lower the sum of squares error (Lines and Treitel, 1984).

$$\boldsymbol{J}^T\boldsymbol{J}\,\Delta\boldsymbol{q}_i = \boldsymbol{J}^T\boldsymbol{g} \qquad \text{(A6)}$$

The $\boldsymbol{J}$ represents the Jacobian matrix (with size m by n) of partial derivatives, while the $\Delta\boldsymbol{q}$ denotes the model parameter change vector. The Jacobian matrix elements describe the change in the ith model response induced by changing the jth model parameter:

$$J_{ij} = \frac{\partial f_i}{\partial q_j}. \qquad \text{(A7)}$$

A new model ($\boldsymbol{q}_{k+1}$) is generated after computing the parameter change vector.

$$\boldsymbol{q}_{k+1} = \boldsymbol{q}_k + \Delta\boldsymbol{q}_k. \qquad \text{(A8)}$$

The parameter change vector generated using the simple least-squares equation (Eq. A6) may contain components that are excessively big, resulting in unrealistic values in the new model ($\boldsymbol{q}_{k+1}$). The Marquardt-Levenberg variation of the Gauss-Newton equation (Eq. A9) is one frequent way to avoid unrealistic values in the new model (Lines and Treitel, 1984; Loke, 2012).

$$(\boldsymbol{J}^T\boldsymbol{J} + \lambda\boldsymbol{I})\Delta\boldsymbol{q}_k = \boldsymbol{J}^T\boldsymbol{g} \qquad \text{(A9)}$$

The λ is referred to as the Marquardt or damping factor, while the $\boldsymbol{I}$ is the identity matrix. This technique is also known as ridge regression (Inman, 1975) . The damping factor (λ) essentially limits the range of values that the components of the parameter change vector ($\Delta\boldsymbol{q}$) can take. The Marquardt-Levenberg technique also reduces the magnitude of the discrepancy vector and the parameter change vector (Loke, 2012).

When the number of model parameters is enormous (e.g., 2-D and 3-D inversion models), the model created by this approach can have an unpredictable model parameter value distribution (Constable et al., 1987). To address this issue, the Gauss-Newton least-squares equation is modified further to reduce the spatial changes in model parameters (e.g., smooth change in the model parameter values). The smoothness-constrained least-squares (l_2 norm) technique (e.g., Ellis and Oldenburg, 1994) can be represented by

$$(\boldsymbol{J}^T\boldsymbol{J} + \lambda\boldsymbol{F})\Delta\boldsymbol{q}_k = \boldsymbol{J}^T\boldsymbol{g} - \lambda\boldsymbol{F}\boldsymbol{q}_k. \qquad \text{(A10)}$$

$$\mathbf{F} = \alpha_x\boldsymbol{C}_x^T\boldsymbol{C}_x + \alpha_y\boldsymbol{C}_y^T\boldsymbol{C}_y + \alpha_z\boldsymbol{C}_z^T\boldsymbol{C}_z \qquad \text{(A11)}$$

$\boldsymbol{C}_x$, $\boldsymbol{C}_y$, and $\boldsymbol{C}_z$ are the roughness filter matrices that relate the model blocks in the x, y, and z directions, while the α_x, α_{xy}, and α_z are the relative weights assigned to the roughness filters in the x, y, and z directions, respectively (Degroot-Hedlin and Constable, 1990).

In certain circumstances, the subsurface geology is divided into distinct zones with sharp boundaries. In such circumstances, Eq. A10 might be changed to minimize the absolute changes in the model resistivity values (Claerbout and Muir, 1973). The equation below represents the l_1 norm smoothness-constrained optimization approach (blocky inversion method) (Wolke and Schwetlick, 1988; Farquharson and Oldenburg, 1998).

$$(\boldsymbol{J}^T\boldsymbol{R}_d\boldsymbol{J} + \lambda\boldsymbol{F}_R)\Delta\boldsymbol{q}_k = \boldsymbol{J}^T\boldsymbol{R}_d\boldsymbol{g} - \lambda\boldsymbol{F}_R\boldsymbol{q}_k. \quad \text{(A12)}$$

$$\boldsymbol{F}_R = \alpha_x\boldsymbol{C}_x^T\boldsymbol{R}_m\boldsymbol{C}_x + \alpha_y\boldsymbol{C}_y^T\boldsymbol{R}_m\boldsymbol{C}_y + \alpha_z\boldsymbol{C}_z^T\boldsymbol{R}_m\boldsymbol{C}_z \quad \text{(A13)}$$

$\boldsymbol{R}_d$ and $\boldsymbol{R}_m$ are weighting matrices introduced to give equal weights to different parts of the data misfit and model roughness vectors during the inversion process (Loke, 2012).

Appendix 2: Sample Program for 3-D Gravity Inversion

```
!-------------------------------------------------------------
!      3-D INVERSION PROGRAM!
!
      Implicit None
      Integer, Parameter :: mxp=9000, mxd=2000, mxn=1000
      Integer, Parameter ::itmax=500, mdata=638
      Real(kind(0d0)), Parameter :: pi=3.14159265358979D0
      Real(kind(0d0)), Parameter :: eps=1.0D-10, epl=0.5D-5
      Real(kind(0d0)) :: par(mxp), dpar(mxp), axis(mxd, 2), obs(mxd)
      Real(kind(0d0)) :: par0(mxp)
      Real(kind(0d0)) :: ajac(mxd+mxp, mxp), dx(mxd+mxp)
      Real(kind(0d0)) :: aj(mxd+mxp, mxp), obs0(mxd), wt(mxd)
!
      Real(kind(0d0)) :: xa(mxn), ya(mxn), za(mxn), wij(mxd, mxp)
      Real(kind(0d0)) :: fnew(mxd), fold(mxd), rnew(mxd), rold(mxd), ptem(mxp)
      Real(kind(0d0)) :: smooth, rmyu, snew, sold
      Real(kind(0d0)) :: rms, abf, abdf, delta, parx, calc
      Real(kind(0d0)) :: rnd1, rnd2
      Real(kind(0d0)) :: x0(650),y0(650),ob(650),a1,b1,z0,x1,y1,z1,x2,y2,z2,rho0,g
      Integer :: i, j, k, nxx, nyy, nzz, npara, npa, np, ierr, icond
      character*10 :: dummy
      character*10 :: fname
!-------------------
!    for LSQR
!-------------------
      External :: aprod
      Integer :: istop, itnlim, nout, m, n, itr, ijk, ijcode, itn
      Real(kind(0d0)) :: damp, dra, rm
!

      Integer, Parameter :: imul=30, maxm=10000*imul, maxn=10000*imul
      Real(kind(0d0)) :: u(maxm), v(maxn), w(maxn), x(maxn), se(maxn)
      Real(kind(0d0)) :: atol, btol, conlim, anorm, acond, rnorm, arnorm, xnorm
!

      Integer, Parameter :: imax=10000, jmax=10000, ijmax=imax*jmax/10
      Real(kind(0d0)) :: val(ijmax)
      Integer :: irow(imax), jcol(ijmax)
      Common /lbl1/val
      Common /lbl2/irow, jcol
!
      call random_seed()
!-----------------------------
!  Location of Observed Points
!-----------------------------
      Open (1, file = 'CVB1_data.txt', Status = 'Old', Action = 'Read')
      read(1,*) dummy
      Do i = 1, mdata
        Read (1, *) x0(i), y0(i), ob(i)
        write(6, *) x0(i), y0(i), ob(i)
        wt(i)= 1.0d0
      End Do
      Continue
```

```
!------------------------------
!  Location of gravity blocks
!------------------------------

      nxx=50

      nyy=40

      nzz=5
!
      do i=1, nxx
        xa(i)=303.0d0+2.00d0*(i-1)
      enddo
!
      do j=1, nyy

        ya(j)=1936.0d0+2.00d0*(j-1)
      enddo
!
      do k=1, nzz
        za(k)=0.0d0+2.00*(k-1)

      enddo
!
      npara = (nxx-1)*(nyy-1)*(nzz-1) ! Caution
!
!-----------------------
!     CALC. JACOBIAN
!-----------------------
      rho0 = 1.0d0
      z0=0.0d0
!
      npa = 0
      Do k = 1, nzz-1
        z1 = za(k)
        z2 = za(k+1)
        Do j = 1, nyy-1
          y1 = ya(j)
          y2 = ya(j+1)
          Do i = 1, nxx-1
            x1 = xa(i)
            x2 = xa(i+1)
            npa = npa + 1
            Do m = 1, mdata
              a1=x0(m)
              b1=y0(m)
              call gbox1(a1,b1,z0,x1,y1,z1,x2,y2,z2,rho0,g)
              wij(m, npa) = g
              ajac(m, npa) = g*sqrt(wt(m))
            End Do
          End Do
        End Do
      End Do
```

```
!-----------------------
!   Calc. Observed Data
!-----------------------
      do i=1, mdata
        obs0(i)= ob(i)
      enddo
      obs=obs0
!---------------------------
!   SMOOTHNESS FACTOR
!---------------------------
      smooth=0.0010d0 ! Original
!      smooth=0.1d0
!      smooth=0.005d0
      rmyu = sqrt(smooth)
!
      Do i = 1, npara
        par(i) = 0.0d0
      End Do
!
      snew = 0.0d0
      Do i = 1, mdata
        rnew(i) = obs(i)*sqrt(wt(i))
        fnew(i) = 0.0d0
        snew = snew + rnew(i)*rnew(i)
      End Do

!========================
!  LEAST SQUARE SOLUTION
!========================
      Do itr = 1, itmax
!-------------------
!  INPUT JACOBIAN
!-------------------
        Do i = 1, mdata
          Do j = 1, npara
            aj(i, j) = ajac(i, j)
          End Do
        End Do
        Do i = 1, npara
          Do j = 1, npara
            aj(i+mdata, j) = 0.0
          End Do
        End Do
!-------------------------------------
!  INPUT SMOOTH PARAMETER TO JACOBIAN
!-------------------------------------
        ijk = 0
        rm = rmyu
        Do k = 1, nzz-1
          rm = rmyu*(1.0+(k-1)/10.0)
          Do j = 1, nyy-1
            Do i = 1, nxx-1
              ijk = ijk + 1
```

```
              If (i/=1) Then
                aj(ijk+mdata, ijk-1) = rm
                aj(ijk+mdata, ijk) = aj(ijk+mdata, ijk) - rm
              End If
              If (i/=nxx) Then
                aj(ijk+mdata, ijk+1) = rm
                aj(ijk+mdata, ijk) = aj(ijk+mdata, ijk) - rm
              End If
              If (j/=1) Then
                aj(ijk+mdata, ijk-nxx) = rm
                aj(ijk+mdata, ijk) = aj(ijk+mdata, ijk) - rm
              End If
              If (j/=nyy) Then
                aj(ijk+mdata, ijk+nxx) = rm
                aj(ijk+mdata, ijk) = aj(ijk+mdata, ijk) - rm
              End If
              If (k/=1) Then
                aj(ijk+mdata, ijk-nxx*nyy) = rm
                aj(ijk+mdata, ijk) = aj(ijk+mdata, ijk) - rm
              End If
              If (k/=nzz) Then
                aj(ijk+mdata, ijk+nxx*nyy) = rm
                aj(ijk+mdata, ijk) = aj(ijk+mdata, ijk) - rm
              End If
!
            End Do
          End Do
        End Do
!
        Do i = 1, mdata
          dx(i) = rnew(i)
        End Do
        Do i = 1, npara
          dx(i+mdata) = 0.0
        End Do
!
!        Call lls(aj, mxd+mxp, mdata+npara, npara, dx, ierr)
!
!-------  use lsqr -------------
        atol = 1.0D-10
        btol = atol
        m = mdata + npara
        n = npara
        damp = 0.0
        itnlim = m + n + 50
        nout = 6
        Do i = 1, m
          u(i) = dx(i)
        End Do
        ijcode = 0
        Do i = 1, m
          irow(i) = ijcode + 1
          Do j = 1, n
```

```
            If (aj(i,j)/=0.0) Then
              ijcode = ijcode + 1
              val(ijcode) = aj(i, j)
              jcol(ijcode) = j
            End If
          End Do
        End Do
        irow(m+1) = ijcode + 1
        Call lsqr(m, n, aprod, damp, u, v, w, x, se, atol, btol, conlim, &
          itnlim, nout, istop, itn, anorm, acond, rnorm, arnorm, xnorm)
!-------  use lsqr -------------
!----------------------
!  CALC. NEW DATA
!----------------------
        Do i = 1, mdata
          fold(i) = fnew(i)
          rold(i) = rnew(i)
        End Do
        Do i = 1, npara

          dpar(i) = x(i)
          ptem(i) = par(i) + dpar(i)
        End Do
!---------------------------
!   CALC. NEW SP VALUES
!---------------------------
        Do i = 1, mdata
          dra = 0.0
          Do j = 1, npara
            dra = dra + ptem(j)*wij(i, j)
          End Do
          fnew(i) = dra
        End Do
!---------------------------------
!   CALC. NEW RESIDUAL
!---------------------------------
        sold = snew
        snew = 0.0
        Do i = 1, mdata
          rnew(i) = (obs(i)-fnew(i))*sqrt(wt(i))
          snew = snew + rnew(i)*rnew(i)
        End Do
        rms = sqrt(snew/mdata)
!----------------------
!   CONVERGENCE CHECK
!----------------------
        If (snew<sold) Then
          abf = 0.0
          abdf = 0.0
          Do i = 1, mdata
            abf = abf + abs(fnew(i))
            abdf = abdf + abs(fold(i)-fnew(i))
          End Do
```

```
          delta = abdf/abf
          If (delta<=epl) Then
            Do i = 1, npara
              par(i) = par(i) + dpar(i)
            End Do
            icond = 0
            Go To 170
          End If
!-----------------------
!   SET NEW PARAMETER
!-----------------------
          Do i = 1, npara
            par(i) = par(i) + dpar(i)
          End Do
          rmyu = 0.5*rmyu
        Else
          Do i = 1, npara
            dpar(i) = 0.0
          End Do
          rmyu = 2.0*rmyu
        End If
!-------------------------------
!  PRINT INTERMEDIATE RESULT
!-------------------------------
!      WRITE(6,*) ' '
!      WRITE(6,*) ' ************************** '
!      WRITE(6,*) '    INTERMEDIATE RESULTS '
!      WRITE(6,*) ' ************************** '
!      WRITE(6,*) '  '
!      WRITE(6,*) '   ITERATION : ',ITR
!      WRITE(6,*) '   RMS       : ',RMS
       Write (6, *) '  ITERATION: ', itr, ' RMS: ', rms
!      WRITE(6,*) '  '
!
!      WRITE(6,*) ' SP POINTS  X-AXIS   Y-AXIS   Z-AXIS   STRENGTH'
!      NP=0
!      DO 981 K=1,NZZ
!       DO 982 J=1,NYY
!         DO 983 I=1,NXX
!          NP=NP+1
!          PARX=PAR(NP)
!          WRITE(6,112) NP,XA(I),YA(J),ZA(K),PARX
!  983    CONTINUE
!  982  CONTINUE
!  981 CONTINUE
!
      End Do
!
170   Continue
!------------------------
!    PRINT FINAL RESULT
!------------------------
       fname='CVB1.txt'
```

```
      open(6,file=fname,status='new')
!     Write (6, *) '  '
!     Write (6, *) ' ************************************************** '
!     Write (6, *) '  3-D Gravity inversion by H.Mizunaga @ Kyushu Univ.  '
!     Write (6, *) ' ************************************************** '
!     Write (6, *) '  '
!     Write (6, 180) smooth
!     Write (6, *) '  '
!180   Format ('    SMOOTHNESS FACTOR   : ', F10.5)
!
!     Write (6, *) ' SP POINTS  X-AXIS   Y-AXIS   Z-AXIS   STRENGTH'
      np = 0
      Do k = 1, nzz-1
        Do j = 1, nyy-1
          Do i = 1, nxx-1
            np = np + 1
            parx = par(np)

            Write (6,  '(i6, 3f8.2, e14.6)') np, (xa(i)+xa(i+1))/2.0, (ya(j)+ya(j+1))/2.0, -(za(k)+za(k+1))/2.0, parx

          End Do
        End Do
      End Do
!190   Format (' ', I7, 2X, 3F8.2, 2E14.6)
!
      Write (6, *) '      '
      Write (6, *) '      '
!     Write (6, *) '  x0(i)    y0(i)     OBS.           CAL.           RES. '
      Do i = 1, mdata
        calc = fnew(i)
!       Write (6, 200) i, obs0(i), calc, obs0(i) - calc
!       Write (6, '(2f10.3,3e15.7)') x0(i), y0(i), obs0(i), calc, obs0(i) - calc
      End Do
!200   Format (' ', I6, 3E15.7)
!
    End Program
!------------------
!   Haaz(1953)
!------------------
subroutine gbox1(a1,b1,z0,x1,y1,z1,x2,y2,z2,rho,g)
  implicit none
  real(kind(0d0)),intent(in)  :: a1,b1,z0,x1,y1,z1,x2,y2,z2,rho
  real(kind(0d0)),intent(out) :: g
!
  real(kind(0d0)),parameter :: pi=3.14159265358979d0, twopi=2.0d0*pi
  real(kind(0d0)),parameter :: gamma=6.670d-11, si2mg=1.0d+5, km2m=1.0d+3
  real(kind(0d0)) :: x(2), y(2), z(2), sum
  real(kind(0d0)) :: rijk, arg1, arg2, arg3
!
  integer :: i, j, k, ijk
  integer :: isign(2)
  data isign /-1, 1/
!
```

```
!
  if(x2-x1 <= 0.0d0) stop 'GBOX1 : x-axis error <= 0.0'
  if(y2-y1 <= 0.0d0) stop 'GBOX1 : y-axis error <= 0.0'
  if(z2-z1 <= 0.0d0) stop 'GBOX1 : z-axis error <= 0.0'
!
  x(1)=a1-x1
  y(1)=b1-y1
  z(1)=z0-z1
  x(2)=a1-x2
  y(2)=b1-y2
  z(2)=z0-z2
  sum=0.0d0
!
  do i=1,2
    do j=1,2
      do k=1,2
        rijk=sqrt(x(i)**2+y(j)**2+z(k)**2)
        ijk=isign(i)*isign(j)*isign(k)
        arg1=atan2(x(i)*y(j),z(k)*rijk)
        if(arg1 < 0.0d0) arg1=arg1+twopi
        arg2=rijk+y(j)
        arg3=rijk+x(i)
        sum=sum+ijk*(z(k)*arg1-x(i)*log(arg2)-y(j)*log(arg3))
      enddo
    enddo
  enddo
  g=rho*gamma*sum*si2mg*km2m
!
end subroutine gbox1
!
!     ***************
!     *     LLS     *
!     ***************
    Subroutine lls(a, max, m, n, b, irc)
      Implicit None
      Integer, Parameter :: mxp=9000
      Integer, intent(in) :: max, m, n
      Integer :: irc, i, j, k, ip
      Integer :: iw(mxp)
      Real(kind(0d0)) :: a(max, n), b(m), w(mxp)
      Real(kind(0d0)) :: sig, sum, temp, dk, bk
      Real(kind(0d0)) :: eps = 16.0d0**(-13)  !  Machine Epsilon
!
!     COMPUTE NORM FOR EACH COLUM OF ORIGINAL MATRIX,
!
!     SET UP PIVOTTING INFORMATIONS.
!
      irc = 0
      sig = -1.0d0
      Do j = 1, n
        sum = 0.0D0
        Do i = 1, m
          sum = sum + a(i, j)*a(i, j)
```

```
        End Do
        w(j) = sum
        iw(j) = j
        If (sig<sum) sig = sum
      End Do
      eps = sig*eps*eps
!
!     HOUSEHOLDER'S TRANSFORMATION
!
      Do k = 1, n
!
!     SEARCH PIVOT COLUMN WHICH HAS THE BIGGEST NORM
!
        sig = -1.0
        Do j = k, n
          If (sig>w(j)) Go To 100
          sig = w(j)
          ip = j
100     End Do
!
!     PIVOTTING (COLUMN INTERCHANGE)
!
        If (ip/=k) Then
          iw(k) = ip
          w(ip) = w(k)
          Do i = 1, m
            temp = a(i, k)
            a(i, k) = a(i, ip)
            a(i, ip) = temp
          End Do
        End If
!
        sum = 0.0D0
        Do i = k, m
          sum = sum + a(i, k)*a(i, k)
        End Do
!
!     SET UP ORTHOGONAL MATRIX OF K-TH STAGE
!
        If (sum>eps) Then
          dk = -sign(sqrt(sum), a(k,k))
          bk = 1.0D0/(sum-a(k,k)*dk)
          a(k, k) = a(k, k) - dk
          w(k) = dk
          Do j = k + 1, n
            sum = 0.0D0
            Do i = k, m
              sum = sum + a(i, j)*a(i, k)
            End Do
            w(n+j) = sum*bk
          End Do
!
          Do j = k + 1, n
```

```
            Do i = k, m
              a(i, j) = a(i, j) - a(i, k)*w(n+j)
            End Do
            w(j) = w(j) - a(k, j)*a(k, j)
          End Do
        Else
          irc = 10
          Return
        End If
      End Do
!
!     APPLY ORTHOGONAL TRANSFORM TO CONSTANT VECTOR
!
      Do j = 1, n
        sum = 0.0D0
        Do i = j, m
          sum = sum + a(i, j)*b(i)
        End Do
        sum = sum/(w(j)*a(j,j))
        Do i = j, m
          b(i) = b(i) + sum*a(i, j)
        End Do
      End Do
!
!     COMPUTE SOLUTION BY BACKWARD SUBSTITUTIONS
!
      b(n) = b(n)/w(n)
      Do i = n - 1, 1, -1
        sum = 0.0D0
        Do j = i + 1, n
          sum = sum + a(i, j)*b(j)
        End Do
        b(i) = (b(i)-sum)/w(i)
      End Do
!
!     REORDER THE SOLUTION ACCORDING TO PIVOTTING HISTORY
!
      Do j = 1, n
        i = n - j + 1
        temp = b(i)
        b(i) = b(iw(i))
        b(iw(i)) = temp
      End Do
      Return
    End Subroutine lls
!
!-------------
!    lsqr
!-------------
    Subroutine lsqr(m, n, aprod, damp, u, v, w, x, se, atol, btol, conlim, &
        itnlim, nout, istop, itn, anorm, acond, rnorm, arnorm, xnorm)
!
      Implicit None
```

```
      External aprod
      Integer  :: m, n, itnlim, nout, istop, itn
      Real(kind(0d0)) :: u(m), v(n), w(n), x(n), se(n), atol, btol, conlim, &
        damp, anorm, acond, rnorm, arnorm, xnorm

!     intrinsics and local variables

      Integer :: i, nconv, nstop
      Real(kind(0d0)) :: dnrm2
      Real(kind(0d0)) :: alfa, bbnorm, beta, bnorm, cs, cs1, cs2, ctol, dampsq, &
        ddnorm, delta, gamma, gambar, phi, phibar, psi, res1, res2, rho, &
        rhobar, rhbar1, rhbar2, rhs, rtol, sn, sn1, sn2, t, tau, test1, test2, &
        test3, theta, t1, t2, t3, xxnorm, z, zbar
!
      Real(kind(0d0)), Parameter :: zero=0.0D+0, one=1.0D+0
!
      Character *16 :: enter, exit
      Character *60 :: msg(0:7)
!
      Data enter/' enter lsqr.    '/, exit/' exit  lsqr.    '/

!-----------------------------------------------------------------------
      itn = 0
      istop = 0
      nstop = 0
      ctol = zero
      If (conlim>zero) ctol = one/conlim
      anorm = zero
      acond = zero
      bbnorm = zero
      dampsq = damp**2
      ddnorm = zero
      res2 = zero
      xnorm = zero
      xxnorm = zero
      cs2 = -one
      sn2 = zero
      z = zero
!
      Do i = 1, n
        v(i) = zero
        x(i) = zero
        se(i) = zero
      End Do
!     set up the first vectors u and v for the bidiagonalization.
!     these satisfy  beta*u = b,  alfa*v = a(transpose)*u.
      alfa = zero
      beta = dnrm2(m, u, 1)
      If (beta>zero) Then
        Call dscal(m, (one/beta), u, 1)
        Call aprod(2, m, n, v, u)
        alfa = dnrm2(n, v, 1)
      End If
```

```
      If (alfa>zero) Then
        Call dscal(n, (one/alfa), v, 1)
        Call dcopy(n, v, 1, w, 1)
      End If
      arnorm = alfa*beta
      If (arnorm==zero) Go To 110
      rhobar = alfa
      phibar = beta
      bnorm = beta
      rnorm = beta
      If (nout>0) Then
        test1 = one
        test2 = alfa/beta
      End If
!     ------------------------------------------------------------------
!     main iteration loop.
!     ------------------------------------------------------------------
100   itn = itn + 1
!     perform the next step of the bidiagonalization to obtain the
!     next  beta, u, alfa, v.  these satisfy the relations
!               beta*u  =  a*v  -  alfa*u,
!               alfa*v  =  a(transpose)*u  -  beta*v.
      Call dscal(m, (-alfa), u, 1)
      Call aprod(1, m, n, v, u)
      beta = dnrm2(m, u, 1)
      bbnorm = bbnorm + alfa**2 + beta**2 + dampsq
      If (beta>zero) Then
        Call dscal(m, (one/beta), u, 1)
        Call dscal(n, (-beta), v, 1)
        Call aprod(2, m, n, v, u)
        alfa = dnrm2(n, v, 1)
        If (alfa>zero) Then
          Call dscal(n, (one/alfa), v, 1)
        End If
      End If
!     use a plane rotation to eliminate the damping parameter.
!     this alters the diagonal (rhobar) of the lower-bidiagonal matrix.
      rhbar2 = rhobar**2 + dampsq
      rhbar1 = sqrt(rhbar2)
      cs1 = rhobar/rhbar1
      sn1 = damp/rhbar1
      psi = sn1*phibar
      phibar = cs1*phibar
!     use a plane rotation to eliminate the subdiagonal element (beta)
!     of the lower-bidiagonal matrix, giving an upper-bidiagonal matrix.
      rho = sqrt(rhbar2+beta**2)
      cs = rhbar1/rho
      sn = beta/rho
      theta = sn*alfa
      rhobar = -cs*alfa
      phi = cs*phibar
      phibar = sn*phibar
      tau = sn*phi
```

```
!     update  x, w  and the standard error estimates.
      t1 = phi/rho
      t2 = -theta/rho
      t3 = one/rho
      Do i = 1, n
        t = w(i)
        x(i) = t1*t + x(i)
        w(i) = t2*t + v(i)
        t = (t3*t)**2
        se(i) = t + se(i)
        ddnorm = t + ddnorm
      End Do
!     use a plane rotation on the right to eliminate the
!     super-diagonal element (theta) of the upper-bidiagonal matrix.
!     then use the result to estimate  norm(x).
      delta = sn2*rho
      gambar = -cs2*rho
      rhs = phi - delta*z
      zbar = rhs/gambar
      xnorm = sqrt(xxnorm+zbar**2)
      gamma = sqrt(gambar**2+theta**2)
      cs2 = gambar/gamma
      sn2 = theta/gamma
      z = rhs/gamma
      xxnorm = xxnorm + z**2
!     test for convergence.
!     first, estimate the norm and condition of the matrix  abar,
!     and the norms of  rbar  and  abar(transpose)*rbar.
      anorm = sqrt(bbnorm)
      acond = anorm*sqrt(ddnorm)
      res1 = phibar**2
      res2 = res2 + psi**2
      rnorm = sqrt(res1+res2)
      arnorm = alfa*abs(tau)
!     now use these norms to estimate certain other quantities,
!     some of which will be small near a solution.
      test1 = rnorm/bnorm
      test2 = zero
      If (rnorm>zero) test2 = arnorm/(anorm*rnorm)
      test3 = one/acond
      t1 = test1/(one+anorm*xnorm/bnorm)
      rtol = btol + atol*anorm*xnorm/bnorm
!     the following tests guard against extremely small values of
!     atol, btol  or  ctol.  (the user may have set any or all of
!     the parameters  atol, btol, conlim  to zero.)
!     the effect is equivalent to the normal tests using
!     atol = relpr,  btol = relpr,  conlim = 1/relpr.
      t3 = one + test3
      t2 = one + test2
      t1 = one + t1
      If (itn>=itnlim) istop = 7
      If (t3<=one) istop = 6
      If (t2<=one) istop = 5
```

```
!     allow for tolerances set by the user.
      If (test3<=ctol) istop = 3
      If (test2<=atol) istop = 2
      If (test1<=rtol) istop = 1
!     stop if appropriate.
!     the convergence criteria are required to be met on  nconv
!     consecutive iterations, where  nconv  is set below.
!     suggested value:  nconv = 1, 2  or  3.
      If (istop==0) nstop = 0
      If (istop==0) Go To 100
      nconv = 1
      nstop = nstop + 1
      If (nstop<nconv .And. itn<itnlim) istop = 0
      If (istop==0) Go To 100
!     ------------------------------------------------------------------
!     end of iteration loop.
!     ------------------------------------------------------------------
!     finish off the standard error estimates.
      t = one
      If (m>n) t = m - n
      If (dampsq>zero) t = m
      t = rnorm/sqrt(t)
      Do i = 1, n
        se(i) = t*sqrt(se(i))
      End Do
110   Continue
      Return
!     end of lsqr
    End Subroutine lsqr
!
    Subroutine dcopy(n, x, incx, y, incy)
      Integer n, incx, incy
      Double Precision x(n), y(n)
!
      Do i = 1, n
        y(i) = x(i)
      End Do
      Return
    End Subroutine dcopy
!
    Double Precision Function dnrm2(n, x, incx)
      Integer n, incx, i
      Double Precision x(n), d
!
      d = 0.0
      Do i = 1, n
        d = d + x(i)**2
      End Do
      dnrm2 = dsqrt(d)
!
      Return
    End Function dnrm2
!
```

```
    Subroutine dscal(n, a, x, incx)
      Integer n, incx
      Double Precision a, x(n)
!
      Do i = 1, n
        x(i) = a*x(i)
      End Do
!
      Return
    End Subroutine dscal
!*************************************************************
!     aprod(1,---) : y = y + a * x
!     aprod(2,---) : x = x + a(transpose) * y
!*************************************************************
    Subroutine aprod(mode, m, n, x, y)
      Implicit None
      Integer :: mode, m, n
      Real(kind(0d0)) :: x(n), y(m)
!         case 1: y = y + a * x
      If (mode==1) Then
        Call aprod1(m, n, x, y)
      End If
!         case 2: x = x + a(transpose) * y
      If (mode==2) Then
        Call aprod2(m, n, x, y)
      End If
!
      Return
    End Subroutine aprod
!
    Subroutine aprod1(m, n, x, y)
!     ----------------------------------------------------------------
!     aprod1  computes  y = y + a*x  for subroutine aprod,
!     ----------------------------------------------------------------
      Implicit None
      Integer :: m, n
      Real(kind(0d0)) :: x(n), y(m)
      Integer :: i, j
!      Integer, Parameter :: imax=3000, jmax=3000, ijmax=imax*jmax/10
      Integer, Parameter :: imax=10000, jmax=10000, ijmax=imax*jmax/10
      Real(kind(0d0)) :: val(ijmax)
      Integer :: irow(imax), jcol(ijmax)
      Common /lbl1/val
      Common /lbl2/irow, jcol
!
      Do i = 1, m
        Do j = irow(i), irow(i+1) - 1
          y(i) = y(i) + val(j)*x(jcol(j))
        End Do
      End Do
!
    End Subroutine aprod1
!
```

```
    Subroutine aprod2(m, n, x, y)
!     ------------------------------------------------------------------
!     aprod2  computes  x = x + a(t)*y  for subroutine aprod,
!     ------------------------------------------------------------------
      Implicit None
      Integer :: m, n
      Real(kind(0d0)) :: x(n), y(m)
      Integer :: i, j
!      Integer, Parameter :: imax=3000, jmax=3000, ijmax=imax*jmax/10
      Integer, Parameter :: imax=10000, jmax=10000, ijmax=imax*jmax/10
      Real(kind(0d0)) :: val(ijmax)
      Integer :: irow(imax), jcol(ijmax)
      Common /lbl1/val
      Common /lbl2/irow, jcol
!
      Do j = 1, m
        Do i = irow(j), irow(j+1) - 1
          x(jcol(i)) = x(jcol(i)) + val(i)*y(j)
        End Do
      End Do
!
    End Subroutine aprod2
```

Appendix 3: Copper Concentration in Soil and Rock Samples in the Vicinity of the Study Area from the Report on the Cooperative Mineral Exploration

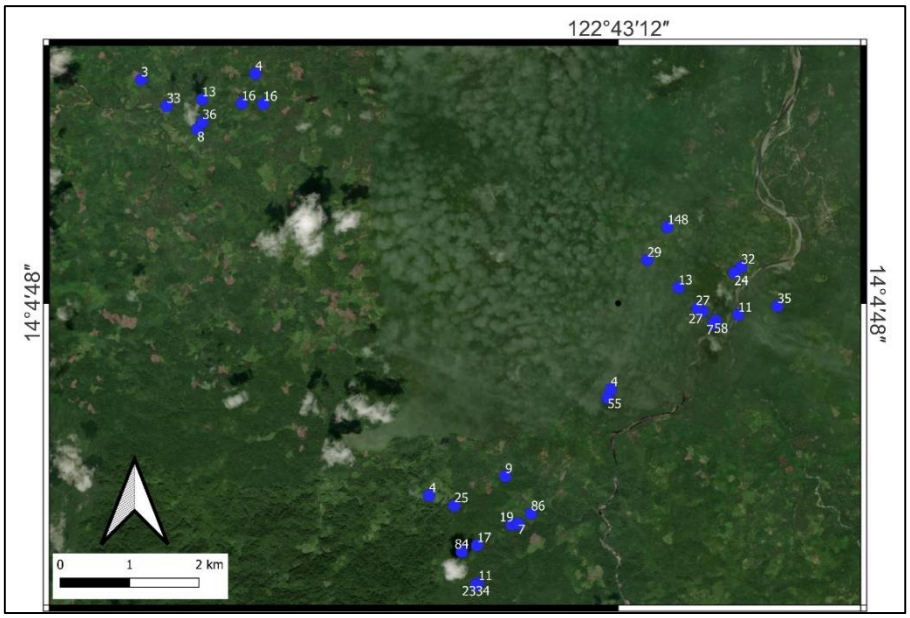

Figure A-1. Sample location map showing the copper concentration (ppm) from whole rock data analysis in the southwestern vicinity of the study area (data from JICA, 2002)

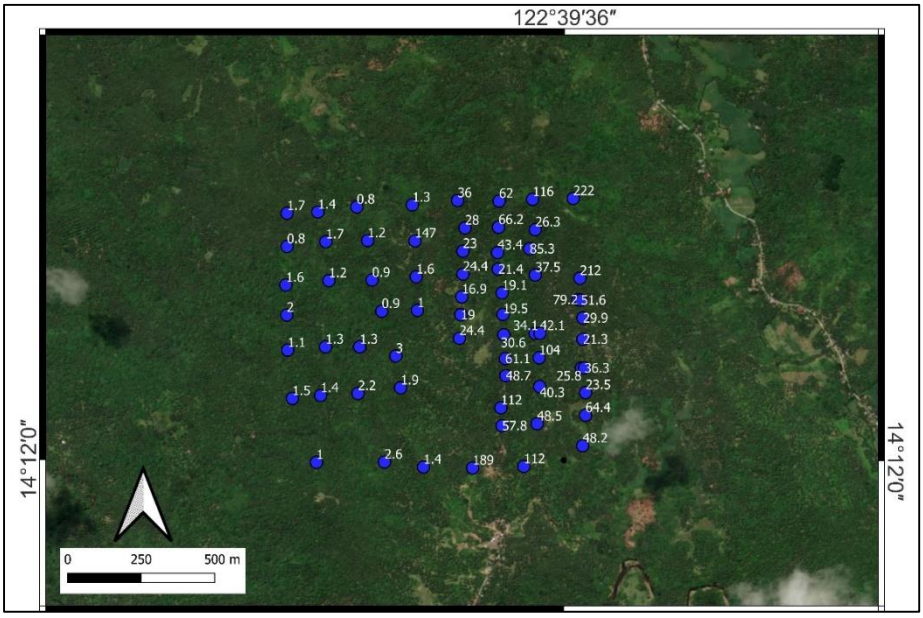

Figure A-2. Sample location map showing the copper concentration (ppm) from soil geochemical analysis in the northwestern vicinity of the study area (data from JICA, 2002)

Appendix 4: Base Maps

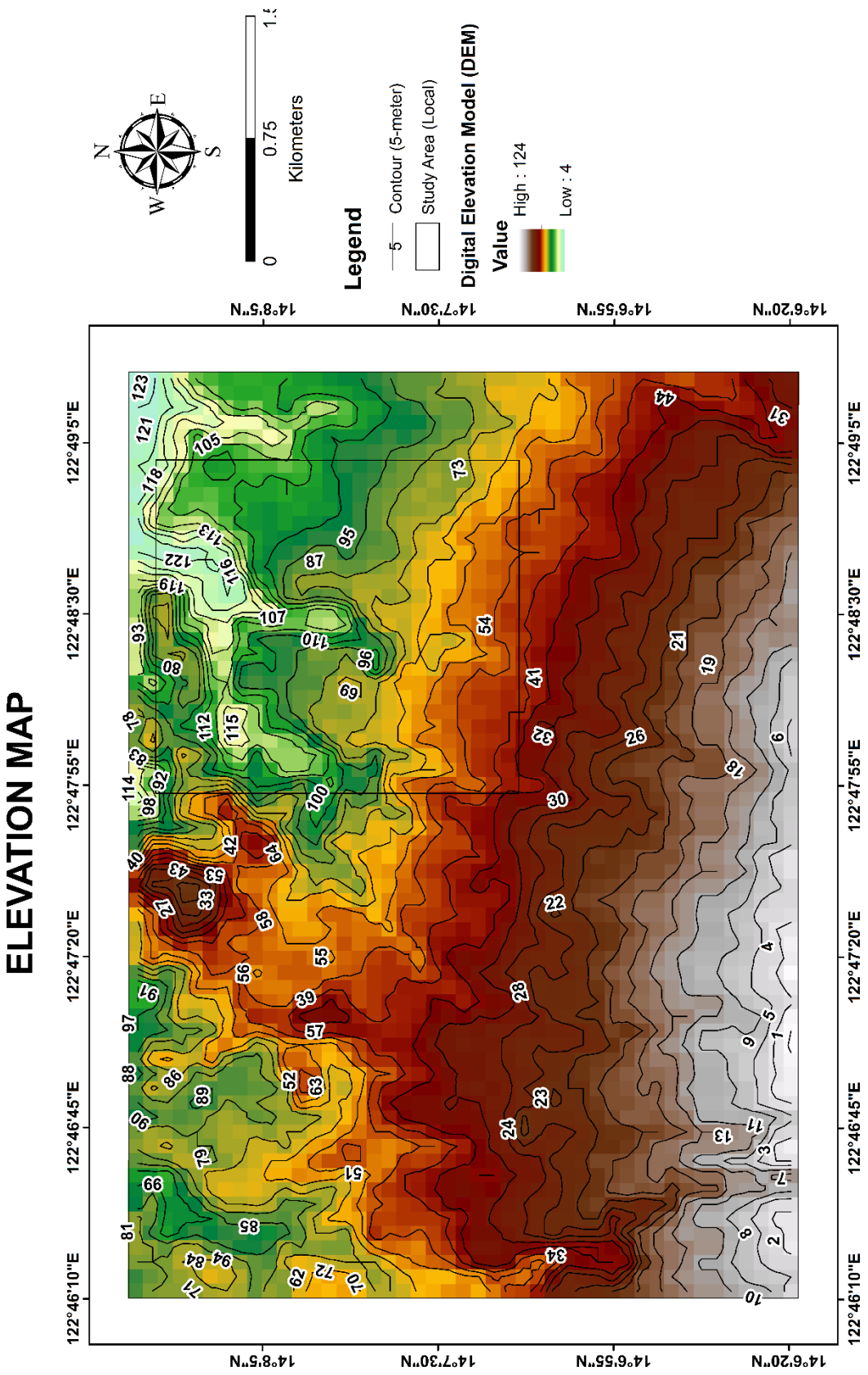

Figure A-3. The elevation map of the study area.

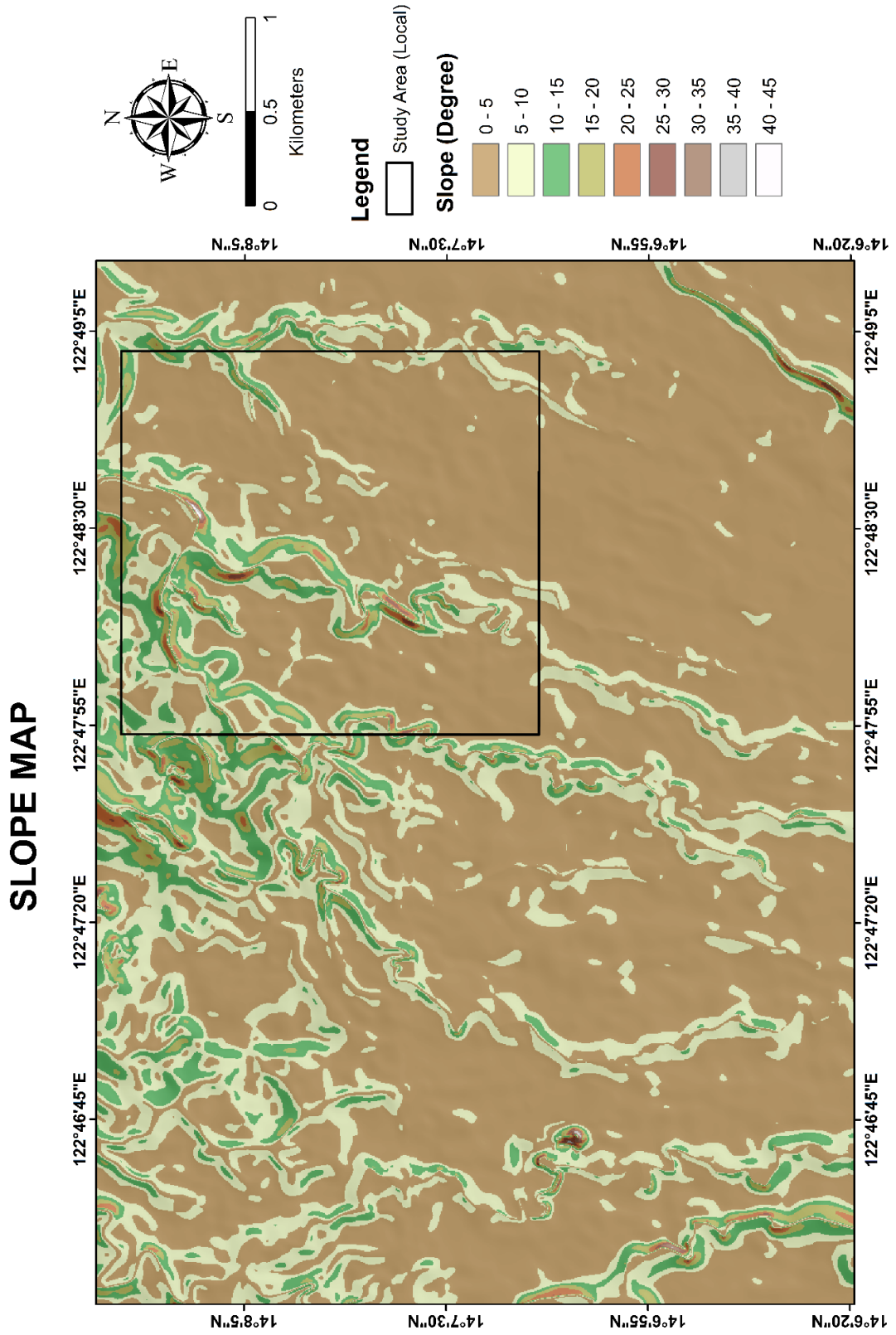

Figure A-4. Slope map of the study area.

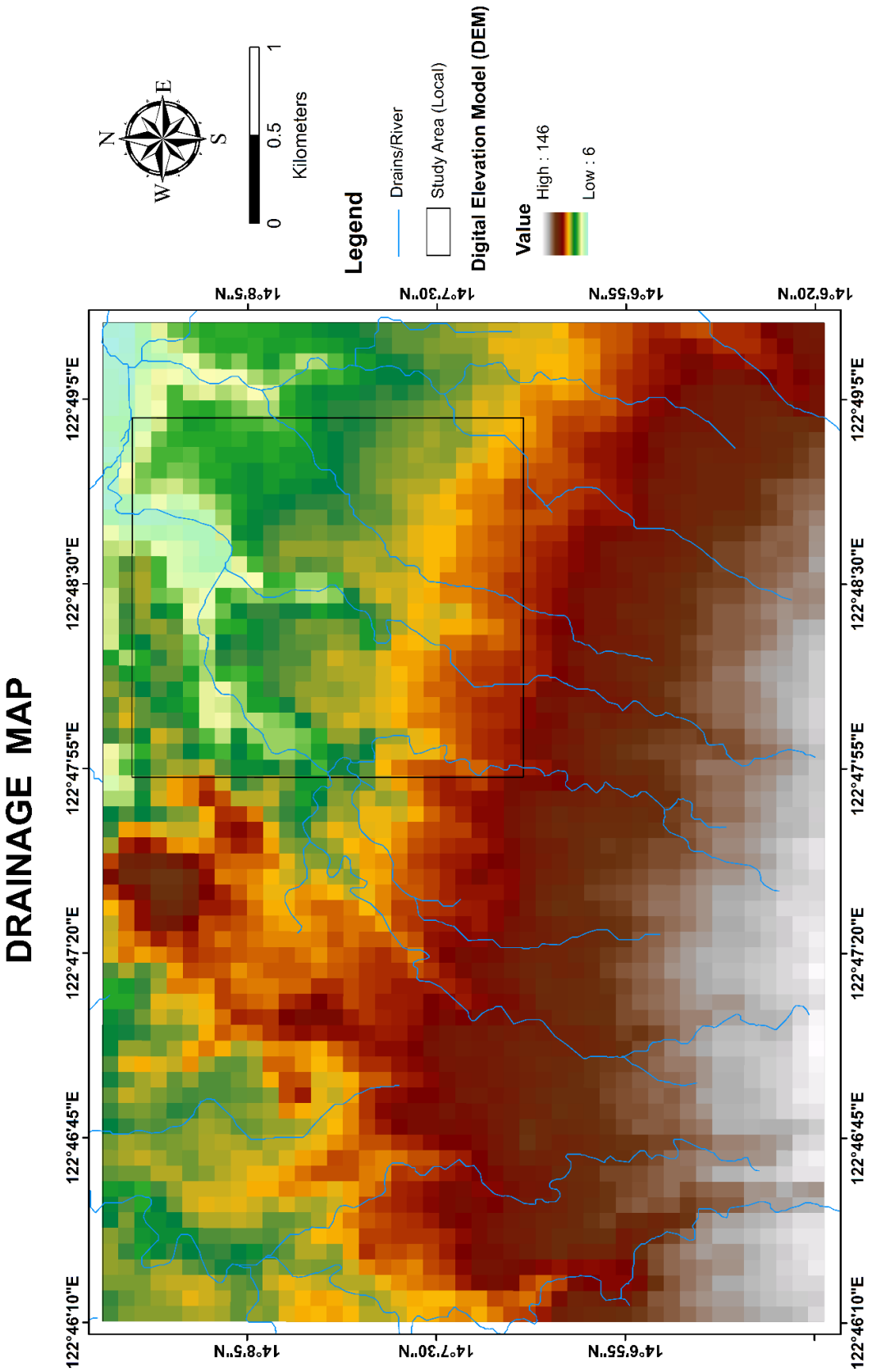

Figure A-5. Drainage map of the study area.

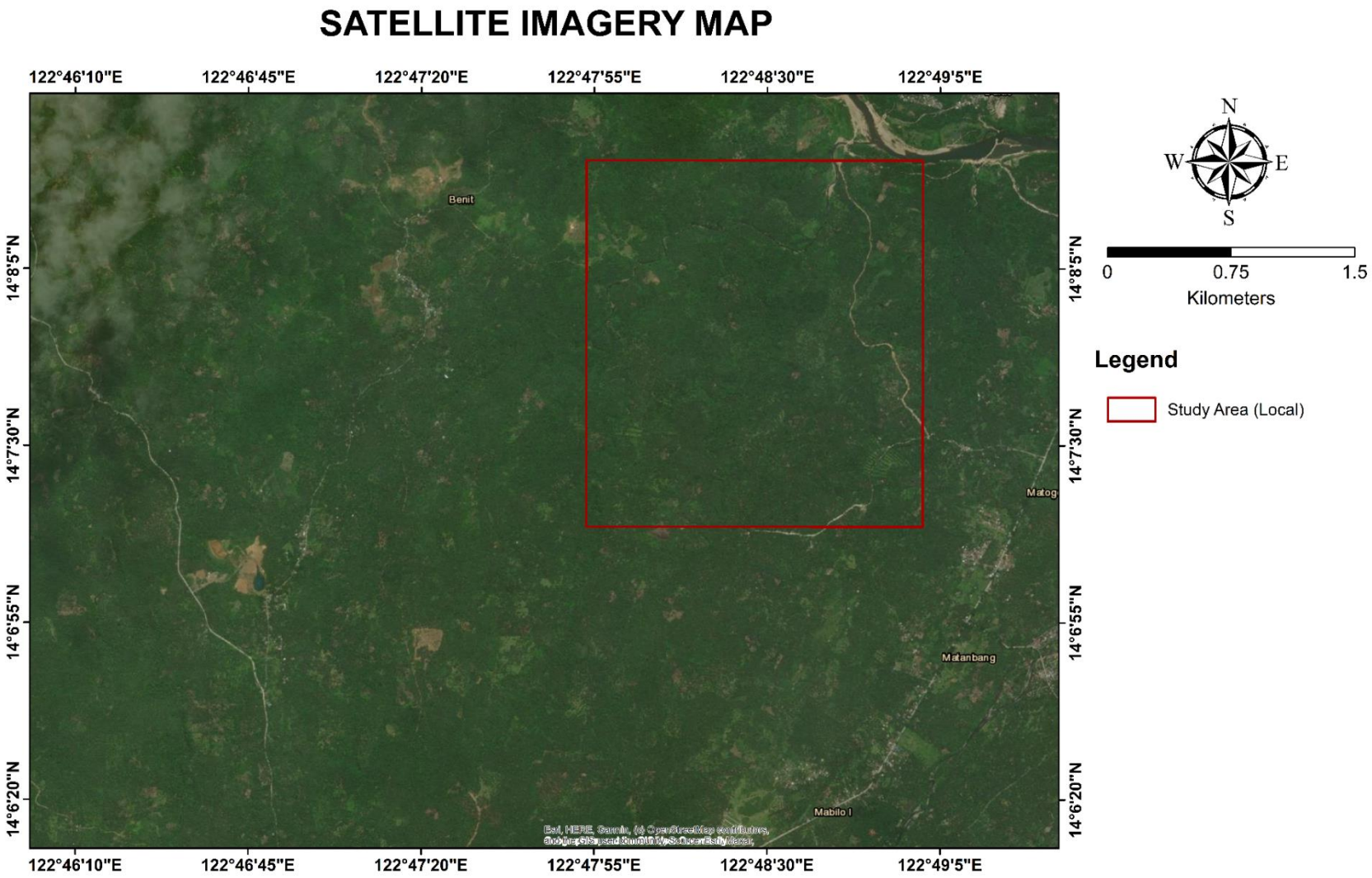

Figure A-6. Satellite imagery map of the study area.

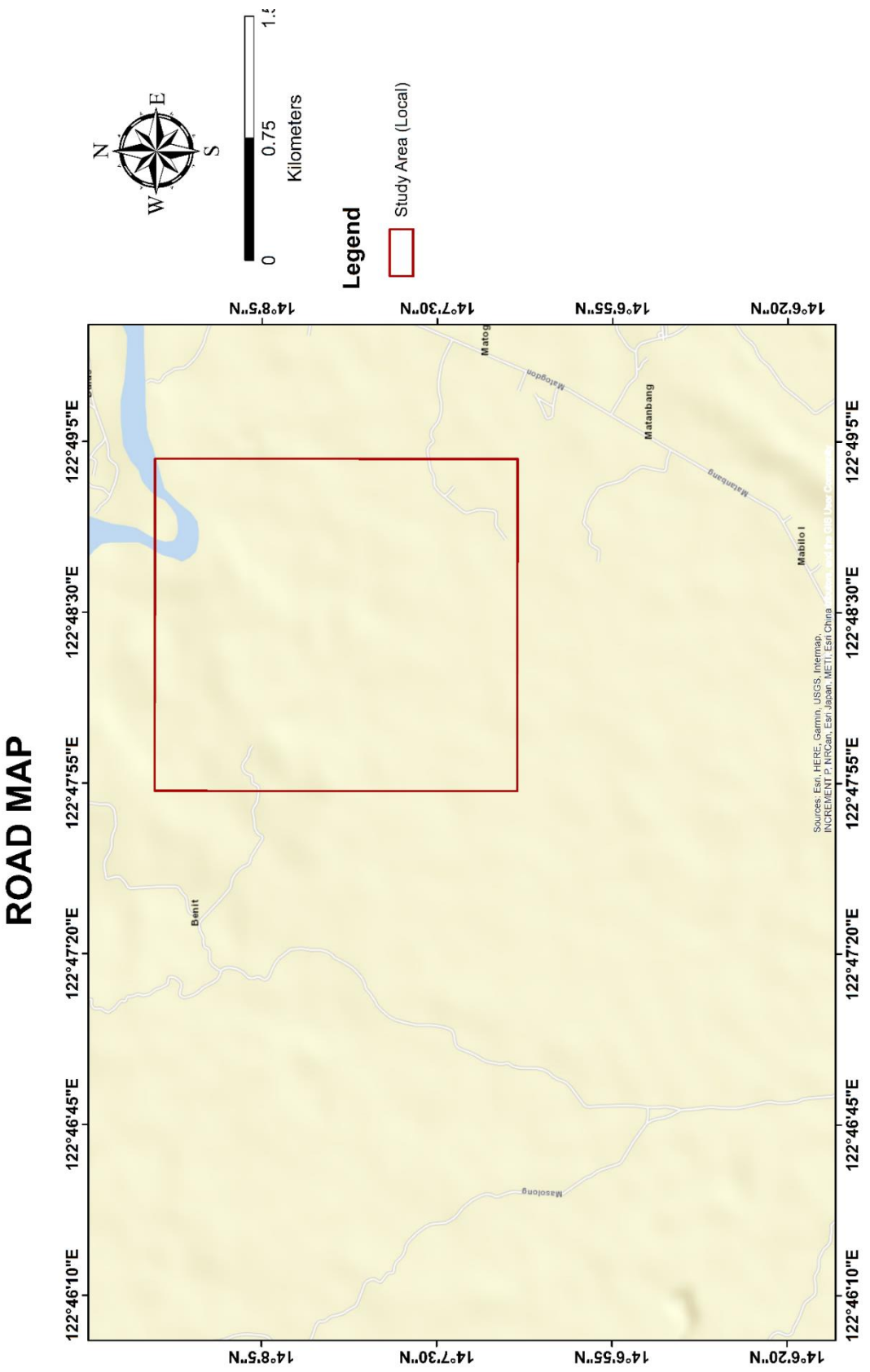

Figure A-7. Road map of the study area.

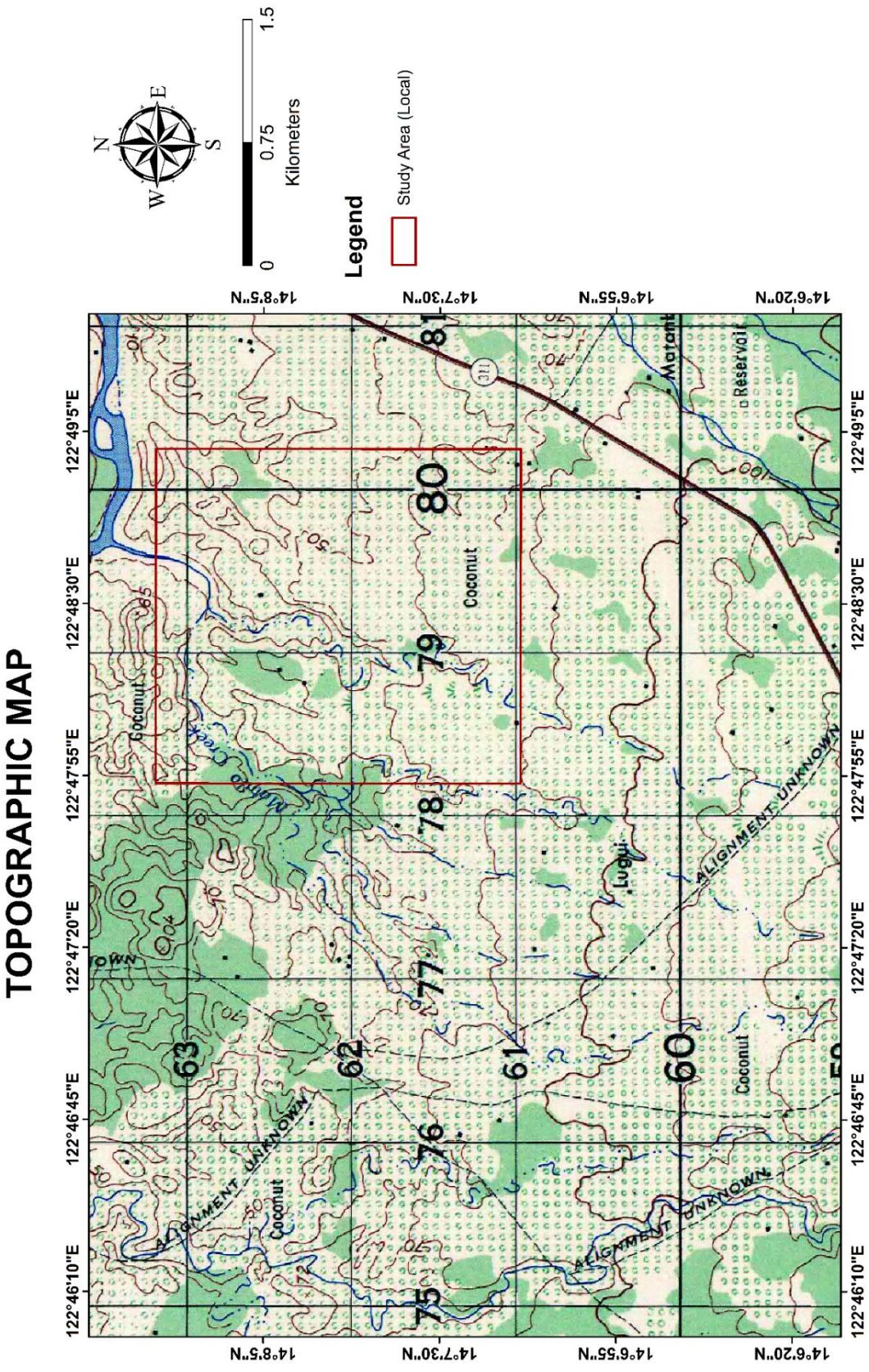

Figure A-8. Topographic map of the study area.

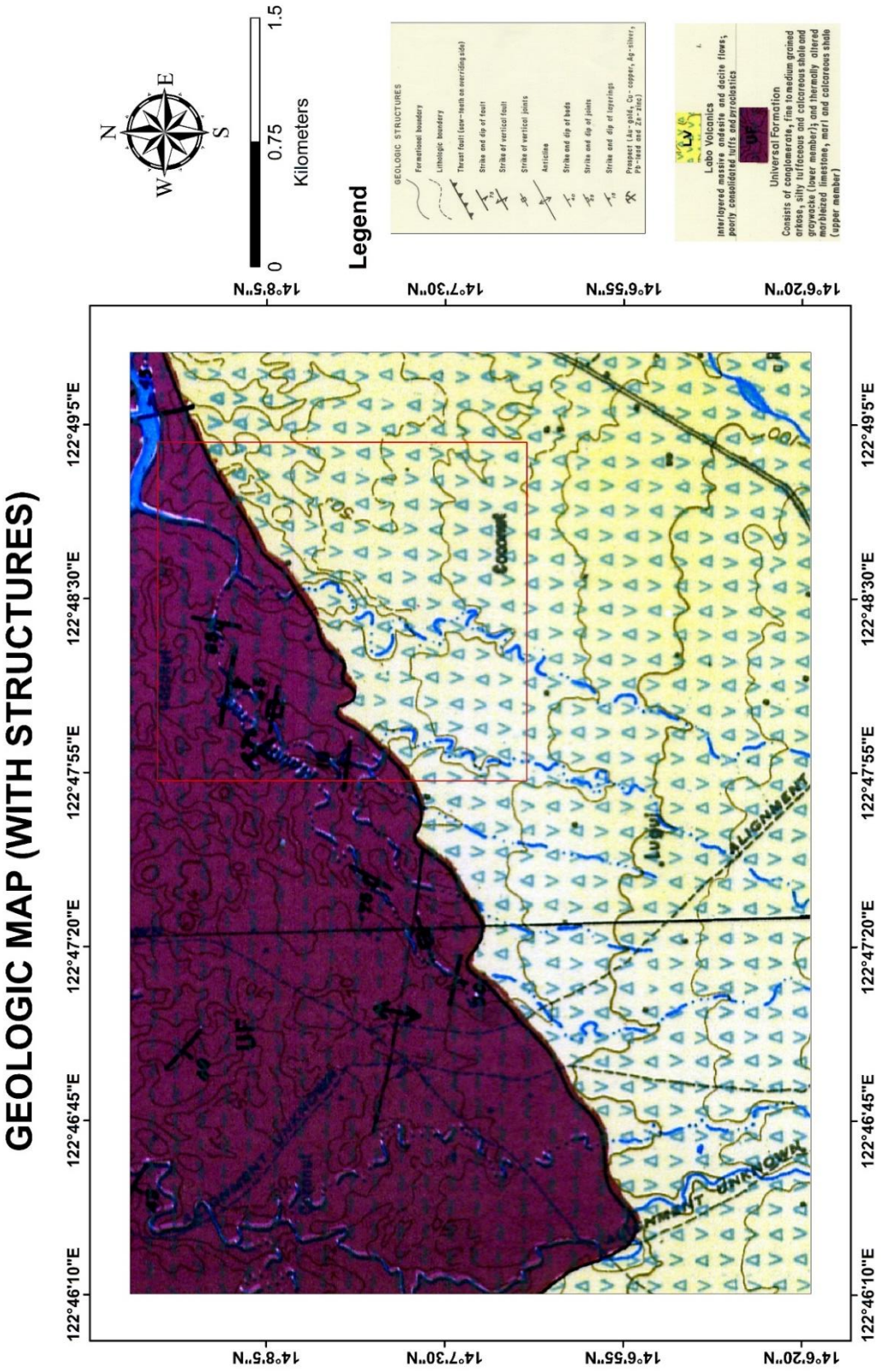

Figure A-9. Geologic map of the study area modified from BMG (1994).

Appendix 5: Representative Remote Sensing Results

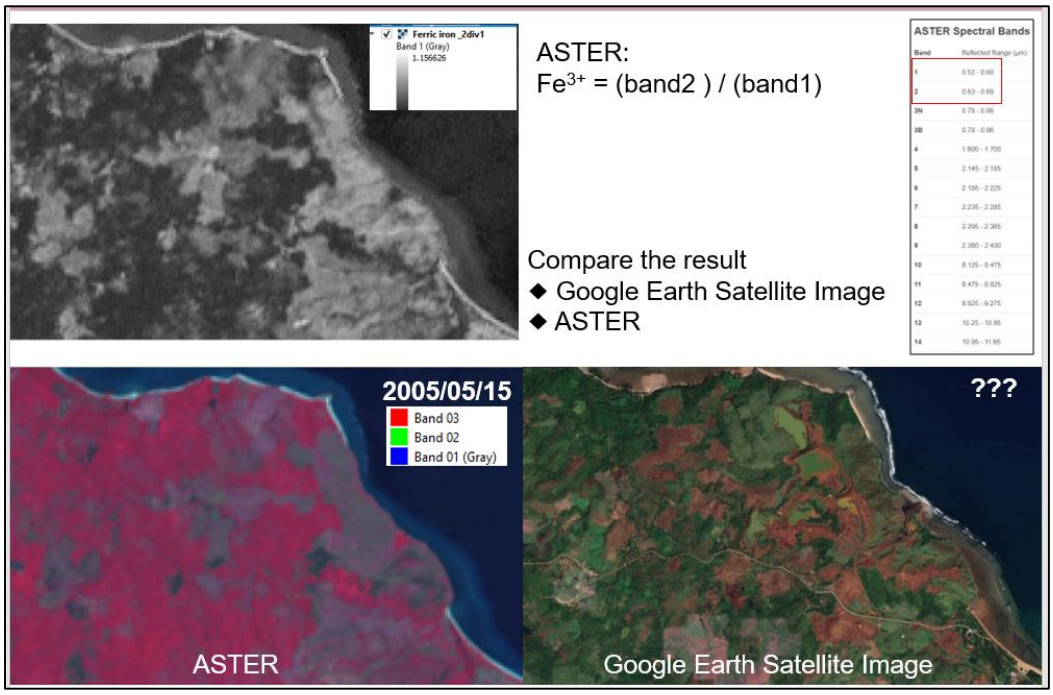

Figure A-10. Ferric iron band combination result compared with Google Earth imagery and ASTER.

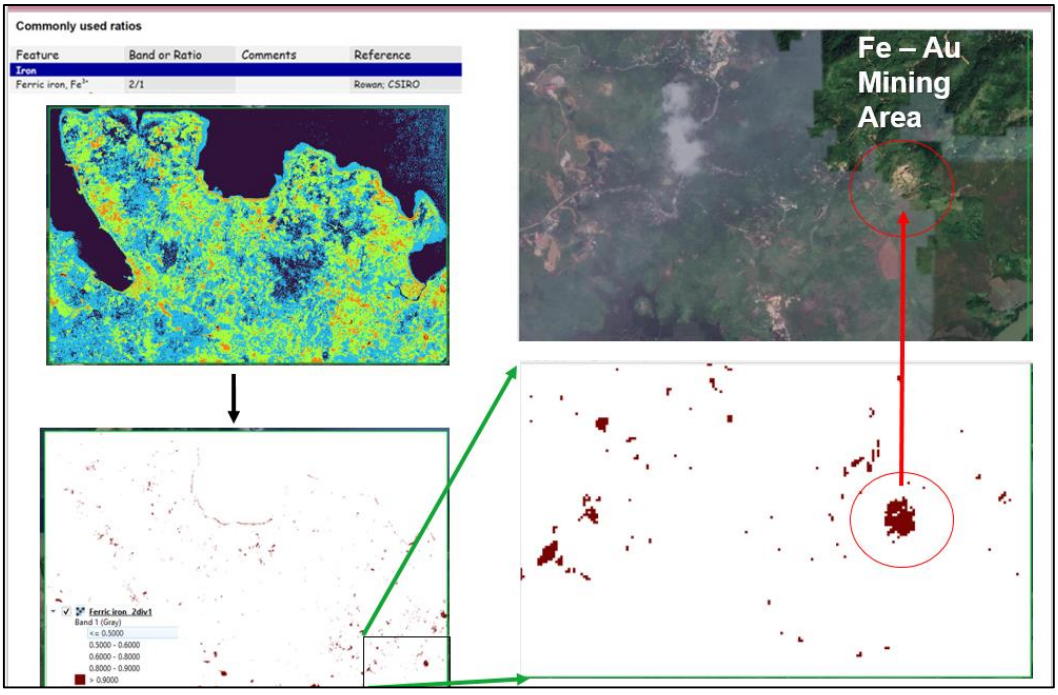

Figure A-11. Setting the threshold for the result of the Ferric Iron ratio band analysis.

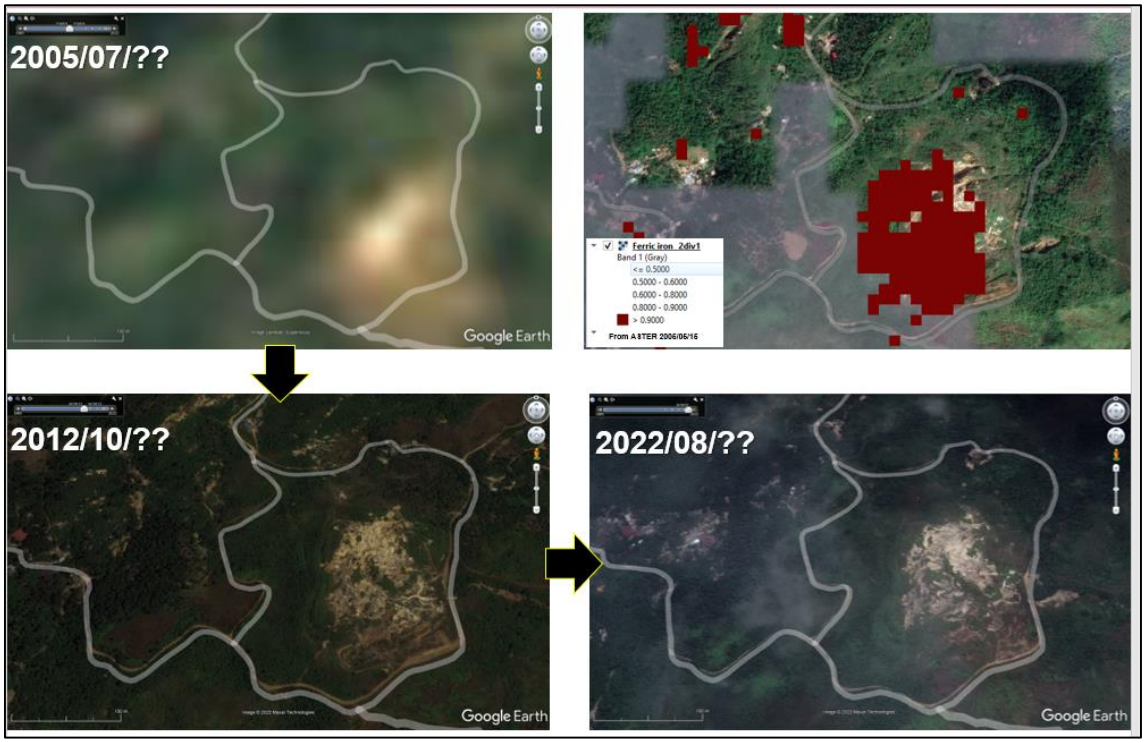

Figure A-12. Comparison between the Ferric Iron ratio band analysis result and Google imagery with different years to confirm the occurrence of the Fe-Au mine.

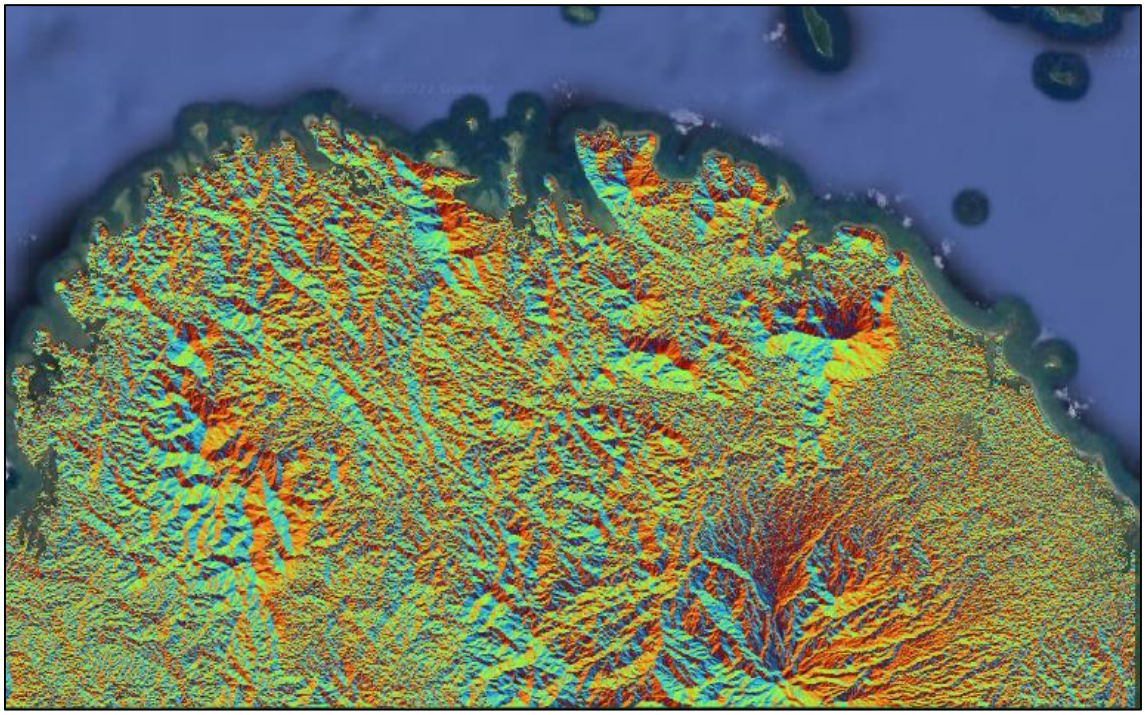

Figure A-13. Result after using the aspect analysis tool in the study area.

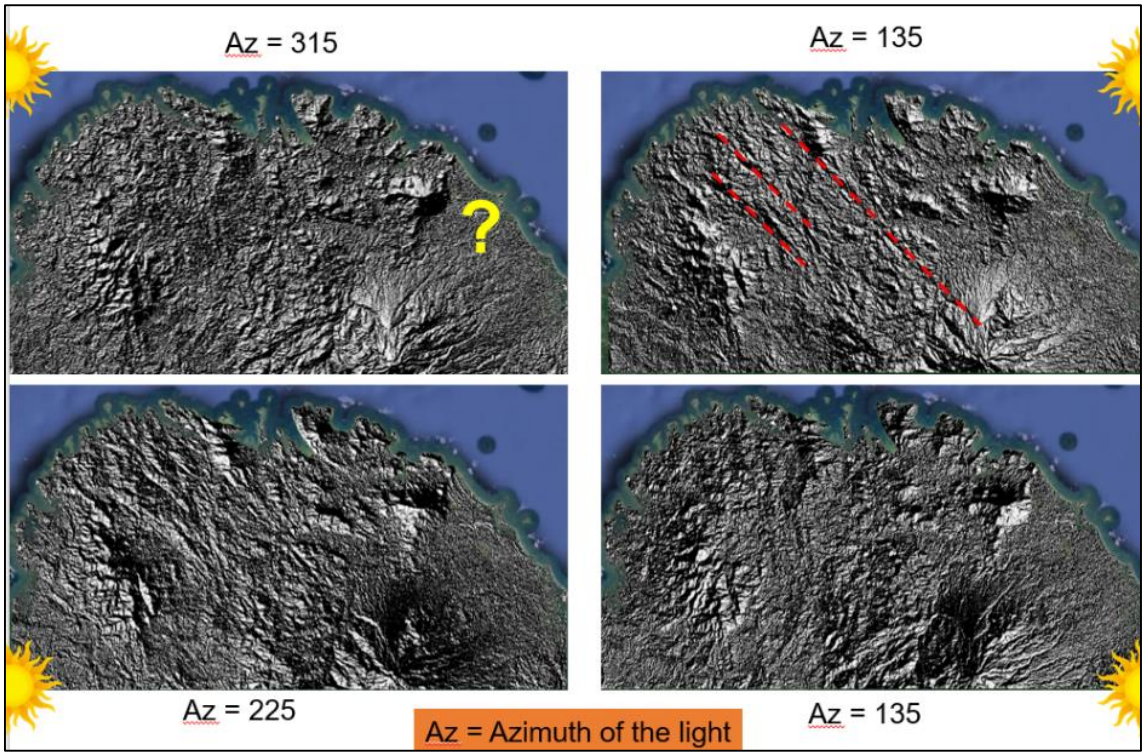

Figure A-14. Hillshade maps showing the differences after changing the azimuth of the light.

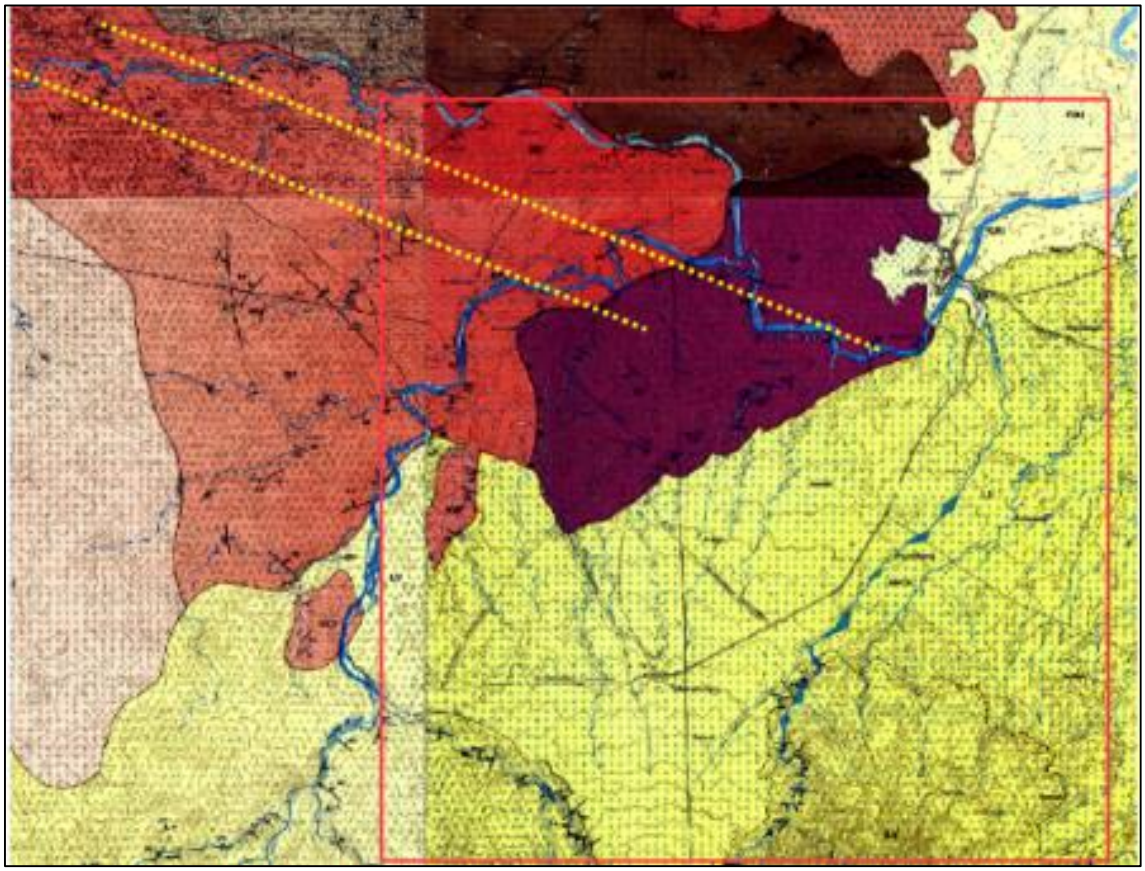

Figure A-15. The comparison between the interpreted lineaments (broken yellow lines) and the geologic map structures. The geologic map is modified from BMG (1994).

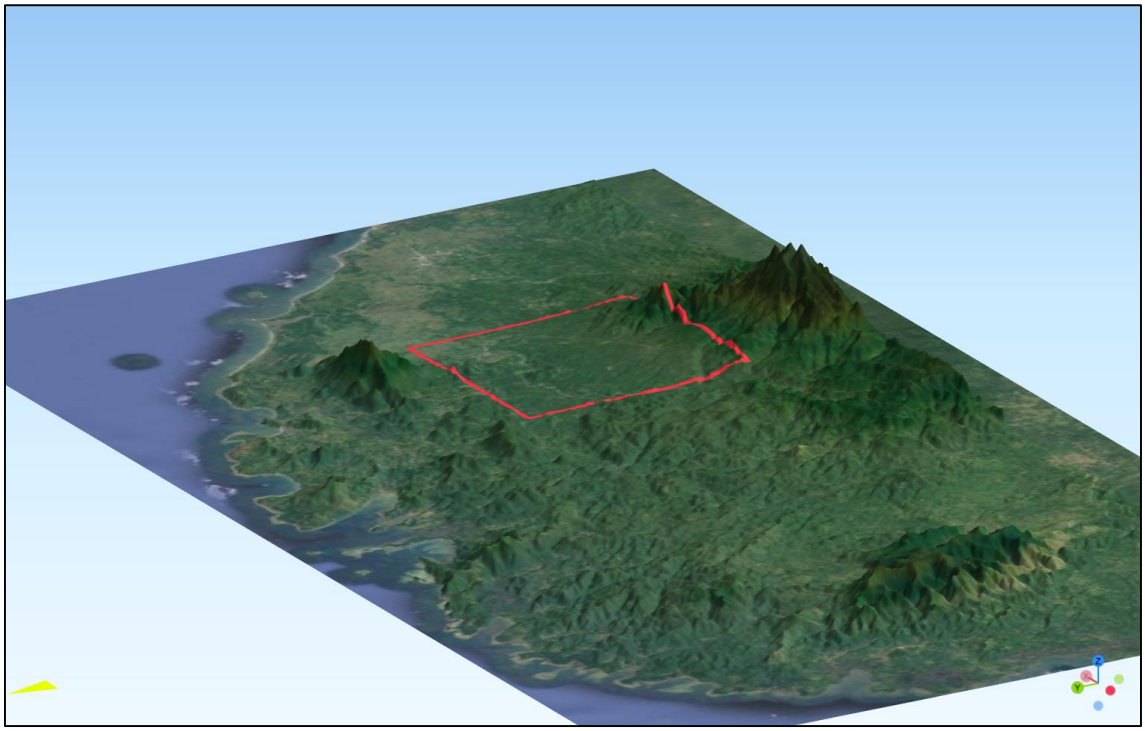

Figure A-16. 3D elevation model of the study area using Qgis2threejs.

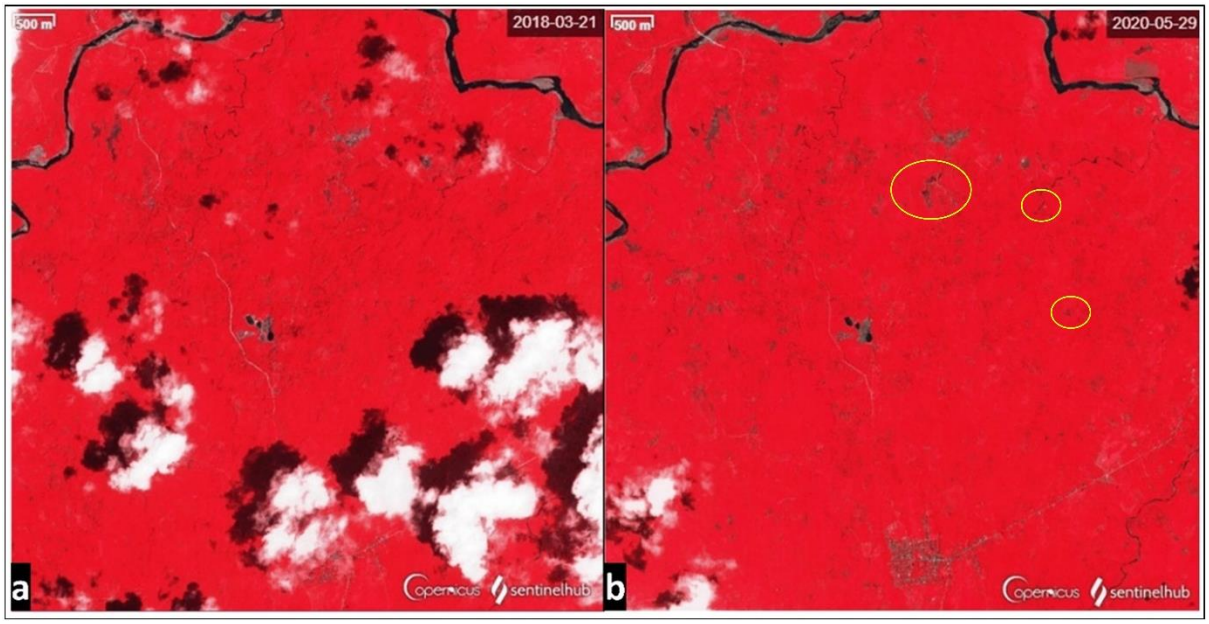

Figure A-17. Land cover changes from (a) 2018 to (b) 2020 in the study area using the Sentinel-2 remote sensing data. Brow colors represent barren lands (yellow circles), which may indicate presence of small-scale mining in the area.

Appendix 6: Photos of the Locations of the ER-IP Surveys

Figure A-18. Photo showing the location of the 2-D ER-IP Profile Line A-A’ center.

Figure A-19. Photo showing the location of the 2-D ER-IP Profile Line B-B’ center.

Figure A-20. Photo showing the location of the 2-D ER-IP Profile Line C-C’ center.

Figure A-21. Photo showing the location of the 2-D ER-IP Profile Line D-D’ center.

Figure A-22. Photo showing the location of the 2-D ER-IP Profile Line E-E’ center.

Figure A-23. Photo showing the location of the 2-D ER-IP Profile Line F-F’ center.

Figure A-24. Photo showing the location of the 2-D ER-IP Profile Line G-G’ center.

Figure A-25. Photo showing the location of the 2-D ER-IP Profile Line H-H’ center.

Figure A-26. Photo showing the location of the 2-D ER-IP Profile Line I-I’ center.

Figure A-27. Photo showing the location of the 2-D ER-IP Profile Line J-J’ center.

Figure A-28. Photo showing the location of the 2-D ER-IP Profile Line K-K’ center.

Figure A-29. Photo showing the location of the 2-D ER-IP Profile Line L-L’ center.

Figure A-30. Photo showing the location of the 2-D ER-IP Profile Line M-M’ center.

Figure A-31. Photo showing the location of the 2-D ER-IP Profile Line N-N’ center.

Figure A-32. Photo showing the location of the 2-D ER-IP Profile Line O-O’ center.

Figure A-33. Photo showing the location of the 2-D ER-IP Profile Line P-P’ center.

Appendix 7: Significant Drill Hole Intersections in the Calibration area

Table A-1. Drillhole data used as a reference in ER-IP Profile O-O' calibration (data from Gordon et al., 2016).

Drillhole code	from (m)	to (m)	interval length(m)	Au (ppm)	Fe (%)	Cu (%)
MDH -093	175.05	177.9	2.85	0.3	7	1.8
MDH -093	191	195	4	0.1	3.2	0.6
MDH -093	276.9	287.8	10.9	0.7	41.5	1.5
MDH -093	296	309	13	1	32.5	1.1
MDH -093	319	325	6	0.6	11.2	0.4
MDH -093	329.9	332	2.1	0.7	7.2	0.3
MDH-101	60.1	64	3.9	0.4	9.7	0.5
MDH-101	263	267	4	0.4	6.7	0.7
MDH-101	270.75	273.15	2.4	0.6	15.2	0.7
MDH-101	279.5	306.35	26.85	1	29.6	1.1
MDH-079	105.9	110	4.1	0.4	6.7	1.5
MDH-068	104	106	2	0.4	6.4	1.6
MDH-068	148.4	153.2	4.8	0.3	5.6	0.6
MDH-068	179.5	182.15	2.65	0.8	22.9	1.9
MDH-068	196	198	2	0.3	5	0.6
MDH-068	208.3	214.2	5.9	0.6	8.4	0.9
MDH-068	218	220	2	2	6	0
MDH-084	42.6	45	2.4	1.1	20.4	0.1
MDH-084	184	193.4	9.4	1.6	10.4	3

Table A-2. Drillhole data used as a reference in ER-IP Profile P-P' calibration (data from Gordon et al., 2016).

Drillhole code	from (m)	to (m)	interval length(m)	Au (ppm)	Fe (%)	Cu (%)
MDH-096	156	195	39	1.7	38	1.2
MDH-096	198.7	202.5	3.8	0.3	3.1	0.6
MDH-057	89.5	111.7	22.2	0.4	4.3	1.2
MDH-057	126	161	35	2.6	52	2.4
MDH-057	165	181.5	16.5	0.7	62.5	0.7
MDH-057	191.25	194	2.75	0.8	50.4	0.7
MDH-057	198	210	12	1.2	8.5	0.8
MDH-057	232	236	4	0.3	5.7	0.6
MDH-057	266	270.5	4.5	0.4	5.7	0.7
MDH-057	273.5	279.8	6.3	0.2	4.6	0.7
MDH-061	123.6	145.47	21.87	11	44.7	0.8
MDH-061	148	164.4	16.4	1	56.1	1